BERGISCHE
UNIVERSITÄT
WUPPERTAL

JÜLICH
Forschungszentrum

Retrieval of atmospheric quantities from remote sensing measurements of nightglow emissions in the MLT region

Dissertation

zur Erlangung des Grades
Doktor der Naturwissenschaften (Dr. rer. nat.)

vorgelegt der

Bergischen Universität Wuppertal
Fakultät für Mathematik und Naturwissenschaften

von

Qiuyu Chen

Wuppertal, 2020

The PhD thesis can be quoted as follows:

urn:nbn:de:hbz:468-20200602-131802-0
[http://nbn-resolving.de/urn/resolver.pl?urn=urn%3Anbn%3Ade%3Ahbz%3A468-20200602-131802-0]

DOI: 10.25926/w7ds-9196
[https://doi.org/10.25926/w7ds-9196]

Abstract

In the mesosphere and lower thermosphere (MLT) region, atomic oxygen and hydrogen are the most abundant reactive trace species and play crucial roles in the photochemistry and energy budget. Meanwhile, the MLT region is profoundly influenced by atmospheric dynamics, and tides and gravity waves are the key features thereof, which can be characterized by, e.g., temperature distributions and variations. A common way for the detection of these atmospheric quantities in the MLT region is by means of remote sensing of airglow emissions from ground or space.

The aim of this work is to offer new insight into atmospheric parameters and distributions in the MLT region. It is focused on constituent and temperature sounding of this region, and presents the retrieval and analysis of atomic oxygen and hydrogen as well as temperature profiles from hydroxyl (OH) and oxygen atmospheric band (O_2 A-band) nightglow observations. Atomic oxygen and hydrogen abundances are obtained from satellite limb radiance measurements of nightglow emissions in the near-infrared region. Temperature profiles are inferred from the rotational structure of nightglow emission lines in a broad spectral region, including observation data from a ground-based instrument and also in-orbit validation data from a new instrument applying the Spatial Heterodyne Interferometer (SHI) technology.

A new dataset of nighttime atomic oxygen density [O] and atomic hydrogen density [H] is derived from the OH(8-4) band emission. The dataset is derived from the atmospheric background radiation observed by the Global Ozone Monitoring by Occultation of Stars (GOMOS) instrument aboard Envisat and with measurements of the Sounding of the Atmosphere using Broadband Emission Radiometry (SABER) instrument aboard the Thermosphere Ionosphere Mesosphere Energetics and Dynamics (TIMED) satellite for the atmospheric background. Raw data are reprocessed into monthly zonal mean values. The dataset spans from 70° S to 70° N in latitude and from 80 km to 100 km in altitude, covering a time period from May 2002 to December 2011 at local times from

10 p.m. to 12 p.m.. The atomic oxygen density peaks at about 95 km and the maximum concentration is in the range of 3-8$\times 10^{11}$ atoms cm^{-3}, while the atomic hydrogen density reaches the peak at around 83 km with a value of 1-4$\times 10^{8}$ atoms cm^{-3}, depending on latitude and season. The annual oscillation (AO), semiannual oscillation (SAO) and the solar cycle impact are clearly visible in the data. This new GOMOS dataset conforms to other published datasets and is consistent with the [O] and [H] datasets obtained from the Scanning Imaging Absorption Spectrometer for Atmospheric CHartographY (SCIAMACHY) OH airglow measurements within $\pm$ 20 %.

The nocturnal mesospheric temperature is obtained from ground-based measurements of the OH(3-1) band emission layer centered near 87 km. The temperature dataset is derived from observations by the GRound-based Infrared P-Branch Spectrometer (GRIPS-F) instrument located in Wuppertal. The temperature profiles fluctuate over the course of night, and the absolute amplitude is varying with season.

For space-based atmospheric observations, a growing trend are miniaturized instruments, which can fly on a nano-satellite platform, e.g., CubeSat. The SHI is a promising technology which fits into this context. With this technology, a minimized limb sounder, Atmospheric Spatial Heterodyne Interferometer Next Exploration (AtmoSHINE), is developed in our research group for temperature detection in the MLT region. An in-orbit demonstration was conducted and the first data analysis is presented herein. The global temperature distribution for the mesopause region is retrieved from measurements of O_2 A-band nightglow emissions. The AtmoSHINE measurements are acquired from four in-orbit tests of the commissioning phase, and the regular observation period of four days. The derived temperature profiles cover the altitude region of around 84 to 96 km with a vertical resolution of 2 km, and its vertical distribution reaches, as expected, its minimum value near the mesopause region. Intercomparisons of the AtmoSHINE measurements with the coincident Optical Spectrograph and Infrared Imager System (OSIRIS) and SABER measurements indicate a general consistency in the observed limb radiances and derived temperature profiles.

Contents

Chapter 1

Introduction

1.1 Composition and structure of the atmosphere

The Earth is a complex system, in which different sub-systems (Atmosphere, Lithosphere, Hydrosphere, Biosphere and Anthroposphere) interact with each other and exchange mass and energy dynamically. The atmosphere is an essential part thereof, which is a layer of gases surrounding the Earth. The atmosphere extends from the ground up to several hundred kilometers, but is relatively thin, as compared to the Earth's radius. It shields the biosphere from strong hazardous solar radiation and harsh outer-space environment (*Riese and Müller*, 2016).

The atmosphere is made up of a mixture of gaseous species. Molecular nitrogen (N_2) and oxygen (O_2) are the prevailing constituents, accounting for $\sim$ 78 % and 21 % of the molecules of the atmosphere, respectively. Other notable components are argon (Ar) and water vapor (H_2O). The atmosphere can be classified by the characteristics of its chemical compositions (*Wallace and Hobbs*, 2006; *Koppmann*, 2015). Up to a height of $\sim$ 100 km, most of the inert species (e.g., O_2, N_2, and carbon dioxide (CO_2)) have a long lifetime, and tend to be well mixed due to the predominant turbulent mixing. They are almost uniform along the altitude in terms of volume mixing ratio (VMR). This region is usually referred to as "homosphere". Whereas above it, molecular diffusion starts to play an important role in that the separation of light and heavy molecules occurs. This region is often referred to as "heterosphere".

Another way to distinguish the atmospheric structure is by its vertical temperature profile (*Chamberlain and Hunten*, 1987; *Brasseur and Solomon*, 2005). Based on the atmospheric temperature gradient signs and changes, the atmosphere is divided into four layers: troposphere, stratosphere, mesosphere and thermosphere. Besides, the upper boundaries of each layer, normally denoted by the suffix "pause", are defined: tropo-

pause, stratopause, mesopause. Figure 1.1 represents a typical profile of the atmospheric temperature structure up to the thermosphere.

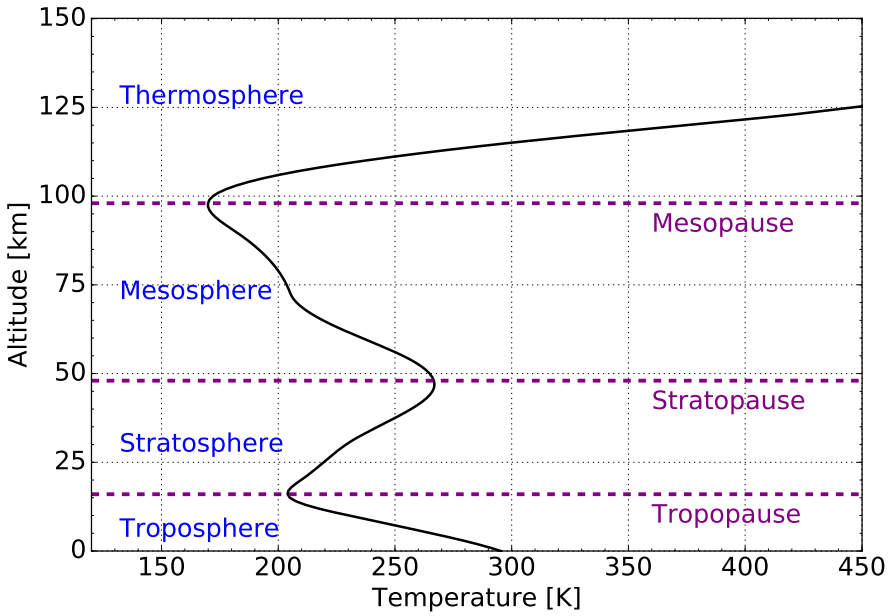

Figure 1.1: Atmospheric temperature structure from the mass spectrometer incoherent scatter (MSIS) simulation model (*Picone et al.*, 2002) for 25° N, 40° E, January 2015.

The bottom layer of the atmosphere is the troposphere, which has a vertical extent of 10-15 km, depending on latitude. The troposphere is characterized by its decreasing temperature with height. This negative temperature gradient, is a consequence of the troposphere being heated by the Earth's surface, which absorbs the solar radiation during the day, and constantly releases the stored energy back to the atmosphere via radiation, conduction and convention (latent and sensible heat). The gradient leads to the instability of the troposphere and relatively well mixed air because of effective turbulence, and most of the weather phenomena (e.g., raining, thunderstorm) occur in this region. At the tropopause, the temperature is almost persistent and acts as a barrier for the vertical exchange of air.

The stratosphere ranges from above the tropopause up to ∼50 km, in which the temperature increases with altitude, and thereby the vertical mixing is strongly inhibited. The stratosphere is rich in ozone, and the main energy source of the temperature increase is the absorbed solar radiation in the ultraviolet (UV) region by O_3. This ozone layer is substantial as it protects the biosphere from the harmful UV radiation. The cooling of this region is dominated by infrared (IR) radiation emitted by CO_2. At the top of the stratosphere, the temperature reaches its local maximum at the stratopause.

Above it, the mesosphere spans from around 50 km up to ∼80 km. The temperature gradient is again negative in this layer, as the (infrared) radiative cooling of CO_2 dominates, and the temperature reaches its minimum at around 95 km, defined as the mesopause. The lowest temperature on the Earth appears here, being around 120 K in summer. Above the mesopause lies the thermosphere (above 100 km), in which the temperature rapidly increases up to 1000 K. The energy comes from the absorption of high-energy UV radiation mostly by O_2 and N_2. This process also leads to the dissociation of molecules and the ionization of atoms. The atmospheric number density is very low, thus the relatively high temperatures, are not related to high heat capacity and transfer.

1.2 The mesosphere and lower thermosphere (MLT)

The mesosphere and lower thermosphere (MLT) region ranges approximately from 50 km up to ∼110 km. It is the transition zone between the lower and the upper atmosphere, where the temperature gradient sign changes from negative to positive. The structure of the MLT relies on the interaction of dynamic, radiative and photochemical processes. The MLT has the remarkable characteristics that it is much colder in summer than in winter, as a consequence of adiabatic cooling in summer and warming in winter associated with air upwelling and downwelling. This dynamic motion in the MLT is a substantial part in the global mean circulation, and is mainly driven by the energy and momentum deposited through gravity wave (GW) breaking and dissipation (*Garcia and Solomon*, 1985; *Smith*, 2012a,b).

The MLT energy mainly originates from the solar UV radiation, absorbed via the photolysis of O_2 and O_3 (e.g. *Riese et al.*, 1994). O_2 absorbs the solar radiation mainly at the Lyman-α line (121.6 nm), in the Schumann Runge continuum (130-175 nm) and bands (175-200 nm) and in the Herzberg continuum (200-242 nm). O_3 absorption mostly occurs in the Hartley band (∼ 200-310 nm) (*Brasseur and Solomon*, 2005). The absorption of solar radiation by H_2O in the UV region and CO_2 at 1-4.3μm are two minor sources also contributing to the energy budget.

The MLT temperature is partially increased due to the kinetic energy, directly released from the collisions of photo-dissociation products with other species (i.e., solar heating, the translational motions of molecules converted from solar energy). Around 70 % of the absorbed solar energy is converted to chemical energy (*Strobel*, 1978) when it breaks the molecular bonds of absorbing species and is then stored in the produced species. The energy can be redistributed by transport over large distances, before it is released via the subsequent exothermic chemical reactions, which significantly heat up the MLT. Most of those reactions are involved with odd hydrogen and odd oxygen species,

Table 1.1: Most important photolysis and chemical reactions heating up the MLT region, and their corresponding heating rates and heating efficiencies (*Mlynczak and Solomon*, 1993; *Brasseur and Solomon*, 2005; *Mlynczak et al.*, 2013a).

No.	Reaction	Heating rate	Heating efficiency	Enthalpy
R1	$O + O + M \rightarrow O_2 + M$	0-4 K day^{-1}	Unity	-119.40 kcal mol^{-1}
R2	$O + O_2 + M \rightarrow O_3 + M$	0-3 K day^{-1}	Unity	-25.47 kcal mol^{-1}
R3	$O + O_3 \rightarrow O_2 + O_2$	0-0.1 K day^{-1}	Unity	-93.67 kcal mol^{-1}
R4	$H + O_3 \rightarrow OH + O_2$	0-4 K day^{-1}	0.6	-76.90 kcal mol^{-1}
R5	$OH + O \rightarrow H + O_2$	0-1 K day^{-1}	Unity	-16.77 kcal mol^{-1}
R6	$HO_2 + O \rightarrow OH + O_2$	0-1 K day^{-1}	Unity	-53.27 kcal mol^{-1}
R7	$H + O_2 + M \rightarrow HO_2 + M$	0-1 K day^{-1}	Unity	-49.10 kcal mol^{-1}
A1	$O_2 \xrightarrow{h\nu} O + O$	0-6 K day^{-1}	1 (60 km) - 0.8 (100 km)	-
A2	$O_3 \xrightarrow{h\nu} O + O_2$	0-3 K day^{-1}	0.95 (60 km) - 0.7 (100 km)	-

as listed in Tab. 1.1. Reaction R1 to R7 are the seven most relevant reactions influencing the MLT heating budget (*Brasseur and Offermann*, 1986; *Mlynczak and Solomon*, 1991; *Riese et al.*, 1994). The corresponding heating rates for both the O_2 and O_3 photolysis and chemical reactions are also summarized in this table. The total chemical heating rate is typically around 1-15 K day^{-1} from 80 to 100 km. Besides of heating, part of the stored energy is radiated via the spontaneous emissions of photochemically excited product species, e.g., hydroxyl radical (OH^*).

The MLT energy budget is balanced by the terrestrial cooling via radiative IR cooling by CO_2, H_2O and O_3 (*London*, 1980; *Dickinson*, 1984; *Fomichev et al.*, 2004; *Feofilov and Kutepov*, 2012). Infrared emissions emitted from vibrationally excited CO_2 molecules at 15 μm are most relevant. They are the dominant cooling sources, with a corresponding cooling rate of around 2-15 K day^{-1} (*Williams and Rodgers*, 1972; *Mlynczak et al.*, 2013a). The 9.6 μm O_3 band and IR H_2O bands have small contributions to the radiative cooling.

Dynamical heating is also of importance in the MLT global energy balance (*Fomichev et al.*, 2002). It includes heat advection associated with global circulation, heating converted from gravity wave breaking or dissipation, heating related to eddy mixing and convective instability. Dynamical heating can be either positive or negative, depending on the conditions. Besides, heat deposited from the thermosphere via molecular diffusion also plays a role in the total energy budget, particularly at the mesopause, which could reach up to 15 K day^{-1} heating rate (*Brasseur and Solomon*, 2005).

1.3 Atomic oxygen and hydrogen in the MLT

Atomic oxygen (O) and atomic hydrogen (H) are of the most abundant reactive trace species in the MLT region and play crucial roles in the photochemical equilibrium and energy balance of this region. As depicted in Sect. 1.2, most exothermic chemical reactions, which dominate the MLT heating, are associated with atomic oxygen and hydrogen (*Brasseur and Offermann*, 1986; *Riese et al.*, 1994; *Mlynczak et al.*, 2013a, 2014). Besides, the collisions between O and infrared-active greenhouse gases like CO_2 predominantly lead to radiative cooling in this region (*Mlynczak et al.*, 2013b). Also, the decrease of atomic hydrogen is an indicator of the existence of polar mesospheric clouds (PMCs), because water vapor, the source of H, starts to condense into cloud ice and the mesopause region is dehydrated (*Siskind et al.*, 2008). It is usually related to extremely low temperature conditions.

Atomic oxygen is mainly generated by the photolysis of molecular oxygen and ozone, and transported downward by diffusion and mixing from the thermosphere to the mesosphere. It is removed by chemical reactions, of which the three body combination (R2 in Tab. 1.1) is most relevant. Its lifetime varies from weeks at 100 km to minutes at 60 km due to its increasing chemical loss rate with decreasing altitude (*Brasseur and Solomon*, 2005). Below 80 km, due to the relatively short photochemical lifetime, atomic oxygen can be considered to be in photochemical equilibrium. Thus, its concentration shows a clear diurnal variation. In the mesopause and lower thermosphere, the spatial and temporal distribution of atomic oxygen is strongly influenced by dynamical processes. Its peak concentration is normally at the altitude range of 90 to 100 km, in dependence of latitude and season. Both molecular and eddy diffusion play important roles in its vertical transport. Advection also contribute to this distribution, while associated (zonal mean) meridional transport affects the latitudinal distribution (*Smith and Marsh*, 2005; *Russell et al.*, 2005; *Smith et al.*, 2010; *Swenson et al.*, 2018).

Atomic hydrogen is produced primarily through photo-dissociation of H_2O in the MLT (*Mlynczak et al.*, 2014). Its chemical lifetime is very short, around seconds at 60 km and increasing to hours at 100 km, which is much shorter than the time constant of dynamic transport. Atomic hydrogen is considered to be in photochemical equilibrium below 100 km. It has the rapid reaction sink with O_3 (R4 in Tab. 1.1), associated with the release of a large amount of heat and the generation of highly vibrationally excited OH^* radicals ($0 <$ vibrational level (v) ≤ 9), subsequently leading to the formation of OH Meinel band airglow emissions in the mesosphere (*Meinel*, 1950a,b; *Mlynczak and Solomon*, 1993; *Kaufmann et al.*, 2013; *Smith et al.*, 2015). The H concentration peak layer in the MLT is around 80-90 km. Above 100 km, atomic hydrogen becomes long-lived, and is continuously transported upward via molecular diffusion due to its lowest molecular weight.

The measurement of atomic oxygen and hydrogen dates back to before the satellite era when the MLT region was explored by means of sounding rocket experiments, hosting mass spectrometers (O measurements by *Offermann and Grossmann* (1973) and *Offermann et al.* (1981)), silver film sensor (O measurements by *Henderson* (1974)) or resonance fluorescence lamps (for instance, O measurements by *Dickinson et al.* (1974), *Dickinson et al.* (1980), *Sharp* (1980), *Offermann et al.* (1981), *Sharp* (1991) and *Gumbel et al.* (1998), and H measurements by *Sharp and Kita* (1987)). A most recent rocket-borne in situ experiment was conducted by the utilization of the solid electrolyte sensors (*Eberhart et al.*, 2019; *Grygalashvyly et al.*, 2019). These experiments are capable of providing direct in situ measurements of atomic oxygen or hydrogen, although it is difficult to obtain a consistent global picture of absolute density values from these measurements.

However, these measurements lead to the development of photochemical models of the Earth's day- and nightglow, which enables the use of proxies of the atomic oxygen and hydrogen abundance obtained from remote sensing observations. Suitable proxies for O are airglow emissions (e.g., OH^*, O_2^*, $O(^1S)$) and thermal emissions (e.g., O_3 at 9.6 μm), in combination with corresponding photochemical models. The OH airglow emissions are associated with the spontaneous radiative transitions of excited OH^* radicals. These OH^* radicals are mainly produced by the chemical reaction of ozone with atomic hydrogen (R4 in Tab. 1.1). Highly excited molecular oxygen (O_2^*) in a metastable state is generated from atomic oxygen recombination (R1 in Tab. 1.1) and can be de-excited by collisions with O or O_2, while the $O(^1S)$, O_2 A-band and infrared $O_2(^1\Delta_g)$ band emissions are radiated from the products. These airglow emissions rely on the atomic oxygen recombination or ozone destruction and can be considered as a kind of chemical afterglow. Therefore, they are frequently used as a proxy to retrieve atomic oxygen abundances. Usually, H can be simultaneously derived along with O from the OH airglow observations (see Sect. 2.3).

Atomic oxygen and hydrogen densities were inferred from airglow emissions measured by rocket-borne instruments (via e.g., $O(^1S)$ emissions by *Dandekar and Turtle* (1971) and *Donahue et al.* (1973), OH emissions by *Evans and Llewellyn* (1973) and *Good* (1976), O_2 A-band emissions by *Melo et al.* (1996) and *Hecht et al.* (2004)) or $O_2(^1\Delta_g)$ emission by *Evans et al.* (1968) and *Evans et al.* (1988). Several rocket experiments have been performed which combined the airglow emissions with direct atomic oxygen (and hydrogen) measurements (for instance, the Energy Transfer in the Oxygen Nightglow (ETON) campaign in 1982 (*Greer et al.*, 1986; *Hedin et al.*, 2009)). Observations of $O(^1S)$ green line emissions (*Thomas and Young*, 1981; *Thomas*, 1981; *McDade et al.*, 1986), O_2 A-band and $O_2(^1\Delta_g)$ emissions (*Witt et al.*, 1984; *McDade et al.*, 1987a; *Murtagh et al.*, 1990) and OH airglow (e.g., in (8-3) band (*Murtagh et al.*, 1987; *McDade et al.*, 1987b) and (3-1) band (*Ulwick et al.*, 1987)) were studied with simultaneously measured atomic oxygen abundance to investigate the underneath pho-

tochemical processes and mechanisms, and an improvement of our knowledge in processes has been achieved (*McDade et al.*, 1984; *Murtagh et al.*, 1986; *McDade and Llewellyn*, 1986, 1988).

More recent satellite measurements were conducted by the Sounding of the Atmosphere using Broadband Emission Radiometry (SABER) instrument on the Thermosphere-Ionosphere-Mesosphere Energetics and Dynamics (TIMED) satellite. The instrument detects OH^* nightglow radiances at 2.0 and 1.6 μm as well as the $O_2(^1\Delta_g)$ emission at 1.27 μm and O_3 thermal emissions at 9.6 μm (*Smith et al.*, 2010; *Mlynczak et al.*, 2013c, 2014, 2018; *Panka et al.*, 2018). The Scanning Imaging Absorption Spectrometer for Atmospheric CHartographY (SCIAMACHY) instrument on the European Environmental Satellite (Envisat) measured the $O(^1S)$ green line at 557.7 nm, O_2 A-band at 762 nm and a broad range of OH^* airglow emissions (*Kaufmann et al.*, 2013, 2014; *Lednyts'kyy et al.*, 2015; *Zhu et al.*, 2015; *Zhu and Kaufmann*, 2018, 2019). The Optical Spectrograph and Infrared Imager System (OSIRIS) instrument on the Odin satellite probes the O_2 A-band, $O_2(^1\Delta_g)$ emission and OH^* airglow at 725-745 nm and 770-815 nm (*Llewellyn et al.*, 2004; *Sheese et al.*, 2011, 2014). During the period of 1991-1995, the Wind Imaging Interferometer (WINDII) instrument aboard the Upper Atmosphere Research Satellite (UARS) also observed the $O(^1S)$ green line and OH(8-3) band emissions at 734 nm(*Russell and Lowe*, 2003; *Russell et al.*, 2005). Other instruments include the high resolution Doppler imager (HRDI) aboard UARS, which also observes O_2 A-band emissions (*Hays et al.*, 1993); the Imager of Sprites and Upper Atmospheric Lightning (ISUAL) instrument aboard the Formosat-2 satellite, which detects the $O(^1S)$ green line emissions (*Gao et al.*, 2012); and the Solar Mesosphere Explorer (SME) spacecraft, which measures the O_2 ($^1\Delta_g$) band and OH(7-5) band emission at 1.87 μm (*Thomas*, 1990).

1.4 Atmospheric waves and temperature observations in the MLT

The MLT region is deeply influenced by dynamics. The much lower temperature at the summer pole than at the winter pole, which deviates from its radiative balanced temperature, is associated with the global meridional circulation mainly driven by gravity wave breaking and dissipation. The distribution of chemical constituents is also affected by transport, dependent on the relative relationship between the chemical lifetime and the time constant for transport. Typically, in atmospheric model, dynamic motions can be characterized in different grid scales: large scale advection related to global meridional circulation, and sub-grid scale diffusion and mixing (*Andrews et al.*, 1987; *Holton*, 2004). The meridional circulation corresponds to a net zonal mean transport from the

summer pole to the winter pole in the mesosphere, normally represented as the transformed Eulerian mean (TEM) or residual circulation (*Dunkerton*, 1978). It is accompanied by small fluctuations, i.e., eddies, which can diffuse chemical constituents into different regions (*Garcia and Solomon*, 1983; *Smith*, 2004; *Garcia et al.*, 2007; *Liu*, 2009). Turbulences associated with gravity wave breaking, along with damped waves or tides, are the dynamical processes that contribute to the eddy diffusion (*Smith et al.*, 1987; *Liu et al.*, 1999; *Li et al.*, 2005; *Grygalashvyly et al.*, 2012). Molecular diffusion also participates in the transport of chemical compositions and heat, as part of dynamic processes (*Beagley et al.*, 2010; *Smith et al.*, 2011).

Waves are key dynamic features in the atmosphere (*Brasseur and Solomon*, 2005). They are defined as disturbances or oscillations propagating in time and space. Among various types of waves, gravity waves and their effects dominate the dynamics of the MLT (*Fritts and Vincent*, 1987; *Fritts and Alexander*, 2003), as discussed above. GWs are usually described in a simple way as small or mesoscale oscillations which occur when air parcels are vertically displaced from a stably stratified background state (*Fritts and Alexander*, 2003; *Alexander et al.*, 2010). The oscillations are caused by buoyancy, and hence GWs are also called as buoyancy waves. GWs are visible as fluctuations in density, temperature, wind or other parameters (e.g., airglow emissions) of the atmosphere. The primary restoring force which balances the acceleration is gravity. Considering a larger scale in time or space, GWs will also be influenced by the Earth rotation, namely the Coriolis force. Typically, the GW horizontal wavelength spectrum ranges from ten to a thousand kilometers, and the vertical wavelength varies from several hundred meters to tens of kilometers (*Preusse et al.*, 2009; *Ern et al.*, 2011), and vertically GWs can extends from troposphere up to mesosphere.

GWs are generated in the lower atmosphere as they can be orographically excited when air flows over mountains, or produced by non-orographic sources, such as convention or jet stream instabilities (*Fritts and Alexander*, 2003; *Kim et al.*, 2003). GWs can propagate upward into middle and upper atmosphere carrying a bulk of momentum. They can accelerate or decelerate the background flow when they are transient, breaking or dissipating (*Lindzen*, 1981; *Andrews et al.*, 1987). At a certain point, which is referred as the critical level, where the phase speed of GWs equals to the zonal wind speed of the background atmosphere, GWs will be absorbed, and cannot propagate further. Despite of this filtering effect, when GWs propagate to a higher altitude, as the kinetic energy is conserved while the air density significantly decreases, the amplitudes of GWs grow exponentially large so that GWs eventually break. The GW breaking and dissipation provide a large amount of momentum flux forcing that drives the mesospheric meridional circulation.

Atmospheric tides are another important component in the MLT dynamics, which are global-scale waves with a period of exactly 24 h (diurnal), 12 h (semidiunral) or an

integer fraction thereof (e.g., terdiurnal, quaterdiurnal). They have high impact on the MLT dynamic features, and as with GWs, they can cause large amplitude perturbations in temperature, wind field, and other atmospheric parameters such as the concentration of chemical species. They are not yet fully understood, and show increasing interest and were a major research topic in recent years (*Smith*, 2012a; *Vincent*, 2015).

Tides in the MLT mainly origin from the troposphere and stratosphere, predominantly excited by heating, and propagate upward (*Lindzen*, 1967; *Forbes*, 1982a,b). In the troposphere, the heating comes from the absorption of solar infrared radiation by H_2O and from latent heat release, while in the stratosphere the solar heating from the absorption of UV radiation by O_3 is the main source. The classical tidal theory from *Chapman and Lindzen* (1970) explains tidal forces well and can predict tides under an isothermal and stationary atmospheric condition with the Hough mode projections. Atmospheric tides can be classified into migrating (Sun-synchronous) and non-migrating (Sun-asynchronous) tidal components, of which migrating tides follow the motions of the Sun and propagate westward, while the non-migrating tides can move either westward or eastward, and even be stationary (*Volland*, 1988; *Hagan and Forbes*, 2003). Besides, non-migrating tides are primarily excited by latent heat release in tropical convective clouds (*Hagan and Forbes*, 2003; *Oberheide and Forbes*, 2008), and are therefore associated with weather activities in the troposphere.

Planetary waves, also referred to as Rossby waves, are planetary-scale waves with low zonal wavenumbers, which contribute significantly to variability in dynamical processes of the middle atmosphere, and bring large disturbances in the MLT region. Planetary waves are mainly generated in the lower atmosphere, owing to the conservation of potential vorticity when air flows over large-scale mountains or through land-sea contrast (*Holton*, 2004; *Wallace and Hobbs*, 2006), and are related to the Earth's rotation and Coriolis parameter. Those waves propagate westward relative to the background flow and can be stationary (forced mode) or travel in longitude with periods of 2, 5, 10 and 16 days (free mode) (*Smith*, 2012a; *Smith and Perlwitz*, 2015). Rossby waves can only propagate vertically upward where the background zonal wind is westerly, which mainly occurs during winter. The MLT planetary waves can be either from the upward propagation of planetary waves in the stratosphere or in situ induced by the dissipation of gravity waves.

In the MLT region, global meridional circulation is mainly driven by the momentum deposited from GW breaking and dissipation. The interaction of GWs and other waves such as tides and quasi-stationary Rossby waves, influences the momentum budget and wave forcing, and consequently leads to a large variability in this region. To obtain information about these waves and dynamical processes, a conventional and effective way is to quantity wave motions by observations of atmospheric parameters, for instance, temperature measurements.

In situ temperature measurements provided by high-altitude balloons, radiosondes or sounding rockets are normally limited to a certain altitude range, and their horizontal coverage is also restricted to local scale (*Allen and Vincent*, 1995; *Vincent et al.*, 2007; *Alexander et al.*, 2010). Hence, in the MLT region, temperature data are typically derived from remote sensing measurements of CO_2 thermal emissions or absorptions of solar radiation by CO_2 at 15 μm (*Mertens et al.*, 2004), 12.6 μm (*Riese et al.*, 1999), 4.3 μm (*Boone et al.*, 2005) or 2.7 μm (*Marshall et al.*, 2011), applying the non local thermodynamic equilibrium (non-LTE) model (*von Clarmann et al.*, 2003). The measurements cover the entire altitude range of MLT from around 60 to 100 km for both day- and nighttime conditions, and the temperature uncertainties are normally on the order of 2 to 10 K (*García-Comas et al.*, 2012; *Dawkins et al.*, 2018). Optionally, atmospheric temperatures can be inferred from observations of airglow emissions, assuming a rotationally LTE condition (see Sect. 2.4). Application examples are nighttime OH emissions centered around 87 km with measurement uncertainties on the order of 3 to 8 K (*Offermann et al.*, 1983; *von Savigny et al.*, 2004), and O_2 A-band for both day and night centered around 90 km with uncertainties on the order of 2 to 6 K (*Sheese et al.*, 2010, 2012). Besides, radar and lidar are also techniques commonly deployed, as they deliver temperature measurements with high vertical and spatial resolution (*Chanin and Hauchecorne*, 1981; *Jacobi et al.*, 2007; *Fritts et al.*, 2016).

Various ground-based instruments including passive airglow imagers (*Zhang et al.*, 1993; *Sargoytchev et al.*, 2004; *Wachter et al.*, 2015) or active radars and lidars (*Parameswaran et al.*, 2000; *Schöch et al.*, 2004; *Tsuda*, 2014), provide a significant amount of temperature data and wave characteristics over the last several decades. In addition, global networks of ground-based stations are being built and the coherent observations from various locations (*Suzuki et al.*, 2013; *Wachter et al.*, 2015) offer a good opportunity to resolve GW parameters (e.g., wavelength, phase speed) with a broad spatial coverage and to investigate latitudinal and longitudinal variations of tides.

Recent developments in satellite-borne instruments have enabled analyses of wave structures and dynamical processes from a much wider perspective (*Preusse et al.*, 2009; *Smith*, 2012a), as satellite limb soundings is capable of providing altitude-resolved temperature data with global coverage in the middle and upper atmosphere. Some important satellite missions are: the Cryogenic Infrared Spectrometers and Telescopes for the Atmosphere (CRISTA) recorded temperature data and wave activities during two space shuttle missions (*Offermann et al.*, 1999; *Riese et al.*, 1999; *Ward et al.*, 1999; *Oberheide et al.*, 2002); the Limb Infrared Monitor of the Stratosphere (LIMS) on Nimbus-7 delivered an analysis of GWs and tides from temperature measurements (*Lieberman*, 1991; *Fetzer and Gille*, 1994); the High Resolution Dynamics Limb Sounder (HIRDLS) aboard the Aura satellite offered information about wave features from temperature data (*Lieberman et al.*, 2004; *Ern et al.*, 2011); the SABER temperature data provide insight into the characterization of tides and waves (*Xu et al.*, 2009; *John and Kumar*, 2012).

GW activities were also reported from observations by the Microwave Limb Sounder (MLS) aboard UARS (*Wu et al.*, 2006).

1.5 Remote sensing techniques and scientific applications

In contrast to the direct *in situ* measurements, *remote sensing* measures in an indirect way where specific radiation from a target in a distance is detected, interpreted and inversed to infer the intended physical quantities (*Liou*, 2002). The remote sensing technique can be classified into different systems. By the type of the radiation source passive and active remote sensing are distinguished. Passive remote sensing measures the natural radiation emitted from the Sun and other astronomical objects (e.g., solar radiation, starlight), or from the Earth-Atmosphere system (e.g., thermal emissions, airglow, aurora), while active remote sensing utilizes artificially generated radiation (e.g., laser). Besides, the remote sensing technique can be characterized by the spectral region of the radiation, for instance, UV, visible, IR and microwave, which are the most popular for atmospheric applications. In view of the hosting platform, the remote sensing instrument can be ground-based or air/space-borne (i.e., aboard sounding rocket, aircraft, space shuttle or satellite).

Since the last decades, the remote sensing/sounding technique has been rapidly developed and widely applied in the field of atmospheric research (*Houghton et al.*, 1984; *Stephens*, 1994). This technique can provide continuous measurements of atmospheric parameters on regional- or global-scale at a comparably moderate expense, while satisfying temporal and spatial resolution can be retained, as already discussed in Sect. 1.3 & 1.4. In this work, remote sensing measurements of the terrestrial nightglow emissions are applied to obtain the atmospheric profiles of atomic oxygen, atomic hydrogen and temperature in the MLT region. The application of remotely sensed data inevitably involves the understanding of the underlying nightglow emissions, and the inversion of the measurements, which are thoroughly discussed in the following Chap. 2 & 3. The quantities of atomic oxygen and hydrogen are derived from the satellite-based observations of OH airglow emissions (Chap. 4), while temperature profiles are retrieved from the ground-based OH nightglow emission data (Chap. 5), and from satellite-borne measurements of the O_2 A-band (Chap. 6).

Chapter 2

Atmospheric nightglow modeling

Airglow is a common atmospheric phenomenon that faint lights illuminate the upper layers of the atmosphere. The radiation originates from excited molecules and atoms as a result of various photochemical reactions initiated by solar energy in this region. Airglow is regarded as the response of the atmosphere to the solar radiation and manifests itself as an indicator of the atmospheric characteristics and variations (*Khomich et al.*, 2008). It has long been studied since it was first documented in the early 20th century (*Yntema*, 1909; *Chamberlain*, 1995). Owing to the advanced developments in spectroscopic techniques, airglow emissions can be detected by the total intensity (e.g., photometer) or resolved in the fine spectral distribution (e.g., spectrometer, interferometer). These measured data provide a good opportunity to characterize the underlying structures and distributions of atmospheric constituents, such as the abundances of atomic oxygen and hydrogen, or the temperature distribution and variation. Thus, knowing the nature of photochemical processes behind the airglow emissions is crucial. The hydroxyl (OH) and oxygen atmospheric band (O_2 A-band) emissions are two prominent emissions in the MLT region, particularly during the night (airglow can happen in both day- and nighttime). In this chapter, the production mechanisms of OH and O_2 A-band emissions are thoroughly reviewed.

2.1 Hydroxyl nightglow emission

The OH airglow was firstly discovered and identified by *Meinel* (1950a,b), thus, it is also named as Meinel band. Since that time, the OH airglow has been widely observed and investigated by many ground-based, rocket-borne and later space-borne spectroscopic instruments (*Broadfoot and Kendall*, 1968; *Offermann et al.*, 1983; *McDade et al.*, 1987b; *Mende et al.*, 1993; *Osterbrock et al.*, 1996; *Osterbrock et al.*, 1997).

The OH airglow origins from the spontaneous radiative decays of ro-vibrationally excited OH^* radicals up to the vibrational level v=9, and the radiative transitions can occur within Δv=1 to 6. The OH airglow appears in a wavelength range from 0.5 up to 4.5 μm (*Meinel*, 1950a, Tab. 6, Fig. 4) and it is considered as an important emission in the IR spectral range. The airglow intensity varies in different wavelengths, and the brightest lines are near 1.6 and 2.8 μm (*Migliorini et al.*, 2015). For a large number of OH emission lines, the atmosphere is optically thin for cloud free conditions, that the emissions can totally transmit without absorption by the gaseous medium (e.g., H_2O) when they propagate. Hence, OH airglow can be detected on ground. Vertically, the OH emissions peak near 87 km with a thickness of around 8 km (*Baker and Stair*, 1988), and different vibrational levels have a difference in emission peak altitudes by several kilometers (*McDade*, 1991; *von Savigny et al.*, 2012).

The measurements of the OH airglow emissions have been applied in many aspects to investigate atmospheric properties and dynamics. The variations in the OH airglow intensities are a proxy to characterize the MLT dynamic activities of GWs and planetary waves, and longterm changes such as the solar cycle response (*Fukuyama*, 1976; *Taylor et al.*, 1987; *Yee et al.*, 1997; *Pedatella and Forbes*, 2012; *Gao et al.*, 2016). The rotational temperature derived from the OH airglow measurements is also used for the study of wave structures, dynamical processes and longtime variations (*Takahashi et al.*, 1998; *Offermann et al.*, 2010; *Kramer et al.*, 2015; *López-González et al.*, 2017; *Silber et al.*, 2017; *Wüst et al.*, 2018). The frequently measured spectra, which are spectrally resolved for temperature retrieval, are mostly confined in a single band in the near-IR range, such as the OH(6-2) band (*Greet et al.*, 1997; *French et al.*, 2000), the OH(8-3) band (*Takahashi et al.*, 1984; *Williams*, 1996), the OH(3-1) band (*Bittner et al.*, 2002; *von Savigny et al.*, 2004; *Oberheide et al.*, 2006; *Pautet et al.*, 2014), the OH(8-4) band (*Suzuki et al.*, 2009) and the OH(7-3) band (*Suzuki et al.*, 2008). Simultaneous observations of multiple bands covering nearly all vibrational levels are also carried out in several ground stations worldwide (*Krassovsky et al.*, 1977; *Takahashi and Batista*, 1981; *Cosby and Slanger*, 2007; *Noll et al.*, 2015, 2016). As already described in Sect. 1.3, the OH airglow measurements are also extensively used to infer the oxygen and hydrogen abundances in many studies.

2.1.1 OH emission characterization

To understand the activities of OH airglow emissions, it is necessary to understand the potential energy configurations of excited OH^* molecules. Generally, there are three energy states in a molecule, which are electronic, vibrational and rotational levels (*Rigamonti and Carretta*, 2009), and the corresponding transitions are electronic, vibrational and rotational transitions, respectively. The electronic state can be considered as the

molecular orbitals, related to the chemical bond of the molecule in terms of internuclear distance. The vibrational state is related to the vibrational motions of molecules, and the rotational state is associated with the molecular rotations. A diagram of the potential curve representing the related energy states of a heteronuclear diatomic molecule, such as OH, is given in Fig. 2.1.

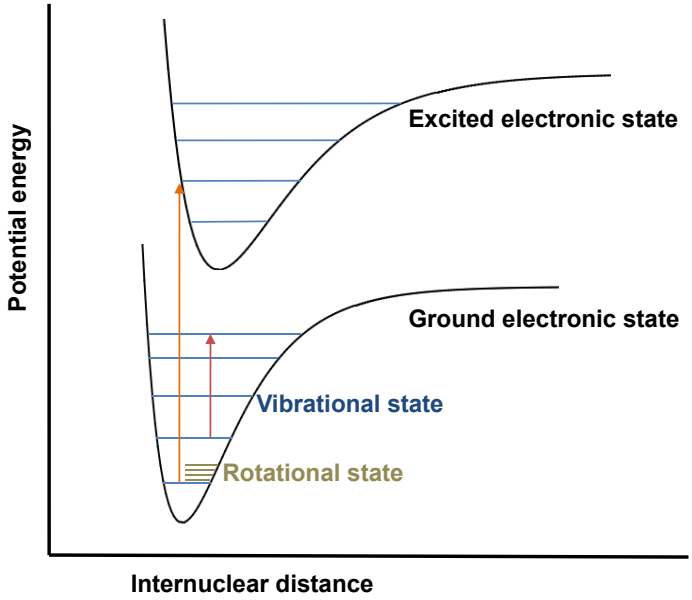

Figure 2.1: Diagram of the potential energy curve of the electronic, vibrational and molecular states versus the internuclear distance for a hypothetical molecule. The potential energy curve is an asymmetric parabola for a heteronuclear diatomic molecule, such as OH, and is often named as the Morse potential.

The OH airglow emissions arise as a consequence of spontaneous radiative transitions of highly ro-vibrationally excited OH^* radicals, from a higher vibrational level v' to a lower one v''. The occurrence probability can be described by the band Einstein coefficients $A_{v',v''}$ ($v'' \leq v'$):

$$OH(v') \xrightarrow{A_{v',v''}} OH(v'') + h\nu \tag{R2.1}$$

where $h\nu$ indicates the energy of emitted photon with the Planck constant h and the frequency ν, following the Plank-Einstein relation.

These transitions are within the ground electronic state $X^2\prod$ of OH^* radicals. The OH molecule has one unpaired electron, which contributes a spin of 1/2, and thus the spin multiplicity is 2S+1=2 (doublet). Due to the interaction of the electron spin and the orbital angular momentum (*Rousselot et al.*, 2000), a doublet structure exists in the

ground electronic state, which consists of two sub systems of $X^2\prod_{1/2}$ and $X^2\prod_{3/2}$. The $X^2\prod_{1/2}$ energy level is higher than $X^2\prod_{3/2}$.

One OH vibrational transition is accompanied by rotational transitions with the change of the electronic dipole moment. They are called ro-vibrational transitions, as schematically shown in Fig. 2.2. One vibrational level can have a number of rotational levels, as numbered by the total angular momentum quantum number J (considering the angular momentum quantum number K plus the electronic spin -1/2 for $X^2\prod_{1/2}$ or +1/2 for $X^2\prod_{3/2}$). The rotational transitions are guided by the selection rules of $\Delta J=\pm 1$, of which the transitions with ΔJ=-1 are defined as P branch, ΔJ=+1 as R branch and ΔJ=0 as Q branch, respectively. For instance, one OH ro-vibrational transition in $X^2\prod_{3/2}$ from v'=3 to v''=1 with J''=5/2 and ΔJ=+1 can be denoted as OH(3-1) band R1(2.5) line. This transition probability is also evaluated by the Einstein coefficients $A^{(v',J')}_{(v'',J'')}$ as:

$$\mathrm{OH}(v',J') \xrightarrow{A^{(v',J')}_{(v'',J'')}} \mathrm{OH}(v'',J'') + h\nu \qquad \text{(R2.2)}$$

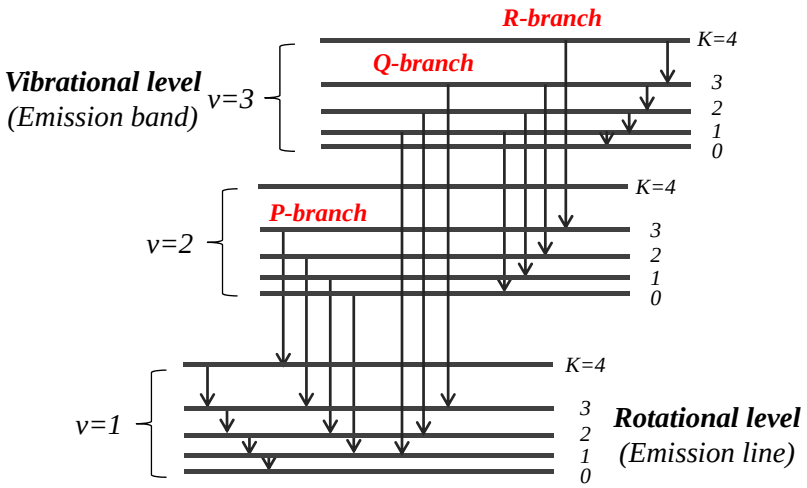

Figure 2.2: Schematic diagram of the ro-vibrational transitions from a higher ro-vibrational state to a lower one. The vibrational transitions correlate to the emission band while rotational transitions correspond to the emission lines in a resolved band spectrum.

Considering the parity of the electronic wave functions to reflection in a plane through the internuclear axis (*Osterbrock et al.*, 1996), each rotational line can be split

into two sub components by Λ-type doubling. The intensities of these two sub lines are presumed to be identical under the thermodynamic equilibrium. The Λ-type doublets are normally considered to be unresolved lines that their intensities are summed up for one rotational line.

Many datasets of Einstein coefficients are available for OH radicals by now, as provided by *Mies* (1974); *Turnbull and Lowe* (1989); *Goldman et al.* (1998); *van der Loo and Groenenboom* (2007, 2008); *Rothman et al.* (2013); *Brooke et al.* (2016); *Gordon et al.* (2017). These coefficient sets are calculated on the basis of the experimental data for the line intensity and line position, and they mainly differ in the dipole moment functions used in the calculation (*Cosby and Slanger*, 2007). Therefore, large differences are found among these sets (*Liu et al.*, 2015, Tab. 1). OH Einstein coefficients from *van der Loo and Groenenboom* (2007, 2008), *Brooke et al.* (2016) and HITRAN molecular spectroscopic database (*Rothman et al.*, 2013; *Gordon et al.*, 2017) are the three latest datasets, and *Noll et al.* (2015) found smaller uncertainties in HITRAN database when rotational temperature is derived from ground-based observations of 25 OH bands. HITRAN 2016 Einstein coefficients (*Gordon et al.*, 2017) remained unchanged in comparison to the HITRAN 2012/2008 (*Rothman et al.*, 2013, 2009), which are used in this work.

2.1.2 OH nightglow photochemistry

The OH^* radicals are mainly formed via the exothermic ozone-hydrogen reaction (R4 in Tab. 1.1), as already discussed in Sect. 1.3. The reacting O_3 is mainly generated by the three body combination reaction involved with atomic and molecular oxygen (R2 in Tab. 1.1) (*Bates and Nicolet*, 1950; *Heaps and Herzberg*, 1952):

$$O + O_2 + M \xrightarrow{k_{OO_2M}} O_3 + M \tag{R2.3}$$

$$H + O_3 \xrightarrow{k_{HO_3}} OH(v \leq 9) + O_2 \tag{R2.4}$$

M indicates background molecules, i.e., N_2 or O_2; k denotes the rate coefficient for the corresponding chemical reaction, normally obtained from laboratory experiments, theoretical calculation or empirical estimations. The values for k_{OO_2M} and k_{HO_3} are both taken from *Sander et al.* (2011), as collected in Appx. A.1.

Krassovsky (1963) proposed an additional mechanism for the OH^* production (R7 & R6 in Tab. 1.1):

$$H + O_2 + M \xrightarrow{k_{HO_2M}} HO_2 + M \tag{R2.5}$$

$$HO_2 + O \xrightarrow{k_{HO_2O}} OH(v \leq 6) + O_2 \tag{R2.6}$$

whereas controversial opinions about its potential contribution have been raised by different researchers and not well settled till now (*Turnbull and Lowe*, 1983; *Sivjee and Hamwey*, 1987; *Kaye*, 1988; *Makhlouf et al.*, 1995). *Xu et al.* (2012) concludes that this mechanism is not necessary for OH airglow modeling in the mesopause region.

The total production rate of excited radicals P_{OH^*} can be written as follows:

$$P_{OH^*} = k_{HO_3} \cdot [H] \cdot [O_3] \tag{2.1}$$

The notations in parentheses denote the concentrations of the corresponding species.

The nascent production rate fraction of one vibrational level is given as follows:

$$P_v = f_v \cdot P_{OH^*} \tag{2.2}$$

The nascent OH^* radicals are distributed to different vibrational levels ($v \leqslant 9$), partitioned by the quasi-nascent branching factor f_v. The values of f_v have been provided by a number of researchers as *Charters et al.* (1971), *Ohoyama et al.* (1985), *Klenerman and Smith* (1987), *Mlynczak and Solomon* (1993) and *Adler-Golden* (1997). The ones published by *Adler-Golden* (1997) are employed this work (see Appx. A.1).

The excited OH^* radicals can be de-excited to lower vibrational levels or totally deactivated to the ground state by spontaneous radiative transitions (photon emissions, airglow) or collisional relaxation with other molecules, while OH^* radicals can also be totally removed by chemical reaction. Under the assumption of photochemical equilibrium, the production of OH^* radicals in each vibrational level equals to its loss (*Zhu*, 2016). The processes related to the production and loss of vibrationally excited OH^* are illustrated in Fig. 2.3.

The collisional quenching process can have different pathways with respect to the relaxation products. The first case is the single-step or cascade pathway, that the radicals in a higher vibrational state are depopulated to a lower state with a quantum number of one ($\Delta v=1$). The second case is called the sudden-death, i.e., the excited radicals are totally de-excited to the ground state. The last one is the multi-quantum quenching pathway as a mixture of the above two cases, and radicals in a higher state are depopulated

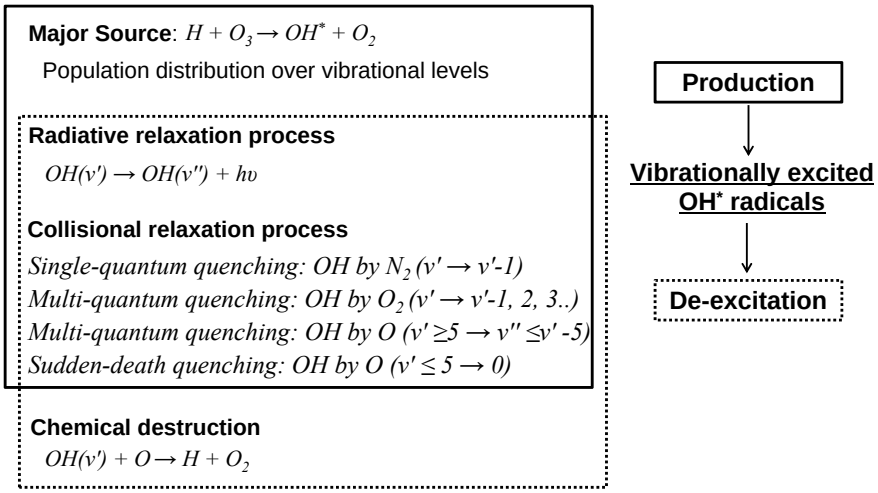

Figure 2.3: The schematic digram summarizing the major production and loss schemes of the excited OH^* radicals.

to a lower state with multiple quantum numbers (Δv=1, 2, 3, ...). For the collisional quenching of OH^*, O_2, N_2 and O are the most relevant and important species. Among various relaxation schemes, the collision process of OH^* with molecular oxygen O_2 is well simulated by the multi-quantum quenching model with coefficients recommended by *Adler-Golden* (1997) and *Xu et al.* (2012). As molecular nitrogen N_2 is not as efficient as O_2, a single-step quenching model is preferred for the collision of OH^* with N_2 and the corresponding coefficients are combined from *Adler-Golden* (1997) and *Kalogerakis et al.* (2011). Additionally, considering the low temperature conditions in the mesopause, a factor of 1.18 and 1.4 was applied to the collisional coefficients of OH with O_2 and N_2 (*Lacoursiére et al.*, 2003; *Panka et al.*, 2017). The collisional rate coefficients used in this work are summarized in Appx. A.2.

There has been a longstanding debate about the mechanism behind the collisional relaxation between OH^* and atomic oxygen, especially about the probable relaxation pathways. Also, a competition channel exits, which is the chemical reaction of OH^* with atomic oxygen (R5 in Tab. 1.1). Laboratory results indicated that the OH^* radicals in high vibrational levels tend to deactivate remarkably fast (*Kalogerakis et al.*, 2011). *Russell and Lowe* (2003), *Smith et al.* (2010), *Xu et al.* (2012) and *von Savigny et al.* (2012) suggested that the sudden-death quenching model is most suitable for OH^* quenching with O. *Kaufmann et al.* (2008) found that a mixture of both-sudden death and single-step quenching models is favorable to simulate the results. A new quenching pathway has been recently proposed by *Sharma et al.* (2015) and *Kalogerakis et al.* (2016), that OH^* radicals from $v' \geq 5$ are directly deactivated to a lower state

of $0 \leq v'' \leq v'-5$:

$$OH(v' \geqslant 5) + O(^3P) \xrightarrow{k_{OHO}} OH(0 \leqslant v'' \leqslant v'-5) + O(^1D) \qquad \text{(R2.7)}$$

The quencher is the ground-state atomic oxygen $O(^3P)$, and the metastable atomic oxygen in the first electronic excited state $O(^1D)$ is one of the products. This process is found to deliver reasonable results when incorporated in the modeling of CO_2 and OH emissions (*Panka et al.*, 2017; *Kalogerakis et al.*, 2018; *Panka et al.*, 2018). In this work, this new relaxation pathway is used for quenching of OH($v \geqslant 5$) with O, while the sudden-death model is adopted for OH($v<5$).

2.1.3 Volume emission rate of OH nightglow

Considering all the processes contributing to a certain vibrational transition, the volume emission rate (in photons cm^{-3} s^{-1}) of the corresponding band can be expressed by the following formula:

$$V_{v',v''} = \left(P_{v'} + \sum_{i=1}^{9-v'} \left[P^*_{v'+i} \cdot \frac{A_{v'+i,v'} + C_{v'+i,v'}}{A_{v'+i} + C_{v'+i}} \right] \right) \cdot \frac{A_{v',v''}}{A_{v'} + C_{v'}} \qquad (2.3)$$

$P_{v'}$ is the initial nascent production rate in vibrational level v' as calculated by Eq. 2.2, while $P^*_{v'+i}$ denotes the total production rate from the nascent production $P_{v'+i}$, and also from the radiative transition and the collisional quenching of higher levels. $P_{v'}$ and $P^*_{v'+i}$ are in units of cm^{-3} s^{-1}. A is the Einstein coefficient, either for the total band from a higher vibrational state v' to a lower state v'', $A_{v',v''}$, or the total probability of transitions from a vibrational level v', $A_{v'}$. C refers to the loss rate by collisional relaxation and chemical reaction, either for the rate for quenching from a higher state to a lower state $C_{v'+i,v'}$, or the total removal rate from a vibrational state $C_{v'}$. $C_{v'+i,v'}$ and $C_{v'+i,v'}$ are in units of s^{-1}, and $C_{v',v''}$ is calculated as:

$$C_{v',v''} = [OH^*(v')] \cdot \left(k_{OHO_2(v',v'')} \cdot [O_2] + k_{OHN_2(v',v'')} \cdot [N_2] + k_{OHO(v',v'')} \cdot [O] \right) \qquad (2.4)$$

Based on Eq. 2.3, as an example, the total volume emission rate (VER) of the OH(8-4) band is modeled and calculated for nighttime conditions in the MLT region. The simulated results are shown in Fig. 2.4. The OH(8-4) band covers a wavelength range of 930 nm to 1000 nm. The background atmosphere profile, including the O_3, O, H, O_2 and N_2, were taken from the Hamburg Model of the Neutral and Ionized Atmosphere (HAMMONIA) (*Schmidt et al.*, 2006). As shown in the plot, the emission peak altitude of OH(8-4) band is around 88 km, and the full width at half maximum (FWHM) of the emission layer thickness is about 9 km.

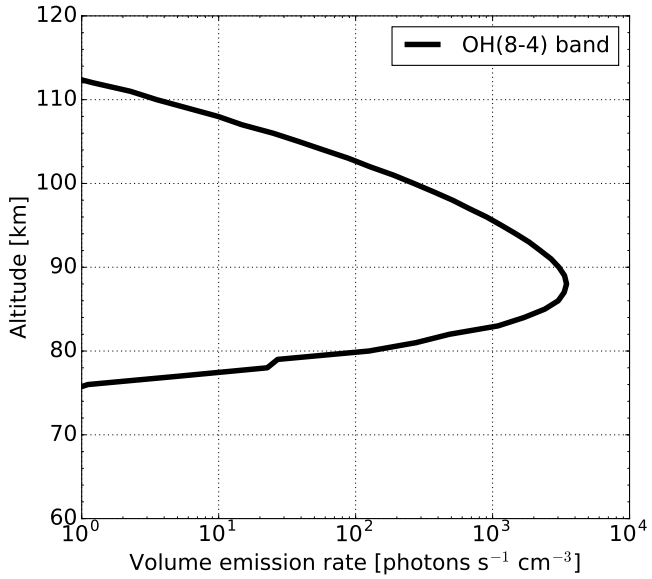

Figure 2.4: The simulated volume emission rate for the OH(8-4) band nightglow versus altitude, for 30° N, 0°, in January with the HAMMONIA atmospheric data.

2.1.4 Rotational structure of OH emission

It is widely accepted and applied, that the OH^* radicals are rotationally in local thermodynamic equilibrium (LTE) at least for low rotational levels, and the OH rotational temperature is close to the ambient kinetic temperature (*Chamberlain*, 1995; *Perminov et al.*, 2007; *Kalogerakis et al.*, 2018). Under thermal equilibrium condition, OH rotational populations in each vibrational level are supposed to follow the Boltzmann distribution at a rotational temperature T_{rot}. It is noted that high rotational states (J$\geqslant$5.5) are found to be strongly overpopulated and deviate from the predicted Boltzmann distribution that no longer persist the LTE condition (*Cosby and Slanger*, 2007; *Noll et al.*, 2015; *Oliva et al.*, 2015). Thus, for a ro-vibrational transition with low rotational quantum states, the line intensity (VER of one emission line) can be calculated as:

$$I^{(v',J')}_{(v'',J'')} = V_{v',v''} \cdot \frac{g'}{Q_{v'}(T)} \cdot \exp(-\frac{hcE_{v'}(J')}{kT}) \cdot \frac{A^{(v',J')}_{(v'',J'')}}{A_{v',v''}} \tag{2.5}$$

$E_{v'}(J')$ denotes the rotational term energy and T refers to the rotational temperature with the Boltzmann constant k, and the speed of light c. g' refers to the statistical weight (also the degeneracy factor) of the upper state and can be calculated as follows when all electronic, vibrational and rotational transitions are assigned (*Šimečková et al.*, 2006):

$$g = g_{rot} = (2J+1) \cdot g_s \cdot g_i \tag{2.6}$$

where (2J+1) is the degeneracy for each rotational state J, and g_s is the state-dependent nuclear spin degeneracy, which is 1 for all the rotational levels of OH molecule, while g_i is the state-independent nuclear spin degeneracy, which is 2 for OH molecule (Λ-type doubling). In this case, g′=2(2J′+1) (*Turnbull and Lowe*, 1989). $Q_{v'}(T)$ indicates the rotational partition function of the vibrational state v′:

$$Q_{v'}(T) = \sum_{J'} \left[g' \cdot \exp(-\frac{hcE_{v'}(J')}{kT}) \right] \tag{2.7}$$

With the equations above, the rotational structure of one OH band can be calculated, as illustrated in Fig. 2.5 as an example of fine structure in the OH(8-4) band.

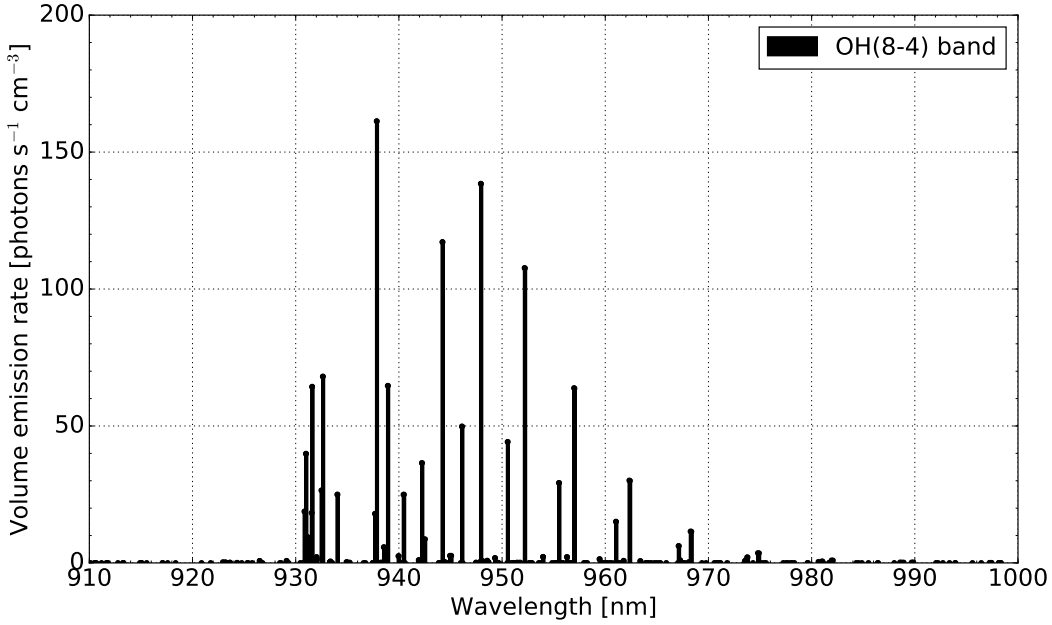

Figure 2.5: Line intensity versus wavelength as a function of the rotational structure of the OH(8-4) band within the wavelength region of 910 to 1000 nm at 89.5 km, for 30° N, 0°, in January, with the HAMMONIA model data as atmospheric background input and the HITRAN 2016 database for Einstein coefficients.

The Einstein coefficient $A_{v',v''}$ indicates the thermally averaged transition probability for the total band, as used in R2.1, Eq. 2.3, and Eq. 2.5, and can also be calculated providing thermal equilibrium (*Turnbull and Lowe*, 1989):

$$A_{v',v''} = \sum_{J'} \sum_{J''} \left[\frac{g'}{Q_{v'}(T)} \cdot \exp(-\frac{hcE_{v'}(J')}{kT}) \cdot A^{(v',J')}_{(v'',J'')} \right] \tag{2.8}$$

2.1.5 OH nightglow observations

The monochromatic emission line is influenced externally, e.g., by collisions and the thermal Doppler broadening when it passes through the atmosphere. It results in the emission line broadening and the observed emissions are nonmonochromatic spectral lines with finite width (*Liou*, 2002). There are two types of line broadening: the collision-induced pressure broadening, and the thermal-motion-induced temperature broadening. In the middle and upper atmosphere, the pressure is decreasing exponentially, and hence the temperature broadening dominates, which is given by the Doppler profile as follows:

$$D(\nu) = \frac{1}{\alpha_D \sqrt{\pi}} \cdot \exp\Big(-[\frac{\nu - \nu_0}{\alpha_D}]^2 \Big) \tag{2.9}$$

where $D(\nu)$ is the line shape broadening for one emission line centered at a wavenumber of ν_0, α_D denotes the Doppler width:

$$\alpha_D = \frac{\nu_0}{c} \cdot \sqrt{\frac{2kT}{m}} \tag{2.10}$$

Here m refers to the mass of the molecule.

The Doppler broadening FWHM is equivalent to $\alpha_D\sqrt{ln2}$. Assuming a temperature of 200 K in the mesosphere, the corresponding broadening FWHM for OH(8-4) band emissions is around 0.0015 nm. It is by orders of magnitude smaller than the spectral resolution of instruments applied in this work ($\geq$ 0.13 nm), and therefore the line broadening effect can be omitted for the OH nightglow observation in this case.

The emitted airglow radiance is transfered through the atmosphere before it reaches the instrument. Hence, the airglow observations are the slant-path radiances integrated along the instrument line of sight (LOS). If the atmosphere is described by simplified discrete shells, given a satellite-borne instrument for limb observation, the optical path for the radiative transfer of the emissions can be represented by segments of LOS with different atmospheric layers, as illustrated in Fig. 2.6. With the optically thin atmosphere considered, the OH airglow observed at the instrument entrance is the accumulative emission along the instrument LOS. Along the LOS, the emission from the lowest tangent point contributes the most to the total integrated radiance. One example of the simulated OH airglow spectra from limb observation is given in Fig. 2.7.

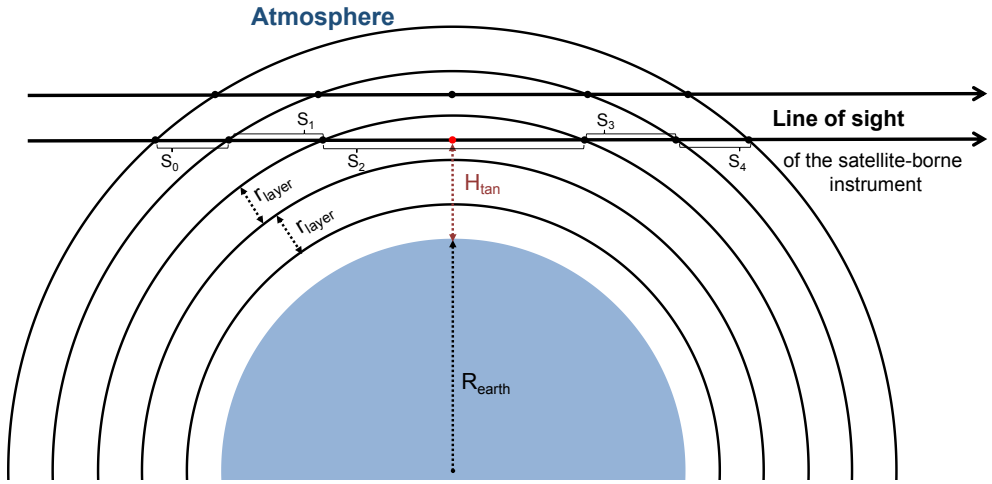

Figure 2.6: The slant paths for the transfer of airglow emission in the atmosphere for limb observation. The atmosphere is simplified as discrete uniform layers. The instrument LOS intersects with the atmospheric layers, and the segments are denoted by S_0 to S_4. The red dot indicates the tangent points of the instrument LOS. The Earth radius, tangent altitude and layer thickness are denoted as R, H and r respectively.

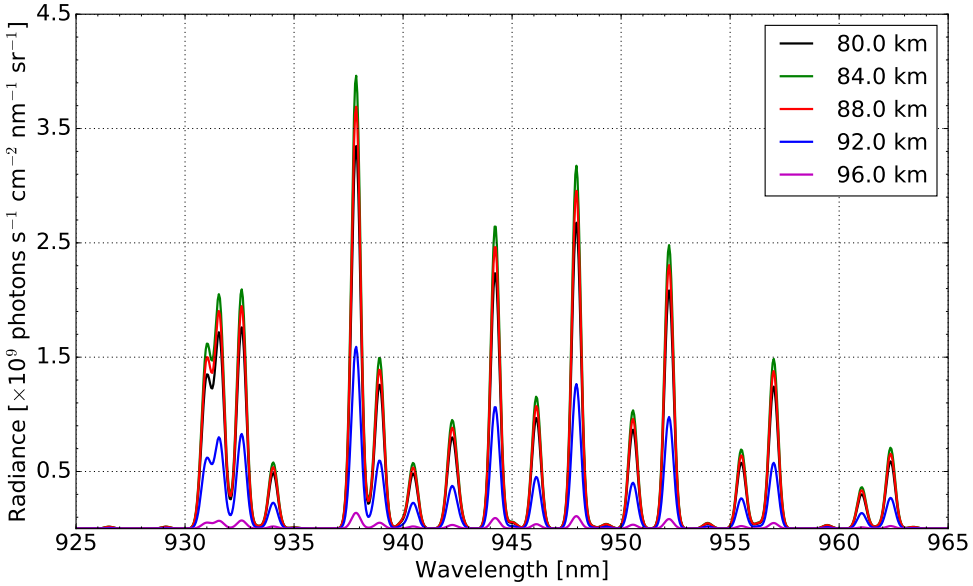

Figure 2.7: Limb spectra of OH(8-4) band emissions at selected tangent altitudes of 80 to 96 km, integrated over the instrument LOS, with the atmospheric layers specified by an altitude interval of 1 km, for 30° N, 0°, in January with the HAMMONIA atmospheric data. The instrument line shape is fitted by a Gaussian function with spectral resolution (FWHM) of 0.5 nm.

2.2 Oxygen atmospheric band emission

The airglow emissions of the oxygen atmospheric system were first observed simultaneously with hydroxyl emissions decades ago (*Meinel*, 1950c; *Chamberlain et al.*, 1954). The radiation origins from the electronic transitions from the metastable excited-state $O_2(b^1\Sigma_g^+)$ to the ground-state $O_2(X^3\Sigma_g^-)$. The O_2 atmospheric system consists of various bands in terms of vibrational states involved, of which the O_2 A(0-0) band centered around 762 nm is the most intense one (*Slanger and Copeland*, 2003). The (0-0) band intensity is by at least one order of magnitude higher than other bands, and this band is also the one mostly frequently studied, whereby O_2 A-band normally refers to this (0-0) band. As O_2 is one of the species widely existing in the atmosphere and most of these O_2 molecules are in the ground state, the emitted O_2 A-band emissions are absorbed by O_2 when they transfer through the atmosphere. As a consequence of this self-absorption effect, the O_2 A-band emissions from the middle and upper atmosphere cannot reach the ground and can only be observed from space. During the night, the peak emission occurs around 94 km (*McDade et al.*, 1986; *Murtagh et al.*, 1990) with an altitude layer of around 10 km at FWHM.

The O_2 A-band emissions have long been extensively used in the space-based remote sensing measurements to determine atmospheric profiles, such as temperature distribution. The mesospheric temperature can be obtained by evaluating the rotational structure of the O_2 A-band emissions by rocket- and satellite-borne experiments (around 60-110 km) (*Heller et al.*, 1991; *Ortland et al.*, 1998; *Sheese et al.*, 2010). The absorption spectra data of the O_2 A-band are exploited to obtain the temperature and pressure of the lower and middle atmosphere (up to $\sim$80 km), due to the constant and known vertical mixing ratio of O_2 (*Pitts*, 1999; *Sugita et al.*, 2001; *Nowlan et al.*, 2007). In addition, this absorption data are also applied for the retrieval of CO_2 concentrations (*Miller et al.*, 2007), for the detection of the cloud-top height and the optical properties of cloud and aerosols in the lower atmosphere (*Long et al.*, 2010). As with OH airglow, the total intensity of the O_2 A-band emissions can be applied to derive the atomic oxygen abundances (*Melo et al.*, 1996; *Sheese et al.*, 2011), and radiance variations are studied for the analysis of GWs and tides (*Burrage et al.*, 1994; *Hays et al.*, 2003).

2.2.1 O_2 A-band nightglow photochemistry

The excitation of O_2 airglow emissions and the absorption of solar radiation by O_2 are highly associated with the electronic configuration of molecular oxygen (*Khomich et al.*, 2008). The relevant potential energy curve of O_2 is illustrated in Fig. 2.8, and plotted herein are seven lowest bound electronic states in the limit of the ground-state atomic oxygen recombination (*Slanger and Copeland*, 2003). The ground-state is $O_2(X^3\Sigma_g^-)$,

with two unpaired electrons, which has a spin multiplicity of three (triplet oxygen). There are six metastable excited-states for O_2^* radicals, which are $a^1\Delta_g$, $b^1\Sigma_g^+$, $A'^3\Delta_u$, $A^3\Sigma_u^+$, $c^1\Sigma_u^-$ and $^5\prod_g$.

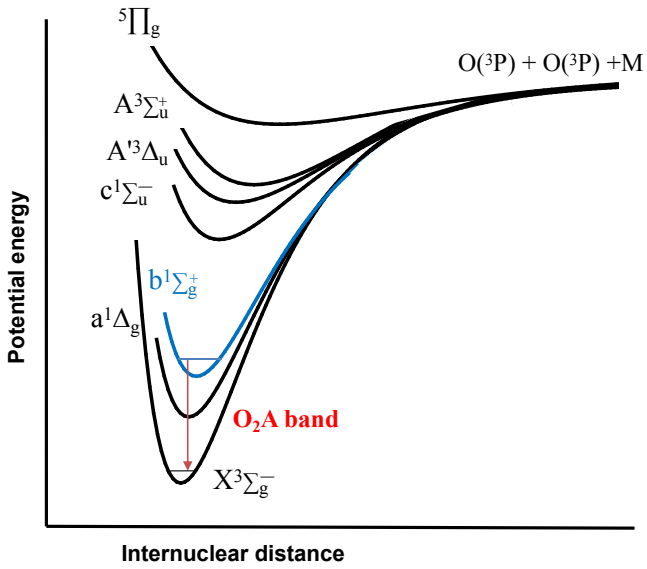

Figure 2.8: Diagram of the potential energy curve of the O_2 molecule, displayed with the seven lowest bound electronic states after *Slanger and Copeland* (2003). The radiative transition of (0-0) O_2 ($X^3\Sigma_g^- - b^1\Sigma_g^+$), which arouses the O_2 A-band airglow, is marked red.

The transitions among the seven states are responsible for a number of oxygen airglow systems. For example, the O_2 A-band from the atmospheric system mentioned above is emitted via:

$$O_2(b^1\Sigma_g^+, v = 0) \xrightarrow{A_{762}} O_2(X^3\Sigma_g^-, v = 0) + h\nu \tag{R2.8}$$

where $O_2(b^1\Sigma_g^+)$ has a multiplicity of one (singlet oxygen). A_{762} is the corresponding Einstein coefficient for the total O_2 A-band. It varies from 0.079 (*Kalogerakis*, 2019), 0.0834 (*Newnham and Ballard*, 1998) to 0.0878 s^{-1} (*Long et al.*, 2010).

The three-body recombination reaction of atomic oxygen (R1 in Tab. 1.1) is considered to be the source of electronically excited O_2^* radicals, which are a precursor for the O_2 airglow emissions:

$$O + O + M \xrightarrow{k^*_{OOM}} O_2^* + M \tag{R2.9}$$

The reaction rate coefficient k^*_{OOM} is available in the literature (*Campbell and Gray*,

1973; *Roble*, 1995; *Smith and Robertson*, 2008). The O_2^* radicals are initially produced with high electronic energy (*Slanger and Copeland*, 2003). The collisional relaxation of O_2^* with other molecules and atoms transfers the energy and redistributes the nascent radicals into the lowest bound electronic states. $O_2(b^1\Sigma_g^+)$ is populated by the collisional relaxation of O_2^* with ground-state O_2:

$$O_2^* + O_2 \xrightarrow{k_{O_2^*O_2}, y_{O_2b}} O_2(b^1\Sigma_g^+, v = 0) + O_2 \tag{R2.10}$$

The quenching rate coefficients $k_{O_2^*O_2}$ for most O_2 electronic states are provided by laboratory measurements (*Huestis*, 2002, Tab. 1; *Krasnopolsky*, 2011, Tab. 4). y denotes the branching ratio, indicating the yield efficiency of certain radicals (e.g., $O_2(b^1\Sigma_g^+)$) in the process. However, y_{O_2b} is not been quantified for different O_2 electronic states, particularly for the MLT condition (*Kalogerakis*, 2019), and only an overall value is approximated by fitting to airglow observations (*McDade et al.*, 1986).

This two-step mechanism, known as the Barth process, was firstly proposed by *Barth* (1961) and *Barth and Hildebrandt* (1961), and further implemented by *McDade et al.* (1986) and *Murtagh et al.* (1990) during the ETON campaign. It is the most important process that accounts for the O_2 A-band nightglow, as there is no solar radiation in the night that can stimulate $O_2(b^1\Sigma_g^+)$ radicals.

Two additional sources of the O_2 A-band emissions were recently proposed by *Kalogerakis* (2019), the first scheme of which involves the electronically excited $O(^1D)$, which populates $O_2(b^1\Sigma_g^+)$ via quenching with ground-state O_2 (*Slanger et al.*, 2017) as:

$$O(^1D) + O_2 \xrightarrow{k_{O_1DO_2}, y_{O_1Db}} O_2(b^1\Sigma_g^+, v = 0) + O(^3P) \tag{R2.11}$$

The values for $k_{O_1DO_2}$ and y_{O_1Db} are provided by *Sander et al.* (2011) and *Burkholder et al.* (2015). As discussed in Sect. 2.1.2, $O(^1D)$ is generated during the night through the vibrational quenching of OH^* radicals by $O(^3P)$, following the reaction as R2.7. Besides, another pathway contributing to the production of $O(^1D)$ was identified. The collisional relaxation of O_2^* with ground-state atomic oxygen can stimulate the second electronic excited-state $O(^1S)$. Its radiative decay emits $O(^1S)$ green line emissions at 557.7 nm whereas $O(^1D)$ is a byproduct (*Barth*, 1961):

$$O_2^* + O(^3P) \xrightarrow{k_{O_2^*O}, y_{O_2O_{1S}}} O(^1S) + O_2 \tag{R2.12}$$

$$O(^1S) \xrightarrow{A_{557}} O(^1D) + h\nu \tag{R2.13}$$

A_{557} is the Einstein coefficient for O(^{1}S – ^{1}D) transition. This pathway R2.12, same as R2.10, is part of the Barth process, the collisional quenching of O_2^* with atomic or molecular oxygen. Some of the related rate coefficients are not well known, and a simplified fitting model (*McDade et al.*, 1986), which can deliver reasonable results, is normally applied instead (*Zhu*, 2016).

The secondly additional scheme for O_2 A-band is the direct collisional relaxation of O_2^* with O(^{3}P) (*Kalogerakis*, 2019):

$$O_2^* + O(^3P) \xrightarrow{k_{O_2^*O}, y_{O_2Ob}} O_2(b^1\Sigma_g^+, v = 0) + O(^3P) \tag{R2.14}$$

Summarizing the above processes related to the $O_2(b^1\Sigma_g^+)$ production shows that the precursors O_2^* play a dominant role and the quenching relaxation schemes are crucial in the O_2 A-band nightglow photochemistry. However, the underlying mechanism is still not yet understood. 1) The scheme of O_2^* excitation from the termolecular association (R2.9) and the yield of O_2 electronic states are not yet well known and the hypothesis is still under discussion (*Smith*, 1984; *Bates*, 1988). 2) The quenching rate coefficients and the corresponding yield efficiencies for O_2 electronic states (R2.10, R2.12 and R2.14) are still not well determined (*Krasnopolsky*, 2011; *Kalogerakis*, 2019). As already mentioned before, the empirical model from *McDade et al.* (1986) is extensively used to represent the Barth process of $O_2(b^1\Sigma_g^+)$ and O(^{1}S) emissions. It has two simpled fitting parameters for O and O_2 to account for all related quenching processes and is capable of delivering fitting results in good agreement with the in situ measurements of O_2 A-band and O(^{1}S) emissions under most conditions (*Murtagh et al.*, 1990). Therefore, this model is adopted in this study. The model parameter and rate coefficients applied in this work are collected in Appx. A.4.

The produced $O_2(b^1\Sigma_g^+)$ radicals can be de-excited via radiation and also via collision with background molecules. The quenching processes can be summarized as:

$$O_2(b^1\Sigma_g^+, v = 0) + M \rightarrow products \tag{R2.15}$$

M includes not only O_2, N_2, but also O_3, O and CO_2. The corresponding reaction coefficients are given in the references (*Slanger and Black*, 1979; *Sander et al.*, 2006, 2011; *Burkholder et al.*, 2015).

2.2.2 Volume emission rate of O_2 A-band nightglow

Including the production and loss processes of $O_2(b^1\Sigma_g^+)$, the volume emission rate of the O_2 A-band can be expressed by the following formula:

$$V_{O_2b} = \frac{k^*_{OOM} \cdot [O]^2 \cdot [O_2] \cdot [M]}{c_{O_2} \cdot [O_2] + c_O \cdot [O]} \cdot \frac{A_{762}}{A_{b\Sigma} + C_{O_2b}} \tag{2.11}$$

The first term to the right of the equal sign is the production rate (cm^{-3} s^{-1}), calculated from the Barth process with the two unitless fitting parameters c_{O_2} and c_O taken from *McDade et al.* (1986). In the second term, $A_{b\Sigma}$ is the Einstein coefficient of all radiative transitions from O_2 ($b^1\Sigma_g^+$, v=0), which is from around 0.083 to 0.0925 s^{-1} (*Burch and Gryvnak*, 1969; *Bucholtz et al.*, 1986; *Zhu and Kaufmann*, 2019). C_{O_2b} refers to the total loss rate from collisional relaxation by all quenchers, stated by R2.15.

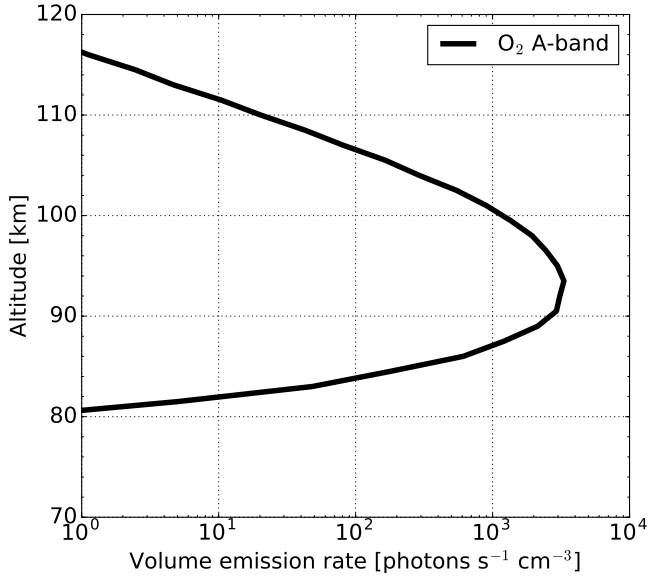

Figure 2.9: The simulated volume emission rate of the O_2 A-band nightglow versus altitude, for 20° N, 0°, in January with the HAMMONIA atmospheric data.

Applying Eq. 2.11, the total volume emission rate of the O_2 A-band can be calculated for the nighttime condition in the MLT. The simulated results are shown in Fig. 2.9. The O_2 A-band covers a spectral region of 758 nm to 768 nm. The background atmospheric profiles, including the O_3, O, O_2, N_2 and CO_2, are taken from the HAMMONIA model (*Schmidt et al.*, 2006). As shown in the plot, the nighttime VER of the O_2 A-band is of the same magnitude as the OH(8-4) emissions, while the emission peak altitude of O_2 A-band , which is around 94 km, is several kilometers higher than the OH emission

layers. The thickness of the O_2 A-emission layer is about 10 km at FWHM, similar to that of the OH emissions.

2.2.3 The rotational structure of the O_2 A-band

The radiative lifetime of the excited O_2 ($b^1\Sigma_g^+$, v=0) radicals is around 12 s, as calculated from the reciprocal of $A_{b\Sigma}$. The lifetime is long enough that O_2 ($b^1\Sigma_g^+$, v=0) is rotationally under the LTE conditions and the rotational and kinetic temperatures are equal. As with the OH^* radicals described in Sect. 2.1.4, the rotational levels of O_2 ($b^1\Sigma_g^+$, v=0) follow a Boltzmann distribution with a rotational temperature T_{rot}. Following Eq. 2.5, the intensity of each O_2 A-band emission line can be calculated as:

$$I_{u,e} = V_{O_2 b} \cdot \frac{g_u}{Q(T)} \cdot \exp(-\frac{hcE_u}{kT}) \cdot \frac{A_{u,e}}{A_{762}} \tag{2.12}$$

u and e denote the upper and lower rotational state, respectively. g_u refers to the statistical weight of the upper state and E_u indicates the upper-state rotational term energy and $A_{u,e}$ refers to the Einstein coefficient. These three parameters used here are derived from the HITRAN 2016 database (*Gordon et al.*, 2017). Q(T) is the rotational partition function of O_2 ($b^1\Sigma_g^+$, v=0):

$$Q(T) = \sum_u \left[g_u \cdot \exp(-\frac{hcE_u}{kT}) \right] \tag{2.13}$$

Similar to Eq. 2.8, the band Einstein coefficient A_{762} can also be calculated assuming this thermal equilibrium as:

$$A_{762} = \sum_u \sum_e \left[\frac{g_u}{Q(T)} \cdot \exp(-\frac{hcE_u}{kT}) \cdot A_{u,e} \right] \tag{2.14}$$

With the equations above, the rotational structure of O_2 A-band is calculated as illustrated in Fig. 2.10. Generally, the O_2 A-band is formed by two envelopes of emissions lines. Compared to OH(8-4) band, more rotational lines are densely dispersed in a shorter spectral range in O_2 A-band, while the line intensity is generally lower.

2.2.4 Radiative transfer of the O_2 A-band

The O_2 A-band emissions observed by the instrument are the integrated radiance along the instrument LOS, as the basic schematics demonstrated in Fig. 2.6. Due to the self-

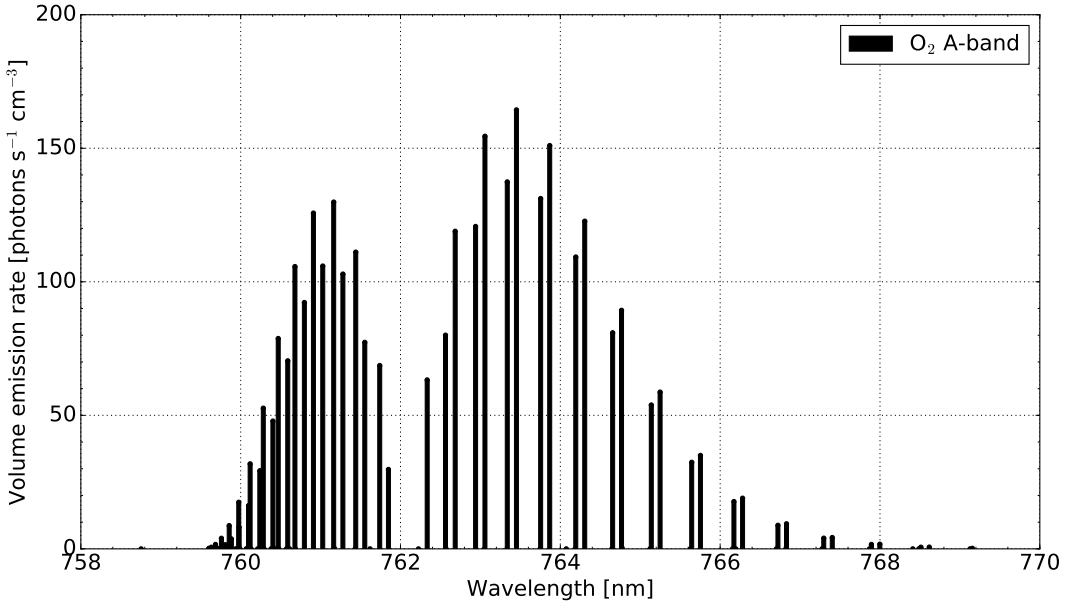

Figure 2.10: The rotational structure of the O_2 A-band within a wavelength of 758 to 770 nm at 92 km, for 20° N, 0°, in January with the HAMMONIA model data as atmospheric background input and the HITRAN 2016 database for Einstein coefficients.

absorption of O_2, only a portion of the emitted O_2 A-band radiation can pass through the atmosphere. Given a certain point along the LOS, according to Lambert-Beer's law, the corresponding atmospheric transmission is:

$$\tau(\nu, s) = \exp\Big(-\int_s^\infty n(s')\sigma(s')D(\nu, s')ds'\Big) \tag{2.15}$$

Here ν is the wavenumber of the spectral line, s denotes the distance along the LOS, n(s) is the number density of O_2. σ is the O_2 absorption cross section, and the data taken from HITRAN 2016 database are applied in this work. $D(\nu, s')$ is the line shape broadening given by Eq. 2.9. Along the instrument LOS, the O_2 A-band absorption cross section is line-by-line calculated with a fine-grid sampling of 0.001 cm^{-1}, on the line-broadened spectral profile. The transmission is unitless, and $\tau(\nu)$=0 implies the optically thick condition with complete absorption, while $\tau(\nu)$=1 means optically thin with no absorption.

Summing over all wavenumbers for the transmission at a certain point, the total O_2 A-band transmissivity can be gained. Fig. 2.11 shows the O_2 A-band transmission of tangent points from 60 to 120 km for a limb observation. The O_2 A-band transmissivity becomes higher with increasing altitude. Below 60 km, the O_2 A-band is totally self-absorbed. Above 88 km, the tangent transmission is $\geq$ 90 %, that most of the O_2 A-band

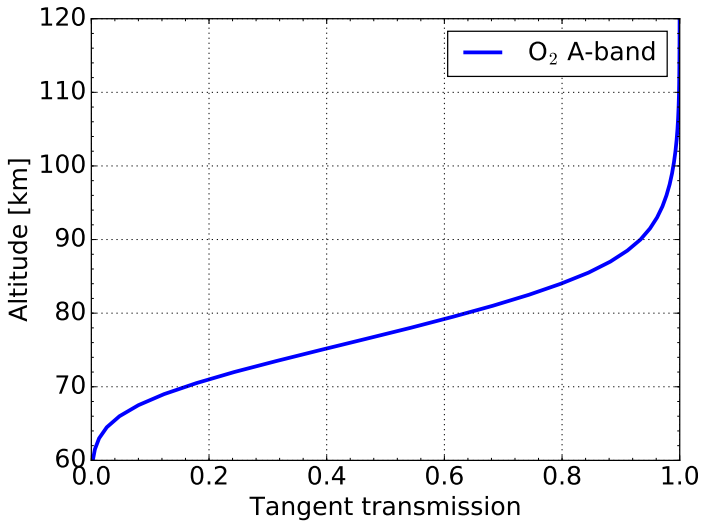

Figure 2.11: Transmission of the O_2 A-band emissions through the atmosphere from tangent points at altitudes from 60 to 120 km.

emissions can reach the instrument entrance.

The spectral irradiance observed by the instrument, with the self-absorption attenuation considered, is given by the Schwarzschild equation in integral form (*Ortland et al.*, 1998):

$$I_{u,e}(\nu) = \int_{-\infty}^{\infty} I_{u,e}(s) D(\nu, s) \exp\Big(- \int_{s}^{\infty} n(s') \sigma(s') D(\nu, s') ds' \Big) ds \tag{2.16}$$

Given in Fig. 2.12 is one example of the limb-integrated spectra of the O_2 A-band nightglow, simulated from the given equations.

2.3 Methodology for the retrieval of atomic oxygen and hydrogen

To derive atomic oxygen abundance from the OH nightglow emissions, the method relies on the chemical equilibrium between ozone production and loss in the MLT region during nighttime. Ozone is produced in the three-body recombination reaction (R2.3). Ozone is destroyed in reactions with atomic hydrogen and oxygen (R2.4). Besides, a minor sink of ozone is the chemical destruction by atomic oxygen (R3 in Tab. 1.1)

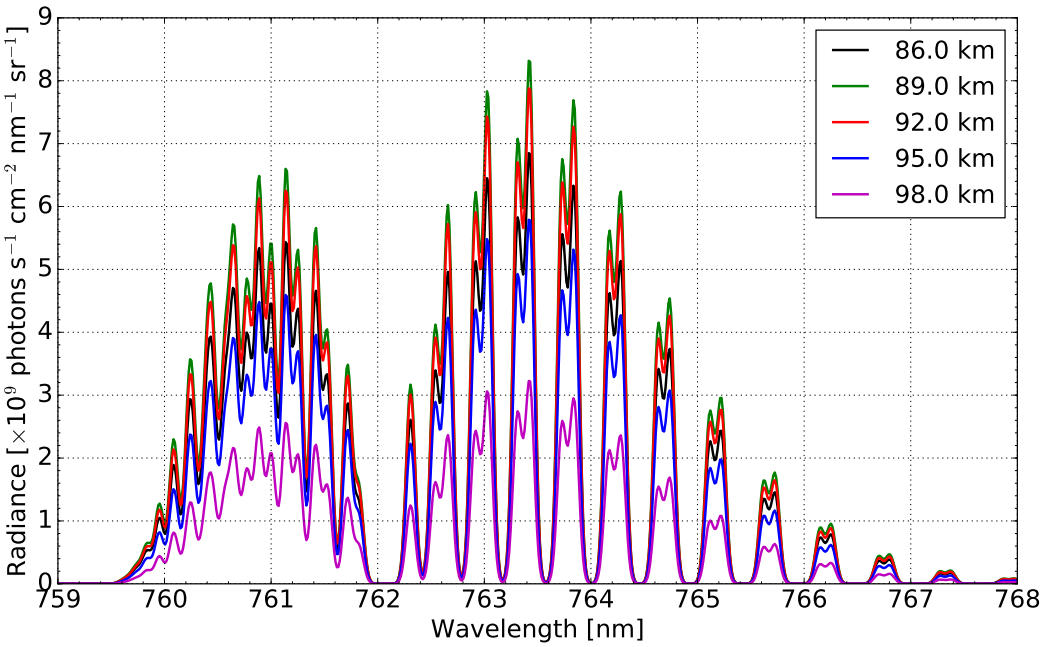

Figure 2.12: Simulated limb spectra of the O_2 A-band nightglow at selected tangent altitudes of 86 to 98 km, integrated over the instrument LOS with an altitude interval of 1.5 km, for 20° N, 0°, in January with the HAMMONIA atmospheric data. The instrument line shape is fitted by Gaussian function with FWHM of 0.1 nm.

(*Smith et al.*, 2008; *Zhu and Kaufmann*, 2018) as:

$$O + O_3 \xrightarrow{k_{OO_3}} O_2 + O_2 \tag{R2.16}$$

Combining R2.3, R2.4 and R2.16 gives:

$$k_{OO_2} \cdot [O] \cdot [O_2] \cdot [M] = k_{OO_3} \cdot [O] \cdot [O_3] + k_{HO_3} \cdot [H] \cdot [O_3] \tag{2.17}$$

During the day, this balance not longer holds. The production of ozone is balanced by the photolysis by UV radiation.

Thereupon, the nighttime atomic oxygen concentration can be expressed by a substitute of Eq. 2.1:

$$[O] = \frac{P_{OH^*}}{k_{OO_2} \cdot [O_2] \cdot [M] - k_{OO_3} \cdot [O_3]} \tag{2.18}$$

where P_{OH^*} is the production rate of OH^* radicals.

The atomic hydrogen abundance can be obtained via:

$$[H] = \frac{P_{OH^*}}{k_{HO_3} \cdot [O_3]} \tag{2.19}$$

In Eq. 2.18 and Eq. 2.19, P_{OH^*} is the total production rate of OH^* radicals, which can be derived from the measured emission rates of one emission band $V_{v',v''}$ or several emission lines $I^{(v',J')}_{(v'',J'')}$, as given by Eq. 2.2, Eq. 2.3 and Eq. 2.5 in Sect. 2.1.

Similarly, the retrieval of atomic oxygen from the O_2 A-band nightglow is implemented by rearranging Eq. 2.11, whereby the abundances can be obtained from the measured O_2 A-band radiance profiles (*Sheese et al.*, 2011; *Zhu and Kaufmann*, 2019).

2.4 Methodology for the retrieval of atmospheric temperature

The atmospheric temperature can be inferred from the rotational structure of OH and O_2 A-band emissions, assuming a Boltzmann distribution of OH^* and $O_2(b^1\Sigma_g^+)$ molecules at a rotational temperature under thermal equilibrium. The main principle is discussed in Sect. 2.1.4 and Sect. 2.2.3.

Figure 2.13 shows the simulated OH(3-1) band spectra at the selected wavelength range of 1500 to 1560 nm for different background temperatures of 100, 200 and 300 K. The spectra are normalized to the total band intensities. At a lower temperature, the OH(3-1) band emissions are mostly concentrated in a shorter spectral region, while with increasing temperature those emissions are shifted to longer wavelengths. Thereby, the rotational temperature T_{rot}, which is equivalent to the kinetic temperature T_{kin}, can be derived by evaluating the relative intensity gradients of several emissions lines.

For OH^* radicals, OH emissions from high rotational levels are not suitable for temperature retrieval. OH emission lines with lower rotational quantum number are highly recommended. Besides, the rotational temperature depends on vibrational states, that the determined T_{rot} with low J quantum number is reported more than 10 K higher from high vibrational levels than lower vibrational levels (*Cosby and Slanger*, 2007; *Perminov et al.*, 2007; *Noll et al.*, 2016). Therefore, OH emission lines from low vibrational quantum states are preferred.

The same basic principle of temperature retrieval using OH nightlow applies to the O_2 A-band emissions. Displayed in Fig. 2.14 is the relative intensity of the O_2 A-band simulated with atmospheric temperatures of 100, 200 and 300 K. At a lower temperature, the two envelopes of emission lines have shrunk to the center of the spectrum, while

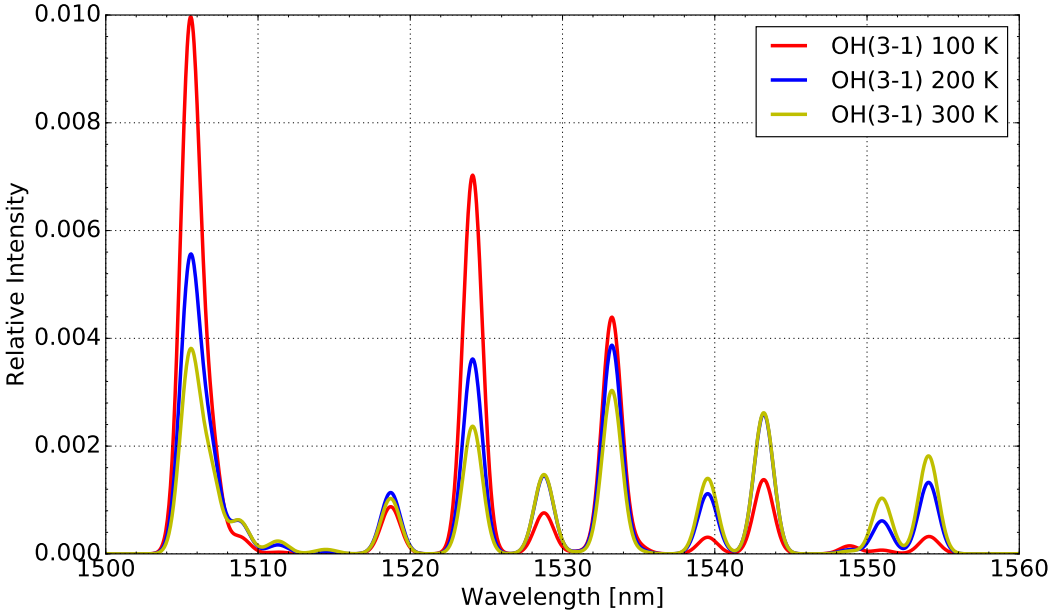

Figure 2.13: The OH(3-1) band emissions in relative intensity, simulated with atmospheric background temperatures of 100, 200 and 300 K, for 20° S, 40° E, 88 km, in January with the HAMMONIA data. The spectral resolution is 1.5 nm at FWHM.

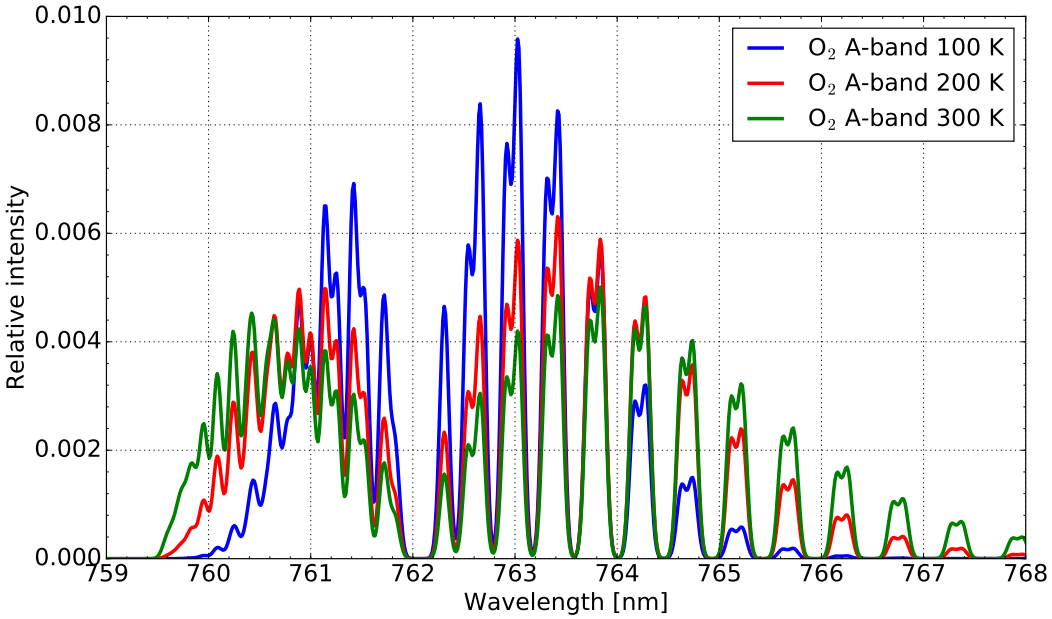

Figure 2.14: The O_2 A-band emissions in relative intensity, simulated with atmospheric background temperatures of 100, 200 and 300 K, for 20° N, 0°, 93 km, in January with the HAMMONIA data. The spectral resolution is 0.1 nm at FWHM.

with increasing temperature they are more discretely scattered to the edges. The different temperature dependence of the emission lines at different wavelengths provides the basis for the temperature retrieval.

Chapter 3

Inverse modeling

The retrieval of atmospheric profiles (e.g. atomic oxygen and hydrogen, temperature) from the observed nightglow spectra is in the context of solving an inverse problem, that target parameters are inferred from their indirect measurements. The inverse problem is nonlinear, normally ill-posed due to the existence of errors, e.g., measurement noises, and sometimes under- and overdetermined at the same time. Therefore, in most cases, the direct inverse calculation is not applicable and a unique solution may not exist. This brings us to an iterative approach, which is based on optimal estimation by means of an a priori regularization to account for the retrieval instability introduced by measurement errors, especially for upper/lower boundary conditions, so that atmospheric profiles can be reconstructed from radiance measurements with known error bounds. This retrieval scheme is extensively adopted in atmospheric remote sensing.

The inverse model herein applies a constrained global-fit method following the formalism of *Rodgers* (2000) and contains both vertical and spectral inversions. The target parameters are normally not only the desired atmospheric quantities (e.g., atomic oxygen abundance, temperature), but also complemented by other variables (e.g., instrument spectral resolution, wavelength shift). They are able to reproduce the spectrum characteristics, which cannot be fully captured only by regulating the atmospheric parameters in the forward model, thus resulting in a better agreement between measured and simulated spectra. Besides, a priori information from the atmospheric state is considered as a regularization term for the retrieval. Thereby, the Tikhonov regularization matrix (*Tikhonov and Arsenin*, 1977) is added and accordingly adjusted, to dampen the effect of measurement noise on the retrieval results. Practically, the Gauss-Newton and Levenberg-Marquardt iterative solvers are the workhorses behind for numerical computation. Indispensably, the retrieval is supplemented by the diagnostic information, which provides insight into the quality of the retrieval result quantitatively.

3.1 Inverse problem

Provided the atmospheric state vector $\boldsymbol{x} \in \mathbb{R}^n$, the OH or O_2 A-band nightglow modeling described in Sect. 2.1 and Sect. 2.2 anticipated as the forward model $\boldsymbol{F}$, the exact limb radiance data vector $\boldsymbol{y} \in \mathbb{R}^m$ would be:

$$\boldsymbol{y} = \boldsymbol{F}(\boldsymbol{x}) \tag{3.1}$$

in which, the mapping $\boldsymbol{F} : \mathbb{R}^n \to \mathbb{R}^m$. In real cases, the observed limb sounding radiances $\boldsymbol{y}_\varepsilon$ are contaminated by the measurement noise $\boldsymbol{\varepsilon} \in \mathbb{R}^m$, expressed by:

$$\boldsymbol{y}_\varepsilon = \boldsymbol{F}(\boldsymbol{x}) + \boldsymbol{\varepsilon} \tag{3.2}$$

An inverse problem is defined as the reconstruction of the target state vector $\boldsymbol{x}$ from the measurements $\boldsymbol{y}_\varepsilon$ as:

$$\boldsymbol{x} = \boldsymbol{F}^{-1}(\boldsymbol{y}_\varepsilon) \tag{3.3}$$

For an ill-posed problem, the direct inversion of the forward model $\boldsymbol{F}^{-1}$ is commonly not feasible. Instead, the inverse problem can be approximated by a minimization problem, in a sense that the differences between the forward model calculations and the actual observations are minimized, as:

$$\min_x \|\boldsymbol{F}(\boldsymbol{x}) - \boldsymbol{y}_\varepsilon\|^2 \tag{3.4}$$

As to mitigate the influence of measurement errors and to ensure the solution uniqueness, a regularization term is included and Eq. 3.4 can be expressed by the cost function $\boldsymbol{J}$:

$$\boldsymbol{J}(\boldsymbol{x}) = (\boldsymbol{F}(\boldsymbol{x}) - \boldsymbol{y}_\varepsilon)^T \mathbf{S}_\varepsilon^{-1} (\boldsymbol{F}(\boldsymbol{x}) - \boldsymbol{y}_\varepsilon) + (\boldsymbol{x} - \boldsymbol{x}_a)^T \mathbf{S}_a^{-1} (\boldsymbol{x} - \boldsymbol{x}_a) \tag{3.5}$$

The solution $\boldsymbol{x}$ for this nonlinear least-squares minimization problem is then the solution for the above inverse problem. $\mathbf{S}_\varepsilon$ denotes the covariance matrix of the measurement noise. $\boldsymbol{x}_a$ denotes the a priori state vector (the a priori information about the atmospheric state, usually from climatological values), and $\mathbf{S}_a$ is the corresponding covariance matrix. Practically, the regularization matrix $\mathbf{S}_a$ is not directly available and is normally constructed by regularization methods.

3.2 Regularization

One of the most widely used regularization methods, the Tikhonov regularization (*Tikhonov and Arsenin*, 1977) is applied in this work. The Tikhonov regularization matrix

$\mathbf{S}_a^{-1}$ is defined as:

$$\mathbf{S}_a^{-1} = \alpha_0^2 \mathbf{L}_0{}^T \mathbf{L}_0 + \alpha_1^2 \mathbf{L}_1{}^T \mathbf{L}_1 + \alpha_2^2 \mathbf{L}_2{}^T \mathbf{L}_2 + \cdots + \alpha_n^2 \mathbf{L}_n{}^T \mathbf{L}_n \tag{3.6}$$

In which, $\mathbf{L}_0$ to $\mathbf{L}_n$ are the zeroth- to *n*th-order Tikhonov regularization matrices respectively, and α_0 to α_n are their corresponding weighting factors.

The zeroth-order Tikhonov regularization matrix $\mathbf{L}_0$ is a diagonal matrix, and in this work chosen as the identity matrix $\mathbf{I}_n$. It constrains the magnitude of the solution to be comparable to the a priori state $\boldsymbol{x}_a$, and also dampens high-frequency oscillations. The first-order Tikhonov regularization matrix $\mathbf{L}_1$ is the first-order derivative operator, and it enforces the solution smoothing towards the first-order derivatives of $\boldsymbol{x}_a$. It is given as the first-order discrete difference of $\mathbf{I}_n$ along the vertical axis:

$$\mathbf{L}_1 = \begin{bmatrix} -1 & 1 & \cdots & 0 & 0 \\ 0 & -1 & \cdots & 0 & 0 \\ \vdots & \vdots & \ddots & \vdots & \vdots \\ 0 & 0 & \cdots & -1 & 1 \\ 0 & 0 & 0 & 0 & 0 \end{bmatrix} \in \mathbb{R}^{n \times n} \tag{3.7}$$

Likewise, the second- to *n*th-order regularization matrix can be defined with respect to the second- to *n*th-order difference.

The first two orders of Tikhonov regularization matrices $\mathbf{L}_0$ and $\mathbf{L}_1$ are used in this work, and the a priori profiles applied in the retrieval from different measurement data are specifically described in the corresponding chapters. Their weighting factors α_0 and α_1 are regulated in such a way, that the contribution from the total regularization term in Eq. 3.5 is comparable to the measurement contribution. In an ideal case, the information content in the retrieval result should come from the measurement itself, while the regularization from a priori knowledge is provided as guidance for meaningful results.

3.3 Minimization

The minimization of the cost function in Eq. 3.5 can be properly addressed by iterative optimization approaches, of which both the Gauss-Newton and the Levenberg-Marquardt algorithms are implemented in this work.

The well-known Gauss-Newton iterative method in the *n* form is given as follows (*Rodgers*, 2000, p. 85). After the *i*-th iteration step, the new target state vector $\boldsymbol{x}_{i+1}$ is

constructed as:

$$\boldsymbol{x}_{i+1} = \boldsymbol{x}_a + (\mathbf{S}_a^{-1} + \boldsymbol{K}_i^T \mathbf{S}_\varepsilon^{-1} \boldsymbol{K}_i)^{-1} \boldsymbol{K}_i^T \mathbf{S}_\varepsilon^{-1} \left[\boldsymbol{y}_\varepsilon - \boldsymbol{F}(\boldsymbol{x}_i) + \boldsymbol{K}_i(\boldsymbol{x}_i - \boldsymbol{x}_a)\right] \tag{3.8}$$

In which $\boldsymbol{K}_i \in \mathbb{R}^{m \times n}$ is the Jacobian matrix, the first-order derivative matrix of the forward model $\boldsymbol{F}(\boldsymbol{x})$ calculated at $\boldsymbol{x}_i$.

The Gauss-Newton method is an efficient minimiser, which converges fast to the adjacent local minimal point. However, it is not always sufficient enough to reach the global minimum, if the iteration point is too far away. Alternatively, the Levenberg-Marquardt method can be applied (*Rodgers*, 2000, p. 93), as:

$$\boldsymbol{x}_{i+1} = \boldsymbol{x}_i + (\mathbf{S}_a^{-1} + \boldsymbol{K}_i^T \mathbf{S}_\varepsilon^{-1} \boldsymbol{K}_i + \lambda_i \mathbf{I}_n)^{-1} \left[\boldsymbol{K}_i^T \mathbf{S}_\varepsilon^{-1} \left[\boldsymbol{y}_\varepsilon - \boldsymbol{F}(\boldsymbol{x}_i)\right] - \mathbf{S}_a^{-1}(\boldsymbol{x}_i - \boldsymbol{x}_a)\right] \tag{3.9}$$

It is modified from the Gauss-Newton method in a way that a scaling factor λ_i together with an identity matrix is added. λ_i is updated at each iteration so that a successive reduction of the cost function is guaranteed.

3.4 Diagnostics

The quality and reliability of the retrieval result are analyzed by means of a diagnostics, which is usually conducted in terms of measurement contribution (spatial resolution) and error analysis.

As already mentioned in Sect. 3.2, the contribution of the measurements should be dominant in the information content of the solution. Therefore, the influences of the regularization (a priori information) and the measurements on the retrieval result are quantitatively evaluated.

Providing that the unknown true atmospheric state vector is $\boldsymbol{x}_t \in \mathbb{R}^n$, and the derived state vector is $\boldsymbol{x}_r \in \mathbb{R}^n$, the following linear expression applies (*Rodgers*, 2000, p. 47):

$$\boldsymbol{x}_r = (\mathbf{I}_n - \mathbf{A})\boldsymbol{x}_a + \mathbf{A}\boldsymbol{x}_t + \mathbf{G}\boldsymbol{\varepsilon} \tag{3.10}$$

Where $\boldsymbol{A} \in \mathbb{R}^{n \times n}$ is the averaging kernel matrix, describing the sensitivity of the derived atmospheric state $\boldsymbol{x}_r$ to the true atmospheric state $\boldsymbol{x}_t$. In an ideal case, $\boldsymbol{A}$ would be the identity matrix. $\boldsymbol{G} \in \mathbb{R}^{n \times m}$ is gain matrix, which describes the sensitivity of the solution to the measurement. It can be regarded as the regularized pseudo inverse of $\boldsymbol{K}(\boldsymbol{x}_r)$, given by *Rodgers* (2000, p. 56):

$$\mathbf{G} = \left[\boldsymbol{K}(\boldsymbol{x}_r)^T \mathbf{S}_\varepsilon^{-1} \boldsymbol{K}(\boldsymbol{x}_r) + \mathbf{S}_a^{-1}\right]^{-1} \boldsymbol{K}(\boldsymbol{x}_r)^T \mathbf{S}_\varepsilon^{-1} \tag{3.11}$$

And consequently,

$$\mathbf{A} = \mathbf{G}\boldsymbol{K}(\boldsymbol{x}_r) = \left[\boldsymbol{K}(\boldsymbol{x}_r)^T \mathbf{S}_\varepsilon^{-1} \boldsymbol{K}(\boldsymbol{x}_r) + \mathbf{S}_a^{-1}\right]^{-1} \boldsymbol{K}(\boldsymbol{x}_r)^T \mathbf{S}_\varepsilon^{-1} \boldsymbol{K}(\boldsymbol{x}_r) \tag{3.12}$$

Equation 3.10 can be interpreted in terms of the contributions from different aspects. The first term to the right of the equal sign indicates the influence from the regularization of a priori information, and if possible, it should be close to zero. The middle term determines how much contribution comes from the unbiased true atmospheric state, and shall be kept maximal. The last term represents the effect of the measurement noise, and shall retain minimal.

Specifically, the measurement contribution can be evaluated by analyzing the averaging kernel matrix. The sum over one row of $\boldsymbol{A}$ characterizes the measurement contribution for the corresponding parameter in the retrieval results. The sum being close to one indicates that this retrieval parameter is mostly derived from the measurement information and is considered to be well constrained. Otherwise, if the value of the measurement contribution approaches zero, the a priori information dominates. The smoothing effect introduced by the regularization in the retrieval result can be quantified by the spatial resolution, which is obtained from the row distribution of $\boldsymbol{A}$ by calculating the FWHM of each row. In an ideal case, the spatial resolution is equal to the vertical grid of limb measurements, and each row of the averaging kernel matrix reaches the maximum at the corresponding tangent altitude.

The retrieval error results from several sources of uncertainties, mainly including the smoothing error, the forward model parameter uncertainty and the measurement uncertainties.

The smoothing error $\mathbf{S}_s$ is a systematic error introduced by the regularization term, and for a Tikhonov type it is given by:

$$\mathbf{S}_s = (\mathbf{A} - \mathbf{I}_n)\mathbf{S}_a(\mathbf{A} - \mathbf{I}_n)^T \tag{3.13}$$

The forward model parameter error $\mathbf{S}_{fb}$ results from inadequate knowledge of the forward model parameters. It accounts for all uncertainties of the applied reaction rate coefficients and parameters in the forward model, and is likely to be the largest source of uncertainties. It can be expressed by:

$$\mathbf{S}_{fb} = \mathbf{G}\mathbf{K}_b\mathbf{S}_b\mathbf{K}_b^T\mathbf{G}^T \tag{3.14}$$

In which $\mathbf{K}_b$ denotes the Jacobian matrix of the forward model parameter, and $\mathbf{S}_b$ refers to the error covariance. In this work, the forward model parameters (e.g., reaction rate coefficients) are in most cases given with known uncertainties, and if not applicable, a

stochastic perturbation of certain uncertainties is applied.

The measurement noise error $\mathbf{S}_\varepsilon$ is caused by the measurement noise, as discussed above. It is stochastic and random with zero mean, and is expressed by:

$$\mathbf{S}_\varepsilon = \mathbf{G}\mathbf{S}_\varepsilon\mathbf{G}^T \tag{3.15}$$

Therefore, the mean square error matrix of the solution is computed as:

$$\mathbf{S}_r = \mathbf{S}_s + \mathbf{S}_{fb} + \mathbf{S}_\varepsilon \tag{3.16}$$

where the retrieval result uncertainty is given by the square root value of the diagonal entries in $\mathbf{S}_r$.

Chapter 4

Atomic oxygen and hydrogen derived from GOMOS OH airglow measurements

Currently, various datasets are available for atomic oxygen and hydrogen, and they are consistent in terms of the overall profile shape of absolute densities. However, some discrepancies still exist (*Mlynczak et al.*, 2013a,b,c; *Kaufmann et al.*, 2014; *Mlynczak et al.*, 2018; *Zhu and Kaufmann*, 2018; *Panka et al.*, 2018). The radiometric calibration of the instruments or differences in airglow model parameters are potential reasons. Some new findings on airglow relaxation modeling and reaction kinetic parameters were recently published, which complicate the topic further.

In this work, a new dataset of atomic oxygen and hydrogen derived from the OH nightglow observed by the GOMOS instrument on the European Space Agency's (ESA) Envisat during the years 2002 to 2012 is presented and discussed. This dataset is particularly valuable in that it was obtained at the same time as the already-published SABER and SCIAMACHY data, but from a different instrument with its own radiometric calibration. Emissions from OH(8-4) are used to obtain O and H abundances, which is a similar proxy to that provided by the SABER and SCIAMACHY OH measurements.

In this chapter, a brief introduction to the instrument and data processing procedure is provided, followed by the description of the retrieval setup, based on Sect. 2.1, Sect. 2.3 and Chap. 3. The derived results are shown in the next two sections, including error analysis as well as latitudinal and temporal analysis. The validation of the dataset is investigated in a broad context, including comparisons with the SCIAMACHY dataset and other data sources.

4.1 Measurements and data processing

4.1.1 GOMOS on Envisat

The GOMOS spectrometer is one of nine instruments aboard Envisat. It is designed to monitor ozone profiles and other trace species using stellar occultation and atmospheric transmission measurements in limb-viewing mode (*ESA*, 2010). Envisat follows a Sun-synchronous orbit with an Equator crossing time (descending node) of 10 p.m. (*Gottwald et al.*, 2011). The operation period of GOMOS dates from April 2002 to April 2012. However, there was an instrument malfunction in summer 2005, resulting in a data gap of nearly three months.

The GOMOS instrument delivered one vertical profile of measurements for each occultation, and the altitude coverage spans from 5 km to 150 km with a vertical sampling rate of better than 2 km (*Kyrölä et al.*, 2012). It has four spectral channels in the ultraviolet to near-infrared. The spectrometer B2 (SPB2), which provides the data used in this work, covers a wavelength range of 925-955 nm with a spectral resolution of 0.13 nm at FWHM and a sampling step of 0.056 nm (*Massimo Cardaci and Lannone*, 2012). The GOMOS detector has three parallel bands. The central band probes the star spectra and the upper/lower bands record the atmospheric background radiation as calibration information, as indicated in Fig. 4.1. The altitudes of tangent points observed by three bands differ roughly by 1.7 km. OH and O_2 A-band are regularly detected in the upper/lower bands, together with auroral emissions and the stray light scattered by particles or molecules in the atmosphere. This dataset, which is used in our analysis, is archived in the level-1b limb dataset but not directly used in the operational level-2 data retrieval routines. The first analyses of the extracted OH and O_2 A-band nightglow measurements from these background datasets were reported by *Bellisario et al.* (2014).

4.1.2 Data selection and resampling

The GOMOS data were processed with the processor version 6.01-2012. The resulting level-1b limb products have already been geolocated and calibrated (*Massimo Cardaci and Lannone*, 2012). The signal-to-noise ratio (SNR) of single spectra is of the order of one, and the averaging of data is required for further processing of the data.

The raw data from level-1b limb products are first filtered with the corresponding auxiliary “quality flag” and “product confidence data”(PCD), which indicate the presence of bad pixels, saturation, cosmic rays, modulation, dark current, flat-field or vignetting correction, with only data in the normal status being kept. This is then followed by a geolocation-related selection, in which the data with ray-tracing errors are eliminated,

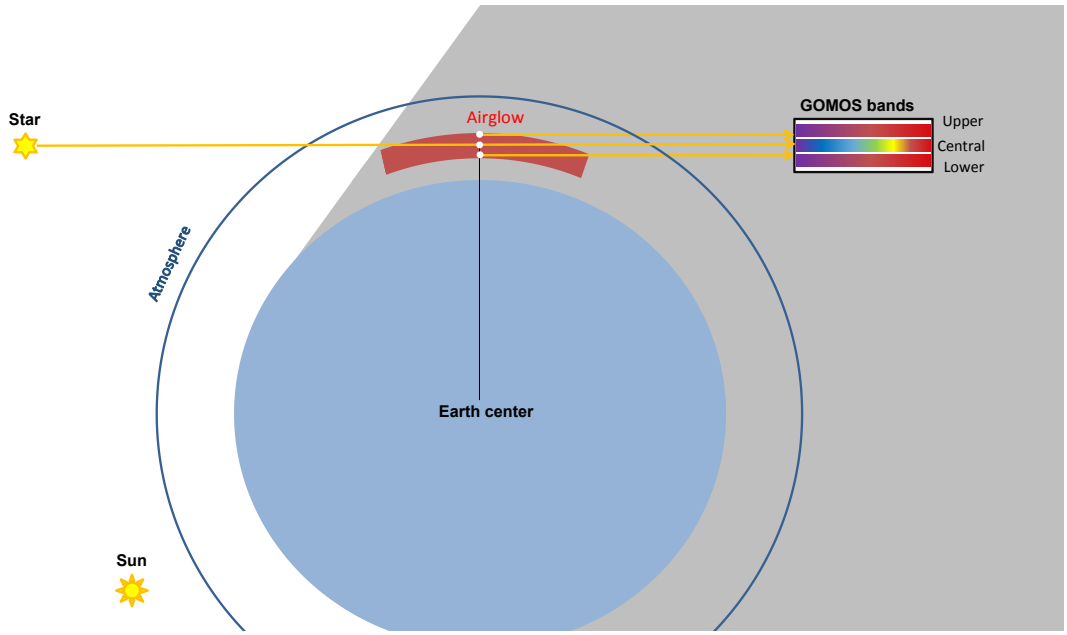

Figure 4.1: Schematic view of the GOMOS stellar occultation observations (*Chen et al.*, 2019). The star transmission spectra are recorded in the central band of the instrument detector, while the atmospheric background radiation is imprinted in the upper/lower bands. The O_2 A-band and OH airglow emissions are detected in the limb observations. For each star spectrum, one upper and one lower spectrum are recorded simultaneously.

and their star IDs and geolocation errors are restricted to within an acceptable range, as recommended by *Dehn* (2012). The stray light entering the instrument's field of view (FOV) affects the illumination of the spectrometer and enhances the background noise. The stray light is characterized by the illumination flags and solar zenith angle (SZA) of satellite and tangent points, which are geometrically computed. The illumination conditions of GOMOS measurements are categorized into five flags (*Kyrölä et al.*, 2010; *van Gijsel et al.*, 2010), and the "bright limb" flag thereof is excluded in this work. SZA > 108° is also applied as selection criteria. Near-infrared aurora at wavelengths of around 939 nm and 947 nm, originating from the atomic nitrogen (N I) emissions and N_2^+ Meinel (2-1) band (*Baker et al.*, 1977) are in the spectral range of SPB2. Observations in polar regions are therefore not considered in our analysis.

Due to the nature of the stellar occultation observations, the tangent points of single vertical profiles diverge significantly and are not stationary in latitude-longitude locations. In the level-2 product, they are characterized by the obliquity (*Kyrölä et al.*, 2010), which is not available in the level-1b data. Therefore, in this work, the latitude spread of tangent points is used instead and profiles with > 4° deviation in tangent point latitudes are disregarded to ensure that every selected profile spans a geographical area

of within $\pm$ 5° latitude.

The archived level-1b data are signals recorded by the detector, which must be dynamically decoded to electrons and then converted to a physical unit of flux with wavelength-specific radiometric calibration factors. The star is a point source, and part of the stellar light is spread to the lower and upper bands, which is supposed to be totally imaged in the central band in an ideal case. Considering the contamination of star leakage and residual stray light, which are assumed to be constant with altitude, the averaged spectra from above 110 km are subtracted from each profile as background radiation. No airglow emissions are found above the region of 110 km in the GOMOS measurements. The subtraction is then followed by the individual "base" removal at each altitude layer, in which this "base" offset is the mean of residual noise of the emission lines. The processed data are resampled into monthly and zonally averaged 10° latitude bins with a fixed altitude grid of 3 km to enhance the spectra SNR and improve retrieval quality. The number of profiles selected for one sample bin (shown in Fig. 4.2) is around 100 to 300. In order to eliminate the effect of random and systematic noise as well as outliers while retaining as many profiles as possible, the largest and smallest 1 % vales are disregarded from the measurements at each sample bin.

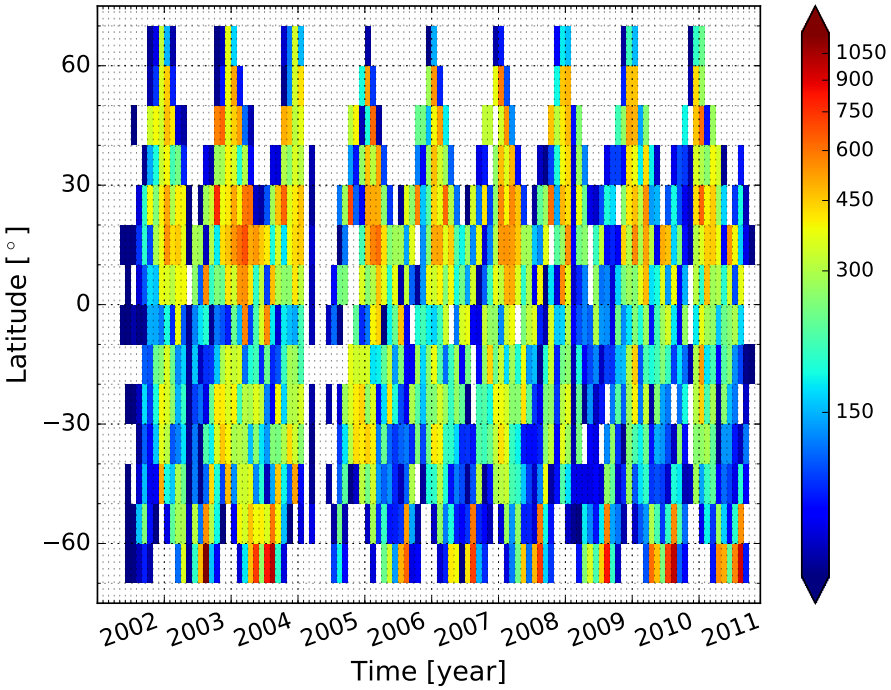

Figure 4.2: Latitudinal distribution of resampled GOMOS data available from 2002 to 2012. Color coding indicates the number of selected profiles for each monthly and zonally averaged 10° latitude bin.

Barrot et al. (2003) reported high photon response non-uniformity (PRNU, deviation of the sensor response from a uniform response) variation of around 12 % in the GOMOS spectrometer B (SPB). For further investigation, a comparison of spectral radiances is made with measurements from the SCIAMACHY instrument, which covers exactly the same OH(8-4) band wavelengths as GOMOS. SCIAMACHY is another limb sounder aboard the Envisat satellite, which observed OH emissions at various wavelengths from visible to infrared emissions (*Bovensmann et al.*, 1999; *Kaufmann et al.*, 2008). Theoretically, the SCIAMACHY and GOMOS measurements should be identical in the same wavelength range. In practice, however, due to effects of various factors, such as instrument characteristics, radiometric calibration and fields-of-view, they do not fully conform with each other in terms of absolute radiance or instrument line shapes.

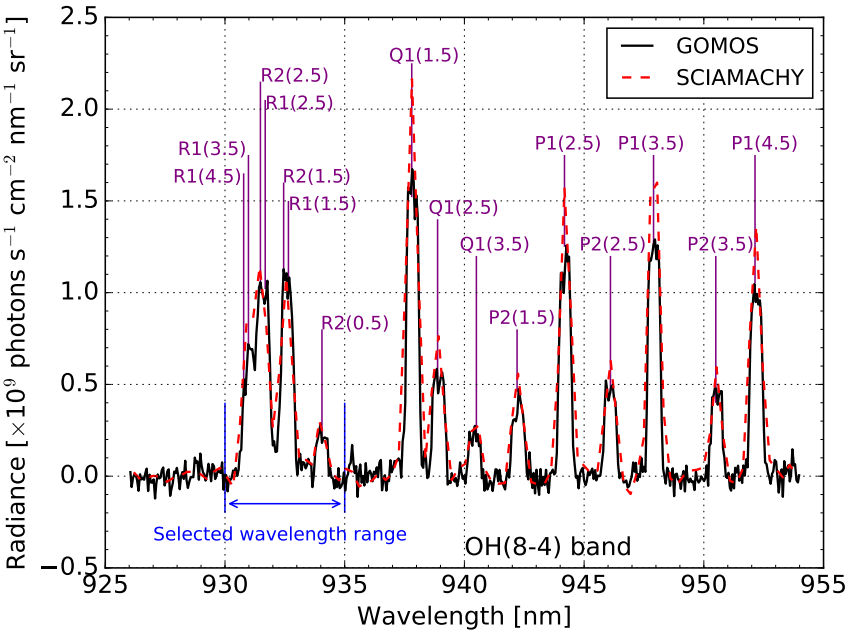

Figure 4.3: Monthly averaged spectrum from GOMOS (black solid line) for Feb. 2004 at 40°-50° N and at a tangent altitude of 89.5 km. Strong emission lines from the OH(8-4) band are annotated with the branch and rotational quantum numbers. The wavelength range from 930 nm to 935 nm is used in the retrieval. The corresponding SCIAMACHY data (red dashed line) are also given here for comparison.

As shown in Fig. 4.3, in the spectral range of our interest (SPB2), we found the GOMOS data show a good agreement with the SCIAMACHY data at the spectral range of 930-935 nm, whereas the GOMOS radiances at the wavelength range of 935-955 nm are always 25-30 % lower compared to the SCIAMACHY measurements, which

is not understood (E. Kyrölä, personal communication, 2019). Therefore, of the entire spectral range, only the wavelength region of 930-935 nm is used in the retrieval to derive the atomic oxygen abundances. It includes a number of emission lines from OH(v=8-4) band, which originates from the radiative transitions of OH(v'=8 $\longrightarrow$ v''=4). The dominant emission lines are mainly in the R branch with a rotational state quantum number of K'' = 1, 2, and 3.

The quality of the reprocessed spectra is evaluated by calculating the standard deviation (STD) of averaged spectra for each sample bin, supplemented by the SNR analysis. The calculations show that the mean STD for a typical sample bin in autumn at midlatitudes is around 2-4$\times 10^9$ photons s^{-1} cm^{-2} nm^{-1} sr^{-1} (comparable to the radiance signal), and that SNR increases to more than 10 at peak altitudes and to around 3-5 at lower altitudes. A typical profile of processed hydroxyl spectra and integrated radiance is illustrated in Fig. 4.4. Three lines are clearly visible in the plot (a), while the emission peak layer appears at the tangent altitude of around 85 km, according to the plot (b). The error bars in the right plot indicate the measurement noise for integrated radiance. The measurement noise is calculated from the standard deviation of the residual noise in the spectral range in between of the emission lines and assumed to be the same for all wavelengths, as the intensities of remaining weak emission lines from high rotational levels in the spectral region are by several orders of magnitude lower and therefore negligible.

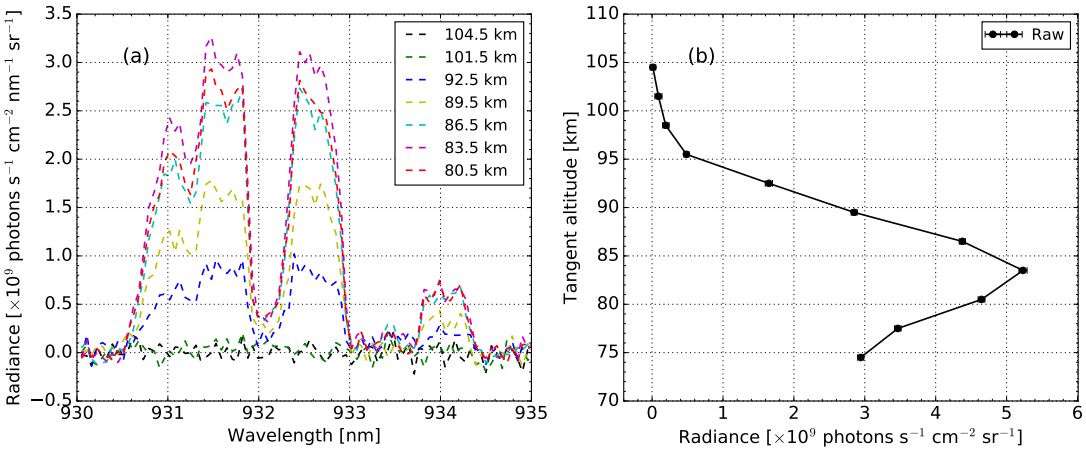

Figure 4.4: (a) GOMOS monthly zonal mean spectra of OH(8-4) emissions at tangent altitudes as given in the figure legend for Oct. 2003 at 0°-10° S and at a local time of 10-12 p.m.. (b) The spectrally integrated radiance over 930-935 nm versus tangent altitude for the same conditions. The error bars indicate the measurement noise for integrated radiance (see text).

4.1.3 Retrieval setup

The method to derive atomic oxygen and hydrogen abundance relies on the chemical equilibrium between ozone production and loss during nighttime, as described in Sect. 2.3. Most of the model parameters are summarized in Appx. A.1 & A.2. Additionally, the rate coefficients for the production of OH(v=8) by the collision of OH(v=9) with oxygen and the collisional removal of OH(v=8) by atomic oxygen are obtained by simultaneously fitting the limb radiances of OH(9-6) and OH(8-5) bands, which are independently taken from the SCIAMACHY measurements. These two parameters are adjusted in such a way that the ratio between the fitted radiances of the two bands is consistent with the ratio calculated from the measurements. Details about the fitting of the parameters are provided in Appx. A.3.

Atmospheric background profiles of temperature, total density, and ozone mixing ratio are taken from SABER measurements (v2.0-2016). The same latitude bins ($\pm$ 5°) and local times ($\pm$ 1 hour) were selected for SABER data as those for GOMOS data. Since SABER cannot measure O_2 and N_2 mixing ratios, these quantities are taken from the MSIS simulation model data (*Picone et al.*, 2002).

The inverse model adopts a global-fit approach following *Rodgers* (2000) as discussed in Chap. 3. The Gauss-Newton iterative method is chosen to minimize the cost function of this inverse problem. The a priori information about atomic oxygen in this work are taken from the MSIS model data, of which the a priori data about the absolute value of atomic oxygen is averaged into the vertical grid of 3 km as the measurements. The first-order regularization is obtained from the linear interpolation of the a priori data given on the measurement grid, i.e., no sub-measurement-grid information is obtained from that data. The regularization strength depends on altitude and its main purpose is to assure meaningful values at the upper and lower boundaries of the altitude regime considered. In between, the regularization has virtually no effect on the retrieved quantities, as can be seen from the retrieval diagnostics. The vertical resolution of the retrieval results is close to the vertical grid of the measurements.

The target parameters of the retrieval are the vertical profiles of atomic oxygen abundance, spectral resolution and a wavelength shift. The latter are both altitude-independent and give a better agreement between measured and simulated spectra. The content of information in the spectra is sufficient to retrieve these additional parameters.

4.2 Retrieval results of atomic oxygen

4.2.1 Atomic oxygen abundances

Applying the global fitting method to GOMOS level-1b limb products, a globally distributed time series [O] dataset is derived, along with other quantities. Shown in Fig. 4.5 (a) is a typical profile of the fitted spectra compared with the measurements. In general, simulations and measurements are in good agreement. The spectrally integrated radiances in Fig. 4.5 (b) also show consistency. The derived oxygen densities are within an altitude range of 80 km to 100 km, covering the period from May 2002 to December 2011 and spanning local times from 10:00 p.m. to 12:00 p.m.. A typical atomic oxygen profile is shown in Fig. 4.6 with a maximum concentration of about 3.5×10^{11} atoms cm^{-3} at 95 km. Above the maximum, there is a downward flux of atomic oxygen by diffusive transport (*Swenson et al.*, 2018). Below the maximum, there is a rapid decrease in atomic oxygen density, which is mainly due to the vertical transport and chemical losses. At an altitude of around 85 km, atomic oxygen density already declines by one order of magnitude to 10^{10} atoms cm^{-3}.

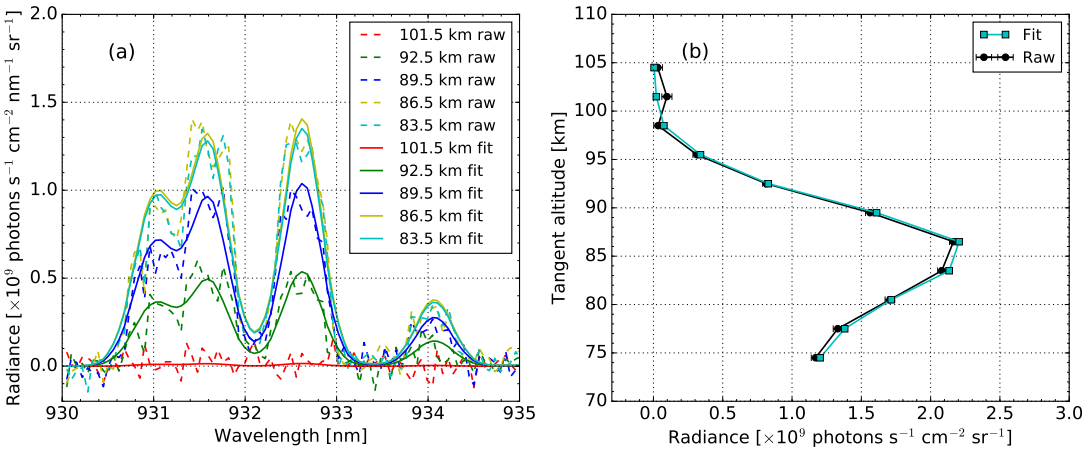

Figure 4.5: (a) Simulated spectra (fit, solid line) and measurements (raw, dashed line) of GOMOS monthly zonal mean measurements of OH(8-4) airglow emissions at tangent altitudes, as given in the figure legend for August 2003 at 30°-40° S and a local time of 10-12 p.m.. (b) The spectrally integrated radiance over 930-935 nm versus tangent altitude for the same conditions.

Along with atomic oxygen abundances, other retrieval target parameters are simultaneously retrieved. The spectral resolution (FWHM) has a typical value of around 0.48 nm, and no wavelength shift of the spectra is found.

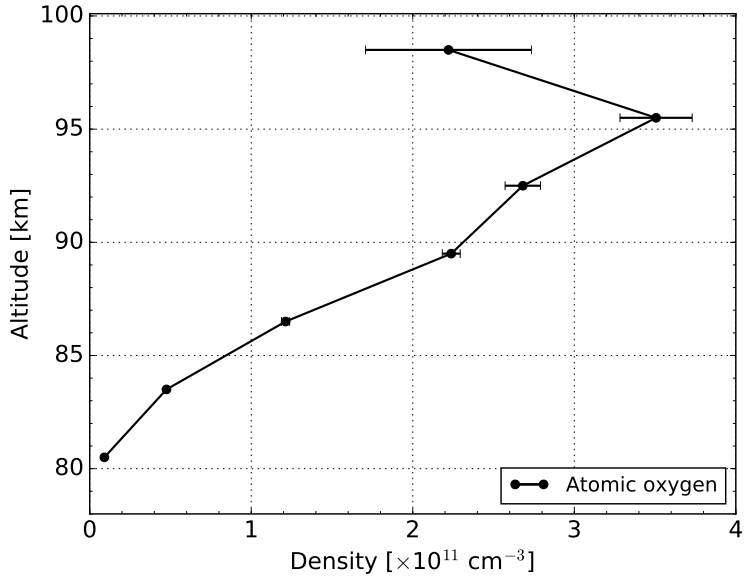

Figure 4.6: Atomic oxygen abundances, derived from GOMOS monthly zonal mean measurements of OH(8-4) airglow emissions for February 2006 at 10°-20° N. The error bar represents the statistical uncertainty coming from the measurement noise. It increases towards higher altitudes as a consequence of the corresponding SNR being lower.

4.2.2 Error analysis

The total uncertainty of the derived atomic oxygen densities not only depends on the measurement noise, but also on the smoothing error as well as on uncertainties in forward model parameters and the background atmosphere input. The largest source of uncertainty is found in the forward model parameters. The influence of these uncertainties on the results is assessed in a sensitivity analysis by the perturbations of forward model parameters. The chemical reaction rate coefficient k_{OO_2M} has an uncertainty of around 20 %, contributing around 15 % uncertainty below 90 km and around 20 % at 95 km in derived abundances. k_{OO_3} introduces an increasing uncertainty of up to 6 % at 95 km. The nascent branching factor (e.g., f_8, f_9) explains the distribution ratio of excited hydroxyl radicals OH^* of different vibrational levels (Eq. 2.2). f_8 has a linear influence on the uncertainty of the results; a perturbation of 10 % on its values results in a similar retrieval uncertainty. The errors of Einstein coefficients correspond to an uncertainty of around 7 % in the results. The uncertainty in the quenching coefficient $k_{N_2(8)}$ of OH^* radicals with nitrogen molecules introduces a uncertainty of 14 % at 80 km, which decreases to 5 % at 95 km, and the uncertainty in the rate coefficient for quenching by

molecular oxygen $k_{O_2(8)}$ corresponds to an uncertainty of 5 % at 85 km and 2 % at 95 km. The influences of other model parameters are on the order of 1-2 % or less. SABER temperature uncertainties are the predominant factor influencing the retrieval results in the background atmosphere. The uncertainties are around 5.5 K at 80 km and increase to 13 K at 90 km (*Dawkins et al.*, 2018). This could lead to an uncertainty of 5 % below 90 km and up to 20 % above 95 km, taking into account the compensation effects of total density changes following the hydrostatic equilibrium (*Zhu and Kaufmann*, 2018).

At the altitude of 80-100 km, the effects of the smoothing error and measurement noise on the uncertainty are on the order of 0.5 % and 5 %, respectively. It is due to a properly chosen regularization in the retrieval procedure that the a priori information is negligible in the retrieval results. As part of a more in-depth look into the retrieval results, the averaging kernel and vertical resolution are investigated, as shown in Fig. 4.7. The summed-up averaging kernels for each row in the altitude region of interest (80-100 km) are equal to one, indicating that the measurements instead of the a priori information contribute to nearly all of the retrieval result. The peaks of averaging kernels are found at the tangent altitudes and the corresponding vertical resolution for each altitude is around 3 km, which is close to the vertical spacing of the limb measurements. Since the sum of the averaging kernels is also near one, the a priori influence is generally low.

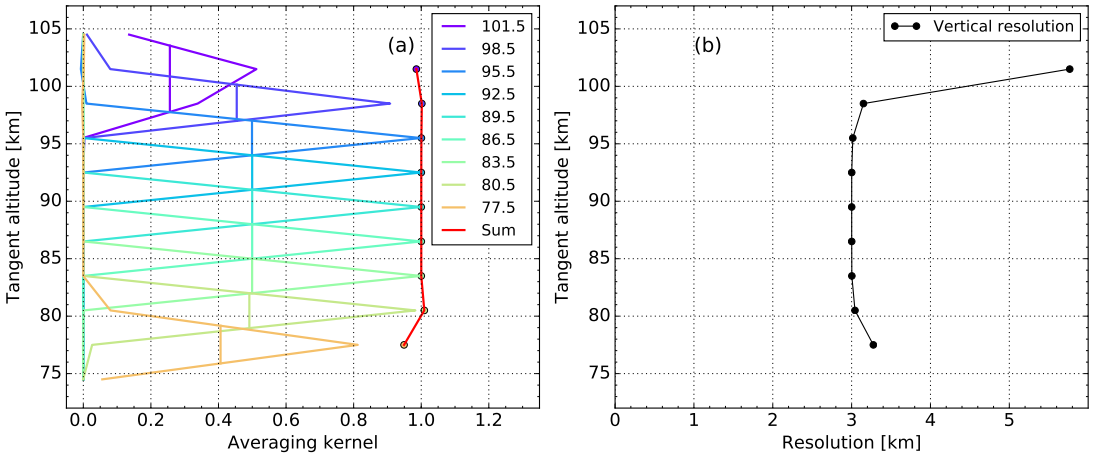

Figure 4.7: (a) The averaging kernel and (b) the vertical resolution of the retrieval for Feb. 2006 at 10°-20° N and a local time of 10-12 p.m.. The vertical resolution is obtained from the distribution of each row in the averaging kernel by calculating the corresponding FWHM.

4.2.3 Spatial and temporal analysis

The global distribution of atomic oxygen in the mesopause region shows spatial and temporal variations, which result from transport by global meridional circulation, diffusion, wave motions, and also from photochemical processes.

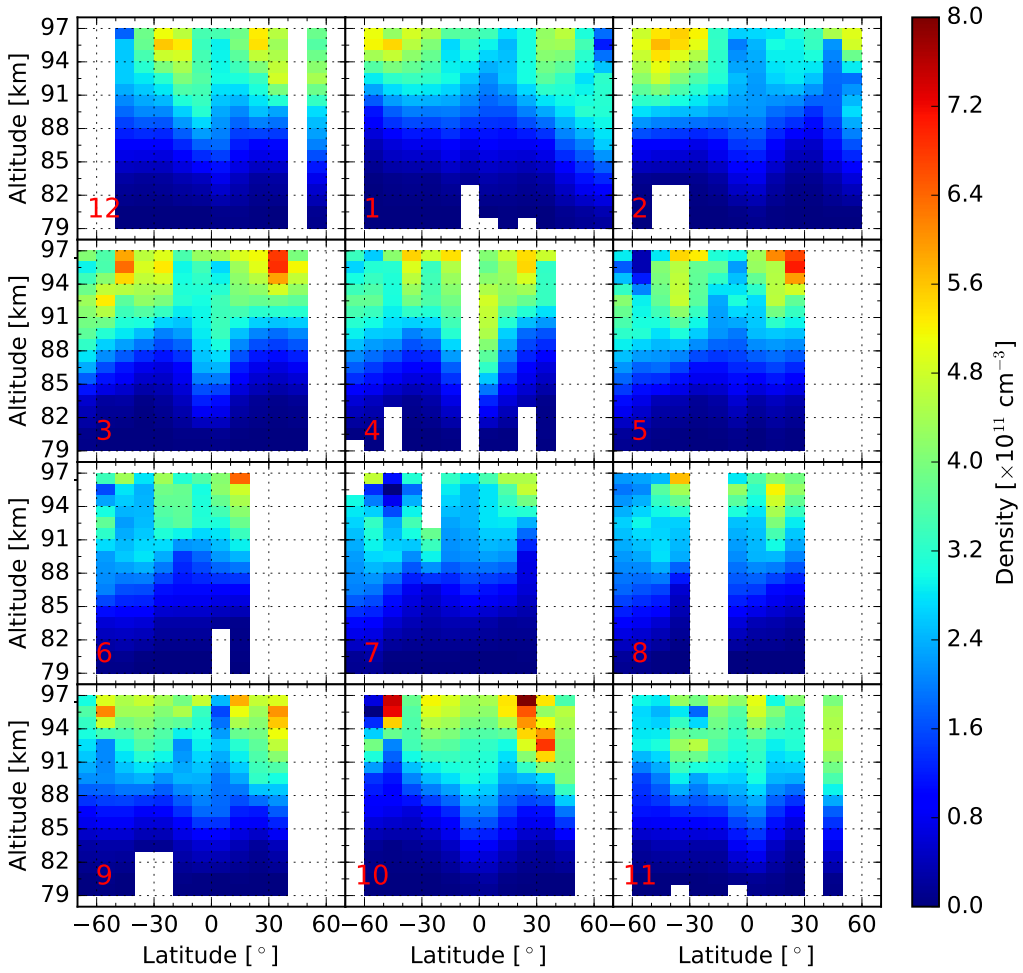

Figure 4.8: Latitude-altitude distribution of the zonal mean atomic oxygen density for 2007. Each row represents approximately a season. The data are linearly interpolated into a 1 km altitude grid for better illustration. The numbers in the subplots indicate the month of the year.

As shown in Fig. 4.8, atomic oxygen reveals a two-cell structure near 95 km at mid-

latitudes, which is most pronounced during the equinox seasons. The smallest values appear over the equatorial region and the largest values are at mid-latitudes. As already mentioned and discussed by *Smith et al.* (2010) and *Xu et al.* (2010), the latitudinal distribution structure of atomic oxygen is influenced by tides. The vertical transport of air caused by tides leads to a vertical displacement of atomic oxygen. At a local time of almost midnight (the mean local time of the GOMOS measurements is around 10 p.m. to 12 p.m.), the atomic oxygen displacement by tides at the mesopause is upward at the Equator (resulting in an [O] decrease) and downward in subtropical latitudes (resulting in an [O] enrichment).

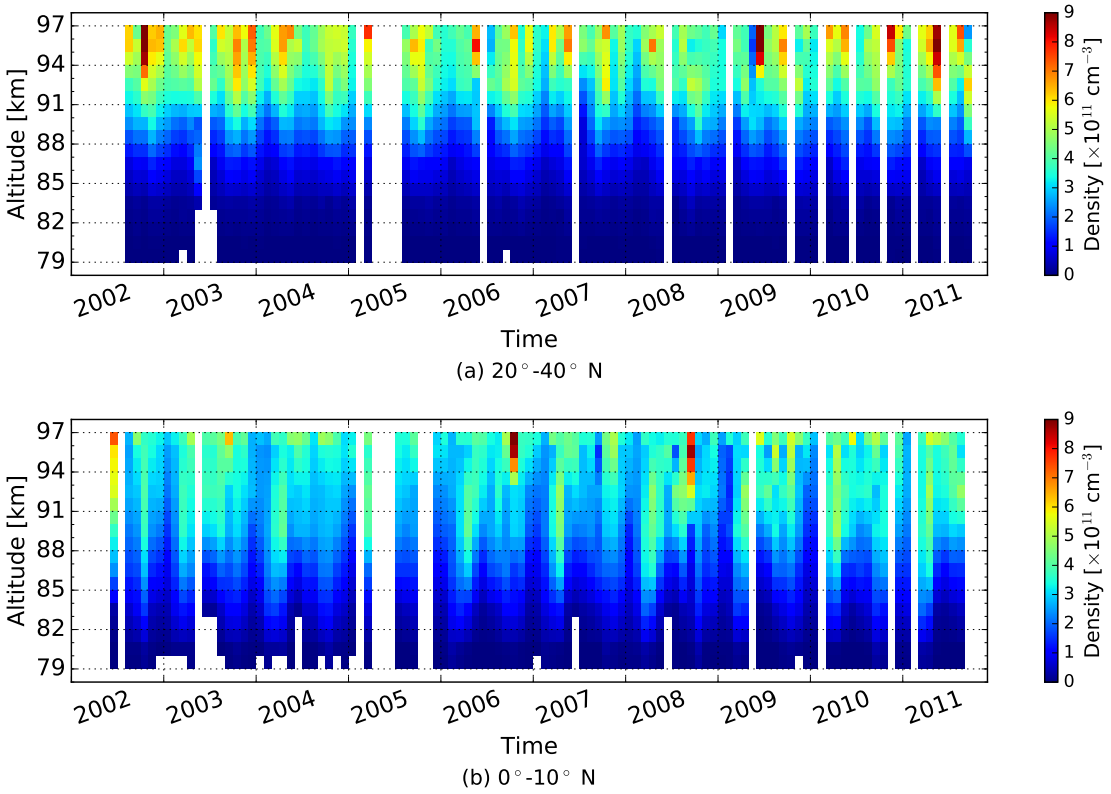

Figure 4.9: Temporal evolution of the vertical distribution of monthly zonal mean atomic oxygen densities for 20°-40° N (a) and 0°-10° N (b). The data are linearly interpolated into a 1 km altitude grid.

In Fig. 4.9, a vertical distribution of derived densities from 2002 to 2011 over the mid-latitude and equatorial regions is shown. Both the annual oscillation (AO) and semiannual oscillation (SAO) can be seen from the temporal evolution of middle and lower latitudes. Predominant annual and semiannual oscillations are observed in the mesospheric wind, temperature and airglow intensity variations (*Dunkerton*, 1982; *Takahashi et al.*, 1995; *Garcia et al.*, 1997; *Xu et al.*, 2007). The AO component has a

radiative origin, related to the annual variation of solar activities, and at the meantime is influenced by wave activities, while the SAO component is believed to be caused by dynamical behavior of tides and waves. Here in this analysis, the SAO reaches its maximum at equinox seasons (Fig. 4.9), which is related to the semiannual variation of the atmospheric tide amplitudes (*Smith et al.*, 2010).

A multiple linear regression analysis is applied to quantitatively analyze the longtime variations of the GOMOS [O] dataset. The monthly mean column density integrated from 80 to 97 km for 20°-30° N is analyzed by harmonic fitting, which includes components such as the solar cycle effect, SAO, AO and QBO (quasi-biennial oscillation), and baseline, as in Eq. 4.1.

$$\begin{aligned}[O]_{Column} = baseline + A_{solar} \cdot I_{solar}(t + shift) + A_{SAO} \cdot cos(\frac{2\pi t}{6} + P_{SAO}) \\ + A_{AO} \cdot cos(\frac{2\pi t}{12} + P_{AO}) + A_{QBO} \cdot cos(\frac{2\pi t}{27.5} + P_{QBO})\end{aligned} \tag{4.1}$$

The variable t represents the month since April 2002 and the column density is fitted by amplitudes (A, atoms cm^{-3}) and phase shifts (P, months) of SAO (period of 6 months), AO (period of 12 months) and QBO (period of 27.5 months), complemented by the amplitude (A_{solar}, atoms cm^{-3} SFU^{-1}) and a shift of the 11-year solar cycle effect, as well as a baseline. The coefficient I_{solar} is the solar radio flux proxy ($F_{10.7}$ cm, in units of SFU) taken from *Tapping* (2013). The QBO is usually confined to the tropical region, predominantly stemming from the interaction of waves with the global mean circulation (*Lindzen and Holton*, 1968; *Mayr and Mengel*, 2005). The typical mesospheric QBO period is about 27.5 months by investigating mesospheric zonal wind measurements (*Ratnam et al.*, 2008; *de Wit et al.*, 2013; *Malhotra et al.*, 2016). The baseline is given as the averaged value of the monthly mean column densities along the time series. The non-linear least squares fitting method (Levenberg-Marquardt algorithm) is applied to derive these fitting parameters, as described in detail by *Kaufmann et al.* (2013) and *Zhu et al.* (2015).

In Fig. 4.10, the raw data and the fitting results are illustrated in the panel (a). Besides, the baseline plus the solar terms are also shown in the plot. The SolarMin and SolarMax values denote the fitted atomic oxygen column densities solely from the solar cycle component, under the solar minimum and solar maximum conditions, respectively. The SAO and AO components from the harmonic fitting are given in the panel (b) and (c) respectively. The [O] longtime variations are well characterized by the fit. The 11-year solar cycle effect is captured, in which the atomic oxygen density is 17 % smaller in 2008/2009 (minimum of solar cycles 23/24) than in 2002 (near solar maximum conditions of solar cycle 23), due to different radiative forcing conditions during

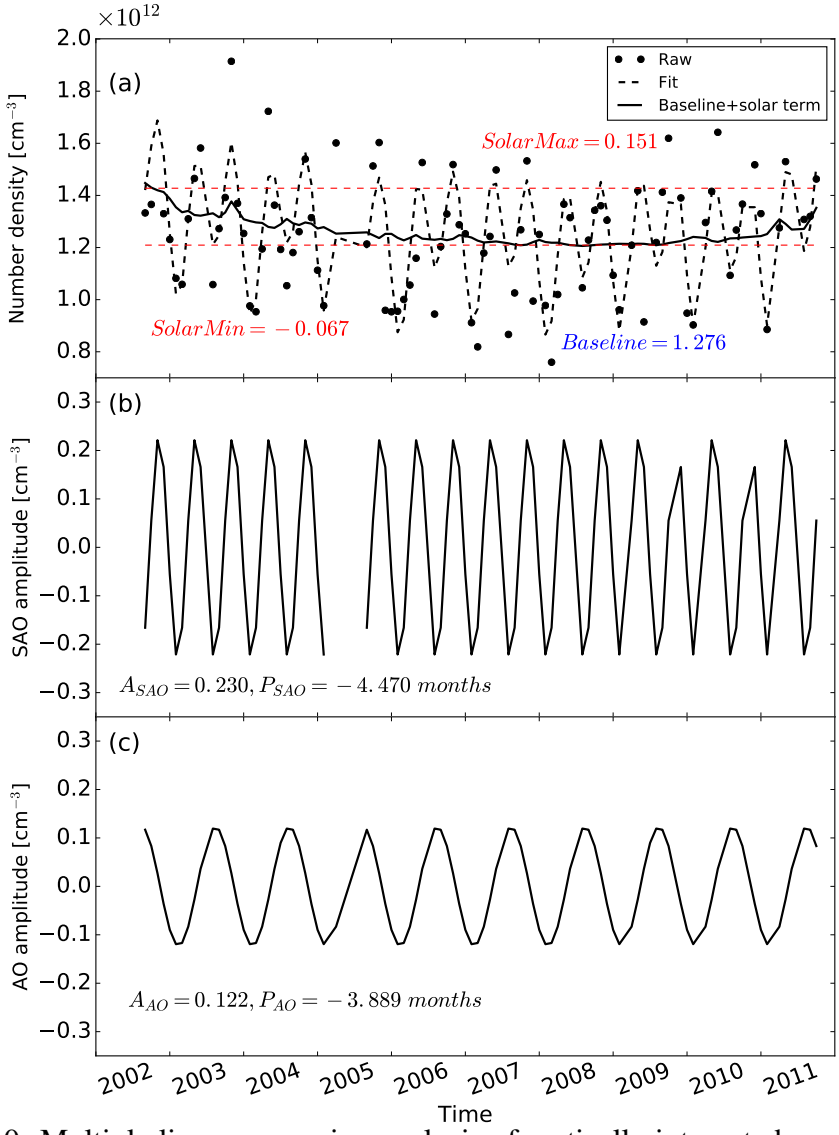

Figure 4.10: Multiple linear regression analysis of vertically integrated, monthly mean atomic oxygen densities of 80-97 km for 20°-30° N from 2002 to 2011. (a) The raw and fitted data are shown along with the baseline plus the solar components in the multiple linear regression results. The SolarMin and SolarMax values denote the fitted atomic oxygen column densities solely from the solar cycle component, under the solar minimum and solar maximum conditions respectively. (b) SAO and (c) AO parts are also illustrated with corresponding parameters. A_{SAO}, P_{SAO}, A_{AO}, and P_{AO} are the amplitudes and phase shifts of SAO and AO, respectively. The quantities of SolarMin, SolarMax, baseline and amplitudes are in units of 10^{12} atoms cm^{-3}. The phase shifts are in units of months. The gap present in the SAO is caused by the data discontinuity.

the solar cycles. During the 11-year solar cycle, the radiative forcing, which is responsible for the yield of atomic oxygen through photolysis of O_2 and O_3, changes by more than 50 % for the Lyman α line, by 10-20 % for the Schumann-Runge-continuum, and by 5-10 % for the Hartley band (*Rottman et al.*, 2006; *Kaufmann et al.*, 2013). This atomic oxygen density change agrees with model investigations and experimental results, which are normally in a range of around 10 % to 30 % (*Schmidt et al.*, 2006; *Marsh et al.*, 2007; *Kaufmann et al.*, 2014; *Zhu et al.*, 2015). A significant semiannual oscillation is observed, reaching a maximum in equinox seasons, which is in agreement with the analysis above for Fig. 4.9. The amplitude is about 18 % with respect to the baseline. The annual oscillation has an amplitude of 10 %, with the maximum being reached near summer solstices and the minimum near winter solstices. These results are consistent with the analyses of *Zhu et al.* (2015) and *Lednyts'kyy et al.* (2017), which reported SAO amplitudes on the order of 15 % and 12 % and AO amplitudes of 11 % and 7 %, respectively. The QBO amplitude is on the order of 2 %. The multiple linear fitting analyses on other latitudinal bands and altitudes also show a similar solar cycle effect as well as AO and SAO variations, as some examples are summarized in Tab. 4.1.

Table 4.1: Summary of multiple linear regression analysis results of monthly mean atomic oxygen column densities integrated over 80-97 km for 20°-30° N, 0°-10° N and 20°-30° S from 2002 to 2011. The SolarMin and SolarMax values denote the fitted atomic oxygen column densities (relative to the baseline) solely from the solar cycle component, under the solar minimum and solar maximum conditions respectively. A_{SAO}, A_{AO} and A_{QBO} are the amplitudes of SAO, AO, and QBO, respectively. The quantities are in units of 10^{12} atoms cm^{-3}.

Latitude bin	Baseline	SolarMax	SolarMin	A_{SAO}	A_{AO}	A_{QBO}
20°-30° N	1.276	0.151	-0.067	0.23	0.122	0.022
0°-10° N	1.221	0.085	-0.044	0.272	0.126	0.05
20°-30° S	1.126	0.097	-0.052	0.183	0.074	0.025

It could be considered to add an additional slope term in the harmonic fitting as well (Appx. A.5). In that case, the agreement between measurements and the fit increases marginally by about 2 %. But the fitting parameters are not independent any longer, because a strong correlation between the slope, the baseline and the solar terms is found, which was not the case before. This indicates that the inversion problem (to obtain the fitting parameters) is now underdetermined.

As an alternative approach, the solar ($F_{10.7}$) fitting parameter could be replaced by the slope term (Appx. A.5). In this case, the residual increases by about 5 % and the fitting parameters are not correlated (except for the offset and slope terms). From a mathematical point of view, this is an alternative to the original fit (with solar but without

slope terms). For this setup, the slope is -0.0002$\times 10^{12}$ cm^{-3} month^{-1}, which means that there is virtually no trend apparent in the data. This can be explained if the change over time is considered as a combination of two linear trends, with a negative slope in the declining phase of the solar cycle and a positive slope in the following inclining phase. This hypothesis can be underpinned by looking at a subset of the time series, covering the time period from 2002 to 2009, only (roughly solar maximum to solar minimum). The slope for this period is about -3 % per year, indicating a linear decrease of atomic oxygen by 21 % for the given period. If the $F_{10.7}$ dependency is considered instead, a similar drop is modeled, if a solar term with an amplitude of 0.0025$\times 10^{12}$ cm^{-3} SFU^{-1} is used. This value is similar to 0.002$\times 10^{12}$ cm^{-3} SFU^{-1}, which is the value obtained when the total time series is considered. This line of arguments indicates that there is more likely a solar $F_{10.7}$ dependency apparent in the data than a plain linear dependency.

4.2.4 Comparison with SCIAMACHY data

As discussed in Sect. 4.1.2, SCIAMACHY data provides us with the best opportunity for a comprehensive joint investigation of the GOMOS [O] dataset. Besides, two more datasets of [O] derived from SCIAMACHY green line emissions (*Kaufmann et al.*, 2014; *Zhu et al.*, 2015) and OH(9-6) band airglow (*Zhu and Kaufmann*, 2018) are currently available.

SCIAMACHY performed the OH airglow measurements in dark limb-viewing mode in the flight direction, with the recorded spectra always near a local solar time of 10 p.m. and a fixed altitude grid of 3.3 km. The OH(8-4) band observation is located in channel 5 with a spectral resolution of 0.54 nm. SCIAMACHY data version 8-2016 is adopted in this work. A continuous observation was performed during the entire lifetime of Envisat. The number of recorded profiles in one sample bin was around 100-300 before 2005 and significantly increased to 400-600 because of a change in instrument operations. SNRs of single profiles are normally on the order of 6 at peak altitudes and decrease to 1 at lower altitudes. After monthly zonal averaging, SNRs are increased by one order of magnitude, and the mean noise level is around 0.6$\times 10^{9}$ photons s^{-1} cm^{-2} nm^{-1} sr^{-1}.

In this study, the two data products are found to be consistent in terms of absolute radiance within $\pm$ 20 % in the peak emissions layer (shown in Fig. 4.11), after monthly zonal averaging. Particularly, the difference between the GOMOS data and the SCIAMACHY data is gradually becoming positive from negative over time. The potential source for the drift could be a degradation of the GOMOS or SCIAMACHY instruments (*Bramstedt et al.*, 2009), which is not fully corrected or overcompensated in the level-0 calibration or the shift of the system sensitivities over time. One specific example of spectra comparison is given in Fig. 4.12. The emission radiances from two

data products are similar, but the GOMOS spectra are more noisy.

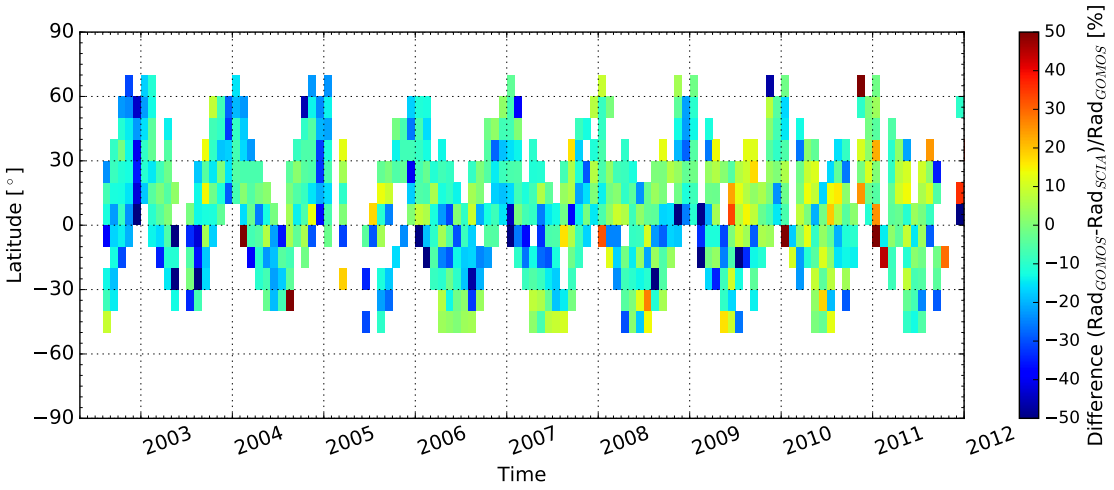

Figure 4.11: Temporal evolution of radiance differences (in percentage) between GOMOS and SCIAMACHY at a tangent altitude of 86.5 km. The radiance is integrated over the wavelength of 930-935 nm. Negative numbers indicate that SCIAMACHY radiances are larger than those of GOMOS.

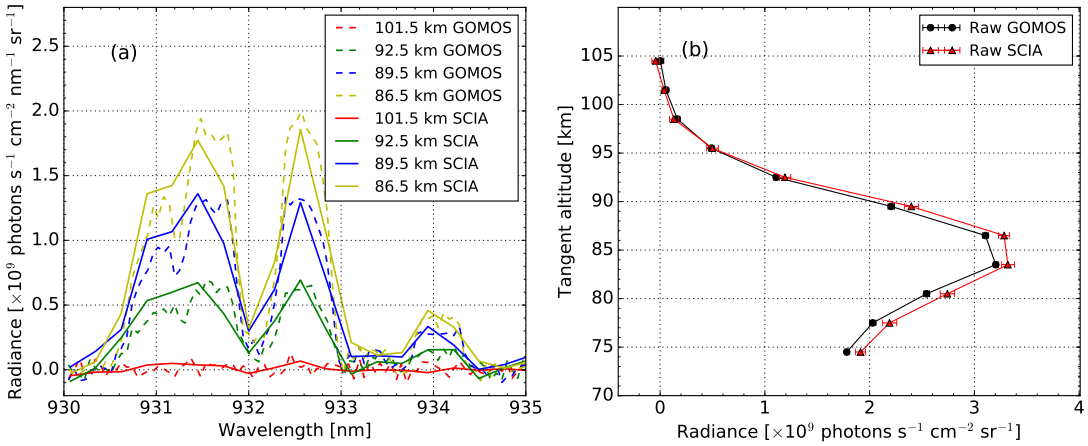

Figure 4.12: (a) SCIAMACHY (solid line) and GOMOS (dashed line) observations of monthly zonal mean OH(8-4) airglow emissions at the tangent altitudes, as given in the figure legend for Apr. 2004 at 20°-30° N and a local time of 10-12 p.m. (b) The spectrally integrated radiance over 930-935 nm versus tangent altitude for the same conditions. The error bars are measurement noise, computed as in Figure 4.4

The same retrieval procedure is applied to the SCIAMACHY data. The differences between the atomic oxygen abundances from the two instruments are illustrated in

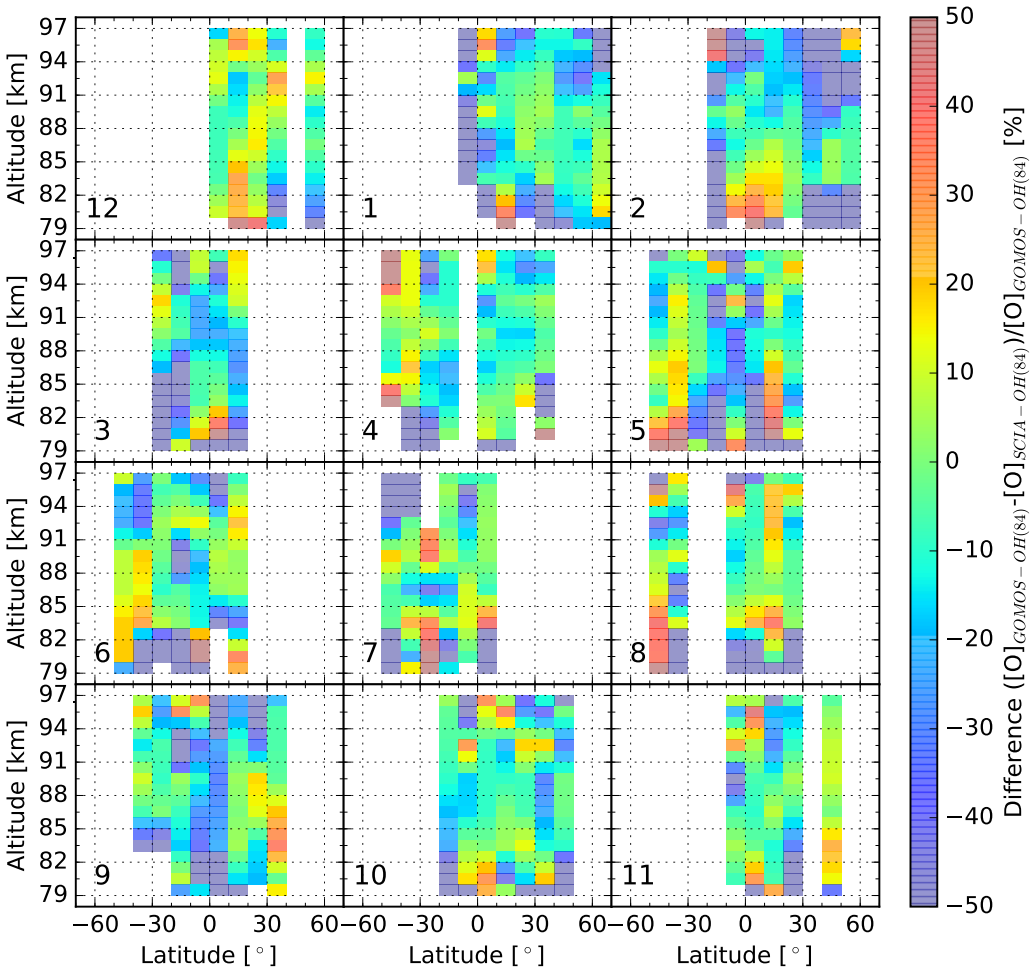

Figure 4.13: Latitude-altitude distribution of percentage differences between zonal mean atomic oxygen densities derived from GOMOS and SCIAMACHY OH(8-4) airglow emissions for 2007. Each row represents approximately a season. Negative numbers indicate that SCIAMACHY abundances are larger than those obtained from GOMOS. The data are linearly interpolated into a 1 km altitude grid. The numbers in the subplots indicate the month of the year.

Fig. 4.13. There are no major systematic discrepancies and they agree within a $\pm$ 20 % difference in most latitude-altitude bins as expected from the differences of the corresponding radiances. The GOMOS data are found to be over 20 % lower in the Northern Hemisphere in February, and also in tropical regions in March, May and September.

GOMOS values appear to be 20 % larger at low altitudes of around 80 km in some scattered bins. In general, these two atomic oxygen datasets derived from OH(8-4) airglow emissions agree with each other within the combined uncertainties in the context of absolute abundances.

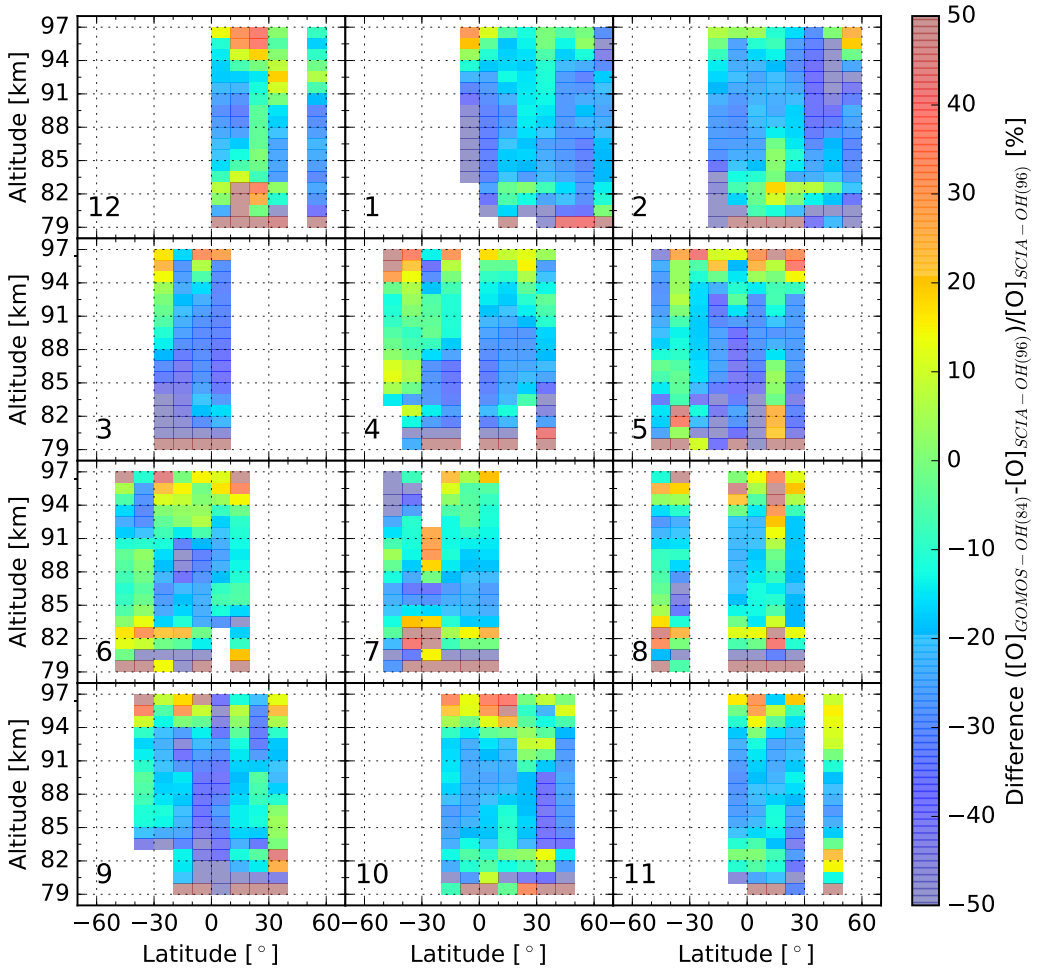

Figure 4.14: Latitude-altitude distribution of percentage differences between zonal mean atomic oxygen densities derived from GOMOS OH(8-4) and SCIAMACHY OH(9-6) airglow emissions for 2007. The SCIAMACHY OH(9-6) are taken from *Zhu and Kaufmann* (2018). This figure is plotted in a similar way to Figure 4.13. Negative numbers indicate that SCIAMACHY OH(9-6) atomic oxygen abundances are larger than the GOMOS OH(8-4) abundances.

Similarly, a latitude-altitude comparison of the GOMOS data with atomic oxygen obtained from SCIAMACHY OH(9-6) emissions (*Zhu and Kaufmann*, 2018) is given in Fig. 4.14 for 2007. In general, these two datasets agree with each other, but the GOMOS OH(8-4) dataset is found to be around 10-20 % lower than the SCIAMACHY OH(9-6) dataset in most latitude bins, especially in the altitude region of 85-95 km. The difference between the two datasets becomes more than 20 % at some data points near the Equator in March, May and September. Combing the derived results from SCIAMACHY OH(8-4), an intercomparison of the three datasets is given in Fig. 4.15 for different latitudinal and seasonal conditions. The absolute abundances of the three datasets are in the same order of magnitude and they agree with each other at the altitude region of interest of 80-95 km. Specifically, atomic oxygen abundances derived from OH(8-4) emissions by both instruments are found to be 10-20 % lower than those derived from OH(9-6) at around 90 km. This might be explained by a slight underestimation of the quenching of OH(v=9) to OH(v=8) by O_2, an overestimation of the deactivation of OH(v=8) due to collisions with atomic or molecular oxygen, or the over-/underestimation of the branching factors f_9 and f_8 in the OH airglow model.

4.2.5 Comparison with other datasets

There are a number of O_2 and O excited state emissions, which can also be used to derive atomic oxygen. This includes the O(^{1}S) green line and O_2 A-band emissions. Their modeling is mostly independent from the calculation of OH(v) emissions, although some processes have to be considered in all models. Rocket-borne in situ measurements of atomic oxygen are the most independent from methods based on nightglow. Mostly performed in the 1970s (e.g., *Dickinson et al.*, 1980; *Sharp*, 1980; *Offermann et al.*, 1981), the measurements are very rare and selective in terms of the local time and location. Figure 4.16 gives an impression of how the various datasets of atomic oxygen available in the literature, obtained from the SCIAMACHY, SABER, WINDII and OSIRIS measurements (see Sect. 1.3), fit to each other. All the sets are selected using a similar local time of around 10-11 p.m., with the exception of OSIRIS (6:30 p.m.) and in situ data with diverse local times at midnight or in the afternoon.

The datasets agree within their combined uncertainties in most cases. The absolute abundances are typically 4-6$\times 10^{11}$ atoms cm^{-3} above 90 km and decrease with descending altitudes by one order of magnitude (at around 80 km) for mid-latitude in autumn. GOMOS data are around 10 % lower than SCIAMACHY-O(^{1}S) and both SABER-OH datasets at 90-95 km, but remain in good agreement with these datasets at lower altitudes below 90 km. The OSIRIS dataset appears as the lower bound of the values above 90 km, as it is always the lowest in this region, while it becomes relatively large below 90 km. The WINDII dataset is around 10 % lower than the GOMOS-OH

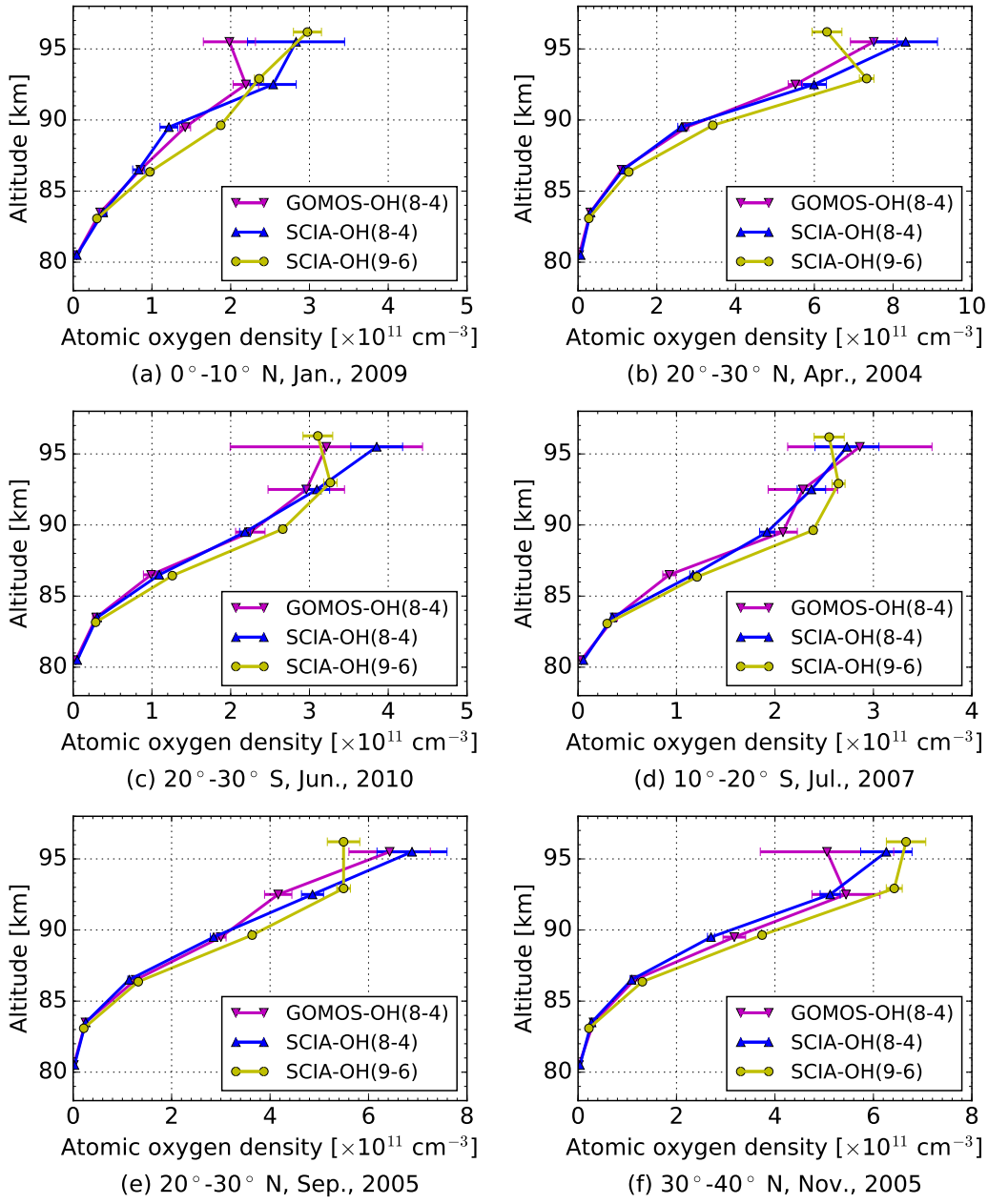

Figure 4.15: Comparison of monthly zonal mean atomic oxygen densities derived from hydroxyl airglow emissions observed by the GOMOS and SCIAMACHY instruments in various latitude bins for different months. SCIA-OH(9-6) represents the atomic oxygen dataset derived from the SCIAMACHY OH(9-6) band by *Zhu and Kaufmann* (2018); SCIA-OH(8-4) is the dataset from the SCIAMACHY OH(8-4) band; and GOMOS-OH(8-4) is from the GOMOS measurements of the OH(8-4) band.

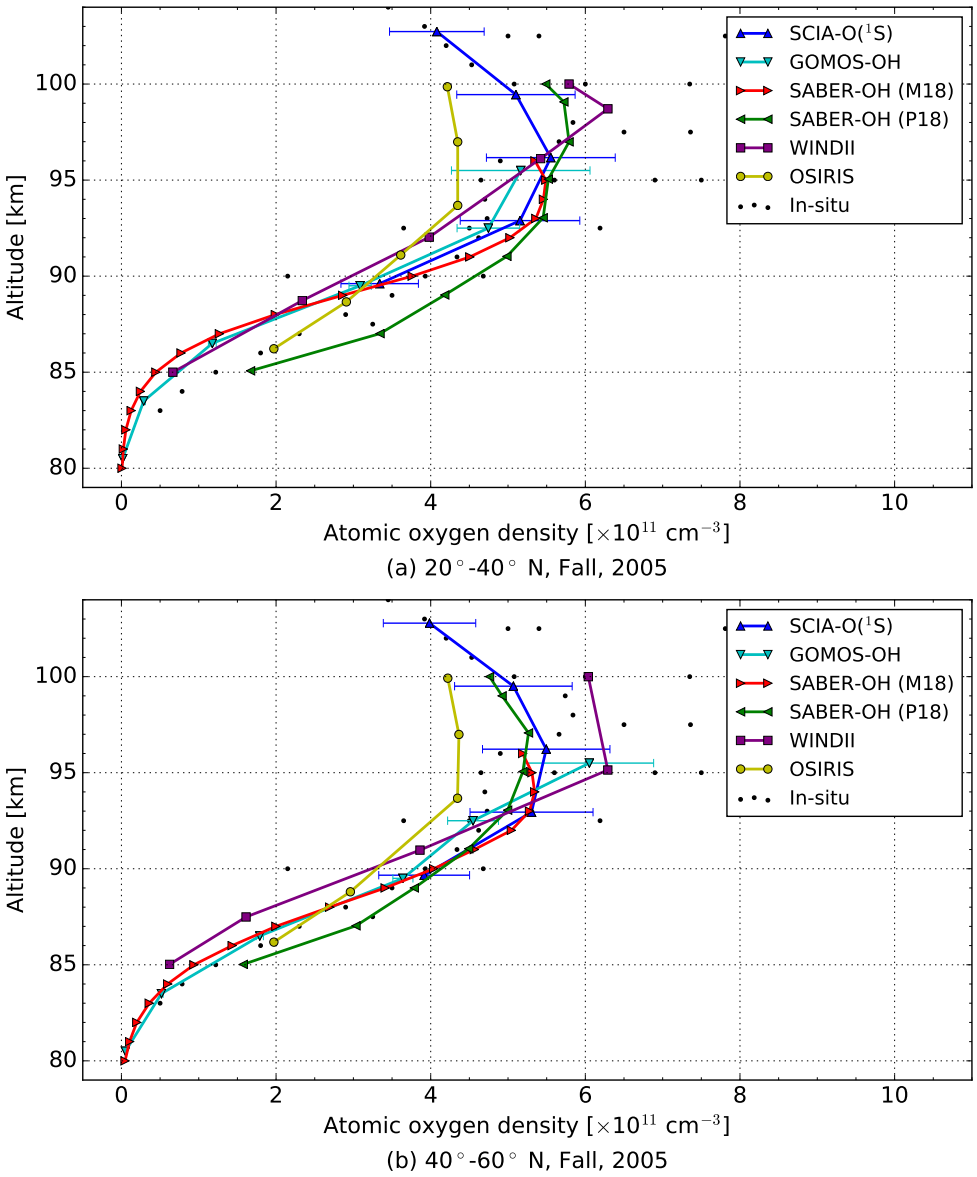

Figure 4.16: Comparison of atomic oxygen densities derived from various instruments and measurement techniques averaged for 20°-40° N (a) and 40°-60° N (b) in autumn (Sep., Oct. and Nov.) 2005. SCIA-O(^{1}S) is the atomic oxygen data derived from SCIAMACHY green line emissions (*Kaufmann et al.*, 2014; *Zhu et al.*, 2015); SABER-OH refers to the atomic oxygen datasets derived by *Mlynczak et al.* (2018) (M18); and *Panka et al.* (2018) (P18) from SABER hydroxyl airglow emissions. The WINDII dataset is obtained from WINDII combined hydroxyl and green line observations, 1993 (*Russell and Lowe*, 2003; *Russell et al.*, 2005), while the OSIRIS dataset is derived from OSIRIS O_2 A band measurements (*Sheese et al.*, 2011). In situ data are obtained from rocket-borne experiments, conducted at different local times at 37-40° N, from 1972 to 1976 (*Offermann and Grossmann*, 1973; *Trinks et al.*, 1978; *Offermann et al.*, 1981).

data at an altitude of 87-92 km, but they generally fit to each other. In situ data scatter in a large variation, which might be caused by the diurnal tides (a variation by a factor up to 2 at mid-latitudes for different local time as reported by *Smith et al.* (2010)), and the GOMOS-OH dataset is still located in its overall range of spread.

4.3 Retrieval results of atomic hydrogen

4.3.1 Atomic hydrogen abundances

A global fitting method as described in Sect. 4.1.3 is applied int the retrieval. Together with the atomic oxygen, a dataset of global atomic hydrogen abundances is simultaneously obtained. Given in Fig. 4.17 is one example of the vertical profile of the derived atomic hydrogen densities. The peak concentration of atomic hydrogen is about 2.2×10^8 atoms cm^{-3} at an altitude of around 83 km. Above the peak altitude, the atomic hydrogen density rapidly decreases with increasing altitudes, and at 95 km it is by one order of magnitude lower. The vertical distribution of atomic hydrogen is the consequence of the atomic hydrogen transported upward by diffusion in the MLT region.

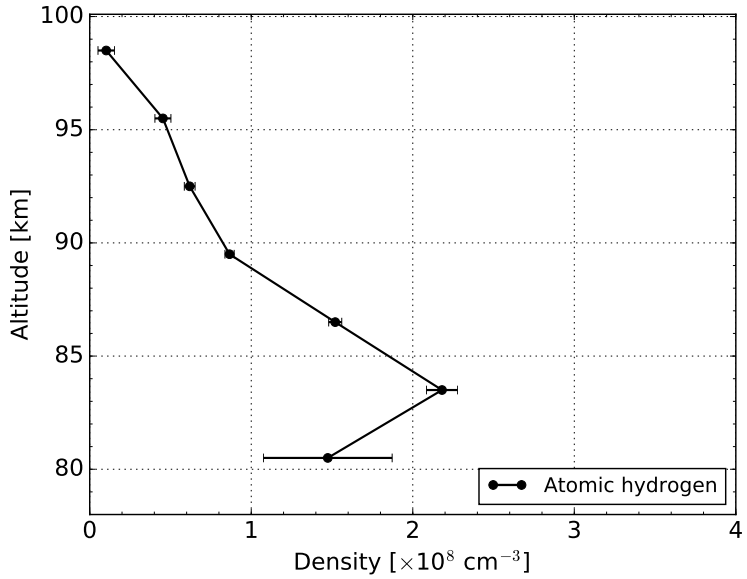

Figure 4.17: Atomic hydrogen abundances, derived from GOMOS monthly zonal mean measurements of OH(8-4) airglow emissions for August 2004 at 10°-20° N. The error bar represents the statistical uncertainty originating from the measurement noise.

4.3.2 Error analysis

As with atomic oxygen, the total uncertainty of the derived atomic hydrogen consists of three sources of uncertainties. The influences of the three error sources on the retrieval results are evaluated, as illustrated in Fig. 4.18.

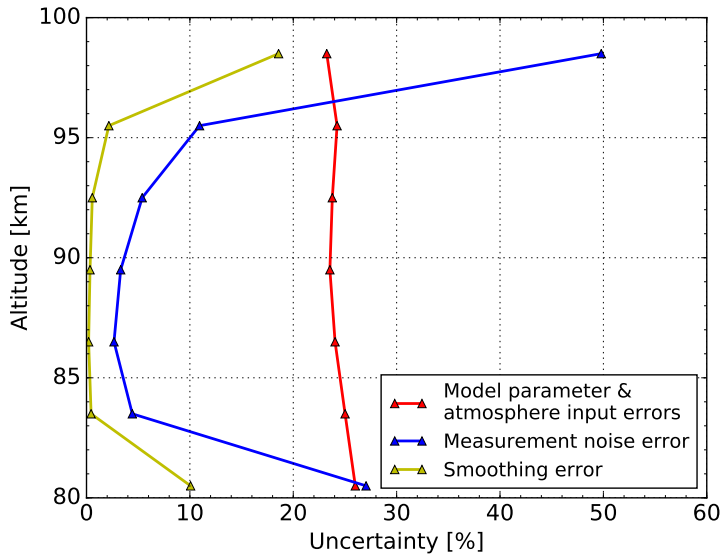

Figure 4.18: The uncertainties of the derived GOMOS atomic hydrogen propagated from different sources of uncertainties.

The forward model parameter and atmospheric background input are the largest sources of uncertainties, which in total contribute an uncertainty of around 23 % at all altitudes. The rate coefficient k_{HO_3} has an uncertainty of around 17 %, and leads to an uncertainty of 14 % in the retrieval results. It is followed by the uncertainties of SABER ozone measurements, which contribute an uncertainty of around 9 % in the derived results. The influence of the SABER temperature uncertainties on the derived results is on the order of 10 % at 95 km, and decreases to 3 % at 85 km. The nascent branching factors f_8 and f_9 result in an uncertainty of 9 % and 8 % at 95 km, and 7 % and 6 % at 85 km, respectively. The uncertainty coming from the Einstein coefficients is about 7 % at 85 km, and decreases to 4 % at 95 km. The influences of other model parameters are found to be generally less than 4 % in the region of interest from 80 to 100 km. Regarding to the measurement noise error, it is on the order of 3-10 % at the altitudes of 85 to 95 km, while the smoothing error is around 1 % or less in this region.

4.3.3 Spatial and temporal analysis

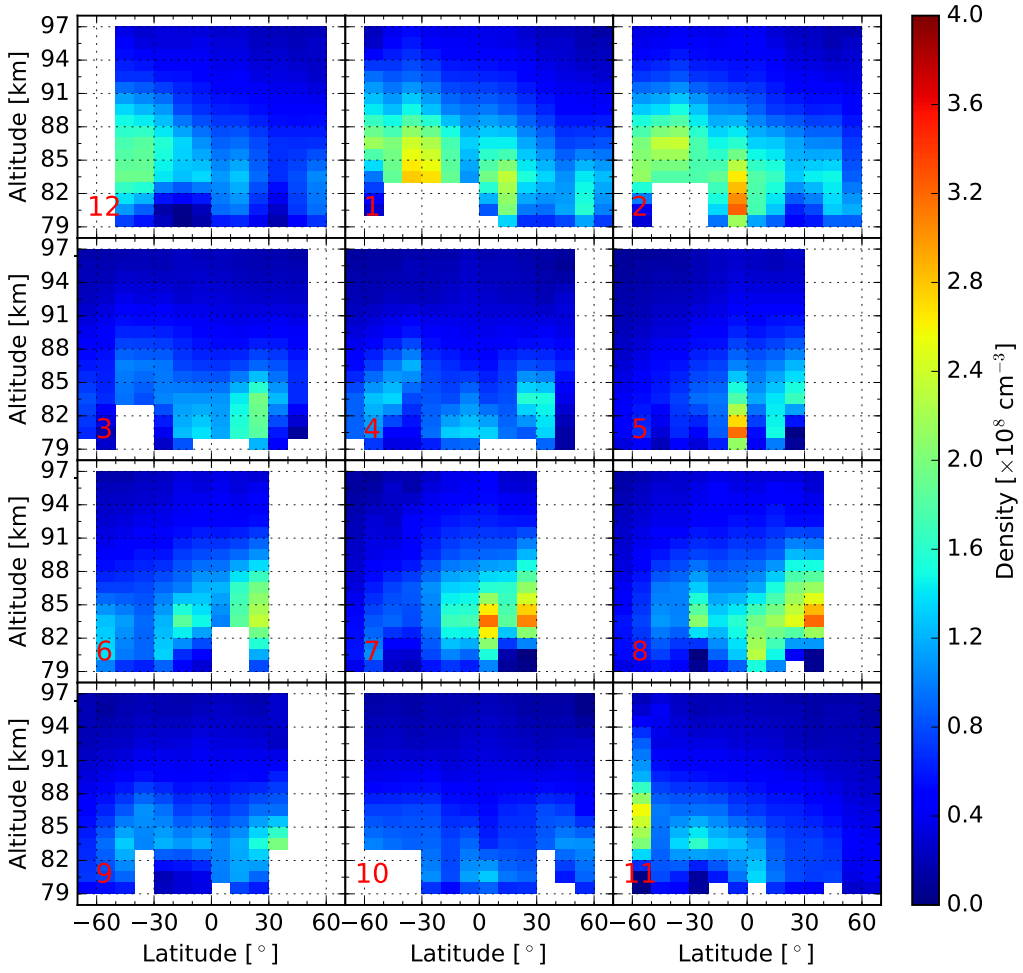

Figure 4.19: Latitude-altitude distribution of the zonal mean atomic hydrogen density for 2005. Each row represents approximately a season. The data are linearly interpolated into a 1 km altitude grid for better illustration. The numbers in the subplots indicate the month of the year.

Figure 4.19 presents the annual latitude-altitude distribution of the atomic hydrogen density for 2004. The highest abundances are discovered in the summer Hemisphere during solstice seasons, for instance, between 0° and 40° S in January and February,or between 0° and 30° N in July and August. The emergence of greater atomic hydrogen

concentration in summer seasons can be attributed to the higher water vapor concentration transported from below by vertical advection associated with the summer-winter meridional circulation (*Smith and Brasseur*, 1991; *Chandra et al.*, 1997; *Smith and Marsh*, 2005), which will lead to an enhancement in the atomic hydrogen production.

In Fig. 4.20, a vertical distribution of the derived hydrogen abundances from 2002 to 2011 over the northern mid-latitude regions is shown in the upper panel. The latitudinal distribution near the peak altitude of atomic hydrogen is given in the lower panel. The annual oscillation is recognized from the temporal evolution of both distributions, and it reaches the maximum during summer solstices.

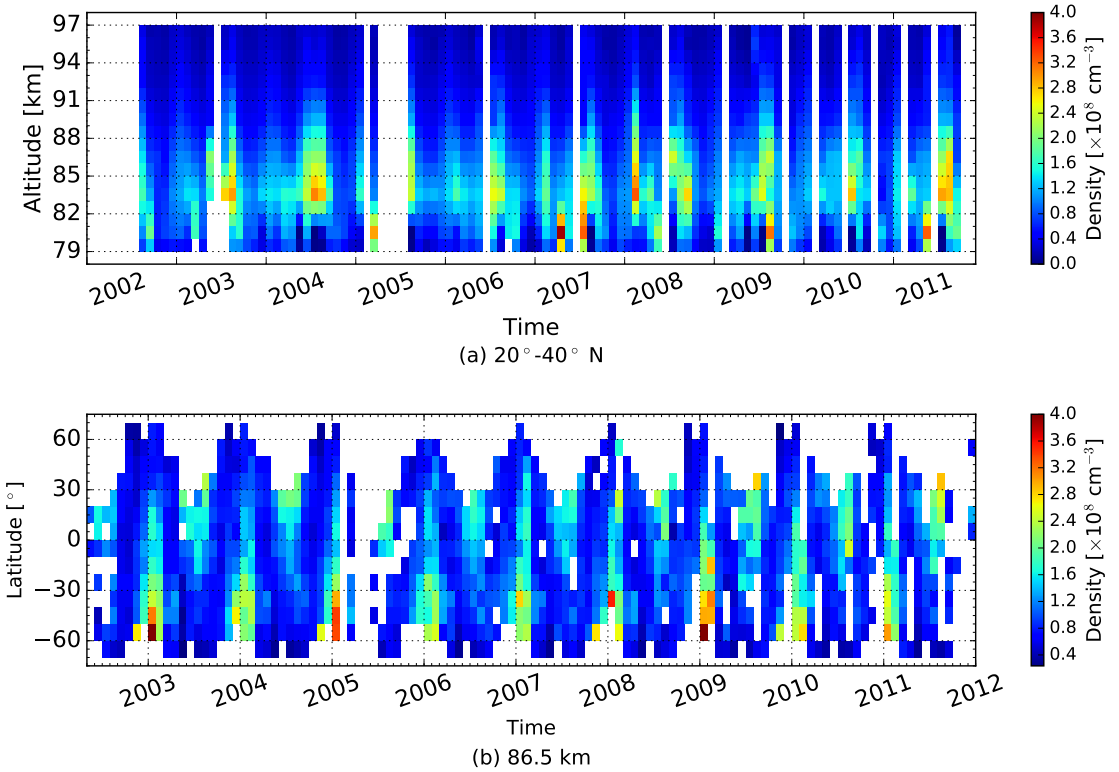

Figure 4.20: Temporal evolution of the vertical distribution of atomic hydrogen densities for 20°-40° N (a) and the latitudinal distribution for 86.5 km (b). The data are linearly interpolated into a 1 km altitude grid.

The temporal oscillations in atomic hydrogen are quantitatively analyzed by a Lomb-Scargle periodogram, which is developed by *Lomb* (1976) and *Scargle* (1982, 1989), and is extensively applied in the data series analysis. One example is taken from the mid-latitudes and the corresponding analysis results are shown in Fig. 4.21. The predominant frequencies of near 6 and 12 months are found, which are the periods of the semiannual and annual oscillations, as also discovered in atomic oxygen abundances.

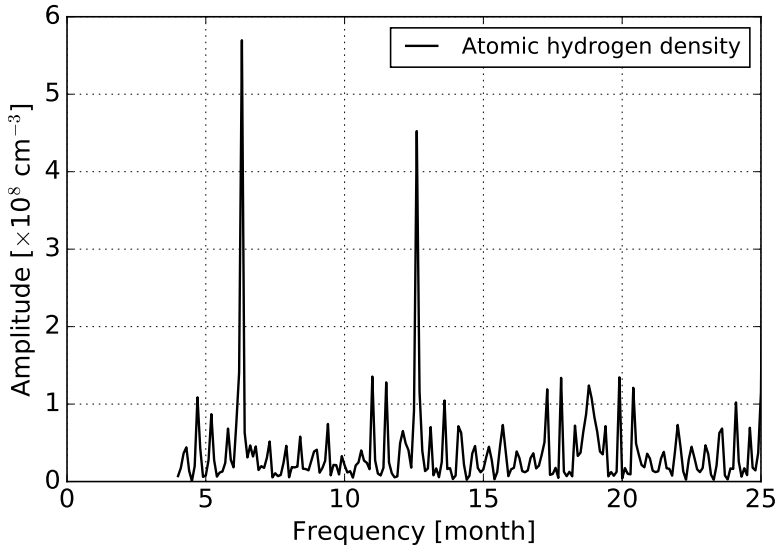

Figure 4.21: Lomb-Scargle periodogram of vertically integrated atomic hydrogen densities of 80-97 km averaged over the latitudinal bins of 20°-40° N from 2002 to 2011.

Figure 4.22 presents in the plot (a) the globally annual mean atomic hydrogen densities for the solar maximum and minimum conditions (the year 2002 and 2008), respectively. As opposite to atomic oxygen, the abundances of atomic hydrogen are lower under the solar maximum than the solar minimum, being contradictory to the solar cycle activities. This anticorrelation relationship is consistent with the findings in the SCIAMACHY atomic hydrogen dataset by *Kaufmann et al.* (2013) and the SABER dataset by *Mlynczak et al.* (2014).

Given in the Fig. 4.22 (b) are the ratios of atomic hydrogen densities between the solar maximum and minimum conditions, and also of atomic oxygen densities and the atmospheric background profiles of temperature, density, ozone and water vapor VMRs. The atomic hydrogen and oxygen data are derived from GOMOS measurements, whereas other atmospheric parameters are taken from SABER measurements (v2.0) for the same conditions. The solar maximum to minimum ratio of water vapor photolysis rate by the Lyman α line is also given here, which is calculated with Solar Radiation and Climate Experiment (SORCE) solar irradiation measurements (*Rottman et al.*, 2006). The solar maximum to minimum ratio of the atomic hydrogen densities is around 0.82 and increases above 95 km up to 0.92. An expansion of the entire atmosphere is noted under solar maximum condition, which is by around 4 % at 80 km to 16 % at 100 km. Water vapor is the source of atomic hydrogen in the MLT region. Its VMR is by 14 % to 18 % lower in the solar maximum condition than the solar minimum, consistent with other instrument observations and model simulations (*Hervig and Siskind*,

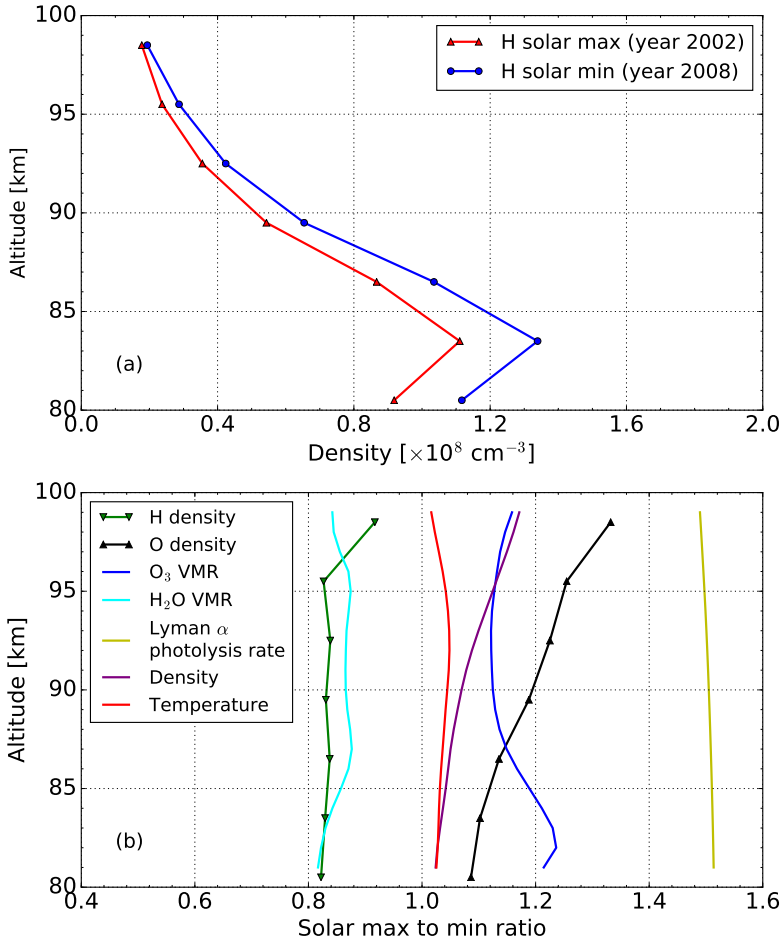

Figure 4.22: (a) The globally annual mean atomic hydrogen density derived from GOMOS measurements for the solar maximum (2002) and solar minimum (2008) conditions. (b) The ratios of the solar maximum to minimum values of atomic oxygen and hydrogen density, obtained from GOMOS measurements, and also of the ozone and water vapor mixing ratio, atmospheric density and kinetic temperature, taken from the SABER dataset, as well as of photolysis rate of water vapor by the Lyman α, calculated from the SORCE dataset.

2006; *Schmidt et al.*, 2006). This decrease of water vapor is found anticorrelated to the solar Lyman α variations (*Chandra et al.*, 1997; *Sonnemann and Grygalashvyly*, 2005; *Remsberg*, 2010). Besides, as shown here the photodissociation rate of water vapor by Lyman α increases by around 50 % between the solar minimum and solar maximum conditions. Comparably, the ozone mixing ratio is by 10 % to 20 % higher for the solar maximum, and the rapid reaction of ozone with hydrogen (R4 in Tab. 1.1), can

lead to an increased atomic hydrogen destruction. In general, in terms of photochemistry, lower atomic hydrogen under solar maximum can be interpreted as the excessive atomic hydrogen production due to enhanced photodissociation is overcompensated by the reduction of water vapor in the MLT region (*Kaufmann et al.*, 2013) and also the strengthened ozone destruction.

4.3.4 Comparison with other datasets

Similar to atomic oxygen, the derived GOMOS atomic hydrogen dataset is compared with the SCIAMACHY dataset, which is simultaneously obtained by performing the retrieval method as described in Sect. 4.2.4 on the SCIAMACHY OH(8-4) measurements. The global differences between the two datasets for 2007 are given in Fig. 4.23. In the altitude range of 85 to 92 km, the GOMOS and SCIAMACHY datasets agree with each other within the difference of $\pm$ 20 % for most months. At around 82 km, some data points in the GOMOS dataset is found by over 20 % higher than in the SCIAMACHY dataset, for example, near the Equator in February, or in the southern mid-latitudes in August. A negative difference beyond 20 % between the GOMOS and SCIAMACHY datasets also appears above 92 km or below 85 km in February, May, June and August. As compared to the atomic oxygen differences shown in Fig. 4.13, atomic hydrogen in Fig. 4.23 shows a similar pattern, except for some discrepancies found at, e.g., 0°-10° N, January, 30°-60° N, February, 20°-50° S, June and 40°-50° N, December. These large differences are due to the atmospheric background temperature and ozone variations by one-hour local time difference between the two datasets.

The GOMOS atomic hydrogen data are compared with the SABER data taken from *Mlynczak et al.* (2018), as presented in Fig. 4.24. At the altitudes of 82 to 88 km, the deviation between the datasets is generally within $\pm$ 20 %, and the GOMOS dataset is found by 10 % to 20 % larger than the SABER dataset at around 85 km. There is a negative bias up to 50 % between the GOMOS and SABER datasets above 90 km and below 82 km. A similar difference pattern was also discovered in the global comparison of the SABER and SCIAMACHY OH(9-6) atomic oxygen datasets by (*Zhu and Kaufmann*, 2018, Fig. 5). This significant differences between the GOMOS and SABER measurements can be attributed to the radiance differences between the two instruments. Besides, the neglected $O + O_3$ loss mechanism (R3 in Tab. 1.1) for ozone chemical equilibrium in the retrieval by *Mlynczak et al.* (2018) can also contribute to the differences. However, solid proofs and specific analyses are still required for further verification.

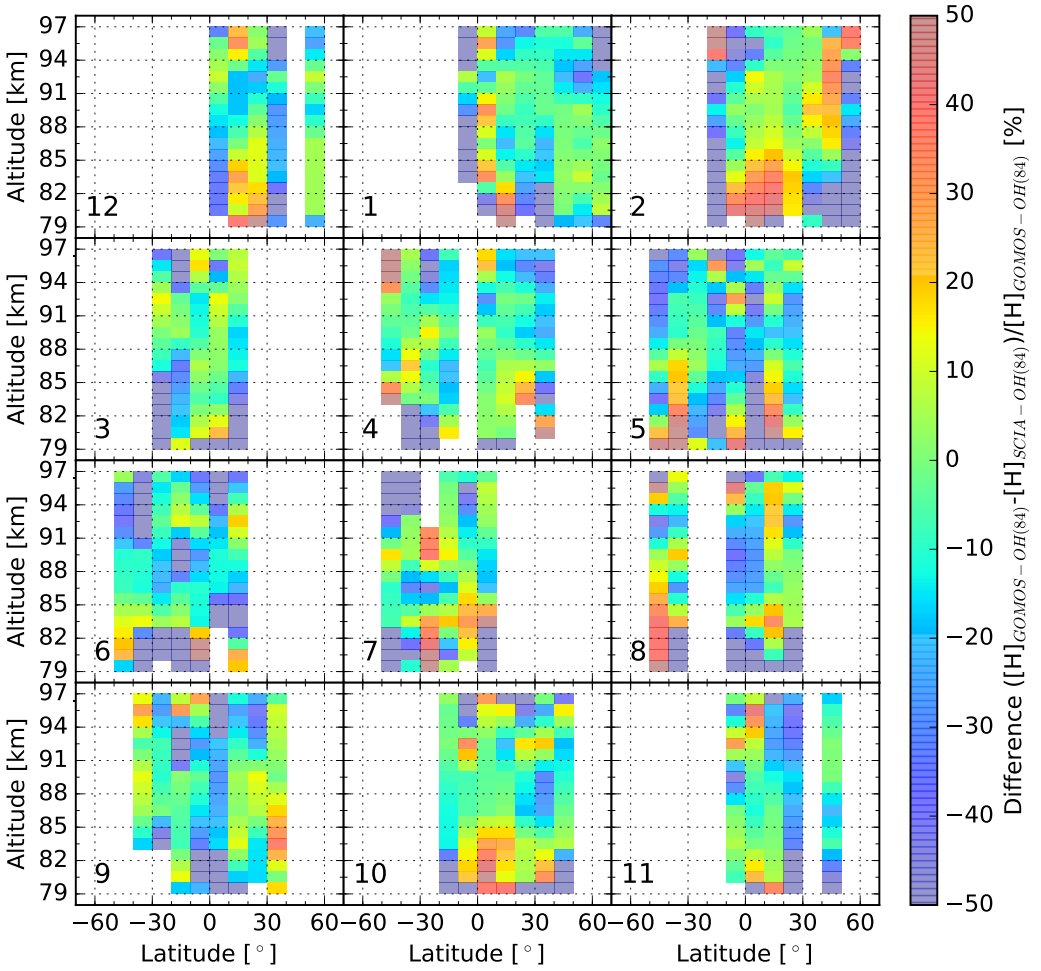

Figure 4.23: Latitude-altitude distribution of percentage differences between the zonal mean atomic hydrogen densities derived from the GOMOS and SCIAMACHY OH(8-4) airglow emissions for 2007. Each row represents approximately a season. Negative numbers indicate that SCIAMACHY abundances are larger than those obtained from GOMOS. The data are linearly interpolated into a 1 km altitude grid. The numbers in the subplots indicate the month of the year.

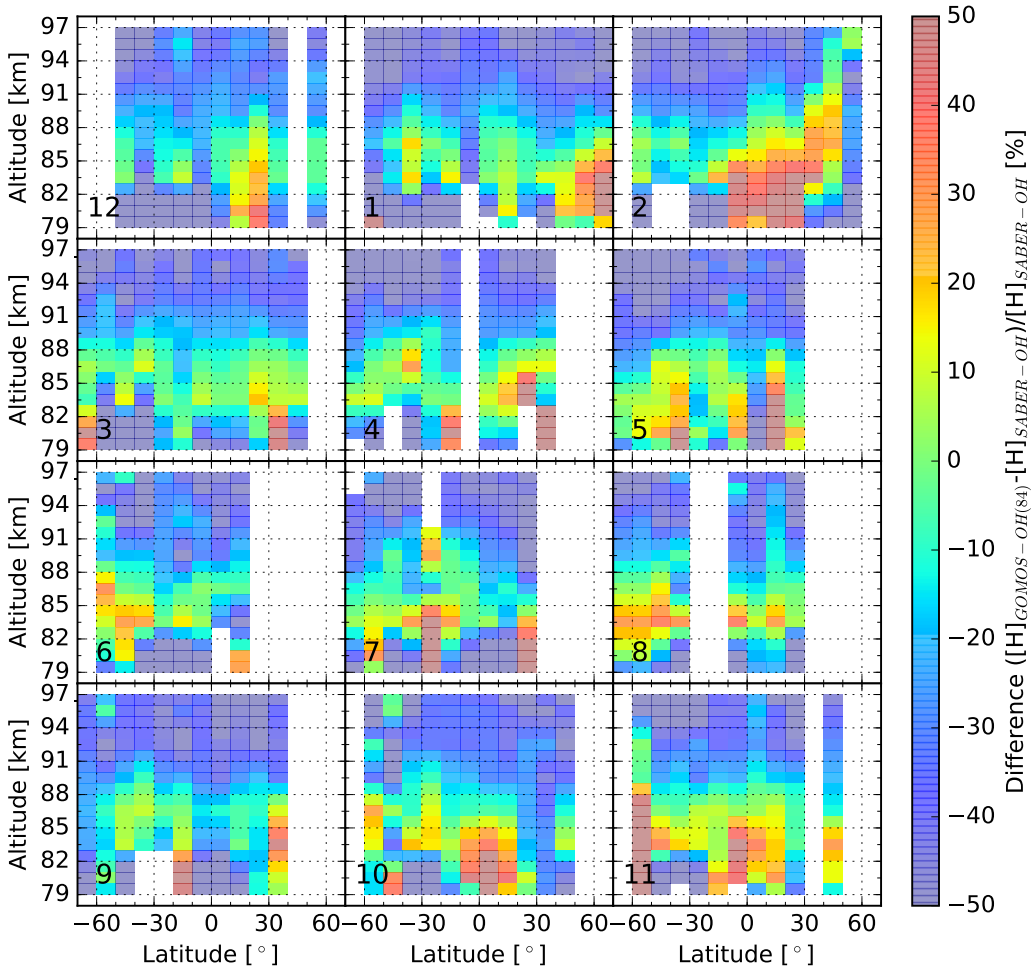

Figure 4.24: Latitude-altitude distribution of percentage differences between the zonal mean atomic hydrogen densities derived from the GOMOS OH(8-4) airglow emissions and SABER OH measurements for 2007. The SABER data are the updated version taken from *Mlynczak et al.* (2018). Each row represents approximately a season. Negative numbers indicate that SABER abundances are larger than those obtained from GOMOS. The data are linearly interpolated into a 1 km altitude grid. The numbers in the subplots indicate the month of the year.

Chapter 5

Atmospheric temperature derived from GRIPS-F OH airglow measurements

Ground-based instruments for observing terrestrial airglow emissions (e.g., spectrometer, imager) have their own advantages in providing continuous measurements, covering local temporal variations and providing a good temporal resolution at considerably low cost, although they lack in spatial information and are geographically restricted. Therefore, they are widely used for middle and upper atmospheric research (*Zhang et al.*, 1993; *Melo et al.*, 2001; *Sargoytchev et al.*, 2004). The GRound-based Infrared P-Branch Spectrometer (GRIPS-F) instrument delivers nighttime airglow spectra of the OH(3-1) band emissions, which enables the retrieval of the (vertically integrated) mean temperature in the mesopause region. The accumulated multiple-year GRIPS-F observation data can be used for the longterm variation analysis and trend study (*Beig et al.*, 2003; *Offermann et al.*, 2010, 2015; *Kalicinsky et al.*, 2016), while the coherent and simultaneous observations by multiple instruments present an approach for comprehensive investigation into the gravity waves characteristics (*Wachter et al.*, 2015).

In this chapter, the temperature retrieval from the GRIPS-F measurements of the OH airglow emissions is discussed. The OH nightglow modeling is described in Sect. 2.1, and the methodology for temperature retrieval is described in Sect. 2.4. An iterative retrieval approach is applied in this work. The data processing, the retrieval setup and the retrieval results are presented in detail. The nocturnal variations of the temperature profiles are analyzed for selected nights from different seasons, followed by error analysis. The retrieval result uncertainty is investigated with respect to various impact factors. The derived results are compared with the results obtained from the traditional three peak method, which is a commonly used temperature retrieval method in the literature (*Mies*, 1974; *Lange*, 1982), for a cross verification.

5.1 Measurements and data processing

5.1.1 Ground-based GRIPS-F instrument

The GRIPS-F instrument is a grating spectrometer, which observes the night sky in the near infrared spectral region, targeted at the OH emission layer centered near 87 km ($\pm$ 4 km) (*Schmidt et al.*, 2013). It is part of the international Network for the Detection of Mesospheric Change (NDMC, `http://wdc.dlr.de/ndmc`) with an instrument serial number of 17, and provides the derived nighttime mesospheric temperature on a daily basis. The instrument is located in Wuppertal, Germany (51.25°N, 7.15°E) and the observation started since April 2015. The instrument is pointed northwestward and has a viewing zenith angle of 45°. As the successor of the GRIPS instrument series (*Offermann et al.*, 1983), which were scanning grating spectrometers with a temporal resolution of 90 s, the GRIPS-F instrument has the grating fixed in one position, so that it can reach a higher temporal resolution of 15 s for one spectrum. Therefore, its name is suffixed with "F", as standing for "Fast".

Following the incident light, the main components of the instrument are: a long pass filter, an entrance slit, a collimating mirror, a reflection grating, a focusing mirror and a detector (*Schmidt et al.*, 2013). The instrument is equipped with an InGaAs photodiode array (PDA) detector, which covers a spectral range between 1.5 and 1.6 μm. The detector has a pixel number of 512 and the corresponding sampling step is 0.195 nm. The width of the instrument entrance slit is 300 μm, which yields a spectral resolution of 3.1 nm at 1550 nm. During routine operation, the instrument measures from sunset until sunrise every night, and the daily observation time is season-dependent, which is around 7 hours in June and 15 hours in December. One typical spectrum from GRIPS-F is illustrated in Fig. 5.1. It mainly includes the P branch of the OH(3-1) band with a rotational state quantum number of K''=2, 3 or 4, which is of interest for temperature retrieval (1517 to 1556 nm), and also the R and Q branches of the OH(4-2) band. Particularly, there is a partly overlapping of the 3-1 P branch with the 4-2 R branch, for example, the 3-1 $P_1(4.5)$ and 4-2 $R_1(6.5)$ emission lines overlap totally.

5.1.2 Data processing

The instrument acquires one raw profile every 15 minutes, which contains totally 60 spectra, along with two dark current measurements, each recorded before and after the spectra measurements. Because of the high thermal background noise in the detector, the dark current is by around one order of magnitude higher than the radiance signal. Therefore, the dark current has to be firstly removed from the spectrum. Following *Schmidt et al.* (2013), a sophisticated dark current correction algorithm is applied here.

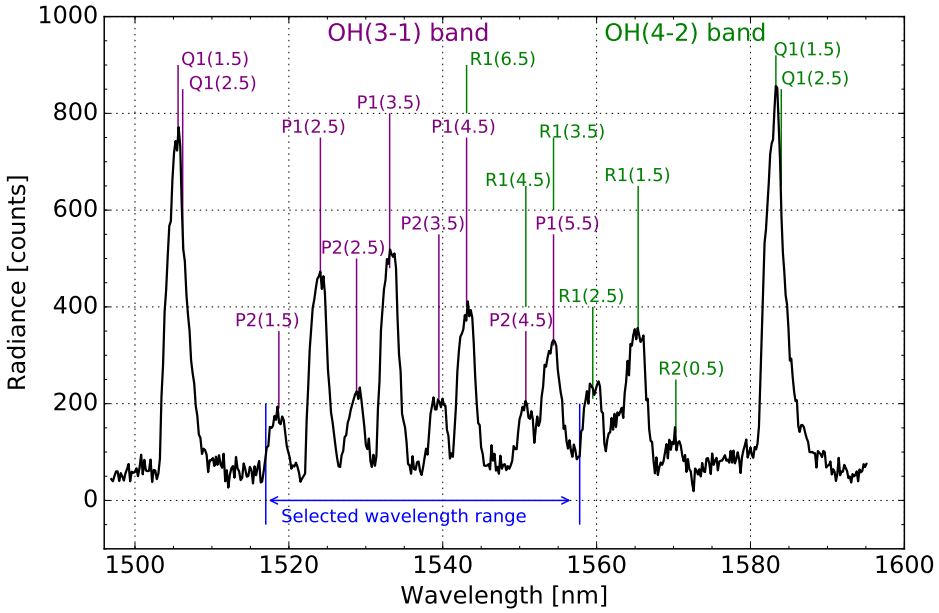

Figure 5.1: One typical example of the GRIPS-F spectra measured on Dec. 14, 2015 at 18:02:26. The spectrum is already calibrated with respect to the dark current removal, wavelength assignment and sensitivity correction. Dominant emission lines from OH(3-1) band (purple) and OH(4-2) band (green) are annotated with the branch and rotational quantum numbers. The wavelength range from 1517 nm to 1556 nm is selected for the temperature retrieval.

It is described in detail in Appx. A.6. The dark current removal is followed by the wavelength calibration and the sensitivity (photon response non-uniformity of detector, PRNU) correction, in reference to the in-house calibration data obtained from experimental measurements (P. Knieling, personal communication, 2016).

5.1.3 Retrieval setup

As discussed in Sect. 2.4, the rotational temperature retrieval only depends on the relative intensities of the emission lines, so that the absolute radiances are not relevant. The detector responsivity at all pixels is calibrated for GRIPS-F, the spectrum signals of which are in units of counts and have a linear relationship with radiances. Therefore, the corrected GRIPS-F spectra can be directly used for the retrieval. The OH modeling as described in Sect. 2.1.1 is applied therein, in which the HITRAN 2016 dataset of Einstein coefficients (*Gordon et al.*, 2017) is applied, and the atmospheric background profiles are taken from the ROSE model (A 3-dimensional middle atmosphere model,

Smith et al., 2003). The retrieval approach scheme applies a spectra fitting method (SFM) with the Levenberg-Marquardt algorithm as the minimiser. The regularization term is not considered in this case, as the retrieval quantities are not altitude resolved, and a priori information about their vertical profiles is not needed. The retrieval targets comprise not only the rotational temperature, but also spectral resolution, wavelength shift, radiance offset and a scaling factor, which scales the model output radiance with respect to the spectrum signal. These parameters are capable of reproducing the spectrum characteristics, which cannot be fully captured only by regulating the temperature in the model, thus resulting in a better fitting result.

5.2 Retrieval results of atmospheric temperature

5.2.1 Atmospheric temperature

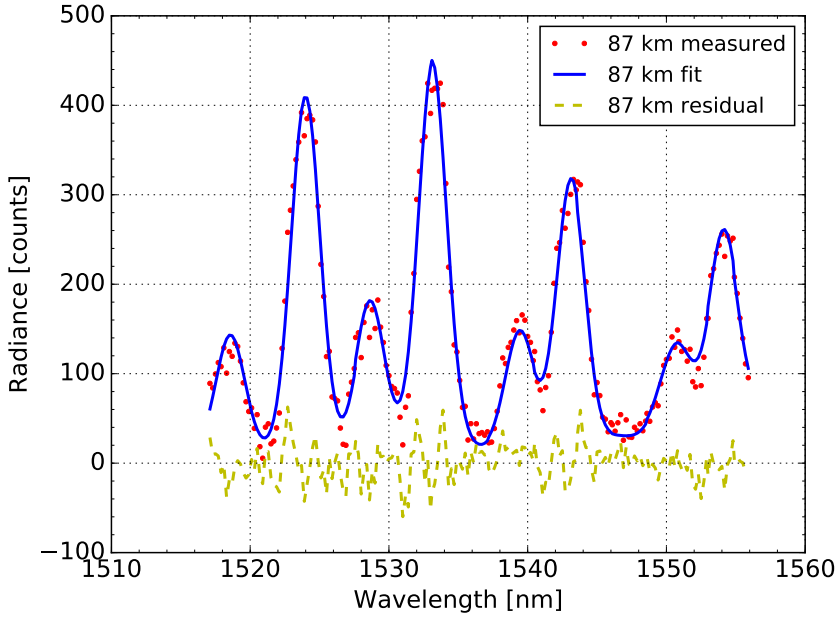

Figure 5.2: Simulated spectra (solid line) and measurements (dotted line), as well as the differences between the two (dashed line) for the GRIPS-F observations of OH(3-1) airglow emissions centered around 87 km for Dec. 14, 2015 at 18:17:11.

The temperature profiles are derived by applying the global fitting method, along with other fitting parameters. A typical fitting example of the spectra is given in Fig. 5.2, the obtained temperature of which is 208.5 K. The fitted spectrum generally agrees

well with the measurement. Due to the lack of the vertical information, the derived temperature is considered to be weighted mean over the atmospheric altitude region of the OH emission layer (*Bittner et al.*, 2002). Other retrieval target parameters are simultaneously obtained. The spectral resolution (FWHM) is typically around 2.4 nm, and the wavelength shift is negligible, while the scaling factor and the offset depend on the intensity of the recorded airglow emissions.

Shown in Fig. 5.3 are two examples of the temperature profiles measured by GRIPS-F during the course of the night selected from different seasons. For the case of April 17-18 2016 (Fig. 5.3 (a)), nearly two thousand data points of temperature are gained during the night, and they show a spread with a nightly mean value of 187.5 K. The half-hour running mean temperatures exhibit a large fluctuation between 178 and 196 K. The temperature variations show an oscillation with a period of around 5 hours, and small fluctuations of nearly one-hour period. This could be the sign of gravity waves, as interpreted by *Offermann et al.* (2006) for a similar plot of nighttime OH temperature variations. Figure 5.3 (b) provides a similar plot of the nighttime temperature variations as for the night of Nov. 26-27, 2015, which is close to the winter solstices. The derived temperature values are around 30 K higher than those in Fig. 5.3 (a). Wave structures with the period of one to several hours are also observed during the course of the night from the running mean values.

5.2.2 Error analysis

The measurement noise error of the derived temperature indicates the statistical uncertainty propagated from the measurement noise, which depends on the spectrum signal-to-noise ratio. For the given example in Fig. 5.3, the measurement noise error for single measured spectrum is on the order of 2 to 7 K.

In addition to the measurement noise, the forward model parameter uncertainties can also introduce uncertainties in the derived results. Since only the relative intensities of the spectra are used in this work for the rotational temperature retrieval, the calculation of the volume emission rate and limb radiance is not necessarily required, and the Einstein coefficients are of the most relevance and also the largest source of uncertainties in the forward model parameters, especially for the absolute temperature accuracy (*Offermann et al.*, 2010). A perturbation of 20 % on the Einstein coefficients corresponds to an uncertainty of around 1 K in the temperature retrieval.

Besides the applied HITRAN 2016 dataset (*Gordon et al.*, 2017), the Einstein coefficients published by *van der Loo and Groenenboom* (2007, 2008) and *Brooke et al.* (2016) are also the most recently published ones. Compared to the HITRAN 2016 dataset, the values for the OH(3-1) band from *van der Loo and Groenenboom* (2007, 2008)

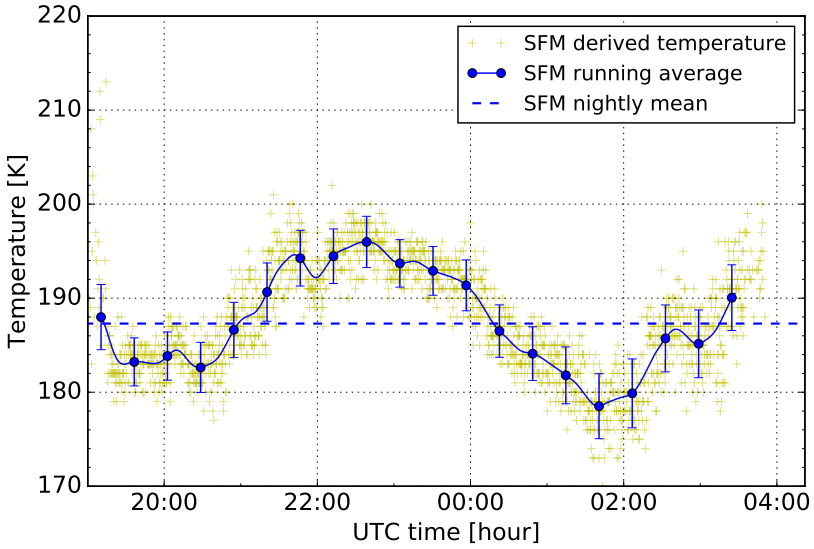

(a) Apr. 17-18, 2016

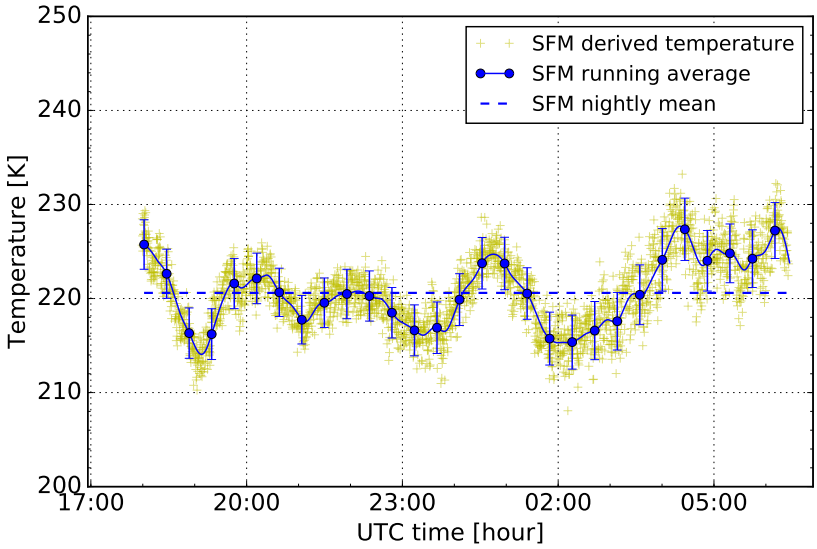

(b) Nov. 26-27, 2015

Figure 5.3: The measured OH temperature profiles during the course of the night by GRIPS-F. Data points (yellow cross mark) are with a temporal resolution of 15 s. The 30-minute running mean values (solid line) are computed with selected points illustrated with error bars. The nightly mean value is also given (dashed line), which is 187.5 K (a) and 220.6 K (b), respectively. SFM indicates it is obtained by the spectra fitting method.

are about 13 % smaller, while the values from *Brooke et al.* (2016) are around 16 % smaller. In comparison to the derived temperature results using HITRAN 2016, a negative bias of around 1.5 K is discovered when applying the *van der Loo and Groenenboom* (2007, 2008) set, and a negative bias of about 2 K is introduced when the *Brooke et al.* (2016) dataset is utilized.

In the airglow modeling of this work, the instrumental line shape is normally simulated by the Gaussian function. However, a trapezoid form appears in the measured line shapes of the GRIPS-F spectra. It is a consequence of the instrument entrance slit being relatively wide, so that a mixture of a rectangular form arises in the line shape, which can not be fully characterized by the Gaussian function. Therefore, other forms of the instrument line shape function are investigated in a case study as presented in Appx. A.7. The employment of different line shape functions is found to have a negligible effect on the temperature uncertainty in the retrieval result, which is generally less than 0.5 K.

5.2.3 Comparison with the three peak retrieval method

Commonly in the literature (*Bittner et al.*, 2000, 2002; *Schmidt et al.*, 2013), the OH(3-1) rotational temperature is calculated by a linear fitting line to the peak intensities of the three emissions lines $P_1(2.5)$, $P_1(3.5)$ and $P_1(4.5)$, which has an inverse logarithmic relationship to the temperature. It is named as the three peak method (TPM) hereafter. This method has been developed for the temperature retrieval half a century ago (*Mies*, 1974; *Sivjee and Hamwey*, 1987), and was improved by *Lange* (1982) who corrected the effect of overlapping with the OH(4-2) band R branch. The TPM is widely used in a number of research projects (e.g., *Oberheide et al.*, 2006; *Offermann et al.*, 2010; *Kalicinsky et al.*, 2016; *Silber et al.*, 2017; *Wüst et al.*, 2017). More details about the three peak method are summarized in Appx. A.8.

In our retrieval scheme, the global spectra fitting method is used as described in Sect. 3.1, that all data points in the selected wavelength range of the spectra are considered in the retrieval process, as to reach the global minimum of the residual between the fitted spectra and the measurements. Therefore, the convoluted intensities (over wavelength) of at least eight emission lines from 3-1 P branch (also the overlapped 4-2 R branch lines, as illustrated in Fig. 5.1) are considered for the rotational temperature retrieval.

Both of the two methods share the same theoretical background, while their major difference lies in the practical implementation approaches. The three peak method only uses a fraction of the spectral information, and it is more sensitive to the noise reduction, such as the offset estimation and the low pass filter for noise smoothing, and also to the

uncertainties of the Einstein coefficients applied. Additionally, the 4-2 correction from *Lange* (1982) can potentially lead to the derived rotational temperature being a few kelvins lower (*Kaufmann and Knieling*, 2013) and is regarded as an additional source of uncertainties in the retrieval.

A comparison between the derived temperatures from the two methods is given in Fig. 5.4 for a period of 15 min measurements. Here the HITRAN 2016 dataset of Einstein coefficients is applied for the two methods. In general, the two temperature profiles are close to each other in terms of the absolute value and the general trend in variations, and in the given example the difference between the averaged TPM and SFM temperatures is within 1 K. However, much larger fluctuations appear in the TPM temperature profiles, and a discrepancy of up to 8 K is discovered in individual sampling points of the two temperature profiles.

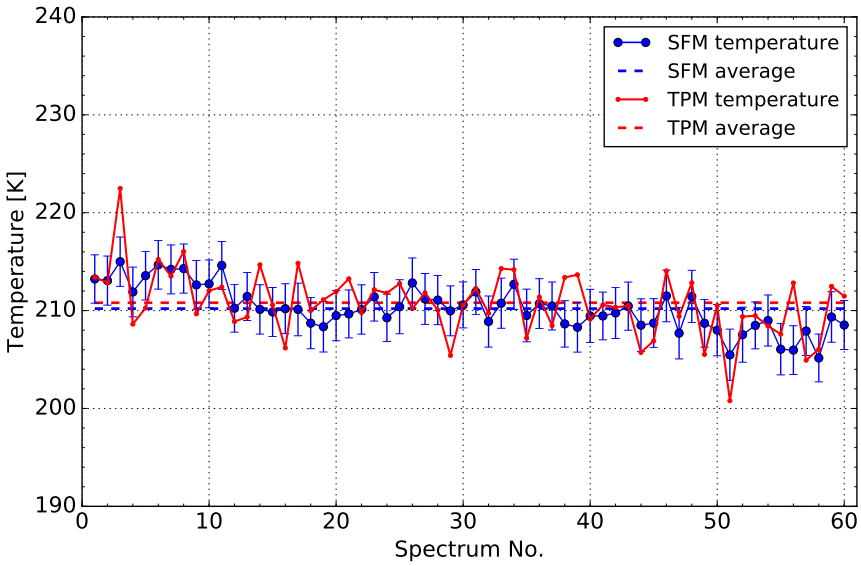

Figure 5.4: The GRIPS-F OH temperature measurements derived from the spectra fitting method (blue solid line) and the three peak method (red solid line) during the 15-min observation time starting from 18:02:26 Dec. 14, 2015. The data points are with a temporal resolution of 15 s, and the x-axis indicates the corresponding spectrum number since the measurements start. The averaged temperature values are 210.2 K for SPM (blue dashed line) and 210.8 K for TPM (red dashed line), respectively.

Chapter 6

Atmospheric temperature derived from AtmoSHINE O_2 A-band measurements

Recent advances in optics and detectors facilitate the instrument development in atmospheric temperature detection, with the concept of inferring temperature profiles from rotational structure of certain emission bands under the LTE condition. This detection concept has its own advantages. It does not rely on the in-flight calibration source and shorter target wavelengths are possible, allowing for smaller sized instruments. The target emission is normally in the wavelength regime from UV, visible to near-infrared (e.g. GRIPS-F), and thereof the oxygen atmospheric band (O_2 A-band) emissions near 762 nm are favored, as no active cooling of the detector for noise suppression is required in this spectral region. O_2 A-band emissions are already successfully deployed for temperature measurements by the HRDI (*Ortland et al.*, 1998; *Talaat and Lieberman*, 1999) and OSIRIS (*Sheese et al.*, 2010, 2012) instruments, which are, however, relatively large. Therefore, a new technology, the spatial heterodyne interferometer (SHI) is introduced whereby a minimized limb sounder could be built. Under this framework, the Atmospheric Spatial Heterodyne Interferometer Next Exploration (AtmoSHINE) instrument is developed (*Kaufmann et al.*, 2018), which provides a global observation of the O_2 A-band nightglow emissions, and is specialized for temperature detection in the MLT region.

Commonly, the temperature distributions of this region are obtained from the spaceborne observations of CO_2 thermal infrared emissions or of the absorption of solar radiation by CO_2 (e.g. CRISTA (*Riese et al.*, 1999; *Offermann et al.*, 1999), Michelson Interferometer for Passive Atmospheric Sounding (MIPAS) (*Fischer et al.*, 2008; *García-Comas et al.*, 2014) and SABER (*Russell III et al.*, 1999; *Dawkins et al.*, 2018)). The temperature retrieval and its uncertainty are subject to the modeling of the non-LTE state of CO_2. However, this technique is not suitable for nano-satellite development.

In this chapter, the temperature retrieval from the AtmoSHINE measurements of the O_2 A-band airglow emissions is discussed. The inversion of the atmospheric temperature is based on the forward modeling and the retrieval methodology as described in Sect. 2.2 and Sect. 2.4, and also the retrieval scheme discussed in Chap. 3. The overall data processing steps are introduced, in which the level-0 processing, geolocation registration and in-flight visibility calibration are applied on the raw data, followed by the retrieval of temperature and other parameters. The retrieval performance and uncertainty are analyzed in detail. A cross-comparison with other space-based measurements is also conducted.

6.1 In-orbit experiments and data processing

6.1.1 AtmoSHINE on Hongyun satellite

The satellite-based AtmoSHINE instrument is a limb sounder developed for the detection of global temperature by means of the O_2 A-band airglow measurements in the MLT region. It mainly consists of a SHI (*Kaufmann et al.*, 2018), which is capable of resolving the rotational structure of the emission band, and thereby the kinetic temperature can be derived from the relative intensities of the emission lines. The instrument development is a joint project by Forschungszentrum Jülich (FZJ) and Bergische Universität Wuppertal (BUW) in collaboration with Max-Planck-Institut für die Physik des Lichts (MPL) and York University. As a precursor mission for the in-orbit technical verification, the AtmoSHINE instrument was brought into space on the 22th of December 2018, on boards the Chinese Hongyun satellite. The satellite follows a dawn/dusk Sun-synchronous orbit with an altitude of 1072 km and an inclination of 99.88°. The instrument is mounted on the deck of the satellite main chamber, and the instrument's central LOS is pointing towards the Earth limb on the dark side, which is 29.68° below the tangent of the satellite orbit.

The AtmoSHINE instrument is a highly minimized payload (Fig. 6.1), with a size of 400 mm×112 mm×141 mm and a mass of 4.7 kg. It has a full FOV of 1.3° (solid angle), corresponding to a vertical coverage of 80 km, roughly extending from 50 km to 130 km. Following the incident light, the instrument comprises a baffle, a bandpass filter, a fore-optics, a SHI, a camera optics and a detector. The SHI generates an interferogram, mapping the wavelengths into spatial frequencies. The instrument detector is a silicon-based CMOS image sensor, which is a two dimensional (2D) array, consisting of 1920×1080 pixels (columns×rows). This enables the instrument to operate at the ambient environment temperature without active cooling, and to achieve a high vertical resolution as desired. The instrument covers a spectral region from 761.9 to 765.3 nm

(wavenumber of 13125 to 13067 cm^{-1}, spatial frequency of 6 to 209 fringes cm^{-1}) with a Littrow wavelength at 761.8 nm, and a spectral resolution of around 0.1 nm could be reached, which is sufficient to discriminate individual emission lines.

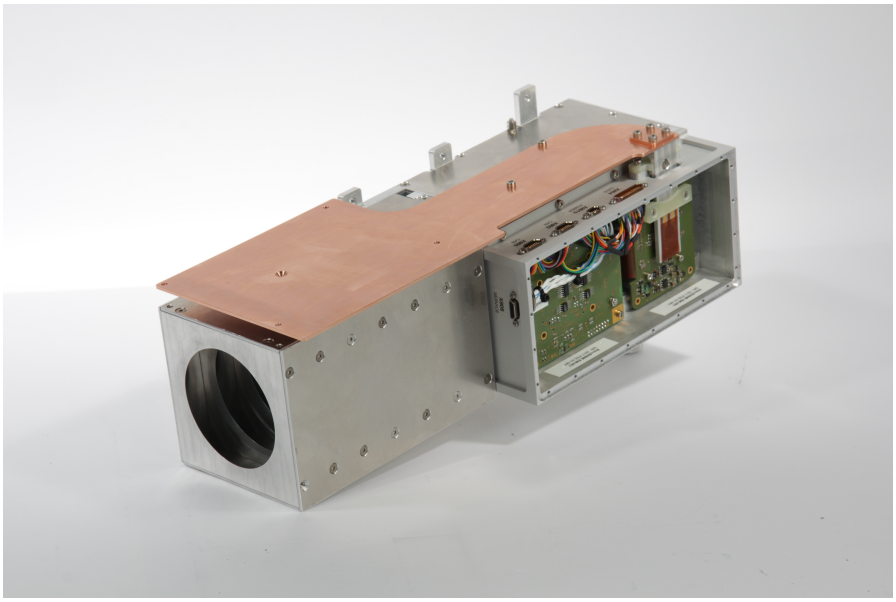

Figure 6.1: The AtmoSHINE instrument flight model developed for atmospheric temperature measurements.

6.1.2 Instrument operation and performance

In order to examine the instrument status and scientific data acquisition, a commissioning phase was defined before the regular observation started. Four experiment tests were implemented in this phase, the first test of which was performed in December 2018, followed by the second in March 2019, the third in April 2019, and the last one in May 2019. Several operation modes were tested during the in-orbit tests, including detector fixed pattern measurements (1 ms integration time) as well as short- and long-integration-time measurements, whereby a sequence of integration times from 1 to 32 seconds were applied to the data acquisition. One measurement profile contains an image. In total around 4000 profiles were recorded.

A four-day regular measurement was carried out during the 5th to 9th of August 2019, and in total 44-hours observation time of the O_2 A-band is accumulated. For the regular measurements, the integration time of 16 s was chosen. About 5200 images were measured during this period. An overview on the commissioning-phase tests and regular observations is summarized in Tab. 6.1. More details are given in Appx. A.9.

Table 6.1: Summary of the AtmoSHINE commissioning-phase tests and regular operations. The date and time are recorded in Universal Time Coordinated (UTC). * The data are not usable. ** The data are partly not usable due to attitude data loss or image data loss.

Test No.	Date	Start & stop time	Duration	Integration time	Status
1	23∼24 Dec. 2018	00:40∼02:00 23:55∼01:00	2.5 h	1∼32 s	Normal**
2	17∼18 Mar. 2019	12:01∼07:59	20 h	8 & 16 s	Satellite attitude control unstable*
3	11∼12 Apr. 2019	16:04∼15:52	24 h	8 & 16 s	Satellite data storage loss*
4	21∼22 May 2019	12:00∼02:44	14.5 h	8 & 16 s	Normal
5 (regular)	5∼9 Aug. 2019	16:00∼03:00	42 h	16 s	Normal**

Four typical images with an integration time of 1 ms to 32 s are shown in Fig. 6.2. A raw image is an interferogram, consisting of a set of vertically arranged interference fringes (bright and dark strips). These overlapping fringes with different spatial frequencies are formed by the interference reaction of wavefronts at different wavelength in the spectrometer. The 2D-interferogram contains spectral information in the horizontal direction and spatial information in the vertical direction. Each row in the image corresponds to one altitude layer and can be converted to one spectrum of a certain vertical layer. The image size is specified as 1920×1080 or 840×1080 pixels, of which the nominal extend of the image is normally 840×840, as considered to be the effective area. The emissions only illuminate around one hundred rows at the center of the image, corresponding to a vertical emission layer of around 10 km. The instrument is configured in such a way that the observed emission layer is imaged as close as possible to the central region of the detector, as at this region the image distortion is found to be smallest and the sensitivity is largest.

During the commissioning-phase experiments and the regular observation period, the AtmoSHINE instrument performed normally and functioned fully as designed. The status of the instrument current, voltage and temperature sensors, data transmission and communication with satellite is reported normally. No instrument malfunctioning or failure was monitored. The AtmoSHINE optics is sensitive to the environmental temperature, and the instrument temperature variations are continuously monitored by six embedded thermal sensors during the operation. Shown in Fig. 6.3 are the monitored temperature fluctuations for the instrument optics and Spatial Heterodyne Spectrometer (SHS) during the regular observation period. On a daily basis, the instrument oper-

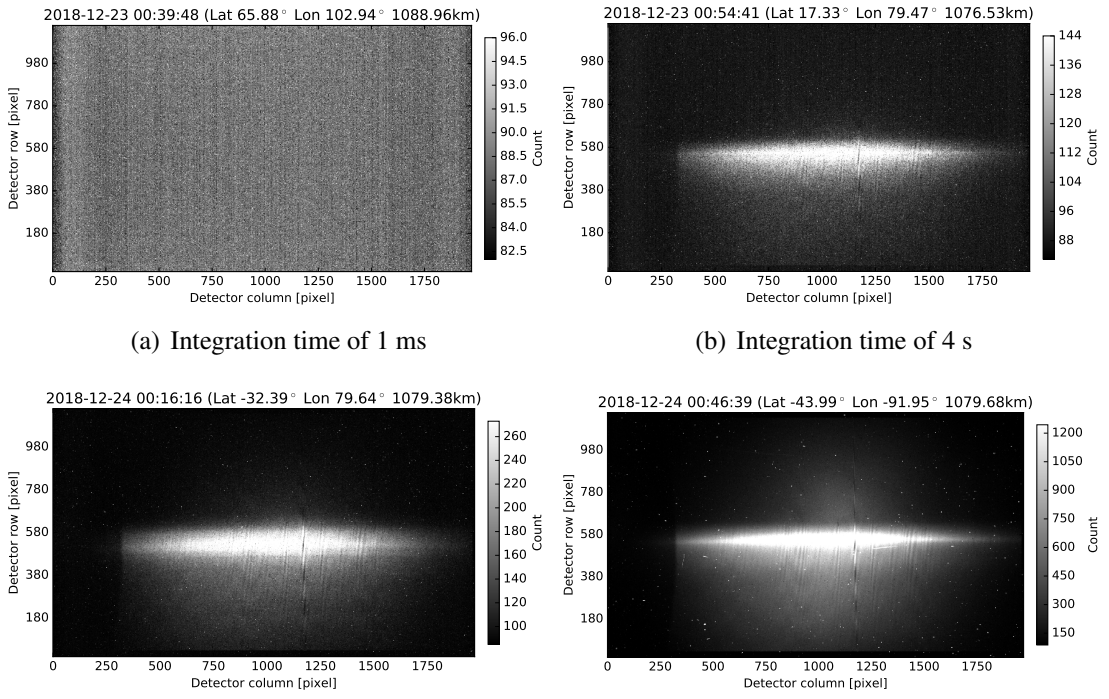

(a) Integration time of 1 ms

(b) Integration time of 4 s

(c) Integration time of 8 s

(d) Integration time of 32 s

Figure 6.2: Examples of the interferogram images taken by the AtmoSHINE instrument. Each image is recorded with a pre-configured integration time. The corresponding timestamps and satellite geolocations of the measurements are also given in the figure caption.

ational temperatures at the optics and SHS are relatively low after the instrument is switched on, and quickly reach a steady stage within around one hour with variations of about 2-3 K, and the optical system remains in a relatively stable thermal status.

6.1.3 Data transmission and processing

The Low-voltage differential signaling (LVDS) bus is implemented as the scientific interface for transmission of the image data measured by the instrument, along with the housekeeping data (monitoring the instrument status, e.g., temperature, current). The measurements which are stored on the satellite computer, are transmitted to ground for following processing when the satellite passes over the ground station. Additionally, satellite attitude GPS data are separately provided.

The raw data are processed offline. It follows the level-0 to level-2 processing chain,

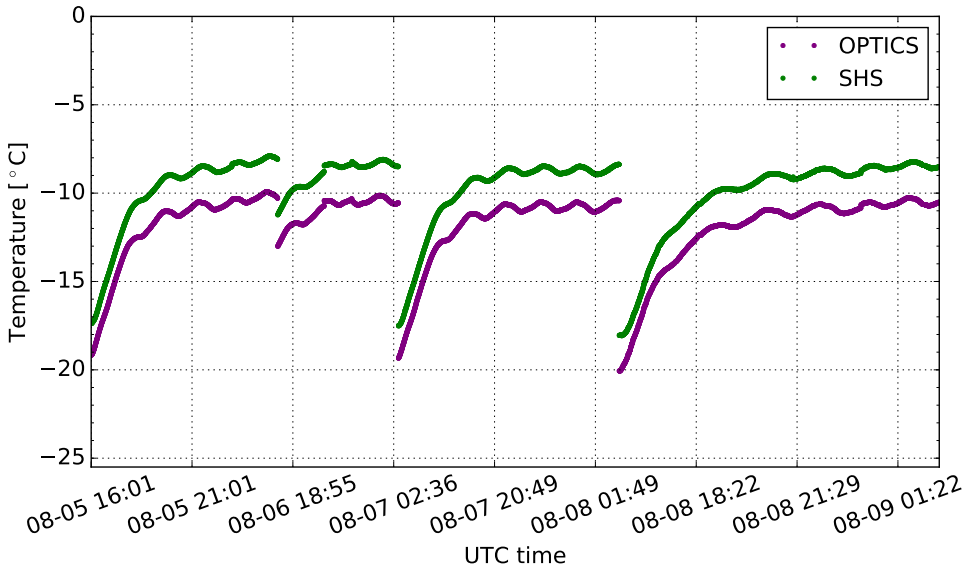

Figure 6.3: The AtmoSHINE operation environmental temperature variations at the optics and SHS as monitored by two thermal sensors during the regular measurement period.

as illustrated in Fig. 6.4. The raw image is directly from the detector readout, the level-0 products are corrected and converted spectra, the level-1 products are calibrated spectra, and the level-2 products are atmospheric temperature data. All data are stored in a SQLite-based database, and the processed intermediate data are preserved as HDF5 file, while the final products are in format of NetCDF file.

The purpose of level-0 and level-1 processing is to deliver the geolocated calibrated spectra, which are ready for the follow-on temperature retrieval processing. Detailed steps in the level-0 and level-1 processing, as well as the selection of valid data are described in the following subsections.

Level-0 processing

Level-0 processing deals with the instrument-related corrections, mainly consisting of two parts: interferogram correction in spatial domain and spectrum correction in spectral domain. In the first part, raw interferograms are processed. Firstly, detector artifacts like offset and dark current from experimental and in-space measurements, are subtracted from the interferograms. Then the bad pixels - due to hot pixel or cosmic ray - are replaced by the median values from nearest neighbour (with a local window-size of 5×5). It is followed by radiometric calibration to correct the non-uniformity of SHS

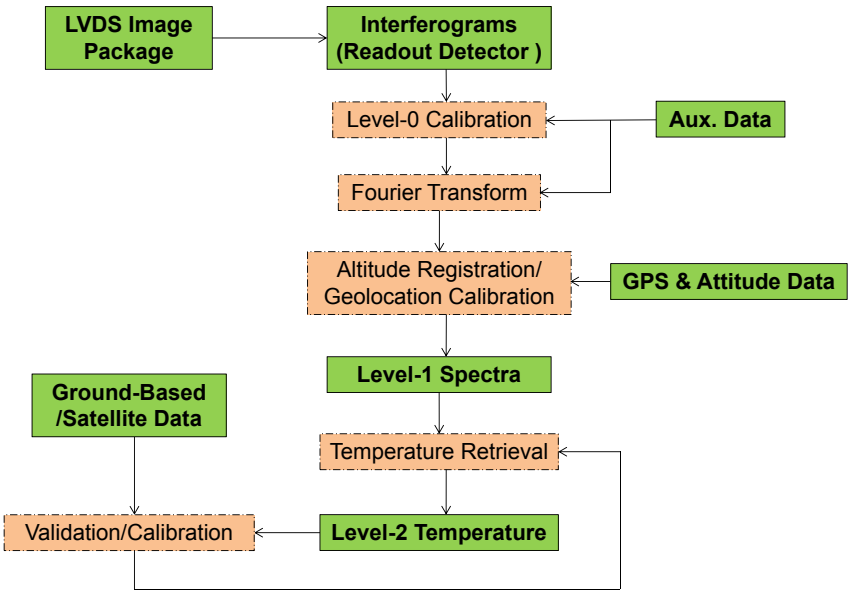

Figure 6.4: Schematic view of the AtmoSHINE data processing chain, from level-0 calibration and spectrum conversion, level-1 geolocation calibration, and level-2 temperature retrieval, followed by validation and comparison with other datasets. Green boxes represent data products and orange boxes indicate data processing steps.

sensitivity response. The calibration factors were obtained from the blackbody experiments. Afterwards, optical distortion correction (*Liu et al.*, 2019) and phase correction are applied. Lastly, the ghost emission lines mapped from other side of the Littrow wavelength are removed by applying a 2D fast Fourier transformation (FFT) on the tilted interferogram. The ghost line removal is essential to eliminate the influence of the unwanted lines, which are not fully filtered by the bandpass filter, and the uncertainty introduced by this removal is on the order of 0.2 %. The output is the level-0A data.

In the second part, the corrected interferogram is converted to a spectrum by Fourier transformation (FT). The Hamming apodization is applied in the FT to suppress the side lobes, as the Hamming window function proves to have small spectral leakage effect and quickly attenuates, while the spectral resolution could still be relatively well reserved. Zero padding by a factor of 10 is also added on the sampled signals during the conversion. Besides, the wavelength is assigned to the spectrum after considering the thermal drift effect of Littrow wavenumber. After that, the spectra are corrected with respect to the system visibility (spectral responsivity, system modulation efficiency variation) at different spatial frequencies, and the corresponding calibration matrix is identified and characterized from on-ground visibility experiments. Finally, the filter

response curve is calibrated for the spectra. The output is the level-0B data. An example of the level-0 processing is given in Fig. 6.5. A more detailed description about the applied algorithms in the level-0 data processing is provided by *Liu* (2019).

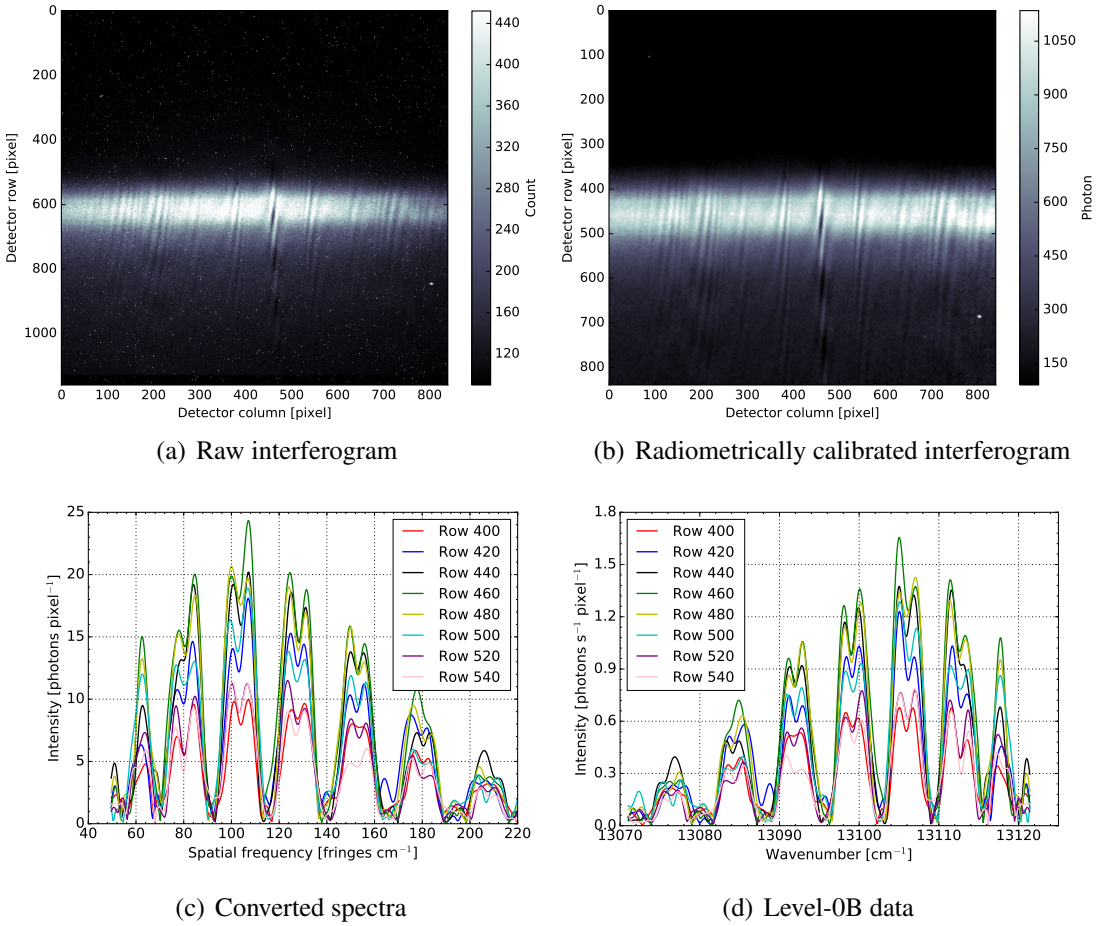

(a) Raw interferogram

(b) Radiometrically calibrated interferogram

(c) Converted spectra

(d) Level-0B data

Figure 6.5: Examples of the level-0 processing and some selected processing results from each step. The raw interferogram is taken with an integration time of 16 s. Dark current removal and bad pixel smoothing are performed before the radiometric calibration on the interferogram. The interferogram correction is followed by the Fourier transformation, which yields the converted spectra, and the level-0B data are obtained from spectrum correction on the spectra.

Level-1 processing

The accurate knowledge of the tangent points is essential for the derived vertical profiles from satellite limb measurements. The geolocation maps the satellite position and

attitude to the instrument LOS and corresponding tangent point positions for each limb measurement. For the AtmoSHINE measurements, the geometrical information is characterized in the level-1 processing. Several factors contribute to it, including the Earth's shape, satellite position, satellite attitude and instrument pointing direction. The instrument pointing direction is fixed relative to the satellite, and therefore, the AtmoSHINE viewing geometry is described in the satellite orbital coordinate system, which is defined as follows: the origin is the satellite mass center, the x-axis is towards the flight direction, the z-axis is towards the Earth geo-center, and the y-axis constitutes the right-hand system together with the other axes, as depicted in Fig. 6.6. The instrument viewing angles are addressed by the azimuth and zenith angles in this coordinate system. The satellite attitude is expressed by the Tait-Bryan angles (*Paul*, 2008), which are the Euler angles in the x-y-z orientation convention. The roll refers to the x-axis, the pitch corresponds to the y-axis and yaw is for the z-axis. The AtmoSHINE LOS is determined by the satellite position and attitude. The attitude variation in x-axis (roll) is of particular importance since it is directly associated with the instrument viewing zenith angle and consequently influences the tangent altitude fluctuations.

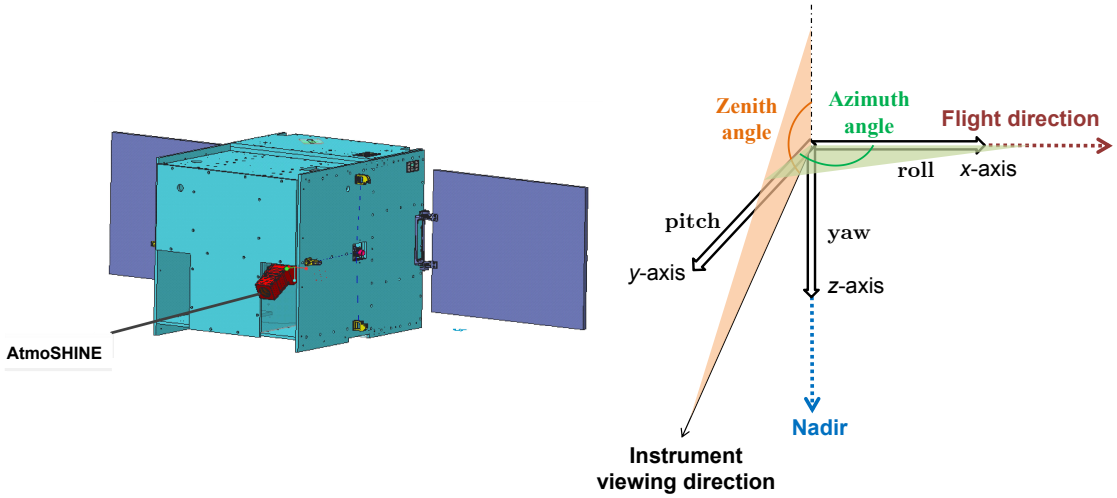

Figure 6.6: Illustration of the satellite coordinate system, which follows a right-handed coordinate system, along with the instrument viewing angles (azimuth and zenith), and the satellite attitude angles (roll, pitch and yaw).

Given the satellite position and attitude data, the instrument viewing direction in the satellite coordinate system can be transformed to a vector starting from the satellite location point in the Earth geocentric Cartesian coordinate system (earth-centered, earth-fixed, ECEF). The closest point to the Earth geo-center along the vector is considered as the tangent point of the instrument observations. The final results are converted to the World Geodetic System 1984 (WGS84) coordinate system. The satellite platform

provides every 10 s the GPS position and velocity, and every 1 s attitude data, which enable a continuous calculation of the instrument LOS and tangent points and an estimation of the variations during the integration time of a single measurement. The computation is implemented through the Atmospheric Radiative Transfer Simulator (ARTS) (*Buehler et al.*, 2005), and is verified by an independent calculation (G. Tang, personal communication, 2019), with a difference of less than 0.1 % between the two calculated results of tangent point locations and altitudes.

Generally, a 0.01° fluctuation in roll angle corresponds to roughly 0.6 km variation in tangent point altitudes. During most of the observation time, the attitude control system of the satellite platform is stable and the attitude determination is accurate, sufficiently satisfying the requirement for data acquisition. As shown in Fig. 6.7, the average values of the roll axis and its variations within the integration time are roughly 0.005° to 0.02°, which corresponds to a tangent altitude variation within 1-2 km. Measurements with a roll variation larger than 0.03° are excluded for further data processing.

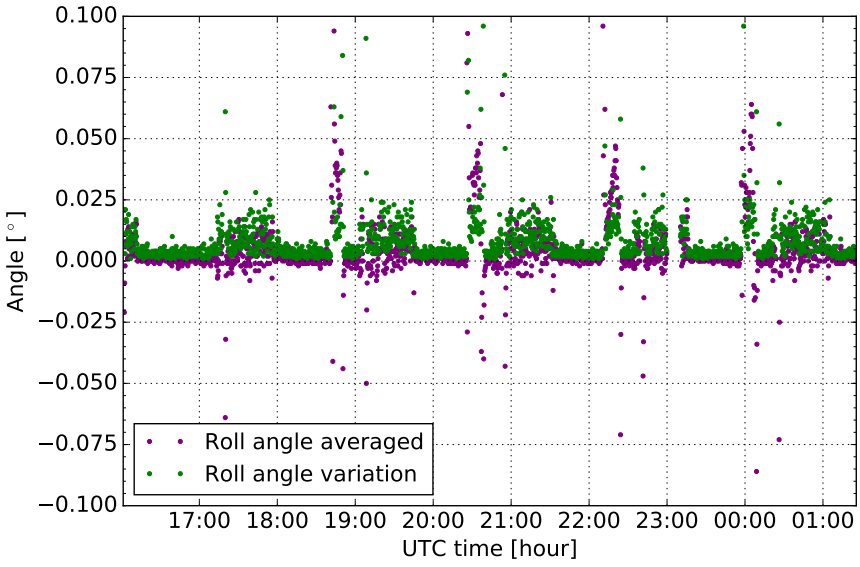

Figure 6.7: The satellite attitude information for the roll axis on the 5th of August during the regular observation period. The roll angle (purple) is averaged over the integration time for each measurement and the roll variation (green) indicates the fluctuations of roll angle within the integration time of each measurement.

The solar illumination condition of the measurements is also addressed here in the level-1 processing. When the instrument LOS, or part of it is illuminated by the Sun, some solar light outside of the nominal FOV, will be reflected or limb-scattered into the instrument's optical system, and lead to the appearance of external straylight in the airglow emission observations (*Chen*, 2019a). The existence of significant straylight

will make the retrieval difficult and influence the accuracy of derived results. In the data processing, this influence can be eliminated by the usage of dark limb measurements, and the fundamental selection criteria are based on the SZAs of the satellite and tangent points, which should be larger than 108°.

Data selection

Generally, the selection of scientifically valid data from the available measurements follows the following criteria: the frame status is flagged as normal (image is recorded correctly with a pre-configured size), the emission layer appears in the effective image area (the central 840 rows), no large attitude variation in roll axis ($\leq$0.03°), the SZAs of the satellite and tangent points is larger than 108°, and no double emission layers appear (no internal stray light). After the screening, about 2400 scientifically valid images are kept for the follow-on processing.

6.2 Characterization of processed spectra

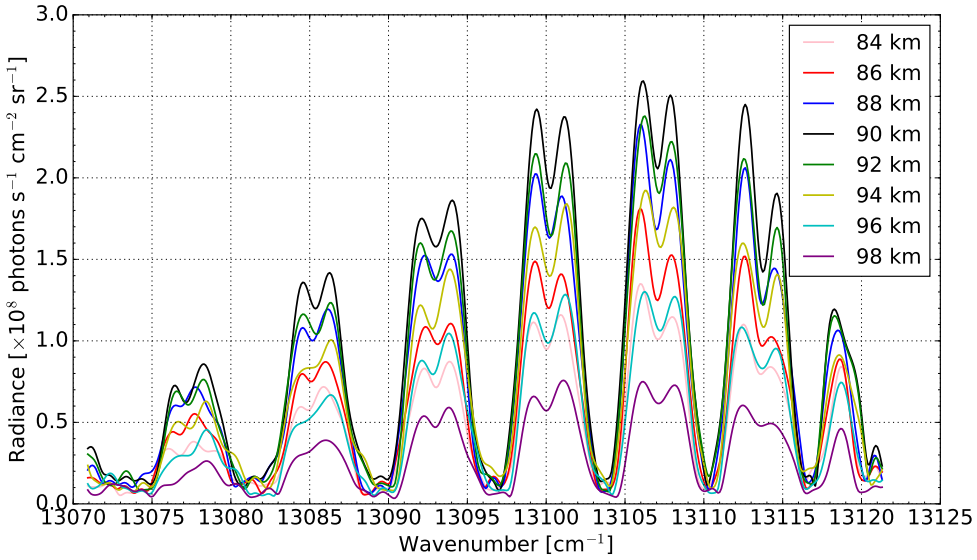

Figure 6.8: AtmoSHINE spectra of the measured O_2 A-band emissions at tangent location of 13.7° N, 62.0° W for tangent altitudes as given in the figure legend and at a UTC time 2019-08-08 00:10:22 with 16 s integration time.

Figure 6.8 gives an example of the processed spectra from AtmoSHINE limb measurements. The measurements are binned in the spectral domain into 2 km vertical grid.

The altitude range spans from 84 to 98 km, where nearly the entire O_2 A-band nightglow emission layer is covered. The spectra cover a wavenumber range of 13071-13121 cm^{-1} (765.1-762.1 nm) with a spectral resolution of around 1.8 cm^{-1} (0.1 nm). The rotational structure of the O_2 A-band airglow is clearly resolved in the spectral range, and apparently individual emission lines can be identified. Vertically, the emission peak occurs at around 90 km, consistent with the forward model calculation as plotted in Fig. 2.12. Besides, the absolute magnitude of measured limb radiances generally fits with forward simulations. An intercomparison of the integrated limb radiance with the coincident OSIRIS observations, however, indicates a difference by a factor of more than 3 in the absolute radiances (see Sect. 6.4.1).

6.2.1 Geographical distribution

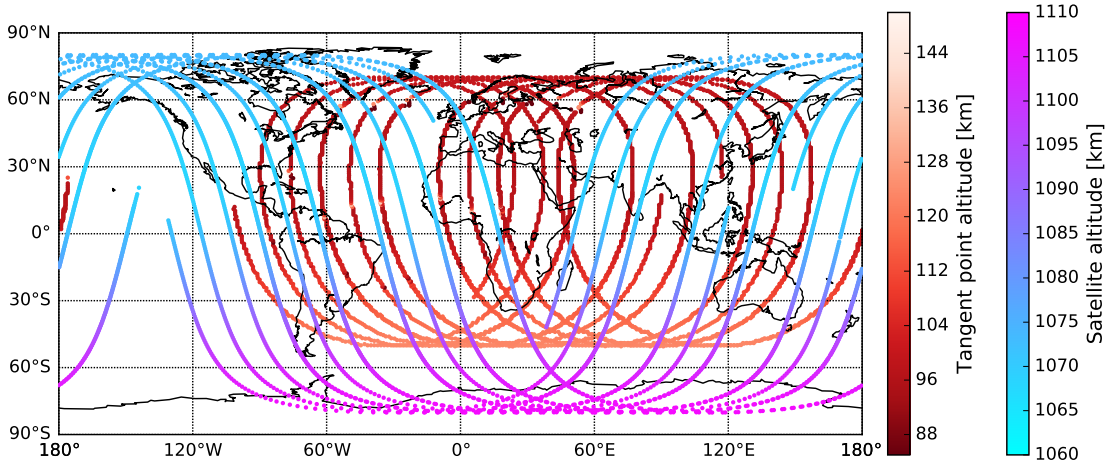

Figure 6.9: The geographical distribution of tangent points (white-red) during the AtmoSHINE regular observation period. The satellite positions (pink-cyan) are also given. The locations are in the WGS84 coordinate.

The tangent point distribution of the nightglow measurements during the regular observation period is illustrated in Fig. 6.9 along with the satellite locations. The AtmoSHINE measurements have a global coverage from the northern polar region (70° N) to the southern middle latitude (50° S). The emission layer is generally within the FOV of the instrument, except for the southern mid-latitudinal regions due to the Earth's oblate spheroidal shape and the unrefined satellite attitude control. During the fourth in-orbit test and the regular observation period, which are close to the summer solstice, the measurements at higher latitudes of the Northern Hemisphere are under solar illumination (SZA < 108°).

6.2.2 SNR analysis

Due to the nature of an interferometer, which generates interference fringes in spatial domain, the measurement noise is estimated on the interferogram and converted to the spectral domain following *Liu* (2019). The total noise is calculated by mainly considering four noise sources, as in Eq. 6.1:

$$\sigma = \sqrt{\sigma_{SN}^2 + \sigma_{DC}^2 + \sigma_{RO}^2 + \sigma_{SL}^2} \tag{6.1}$$

σ_{SN} refers to the shot noise, normally considered as the square root value of incoming photon noises. It is found to be the dominant source of noise in this analysis. σ_{DC} represents the noise caused by detector dark current. The dark current profiles are subtracted from the unilluminated region near the detector boundary of the images. σ_{RO} is the detector readout noise, and is negligible for long integration time here. σ_{SL} refers to the error associated with the straylight, and is not considered in this analysis since only the dark limb measurements without straylight are selected for data processing.

For a typical profile of 16 s integration time, as shown in Fig. 6.5(b), the emission signal in the central peak region is around 1000 photons pixel^{-1}, after the detector fixed pattern and dark current offset are subtracted from the raw interferogram, and the corresponding shot noise is around $\sqrt{1000} \approx 31.6$ photons pixel^{-1}. The noise transmission factor from spatial to spectral domain depends on the sampling number in columns in the FT, and is about $1/\sqrt{\frac{560}{2}} \approx 0.06$ when 560 sampling pixels are applied. The equivalent noise in the spectral domain is around 1.9 photons pixel^{-1}. Including the effect of Hamming apodization, which increases the noise by 1.36 (*Liu*, 2019), the total noise is about 2.6 photons pixel^{-1}. For the calibrated spectra, the averaged intensity for each emission line is around 33 photons pixel^{-1}, and the corresponding SNR is around $\frac{33}{2.6} \approx 12.7$ in the spectral domain. After averaging into 2 km altitude layers, the corresponding noise level is around 2 % in the peak altitude region.

The SNRs strongly depend on the integration time. As the shot noise dominates the system, the SNR increases by a factor of $\sqrt{2}$ when the integration time is doubled or binning by a factor of 2 is adopted. Longer integration time increases the SNR but reduces the spatial resolution for the horizontal direction, and also requires a higher satellite attitude control stability. Therefore, integration time from 8 s to 16 s is mostly suitable.

6.2.3 In-orbit visibility calibration

As already briefly discussed in Sect. 6.1.3, the system visibility represents the instrument modulation efficiency (ME), and is related to the modulation transfer function (MTF) of the detector optics and defects in the optical system (*Liu*, 2019). The instrument visibility function highly relies on the environment temperature, which means that the drop of instrument visibility along the spatial frequency varies under different temperature. A difference of more than 5 % in the visibility variations is noted for a temperature change of 50 K at a lower wavenumber (*Chen*, 2019b).

In the level-0 data processing, the instrument visibility is characterized and corrected. However, the applied calibration matrix was obtained on ground at room temperature, while the actual in-orbit operation temperature for optics and SHS is around -10°C, as illustrated in Fig. 6.3. Due to the temperature dependence of system visibility, the large difference between the on-ground and in-orbit temperatures leads to a deviated visibility function, and an unknown uncertainty is introduced in the visibility calibration of the level-0 processing. This temperature-dependent error in the processed spectra can be cross-corrected by performing an in-flight visibility calibration, in reference to the coincident SABER temperature data, as illustrated in Fig. 6.10. The coincident SABER temperature profiles are applied in the O_2 A-band forward model calculation as described in Sect. 2.2, and evaluated with respect to the corresponding original AtmoSHINE spectra to obtain additional calibration factors for instrument spectral responsivity, which are then used for the in-orbit visibility correction.

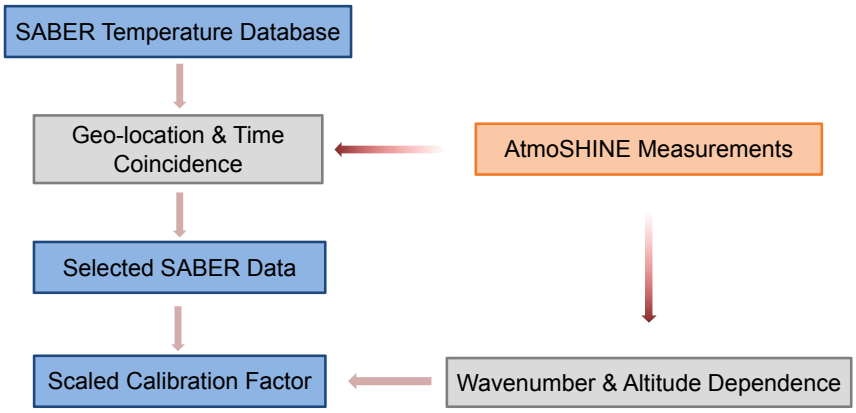

Figure 6.10: Schematic view of the AtmoSHINE in-flight calibration with respect to the coincident SABER data.

For a single AtmoSHINE profile, the coincident SABER data are acquired and averaged with a criteria of ± 5° latitude, ± 15° longitude, ± 1 hour in UTC time with respect to the tangent point location. In total, around 400 coincidences are found between the

AtmoSHINE and SABER measurements during the fourth in-orbit test and regular observation period (Fig. 6.11). For one collocated pair, normally 2 to 5 SABER profiles are selected for one AtmoSHINE profile. The coincidences mainly appear in the tropical and midlatitudinal regions, and the distribution of collocated pairs in latitude from 30° N to 50° S are generally balanced. The calibration factors for spectral responsivity are wavenumber- and altitude-dependent, and they are derived using a non-linear least squares fitting method (Levenberg-Marquardt algorithm) along with a wavenumber shift and a vertical shift of emission peak for each collocated pair. The wavenumber dependence of the calibration factors is found latitude-related. The changes of calibration factors are generally by 10-20 % larger at middle latitudes than near the Equator. Currently, the averaged values over 400 profiles of the calibration factors are applied on the AtmoSHINE spectral measurements. More details about the in-orbit visibility calibration is provided by *Chen* (2019b).

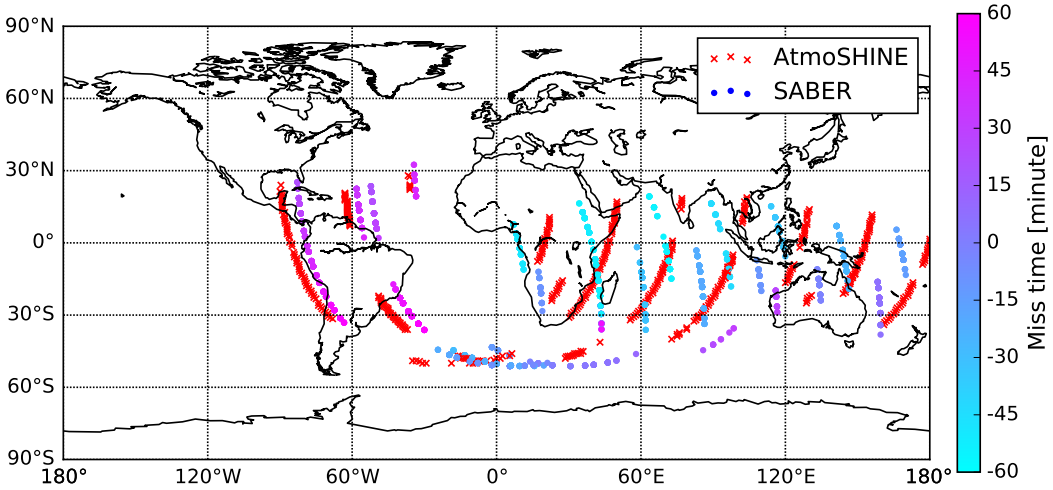

Figure 6.11: The map of coincidence between the AtmoSHINE measurements (red cross) and SABER observations (pink-cyan dot). The colorbar represents the miss time (difference in UTC time) between the SABER and AtmoSHINE measurements for each collocated pair, of which a positive value indicates the SABER observation time is later than the AtmoSHINE measurements.

6.3 Result evaluation

6.3.1 Retrieval setup

For the temperature retrieval, the O_2 A-band nightglow modeling as discussed in Sect. 2.2 is applied, and the used model parameters are summarized in Appx. A.4. The atmospheric quantities of total density, temperature, O_2, N_2, O and O_3 mixing ratios from the HAMMONIA model (*Schmidt et al.*, 2006) are taken as the model atmospheric background input. The inversion regime follows the methodology as described in Sect. 2.4, and the regularized Levenberg-Marquardt algorithm as described in Chap. 3 is adopted for an iterative retrieval. The a priori data are also obtained from the HAMMONIA model, with monthly mean values of the same latitude and longitude conditions, and the zeroth- and first-order regularization matrices are constructed in a vertical retrieval grid of 2 km as the measurements. The regularization strength is adjusted accordingly to ensure that the derived results are physically meaningful. Besides of the vertically resolved temperature profiles, the retrieval target also includes the altitude dependent scaling factors (on the volume emission rate), the spectral resolution and a wavenumber shift. For the retrieval, the atmosphere is assumed to be in optically thin condition above 84 km, as already discussed in Sect. 2.2.4.

6.3.2 Derived temperature

Illustrated in Fig. 6.12 are several typical profiles of the derived vertical temperature distributions, by applying the global fitting method on the calibrated AtmoSHINE measurements. The temperature decreases with increasing height, and reaches the minimal values of around 140 to 160 K above the altitude of 90 km. The overall shape of the temperature profile results from the balance of heating and cooling in this region, and is influenced by many factors, e.g. global circulation and waves. The absolute magnitude of temperature values are also within the typical temperature range in the MLT region. Other retrieval target parameters are simultaneously obtained, the spectral resolution (FWHM) of which is approximately 1.8 cm^{-1}, while the wavenumber shift is negligible ($\leqslant$0.02 cm^{-1}). As shown in Fig. 6.13, the fitting results and the measurements are generally in good agreement.

6.3.3 Error analysis

The total uncertainty of the derived temperatures can be accounted for by the measurement error, the effect of regularization and the forward model uncertainties. Mean-

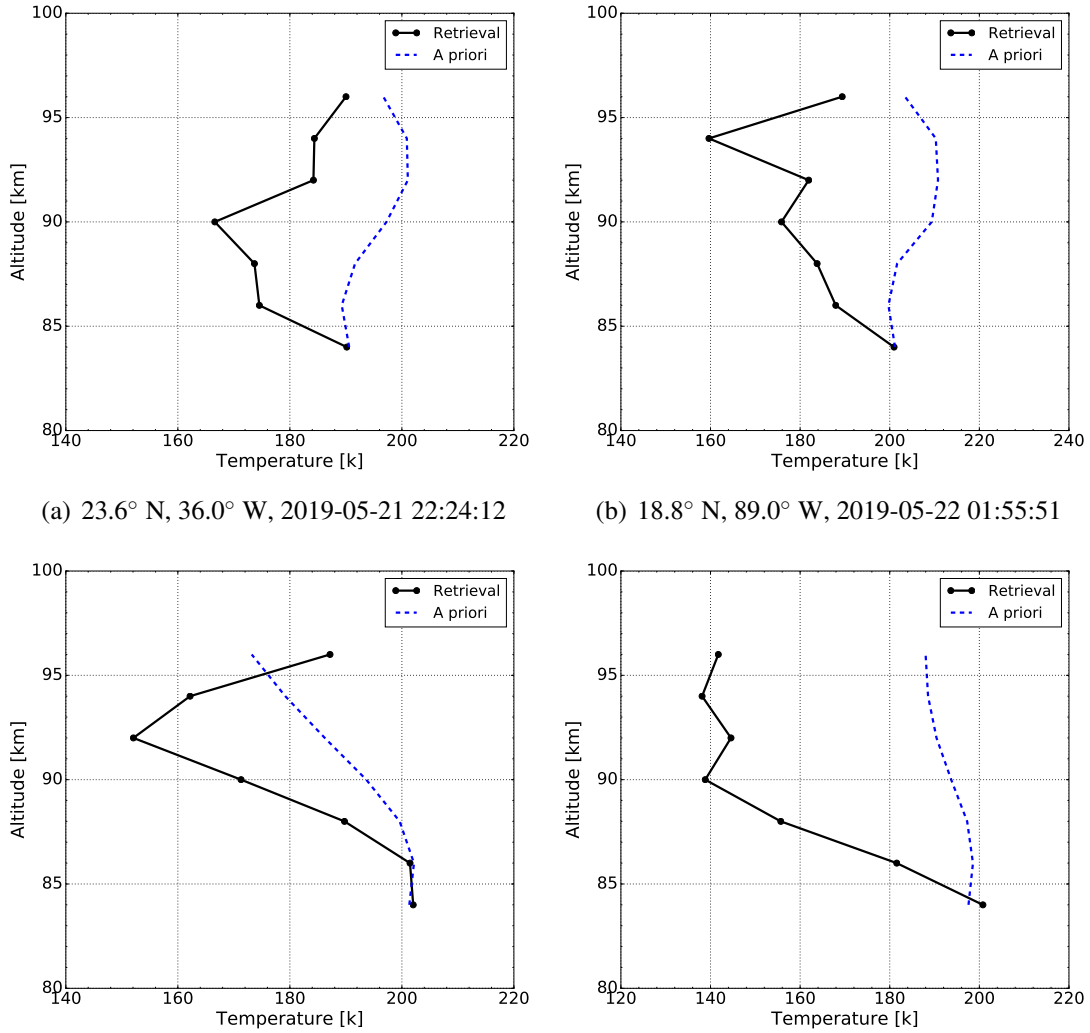

(a) 23.6° N, 36.0° W, 2019-05-21 22:24:12

(b) 18.8° N, 89.0° W, 2019-05-22 01:55:51

(c) 12.1° S, 69.0° E, 2019-08-05 23:20:52

(d) 16.2° S, 147.0° E, 2019-08-07 18:02:34

Figure 6.12: Examples of Atmospheric temperature profiles (solid), derived from the corrected AtmoSHINE O_2 A-band measurements. The a priori temperature data are also given (dashed) for comparison. The corresponding timestamps in UTC and tangent point geolocations of the measurements are also given in the figure caption.

while, the applied in-orbit visibility calibration factors for spectral responsivity (see Sect. 6.2.3) introduce additional uncertainties in the retrieval results, but at the same time compensate some effects, such as uncertainties in Einstein coefficients and measurement noises. Nevertheless, the uncertainty of derived temperature profiles can be quantified from the following aspects.

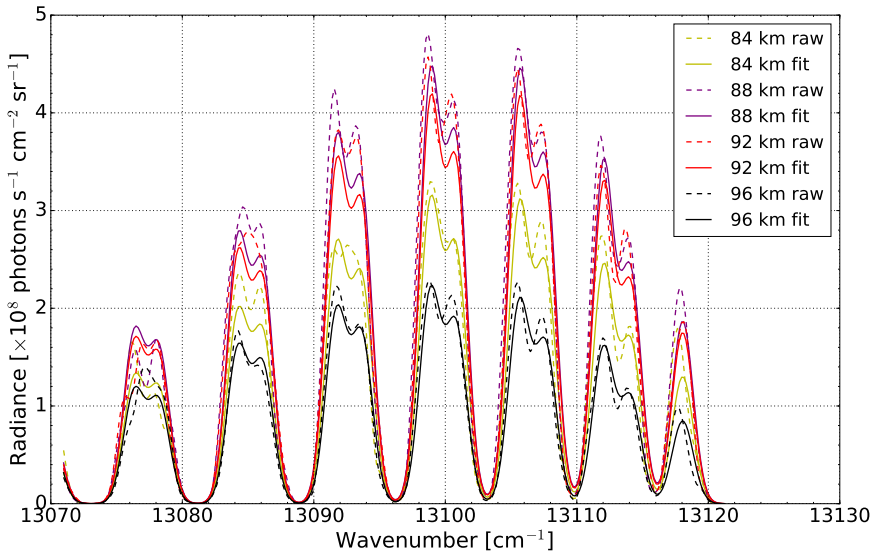

Figure 6.13: Simulated spectra (fit, solid line) and measurements (raw, dashed line) of the AtmoSHINE O_2 A-band emissions at tangent point location of 16.2° S, 147.0° E for tangent altitudes as given in the figure legend and at a UTC time 2019-08-07 18:02:34.

The measurement error, which considers the spectra noise after binning (averaging into 2 km vertical grid), introduces an uncertainty on the order of 1 % to 2 % in the retrieval results for an integration time of 16 s at altitudes of 98 to 88 km, which corresponds to a temperature uncertainty of around 2 to 4 K. In the altitude region of 98 to 88 km, the impact of regularization on the uncertainty is generally within 1 K. The retrieval results are diagnosed, in doing so the obtained averaging kernels are calculated as illustrated in Fig. 6.14. The summed averaging kernels in the altitude region of 96-88 km are nearly one, which indicates that the temperature profiles are fully retrieved from the measurement information of the adjacent tangent altitude layers, and the contributions from the a priori data are negligible. Below 88 km, however, the averaging kernel decreases and is close to zero at 84 km, which indicates that there is not much information from measurements at this altitude, and the a priori information dominates the retrieval results. A temperature uncertainty of around 3 to 5 K from the measurement noise is found in the measurements with 8 s integration time, which is generally lower compared to the uncertainty of 16 s measurements due to the reduced SNR by $\sqrt{2}$.

The retrieval process is configured in such a way that it is independent from the variations of O_2 A-band volume emission rate, i.e., from the atmospheric background input and reaction rate coefficients. Hence, only the Einstein coefficients are substantial to the uncertainty of the derived temperatures in terms of the forward model parameters and atmospheric background profiles. The HITRAN 2016 Einstein coefficients are ap-

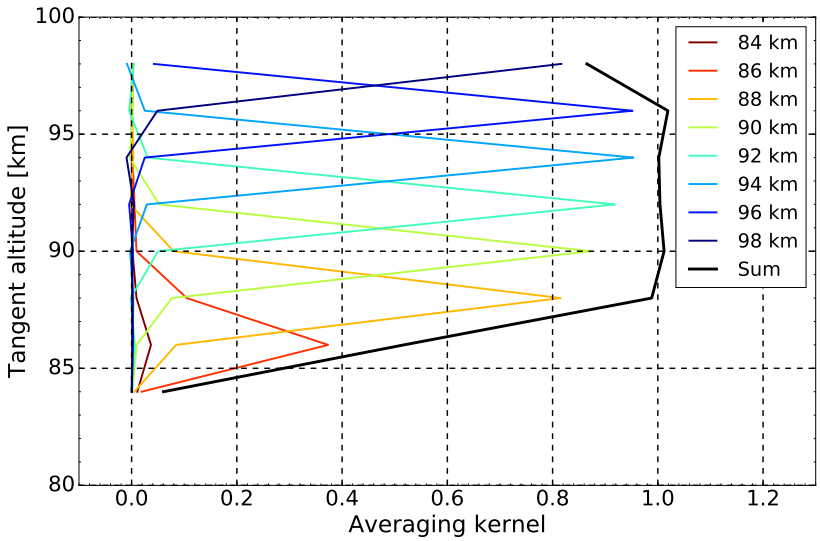

Figure 6.14: The averaging kernels of the temperature retrieval at tangent location of 16.2° S, 147.0° E and at a UTC time 2019-08-07 18:02:34.

plied in this work, which are found to have a difference of around 10 % at maximum in comparison to other Einstein coefficient sets (*Zhu and Kaufmann*, 2019). Therefore in this work, an perturbation of 10 % is imposed on the Einstein values, which introduces an uncertainty of less than 1 K in the temperature results for all altitudes.

6.4 Comparison of the results

6.4.1 Comparison of limb radiance with OSIRIS

The OSIRIS instrument on the Odin satellite, which follows a dawn/dusk Sun-synchronous orbit similar to the Hongyun satellite, observes the global airglow radiances and covers the wavelength region of the O_2 A-band emissions (759-767 nm) for an altitude region of around 85 to 105 km (*Sheese et al.*, 2010, 2012). It measures since 2001 till now. It is straightforward to compare the AtmoSHINE limb radiances with the OSIRIS measurements. Because only several orbits of OSIRIS data are available during the AtmoSHINE observation period, highly relaxed criteria are applied for the selection of the coincident measurements as: $\pm 15^\circ$ latitude, $\pm$ 1 hour local time within $\pm$ 1 month. Additionally, OSIRIS observes for both daytime and nighttime conditions, and only the OSIRIS dark limb measurements with SZA>98° are chosen for comparison.

Due to strictly limited data availability for both datasets, only a few collocated pairs

are acquired, and a systematic comparison is not feasible. Shown in Fig. 6.15 is one example of the limb radiance comparison between AtmoSHINE and OSIRIS, and thereof the AtmoSHINE measurements are obtained from the level-0 & 1 processing, without the in-orbit visibility calibration. Only considering the limited cases which are currently available, the two datasets are discovered in a general consistency with respect to the magnitude of integrated limb radiances, the peak emission altitude, and also the vertical distribution profile, despite of the large differences in time and distance. However, a discrepancy by a factor of more than 3 is noted in absolute radiances between the two datasets, which can be explained due to the mostly missing radiometric calibration of the AtmoSHINE instrument.

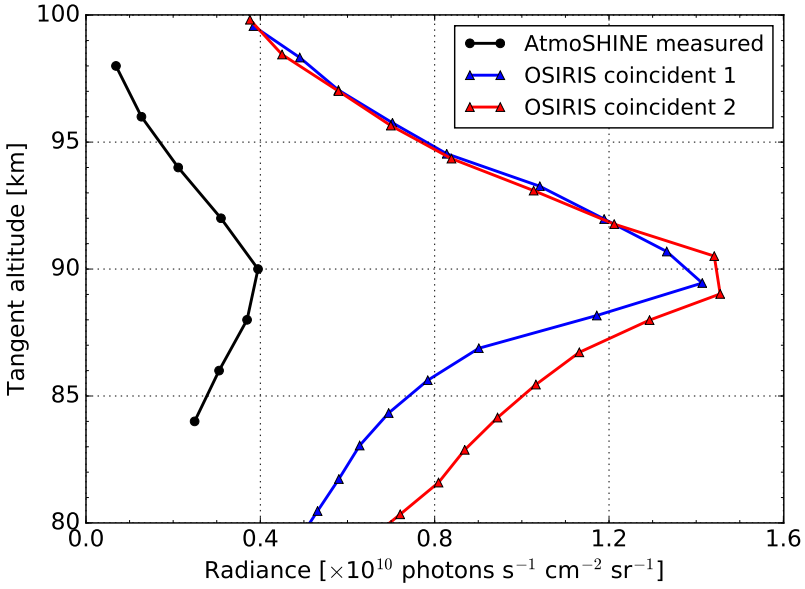

Figure 6.15: Comparison of the integrated limb spectra between the corrected AtmoSHINE (black) and the coincident OSIRIS (red, blue) measurements. The AtmoSHINE profile is taken from a tangent location of 48.0° S, 54.4° E at a UTC time 2019-05-21 21:47:31, and is obtained from the level-0 & 1 processing, without the in-orbit visibility calibration. The OSIRIS measurements have (coincident profile 1) a tangent location of 55.9° S, 114.8° E at a UTC time 2019-04-20 22:18:48 and a solar zenith angle of 100°; (coincident profile 2) a tangent location of 62.8° S, 110.6° E at a UTC time 2019-04-20 22:20:46 and a solar zenith angle of 101°.

6.4.2 Comparison of temperature with SABER measurements

Due to the lack in the AtmoSHINE observation time, a systematic comparison (e.g., by season or month) between the derived AtmoSHINE temperature profiles and coincident SABER temperature measurements cannot be fulfilled. Instead, a profile-to-profile intercomparison between the SABER and AtmoSHINE measurements is implemented. The same coincidence criteria as in Sect. 6.2.3 are applied on the two datasets. It is noteworthy that this cross-comparison is affected by the applied in-orbit SABER visibility calibration, which introduces a systematic correction to the temperature results towards SABER data. Nevertheless, at the level of single individual profile, this comparison can be considered relatively independent from this in-orbit calibration, as the calibration factor is extracted from over 400 AtmoSHINE profiles, and is considered as a global correction.

Two examples of the AtmoSHINE measurements in comparison to both the averaged and individual SABER profiles are shown in Fig. 6.16, along with a priori temperatures, which are monthly mean values with the same latitude and longitude condition, taken from the HAMMONIA model. AtmoSHINE data are mostly within the variability of the SABER profiles. As compared to a priori temperature data, the overall vertical shape of AtmoSHINE and SABER temperature profiles is closer and similar, although SABER profiles are much more variable, resulting in temperature differences of up to 30 K at some altitudes. This large temperature variation is also noted among the individual SABER profiles, which differ from each other by several to tens of Kelvin. The actual miss time between the AtmoSHINE and SABER profiles is about one hour with several hundred kilometers difference in the distance, and both tides and waves could induce large temperature variations in the local mesospheric temperature, as observed in this case.

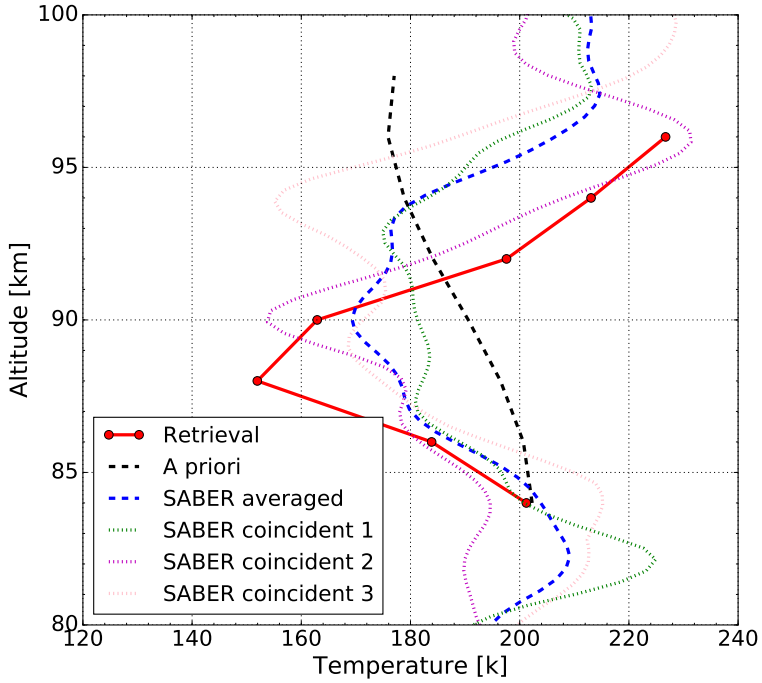

(a) 2019-08-05 21:32:51, 8.3° S, 97.3° E

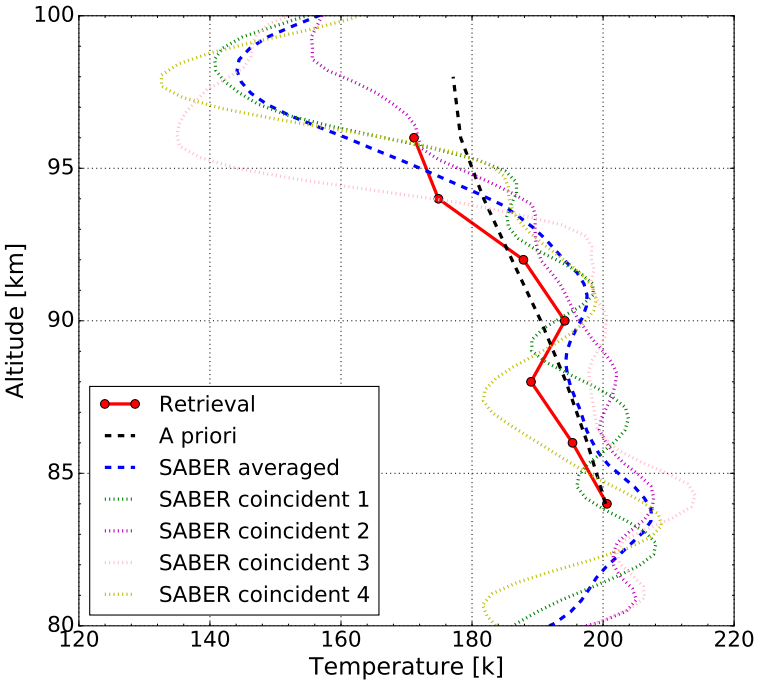

(b) 2019-08-08 01:00:45, 8.2° N, 49.0° E

Figure 6.16: Comparison of the derived AtmoSHINE temperature profiles (red solid line) with the coincident averaged (blue dashed line) and individual (dotted line) SABER temperature measurements at the given UTC time and tangent location. The a priori temperature data (black dashed line) are taken from the HAMMONIA model.

Chapter 7

Summary and outlook

This work deals with atmospheric remotely sensed data of the OH and O_2 A-band nighttime airglow emissions and presents the retrieval and analysis of atomic oxygen and hydrogen abundances and also temperature profiles in the MLT region. The OH and O_2 A-band emission limb observations are simulated by forward modeling. For inverse modeling a constrained global fit approach with New-Gaussian and Levenberg-Marquardt iterative methods is employed.

GOMOS limb observations of the atmosphere provide the opportunity to retrieve atomic oxygen and hydrogen abundances from OH(8-4) band emissions at the mesopause. A global nighttime dataset of monthly zonal mean [O] and [H] is obtained from GOMOS limb measurements, with the atmospheric background profiles of temperature, total density and ozone taken from the SABER measurements. The atomic oxygen density peaks at about 95 km and the highest values are in the range of 3-8$\times 10^{11}$ atoms cm^{-3}, while the atomic hydrogen density reaches the peak at around 83 km with a value of 1-4$\times 10^{8}$ atoms cm^{-3}, depending on latitude and season. Its uncertainty comes from the measurement noise (around 3-10 %), relaxation schemes and kinetic parameters in OH modeling (contributing around 20 % in total) and background atmosphere inputs, atmospheric temperature and ozone (around 5 % to 20 %). The obtained profiles present an overall picture of the vertical distribution of atomic oxygen and hydrogen from 80 km to 100 km. Temporal analyses of the profiles show 11-year solar cycle effect tendencies as well as semiannual and annual variations, of which SAO is the most prominent.

The GOMOS data agree with the SCIAMACHY OH(8-4) measurements, with deviations typically smaller than 20 %. For atomic oxygen, the GOMOS abundances are, on average, about 10-20 % lower than atomic oxygen data obtained from SCIAMACHY OH(9-6) observations. Compared to other atomic oxygen datasets derived from various instrument measurements, such as SABER, WINDII, OSIRIS and in situ rocket experiments, the GOMOS [O] data agree with these datasets within their combined un-

certainties. For atomic hydrogen, the comparison with SABER [H] dataset shows the GOMOS data are generally by 10-20 % larger at around 85 km, and up to 50 % lower than the SABER measurements above 90 km and below 82 km.

The ground-based GRIPS-F measurements of OH(3-1) band nightglow facilitates the retrieval of the nocturnal temperature for the mesopause region locally near the region of Wuppertal. The derived temperature fluctuates over the course of night, while its absolute amplitude varies with season. Temperature is much higher during winter than during summer. The temperature uncertainty mainly comes from the measurement noise, which is on the order of 2 to 7 K, while the influence of the forward model uncertainty on the derived result is around 1 K. The application of different instrument line shape functions in the retrieval leads to a deviation which is generally within 0.5 K. With respect to the commonly used three peak temperature retrieval method, the applied global fit method results in less temporal fluctuation. However, both methods agree with each other in terms of large-scale variations.

The first data from the Earth limb-viewing AtmoSHINE instrument deliver global observations of the nighttime O_2 A-band emissions. The obtained AtmoSHINE limb radiance values agree with OSIRIS observations concerning the vertical structure including the altitude of the peak emission. However, the absolute radiance values show a discrepancy. Owing to the difference in environmental temperature between the on-ground calibration and in-orbit operation, an in-orbit calibration factor was derived in data processing to correct for these discrepancies. This correction factor is obtained from multiple collocated pairs of the AtmoSHINE and SABER measurements. Finally, altitude resolved temperature profiles are derived from the corrected AtmoSHINE spectra. They are compared and evaluated with respect to the coincident SABER measurements, which indicates a general consistency concerning the vertical temperature distribution.

With the new SHI technology successfully tested by the AtmoSHINE instrument, future missions can deliver temperature data obtained from nano-satellites at significantly lower cost than before. With this technology, multi-satellite constellations can provide data with unprecedented spatial resolution for the study of gravity waves. These measurements represent a good proxy for the characterization of waves and tides in the MLT region, which is needed to improve climate modeling in decadal time scales. For the measurement itself, it is important to extend the current radiative transfer model to daytime conditions. The improved day- and night-time observations will provide a continuously and consistently global view, and advance our current understanding of the middle atmosphere.

Appendix A

A.1 Chemical reaction parameters in OH airglow modeling

Table A.1: Chemical reaction parameters in OH airglow modeling used in this work. k_{OO_2M}, k_{HO_3} and k_{OO_3} represent the corresponding rate coefficient, and f_v refers to the OH^* nascent production branching ratio for the corresponding vibrational level v.

Parameter	Rate constant	Reference
k_{OO_2M}	$6.0 \times 10^{-34}(300/T)^{2.4} cm^6 s^{-1}$	*Sander et al.* (2011)
k_{HO_3}	$1.4 \times 10^{-10} exp(-470/T) cm^3 s^{-1}$	*Sander et al.* (2011)
k_{OO_3}	$8.0 \times 10^{-12} exp(-2060/T) cm^3 s^{-1}$	*Sander et al.* (2011)
f_v	0.47, 0.34, 0.15, 0.03, 0.01, 0, 0, 0, 0, 0 (v=9, 8, ..., 0)	*Adler-Golden* (1997)

A.2 Collisional rate coefficients in OH airglow modeling

Table A.2: Collisional reaction parameters for the corresponding vibrational level v in OH airglow modeling used in this work. k_{OHN_2}, k_{OHO_2}, and k_{OHO} represent the quenching coefficients of OH^* radicals by N_2, O_2, and O.

Vibrational level v	[a]k_{OHN_2}∗ (OH(v)+N_2)	[a]k_{OHO_2}⋆ (OH(v)+O_2)	k_{OHO}† (OH(v)+O)
9	7.0±2.0	22.0±6.0	2.3±1
8	7.0±4.0	8.0±1.0	0.65
7	1.6	7.0±2.0	2.0
6	0.91	3.1	2.0
5	0.52	1.8	2.0
4	0.3	0.94	2.0
3	0.17	0.56	2.0
2	0.1	0.29	2.0
1	0.058	0.14	2.0

[a] A low temperature scale factor, as the mesopause temperature is normally much lower than the laboratory conditions,which is 1.4 for N_2 and 1.18 for O_2 (*Lacoursiére et al.*, 2003).

∗ Unit: $\times 10^{-13} cm^3 s^{-1}$; References: *Makhlouf et al.* (1995); *Dyer et al.* (1997); *Adler-Golden* (1997); *Kalogerakis et al.* (2011)

⋆ Unit: $\times 10^{-12} cm^3 s^{-1}$; References: *Knutsen et al.* (1996); *Dyer et al.* (1997); *Adler-Golden* (1997); *Kalogerakis et al.* (2011); *Xu et al.* (2012); $k_{OHO_2(v,v')} = C \times [P_v]^{v-v'}$, with $C = 4.4 \times 10^{-13} cm^3 s^{-1}$ (*Adler-Golden*, 1997) and P_v = 0.95, 0.75, 0.72, 0.5, 0.36, 0.23, 0.15, 0.083, 0.043 (v=9, 8, ..., 1), modified as $C = 0.723 \times 4.4 \times 10^{-13} cm^3 s^{-1}$ by *Xu et al.* (2012)

† Unit: $\times 10^{-10} cm^3 s^{-1}$; References: *Adler-Golden* (1997); *Kalogerakis et al.* (2016)

A.3 Fitting of collisional rate coefficients in OH airglow modeling for v=8

A.3.1 Selection of the collisional rate coefficients for OH(v=8)

The determination of the coefficient $k_{OHO(8)}$ for OH(8)+O is discussed here. Some of the reported values for the total removal rate of OH(v=8) by O from the literature are listed below in Tab. A.3. These values vary from 4.5×10^{-11} cm^3 s^{-1} to 2.5×10^{-10} cm^3 s^{-1} by nearly one order of magnitude, and currently there are no values being well validated. Therefore, it is decided in this work to adjust the rate of this process to bring SCIAMACHY OH(9-6) and OH(8-5) measurements into a consistent picture.

Table A.3: Some reported values for the reaction rate constant $k_{OHO(8)}$ from literature.

$k_{OHO(8)}$ $\times10^{-10}$ cm^3 s^{-1}	Reference	Source	Note
2.5	*Makhlouf et al.* (1995)	Empirical estimation	Relevant parameters are adjusted
2.0	*Adler-Golden* (1997)	Empirical estimation	Relevant parameters are adjusted
0.45	*Varandas* (2004)	Theoretical calculation	/
1.0	*Copeland et al.* (2006)	Laboratory measurement	/
0.5	*Smith et al.* (2010) *Mlynczak et al.* (2013c)	Adjustment to SABER measurement	Relevant parameters are adjusted
0.65	*Xu et al.* (2012)	Fitting to SABER measurement	Relevant parameters are adjusted
0.87 $\times(2.3\pm1)$	*Panka et al.* (2017, 2018) *Kalogerakis* (2019)	Adjustment to laboratory measurement	/
1.5	*Mlynczak et al.* (2018)	Adjustment to SABER measurement	Relevant parameters are adjusted

The values of the rate coefficient $k_{OHO_2(8)}$ for OH(8)+O_2 are available from the theoretical calculation or laboratory measurements (Tab. A.4). *Adler-Golden* (1997) summarized in Table 2 the derived values for every vibrational level, and also provided the laboratory measurements in Table 1, as measured by *Dyer et al.* (1997). These two values of $k_{O_2(8)}$ do not fit with each other. *Xu et al.* (2012, Tab. 3 & Fig. 7) applied a fitting parameter of 0.723 on the derived values of by *Adler-Golden* (1997), and brought them into an agreement with the laboratory measurements. This laboratory value is also applied by *Mlynczak et al.* (2013c). Therefore, we took this value from the laboratory

measurements in our model.

Table A.4: Some reported values for the collisional rate constant $k_{OHO_2(8)}$ from literature.

$k_{O_2(8)} \times 10^{-12}$ cm^3 s^{-1}	Reference	Source
8±1	*Adler-Golden* (1997) *Dyer et al.* (1997)	Laboratory measurement
11.9	*Adler-Golden* (1997)	Fitting to airglow measurement
8.6 (11.9×0.723)	*Xu et al.* (2012)	Fitting to SABER measurement
8.0	*Mlynczak et al.* (2013c)	*Adler-Golden* (1997)

With respect to the rate coefficient $k_{OHN_2(8)}$ for OH(8)+N_2, we took the measured value by *Dyer et al.* (1997), which is $7\pm4\times10^{-13}$ cm^3 s^{-1}. It is applied by *Adler-Golden* (1997), *Xu et al.* (2012), *Smith et al.* (2010), *Mlynczak et al.* (2013c, 2018) and *Panka et al.* (2017, 2018).

Regarding to $k_{OHO_2(9,8)}$ for OH(9)+O_2 → OH(8)+O_2, *Adler-Golden* (1997) provided a value of 41.8×10^{-13} cm^3 s^{-1} based on the empirical expression, and *Xu et al.* (2012) modified it as 30.2×10^{-13} cm^3 s^{-1} with a fitting parameter of 0.723. *Smith et al.* (2010) and and *Mlynczak et al.* (2013c) also applied a value of 42.0×10^{-13} cm^3 s^{-1} following *Adler-Golden* (1997). These parameters are summarized in Tab. A.5. And we firstly applied the value of 42.0×10^{-13} cm^3 s^{-1} in this model.

Table A.5: Some reported values for the collisional rate constant $k_{OHO_2(9,8)}$ from literature.

$k_{O_2(9,8)} \times 10^{-13}$ cm^3 s^{-1}	Reference	Source
41.8	*Adler-Golden* (1997)	Fitting to airglow measurement
30.2 (41.8×0.723)	*Xu et al.* (2012)	Fitting to SABER measurement
42.0	*Smith et al.* (2010) *Mlynczak et al.* (2013c)	*Adler-Golden* (1997)

A.3.2 Fitting of the collisional rate coefficients for OH(v=8)

Some rate coefficients used in this work for the OH(v=8) airglow modeling are obtained by simultaneously fitting the OH airglow model to measured limb radiances of OH(9-6) and OH(8-5) bands. The measurements are taken from SCIAMACHY channel-6 radiances. The OH(9-6) band radiance is integrated over the wavelength range of 1378-1404 nm, and the OH(8-5) band is integrated over 1297-1326 nm. The selected parameters are adjusted in such a way that the ratio between the simulated radiances of the two bands is consistent with the ratio obtained from the measurements. Several cases with different rate coefficients or combinations being adjusted in the fitting are considered, as given in the Tab. A.6. The fitting results of different cases are illustrated in the Fig. A.1, as compared to the SCIAMACHY measurements. Model simulations of cases b, c and d have good agreement with the measurements. The rate coefficient for the collisional removal of OH(v=8) by atomic oxygen from the literature differs by nearly one order of magnitude (*Xu et al.*, 2012), and the fitted parameters should agree with the laboratory measurements within the combined uncertainties if available (*Dyer et al.*, 1997). Therefore, case b is chosen and applied in this work. The utilization of cases c and d will influence the retrieval results that atomic oxygen abundances will differ by around 5 % above 90 km and 15 % at 80 km compared to case b.

Table A.6: The comparison of study cases with the applied rate coefficients being summarized. The adjusted parameters and their fitted values are marked in bold, while the coefficients taken from laboratory measurements are underlined and marked in italic.

Study case	$k_{OHO(8)}$ $\times 10^{-10} cm^3 s^{-1}$	$k_{O_2(8)}$ $\times 10^{-12} cm^3 s^{-1}$	$k_{OHN_2(8)}$ $\times 10^{-13} cm^3 s^{-1}$	$k_{OHO_2(9,8)}$ $\times 10^{-13} cm^3 s^{-1}$
a	**1.2**	*8.0*	*7.0*	42.0
b	**0.65**	*8.0*	*7.0*	**8.9**
c	**0.25**	**12.0**	*7.0*	42.0
d	**0.35**	*8.0*	**15.0**	42.0
e	2.0	**5.5**	*7.0*	42.0
f	2.0	*8.0*	**4.5**	42.0

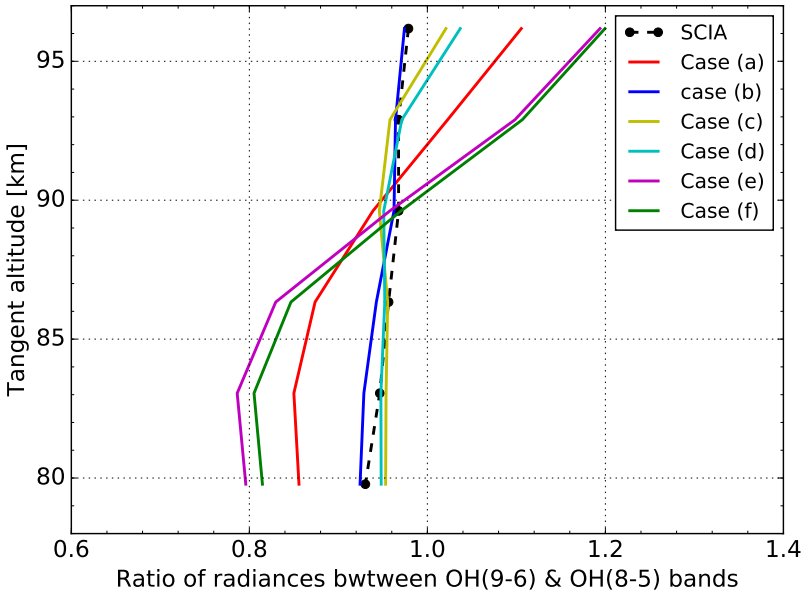

Figure A.1: The ratio of the integrated limb radiances between the OH(9-6) (1378-1404 nm) and OH(8-5) (1297-1326 nm) bands versus tangent altitude. The raw data (black dashed line) are taken from the SCIAMACHY channel-6 measurements. The fitted results (solid line) are obtained by applying the rate coefficients with respect to different cases.

A.4 O_2 A-band nightglow modeling parameters

Table A.7: O_2 A-band nightglow modeling parameters used in this work. The corresponding reaction processes are also given.

Parameter	Process	Rate constant	Reference
k^*_{OOM}	$O+O+M \rightarrow O_2^*+M$	$4.7\times10^{-33}(300/T)^2 cm^6 s^{-1}$	*Campbell and Gray* (1973)
c_{O_2}	Fitting parameter	7.5	*McDade et al.* (1986)
c_O	Fitting parameter	33.0	*McDade et al.* (1986)
$k_{O_2bN_2}$	$O_2(b^1\Sigma_g^+, v=0)+N_2$	$1.8\times10^{-15} exp(45/T) cm^3 s^{-1}$	*Sander et al.* (2011)
$k_{O_2bO_2}$	$O_2(b^1\Sigma_g^+, v=0)+O_2$	$3.9\times10^{-17} cm^3 s^{-1}$	*Sander et al.* (2011)
k_{O_2bO}	$O_2(b^1\Sigma_g^+, v=0)+O$	$8.0\times10^{-14} cm^3 s^{-1}$	*Slanger and Black* (1979)
$k_{O_2bO_3}$	$O_2(b^1\Sigma_g^+, v=0)+O_3$	$3.5\times10^{-11} exp(135/T) cm^3 s^{-1}$	*Sander et al.* (2011)
$k_{O_2bCO_2}$	$O_2(b^1\Sigma_g^+, v=0)+CO_2$	$4.2\times10^{-13} cm^3 s^{-1}$	*Sander et al.* (2011)

A.5 Multiple linear regression analysis of atomic oxygen for different cases

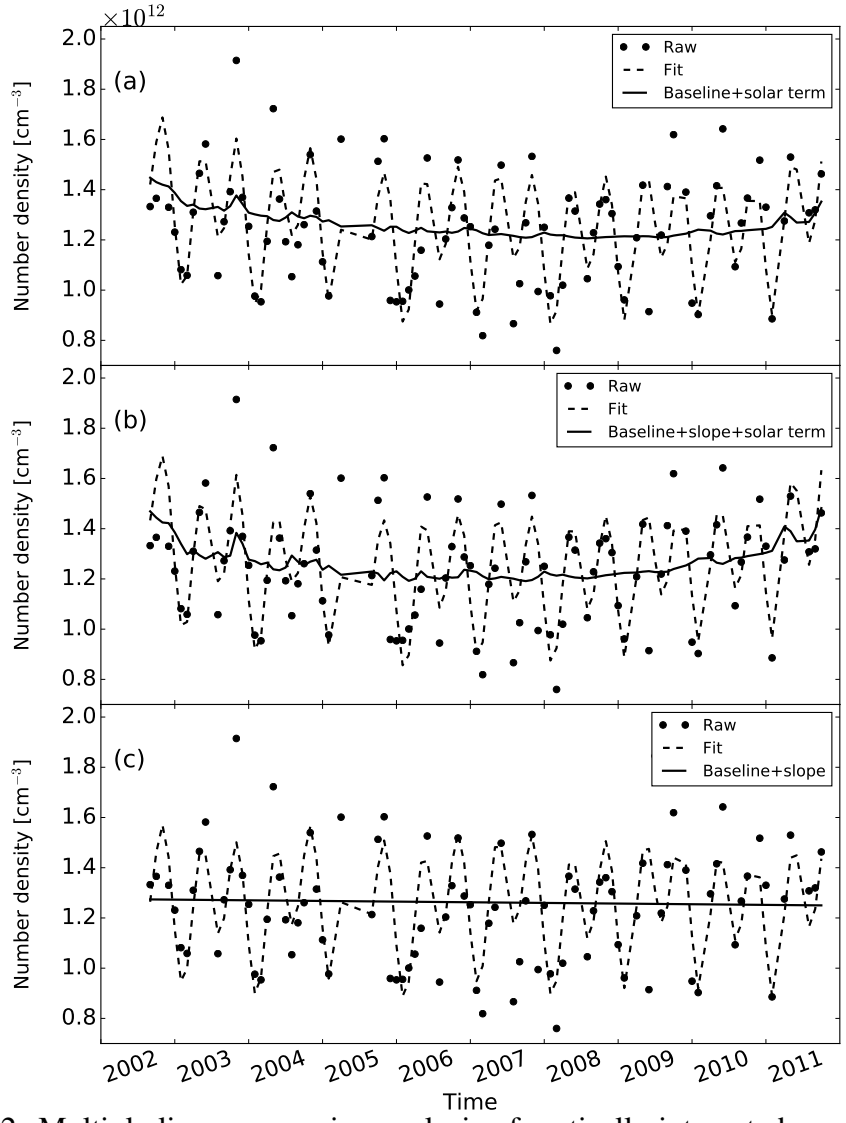

Figure A.2: Multiple linear regression analysis of vertically integrated, monthly mean atomic oxygen densities of 80-97 km for 20°-30° N from 2002 to 2011. Comparison of different analysis cases with raw and fitted data are shown. (a) The fitting is obtained by considering the baseline, the solar term, SAO, AO and QBO terms in the harmonic analysis. The baseline plus the solar term is given additionally. (b) A slope term is included in the fitting along with the solar term. (c) The solar term is replaced by a slope term.

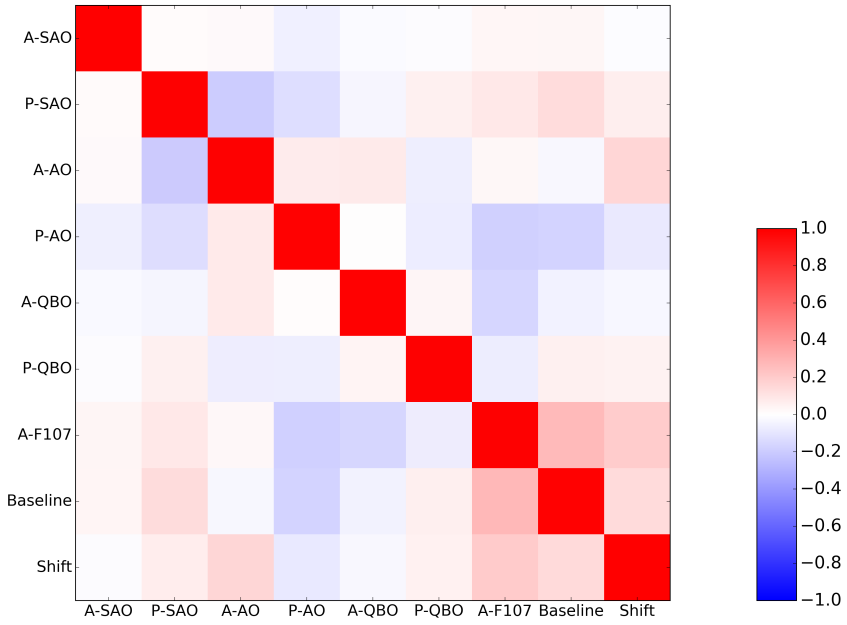

Figure A.3: The correlation matrix of the fitted parameters for the case with the solar but without the slope term. The colorbar indicates the correction strength between each two fitting parameters.

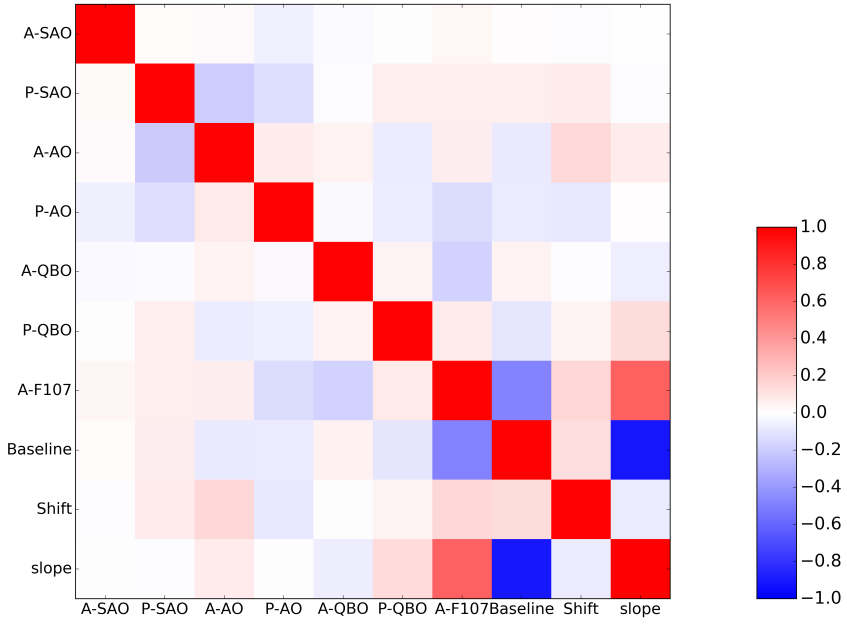

Figure A.4: The correlation matrix of the fitted parameters for the case with the solar term and plus an additional slope term.

A.6 GRIPS-F dark current correction algorithm

During routine operation during the night, the dark current profiles are recorded once before and after every 15 minutes measurements of the airglow signal. The observation is continuously carrying on, which means, two subsequent dark current profiles are nearly simultaneously measured every 15 minutes. Following *Schmidt et al.* (2013), the dark current profiles are processed individually for the measurements of each single nights. The variations are monitored over the operation hours during the night at all pixels, and then accordingly calibrated.

Firstly, the dark current profiles during the course of one night are sorted according to the time stamp and the pixel number.

Then, all dark current measurements are averaged for every single pixel over all dark current profiles over one night as:

$$\bar{D}_i = \sum_{n=1}^{N} \left(D_{n,i}\right) \cdot \frac{1}{N} \tag{A.1}$$

$D_{n,i}$ denotes the dark current counts for the nth profile at the ith pixel. N refers to the number of total measured dark current profiles. The total pixel number is 512.

Afterwards, the averaged dark current over all pixels is calculated:

$$\bar{D} = \sum_{i=1}^{512} \left(\bar{D}_i\right) \cdot \frac{1}{512} \tag{A.2}$$

Next, the dark current measurements are averaged for each profile over all pixels as:

$$\breve{D}_n = \sum_{i=1}^{512} \left(D_{n,i}\right) \cdot \frac{1}{512} \tag{A.3}$$

And then the original dark currents are smoothed accordingly:

$$\tilde{D}_{n,i} = \frac{\bar{D}_i}{\bar{D}} \cdot \breve{D}_n \tag{A.4}$$

Lastly, the corrected dark current profiles are interpolated into each airglow spectrum measured in between the dark current profiles and subtracted from the raw airglow signal.

Figure A.5 illustrates an example of the nocturnal evolution of the GRIPS-F dark current measured at selected pixels and averaged over all pixels. The corresponding calibrated dark current profiles are also given for comparison.

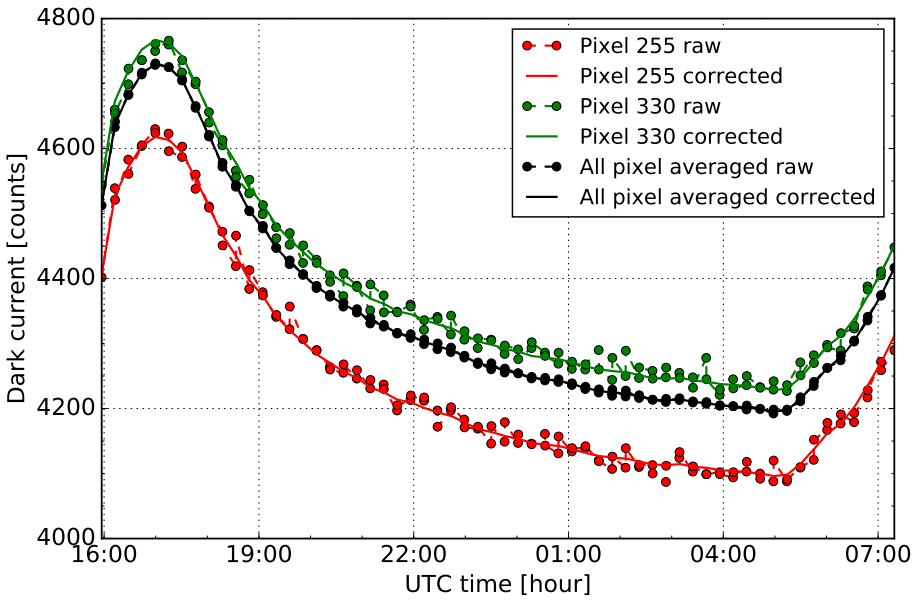

Figure A.5: The nocturnal changes of the dark current profiles measured at pixel 255 (red), pixel 330 (green), and averaged over all pixels (black) during the operation hours for the night of Dec. 14-15 2015. The raw measurements (dashed line) are recorded by the GRIPS-F detector twice every 15 minutes. The corrected dark current profiles (solid line) are estimated for each measured spectrum at corresponding timestamps. Pixel 255 corresponds to a wavelength of 1547.7 nm, where no emission lines exit but only noises. Pixel 330 corresponds to 1533.2 nm, close to the peak emissions line of OH(3-1) $P_1(3.5)$.

A.7 GRIPS-F instrument line shape function

For an instrument with an entrance slit which is narrow enough, the instrumental line shape is normally regarded as the Gaussian function. However, in the GRIPS-F spectra, a trapezoid form appears in the measured line shapes. Hence, for the GRIPS-F temperature retrieval, three different instrument line shape functions (Gaussian, mixture of rectangular form with Gaussian, and the asymmetric double sigmoidal function) are investigated here. Two aspects are mainly investigated, which are the influence on the derived temperature and the residual between the fitted spectrum and the measurement.

The normalised Gaussian function for a unit area can be written as:

$$G_\beta(x) = \sqrt{\frac{4 \cdot ln2}{\pi}} \cdot \frac{1}{\beta} \cdot \exp(-4 \cdot ln2 \cdot \frac{x^2}{\beta^2}) \tag{A.5}$$

in which β denotes the FWHM, and x is wavelength, in units of nm.

In order to fully represent the trapezoid form in the instrument line shape, a rectangular form is introduced in the Gaussian function as:

$$M_\beta(x) = \begin{cases} G_\beta(x) \cdot r + \frac{1}{\beta} \cdot (1-r) & \text{if } \frac{-\beta}{2} \leqslant x \leqslant \frac{\beta}{2} \\ G_\beta(x) \cdot r & \text{if } x < \frac{-\beta}{2} \text{ or } x > \frac{\beta}{2} \end{cases} \tag{A.6}$$

in which r indicates the ratio of Gaussian function in the mixture.

Additionally, the normalised asymmetric double sigmoidal function (Asym2Sig, ADS) for a unit area can be used for the instrument line shape as:

$$A_\beta(x) = \frac{1}{2.7} \cdot \frac{1}{1+\exp\frac{-(x+1.35)}{0.27}} \cdot (1 - \frac{1}{1+\exp\frac{-(x-1.35)}{0.32}}) \tag{A.7}$$

in which, the parameters are obtained by fitting a reference line, which is taken from the measurement of an office lamp (Hg) at 1529.58 nm with a FWHM of 2.5 nm (P. Knieling, personal communication, 2016).

As for the retrieval results, the fitted spectra using the three functions as the instrument line shape are illustrated in Fig. A.6. The corresponding derived temperature, overall residual (difference between the measurement and fitted spectrum), and other retrieval parameters are given in Tab. A.8.

Generally, the comparison results indicate that the derived temperatures with different line shape functions vary within around 0.5 K, and the overall residuals differ within around 50 counts. Therefore, the instrument line shape function has a inconsequential impact on the temperature retrieval. The mixed function delivers the lowest temperature

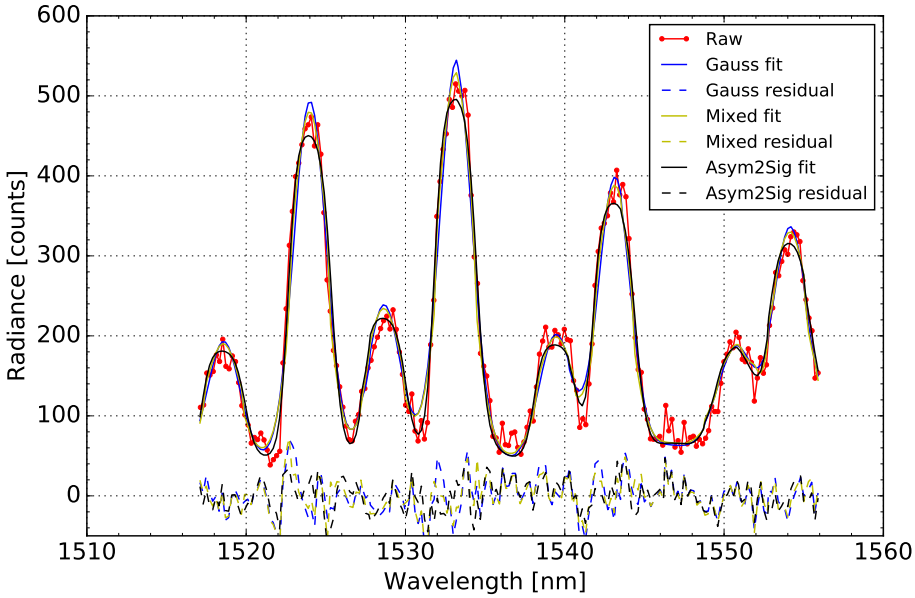

Figure A.6: Fitted spectra (solid line) with various instrument line shape functions including Gaussian (blue), Gaussian mixed with a rectangular form (yellow), and Asym2Sig (black) for the GRIPS-F observations of OH(3-1) airglow emissions on Dec. 14, 2015 at 18:01:52. The corresponding residuals (dashed line) between the measurement (dotted red line) and the fitted spectra are also given.

Table A.8: The comparison of the derived temperature, overall residual and retrieval target parameters, which include spectral resolution (FWHM), function mixing ratio, scaling factor and offset. The wavelength shift is negligible. The overall residual is calculated from the square root value of the differences at all wavelength points between the raw and fitted spectrum. Mixed (2.5 nm) indicates the Gaussian function has a fixed FWHM of 2.5 nm in the mixed form.

Function	Temperature [K]	Overall residual [count]	FWHM [nm]	Function mixing ratio r [-]	Scaling factor [-]	Offset [count]
Gauss	212.9	327.9	2.38	/	2.46	42.5
Mixed	212.4	300.6	2.45	0.845	2.42	45.4
Mixed (2.5 nm)	212.6	301.9	/	0.834	2.46	42.6
Asym2Sig	213.0	278.4	/	/	2.40	45.8

of 212.4 K. The Asym2Sig one reaches the lowest overall residual. In terms of the fitting results in the spectra, the Gaussian function overestimates the peak values, and the

line width is relatively narrow; the mixed form gives a considerably good representation of the measurement features; the Asym2Sig achieves the best overall fitting output, but an underestimation of the peak values are observed. In conclusion, the applied Gaussian line shape function is competent for the GRIPS-F temperature retrieval.

A.8 Three peak method for OH(3-1) rotational temperature retrieval

The three peaks denoted in the method refer to the three emission lines of $P_1(2.5)$, $P_1(3.5)$, $P_1(4.5)$ from OH(3-1) band, as selected for the temperature retrieval. For this method, the accuracy of derived temperature highly depends on the recognition of peak intensities and wavelength positions of the three emission lines, which have to be carefully determined. To eliminate the noise influence on the emission line signal, a low-pass-filter (the Fourier Transform (FT) filter) is applied on the airglow spectra for smoothing. The spectra background offset is assumed to be constant and is then estimated from the local minimal intensity near the $P_1(4.5)$ line (*Bittner et al.*, 2002). Afterwards, the line intensities are calculated by subtracting the offset from the corresponding peak intensities.

As derived from Eq. 2.5, the relationship between the rotational temperature and emission line intensity can be arranged as

$$ln\frac{I^{(v',J')}_{(v'',J'')}}{2(2J'+1)A^{(v',J')}_{(v'',J'')}} = -\frac{hcE_{v'}(J')}{kT_{rot}} + constant \tag{A.8}$$

in which $-\frac{hc}{kT_{rot}}$ can be considered as the slope of the variable $E_{v'}(J')$ to the logarithmic line intensity. The temperature T_{rot} can be then derived from the straight line fitting to the three peak emission lines versus $E_{v'}(J')$.

The 3-1 $P_1(4.5)$ line is overlapped with 4-2 $R_1(6.5)$, which may lead to a positive bias in the calculated temperature. Thus, an empirical correction factor is introduced to calibrate this effect (*Lange*, 1982) by iterative calculations of the $P_1(4.5)$ intensity and rotational temperature, as given below:

$$I'_{P_1(4.5)} = I_{P_1(4.5)} \cdot (1 - corr) \tag{A.9}$$

in which the boundary condition of the iteration is set as 0.1 K in the temperature changes. The correction factor *corr* is temperature dependent:

$$corr = 1.5 \times 10^{-11} T^{-4.07} \tag{A.10}$$

Kaufmann and Knieling (2013) found that the Lange correction factor could potentially overcompensate the overlapping influence of the 4-2 band, and provided an updated correction factor as follows:

$$corr = 1.5 \times 10^{-13} T^{4.87} \tag{A.11}$$

A.9 AtmoSHINE in-orbit tests

The AtmoSHINE first in-orbit test was fulfilled on the 23rd and 24th of December 2018, and two orbits of the Earth limb measurements were obtained. The geographical location is shown in Figure A.7 and the corresponding information is summarized in Table A.9. The obtained data are only partly applicable for the temperature retrieval as only 20-minutes auxiliary attitude data are available for those measurements. Different integration time from 1 to 32 seconds was tested for data acquisition, and it was found that an integration time of $\geq$ 8 s is required to obtain the designed signal-to-noise ratio.

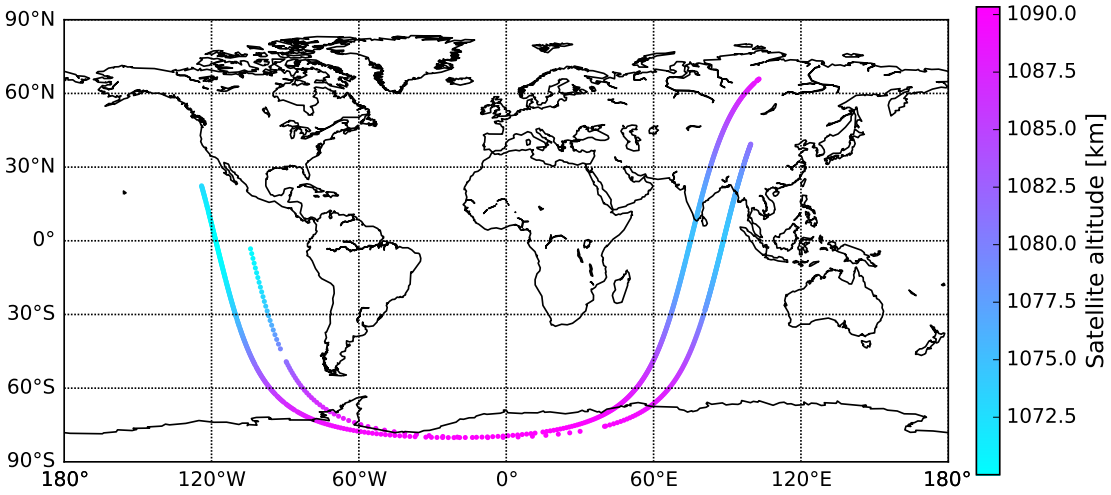

Figure A.7: The geographical projection of satellite track during the first commissioning-phase test in December 23 & 24, 2018. The color indicates the satellite altitude in the WGS84 coordinate.

Table A.9: Data overview of the AtmoSHINE first commissioning-phase test. The date and time are recorded in UTC.

Orbit No.	Date	Start time	Stop time	Duration	Integration time	Image No.
1	23 Dec. 2018	00:39:55	02:00:15	80 min	4 s	710
2	23∼24 Dec. 2018	23:54:48	00:59:43	65 min	1, 2, 8, 16, 32 s	406

The second in-orbit test was conducted on the 17th and 18th of March 2019. The double-vector attitude determination (two non-parallel vectors were measured to determine the attitude matrix between two coordinates) instead of the star sensor was utilized for the satellite platform control during that period, which led to a high satellite attitude variation, and the instrument LOS was not pointed to the target altitude region.

The third in-orbit test was conducted on the 11th and 12th of April 2019. An error arose during the data storage in the satellite, and all transmitted images were erroneous because of byte loss in data stream.

The fourth in-orbit test was successfully implemented on the 21st and 22nd of May 2019 and around 9 orbits of measurements were acquired, as shown in Fig. A.8. The satellite attitude information was delivered and in total approx. 2800 images are gained from this test.

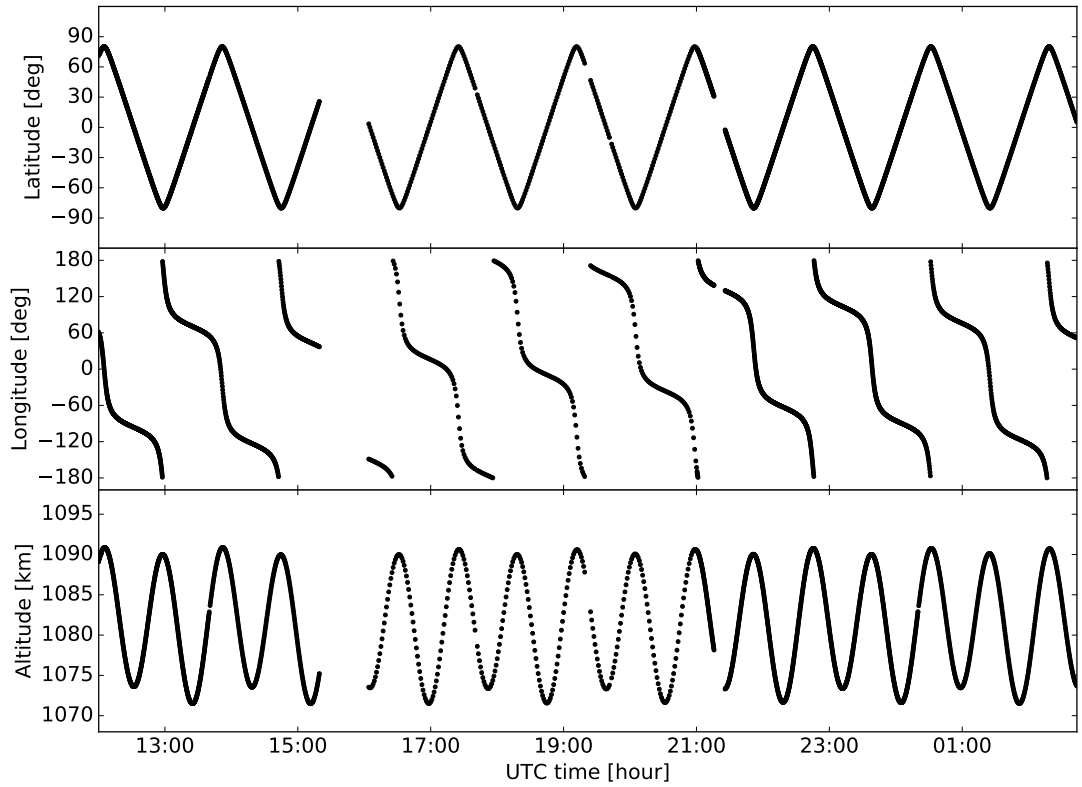

Figure A.8: The satellite geolocation during the fourth commissioning-phase period. The latitude, longitude and altitude are converted from the GPS information to the WGS84 coordinate. The different time sampling density is caused by the change of the image frame time during the observation.

The fifth in-orbit test (a four-day regular measurement) was carried out from Aug. 05, 2019 to Aug. 09, 2019, as summarized in Tab. A.10. Part of the data from the 6th of August were not transmitted, while the measured images from the 8th of August were totally damaged because of the byte loss during the in-orbit satellite storage. The corresponding satellite attitude data were provided.

Table A.10: Data overview of the AtmoSHINE regular observation period. The date and time are recorded in UTC.

No.	Date	Start time	Stop time	Duration	Integration time	Image No.
1	5 Aug. 2019	16:01:24	01:25:53	9.5 h	16 s	1845
2	6 Aug. 2019	18:09:45 22:19:03 00:31:57	20:28:36 23:39:41 02:49:54	6 h	16 s	1196
3	7 Aug. 2019	16:04:04	03:00:41	11 h	16 s	2190
4	8 Aug. 2019	16:04:22	03:00:45	11 h	16 s	-

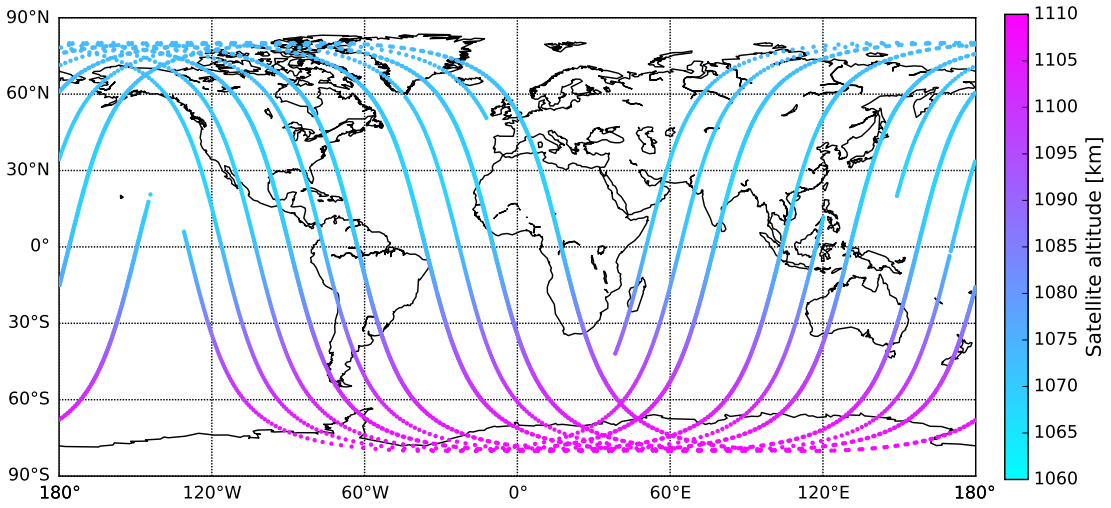

Figure A.9: The geographical projection of satellite track during the regular observation period in August 2019. The latitude, longitude and altitude are in the WGS84 coordinate.

Acknowledgements

Foremost, I would like to express my profound gratitude to my doctoral supervisor Prof. Dr. Martin Riese, who has given me the opportunity to work at IEK-7, Forschungszentrum Jülich, and provided the continuous support for my Ph.D. project. I am also deeply grateful to Prof. Dr. Ralf Koppmann for offering me the opportunity to study at Bergische Universität Wuppertal and for the invaluable advices on research.

I would like to address my special and sincere thanks to my academic supervisor Dr. Martin Kaufmann. He has brought me into the topic and offered me to join the AtmoHIT and AtmoSHINE projects. He has constantly supported me with his knowledge and experiences while encouraging me on my research project and career development. I take this opportunity to especially acknowledge Dr. Yajun Zhu, who has always been open for discussions, and provided me with an enormous amount of insightful and constructive advices and suggestions.

Many thanks go to Friedhelm Olschewski, Peter Knieling, Dr. Heinz Rongen and Tom Neubert for their continued support in my Ph.D. project and for sharing their expertise in the instruments and data processing. I wish to warmly thank Daikang Wei, Dr. Jilin Liu, Lauther Valentin, Dr. Michael Deiml, Oliver Wroblowski, Qiucheng Gong, Dr. Rui Song and other colleagues at IEK-7 and Bergische Universität Wuppertal for the pleasant time we worked together.

Last but not least, I am deeply and heartfeltly indebted to my parents, my family and my friends for their continuous encouragement and tremendous support with infinite patience. Without their unconditional support, my dissertation work would have never been close to completion.

Acronyms

2D Two Dimensional.

ADS Asymmetric Double Sigmoidal function.

AO Annual Oscillation.

ARTS Atmospheric Radiative Transfer Simulator.

AtmoSHINE Atmospheric Spatial Heterodyne Interferometer Next Exploration.

BUW Bergische Universität Wuppertal.

CMOS Complementary Metal-Oxide-Semiconductor.

CRISTA Cryogenic Infrared Spectrometers and Telescopes for the Atmosphere.

ECEF Earth-Centered, Earth-Fixed.

Envisat Environmental Satellite.

ESA European Space Agency.

ETON Energy Transfer in the Oxygen Nightglow campaign.

FFT Fast Fourier Transformation.

FOV Field Of View.

FT Fourier Transformation.

FWHM Full Width at Half Maximum.

FZJ Forschungszentrum Jülich.

GOMOS Global Ozone Monitoring by Occultation of Stars.

GPS Global Positioning System.

GRIPS-F GRound-based Infrared P-Branch Spectrometer.

GW Gravity Wave.

HAMMONIA Hamburg Model of the Neutral and Ionized Atmosphere.

HDF Hierarchical Data Format.

HIRDLS High Resolution Dynamics Limb Sounder.

HITRAN High-resolution Transmission molecular absorption database.

HRDI High Resolution Doppler imager.

IR Infrared.

ISUAL Imager of Sprites and Upper Atmospheric Lightning.

LIMS Limb Infrared Monitor of the Stratosphere.

LOS Line Of Sight.

LTE Local Thermodynamic Equilibrium.

LVDS Low-voltage differential signaling.

ME Modulation Efficiency.

MIPAS Michelson Interferometer for Passive Atmospheric Sounding.

MLS Microwave Limb Sounder.

MLT Mesosphere and Lower Thermosphere.

MPL Max-Planck-Institut für die Physik des Lichts.

MSIS Mass Spectrometer Incoherent Scatter simulation model.

MTF Modulation Transfer Function.

NDMC Network for the Detection of Mesospheric Change.

NetCDF Network Common Data Form.

O_2 A-band Oxygen Atmospheric band.

OH Hydroxyl.

OSIRIS Optical Spectrograph and Infrared Imager System.

PCD Product Confidence Data.

PDA Photodiode Array.

PMC Polar Mesospheric Cloud.

PRNU Photon Response Non-uniformity.

QBO Quasi-biennial Oscillation.

ROSE A 3-dimensional middle atmosphere model.

SABER Sounding of the Atmosphere using Broadband Emission Radiometry.

SAO Semiannual Oscillation.

SCIAMACHY Scanning Imaging Absorption Spectrometer for Atmospheric CHartographY.

SFM Spectra Fitting Method.

SFU Solar Flux Unit.

SHI Spatial Heterodyne Interferometer.

SHS Spatial Heterodyne Spectrometer.

SME Solar Mesosphere Explorer.

SNR Signal-to-noise Ratio.

SORCE Solar Radiation and Climate Experiment.

SPB Spectrometer B.

STD Standard Deviation.

SZA Solar Zenith Angle.

TEM Transformed Eulerian mean.

TIMED Thermosphere Ionosphere Mesosphere Energetics and Dynamics satellite.

TPM Three Peak Method.

UARS Upper Atmosphere Research Satellite.

UTC Universal Time Coordinated.

UV Ultraviolet.

VER Volume Emission Rate.

VMR Volume Mixing Ratio.

WGS84 World Geodetic System 1984.

WINDII Wind Imaging Interferometer.

List of Figures

List of Tables

Bibliography

Adler-Golden, S. (1997), Kinetic parameters for OH nightglow modeling consistent with recent laboratory measurements, *Journal of Geophysical Research: Space Physics*, *102*(A9), 19,969–19,976, doi:10.1029/97JA01622.

Alexander, M. J., M. Geller, C. McLandress, S. Polavarapu, P. Preusse, F. Sassi, K. Sato, S. Eckermann, M. Ern, A. Hertzog, Y. Kawatani, M. Pulido, T. A. Shaw, M. Sigmond, R. Vincent, and S. Watanabe (2010), Recent developments in gravity-wave effects in climate models and the global distribution of gravity-wave momentum flux from observations and models, *Quarterly Journal of the Royal Meteorological Society*, *136*(650), 1103–1124, doi:10.1002/qj.637.

Allen, S. J., and R. A. Vincent (1995), Gravity wave activity in the lower atmosphere: Seasonal and latitudinal variations, *Journal of Geophysical Research: Atmospheres*, *100*(D1), 1327–1350, doi:10.1029/94JD02688.

Andrews, D., C. Leovy, and J. Holton (1987), *Middle atmosphere dynamics*, International Geophysics, Elsevier Science.

Baker, D., W. Pendleton Jr., A. Steed, R. Huppi, and A. T. Stair Jr. (1977), Near-infrared spectrum of an aurora, *Geophysical Research Letters*, *82*(10), 1601–1609, doi:10.1029/JA082i010p01601.

Baker, D. J., and A. T. Stair (1988), Rocket measurements of the altitude distributions of the hydroxyl airglow, *Physica Scripta*, *37*(4), 611–622, doi:10.1088/0031-8949/37/4/021.

Barrot, G., J.-L. Bertaux, R. Fraisse, and A. Mangin (2003), GOMOS calibration on Envisat-status on December 2002, in *Proceedings of Envisat Validation Workshop*.

Barth, C. A. (1961), 5577-angstrom airglow, *Science*, *134*(348), 1426.

Barth, C. A., and A. F. Hildebrandt (1961), The 5577 A airglow emission mechanism, *Journal of Geophysical Research (1896-1977)*, *66*(3), 985–986, doi:10.1029/JZ066i003p00985.

Bates, D. (1988), Excitation and quenching of the oxygen bands in the nightglow, *Planetary and Space Science*, *36*(9), 875 – 881, doi:https://doi.org/10.1016/0032-0633(88)90093-1, special Issue: Atomic Oxygen Abundance in Thermosphere.

Bates, D. R., and M. Nicolet (1950), The photochemistry of atmospheric water vapor, *Journal of Geophysical Research (1896-1977)*, *55*(3), 301–327, doi:10.1029/JZ055i003p00301.

Beagley, S. R., C. D. Boone, V. I. Fomichev, J. J. Jin, K. Semeniuk, J. C. McConnell, and P. F. Bernath (2010), First multi-year occultation observations of co_2 in the MLT by ACE satellite: 0bservations and analysis using the extended CMAM, *Atmospheric Chemistry and Physics*, *10*(3), 1133–1153, doi:10.5194/acp-10-1133-2010.

Beig, G., P. Keckhut, R. P. Lowe, R. G. Roble, M. G. Mlynczak, J. Scheer, V. I. Fomichev, D. Offermann, W. J. R. French, M. G. Shepherd, A. I. Semenov, E. E. Remsberg, C. Y. She, F. J. Lübken, J. Bremer, B. R. Clemesha, J. Stegman, F. Sigernes, and S. Fadnavis (2003), Review of mesospheric temperature trends, *Reviews of Geophysics*, *41*(4), doi:10.1029/2002RG000121.

Bellisario, C., P. Keckhut, L. Blanot, A. Hauchecorne, and P. Simoneau (2014), O_2 and OH night airglow emission derived from GOMOS-Envisat instrument, *Journal of Atmospheric and Oceanic Technology*, *31*(6), 1301–1311, doi:10.1175/JTECH-D-13-00135.1.

Bittner, M., D. Offermann, and H. H. Graef (2000), Mesopause temperature variability above a midlatitude station in Europe, *Journal of Geophysical Research: Atmospheres*, *105*(D2), 2045–2058, doi:10.1029/1999JD900307.

Bittner, M., D. Offermann, H.-H. Graef, M. Donner, and K. Hamilton (2002), An 18-year time series of OH rotational temperatures and middle atmosphere decadal variations, *Journal of Atmospheric and Solar-Terrestrial Physics*, *64*(8), 1147 – 1166, doi:https://doi.org/10.1016/S1364-6826(02)00065-2, pSMOS 2000 Workshop - Planetary Scale Mesopause Observing System.

Boone, C. D., R. Nassar, K. A. Walker, Y. Rochon, S. D. McLeod, C. P. Rinsland, and P. F. Bernath (2005), Retrievals for the atmospheric chemistry experiment Fourier-transform spectrometer, *Applied optics*, *44*(33), 7218–7231, doi:10.1364/AO.44.007218.

Bovensmann, H., J. P. Burrows, M. Buchwitz, J. Frerick, S. Noël, V. V. Rozanov, K. V. Chance, and A. P. H. Goede (1999), SCIAMACHY: Mission objectives and measurement modes, *Journal of the Atmospheric Sciences*, *56*(2), 127–150, doi:10.1175/1520-0469(1999)056<0127:SMOAMM>2.0.CO;2.

Bramstedt, K., S. Noël, H. Bovensmann, J. P. Burrows, C. Lerot, L. Tilstra, G. Lichtenberg, A. Dehn, and T. Fehr (2009), SCIAMACHY monitoring factors: Observation and end-to-end correction of instrument performance degradation, in *Proceedings of Atmospheric Science Conference*, European space agency, Barcelona, Spain.

Brasseur, G., and D. Offermann (1986), Recombination of atomic oxygen near the mesopause: Interpretation of rocket data, *Journal of Geophysical Research: Atmospheres*, *91*(D10), 10,818–10,824, doi:10.1029/JD091iD10p10818.

Brasseur, G. P., and S. Solomon (2005), *Aeronomy of the middle atmosphere: Chemistry and chysics of the stratosphere and mesosphere*, *Atmospheric and Oceanographic Sciences Library*, vol. 32, 3 ed., Springer Netherlands.

Broadfoot, A. L., and K. R. Kendall (1968), The airglow spectrum, 3100-10,000 A, *Journal of Geophysical Research (1896-1977)*, *73*(1), 426–428, doi:10.1029/JA073i001p00426.

Brooke, J. S., P. F. Bernath, C. M. Western, C. Sneden, M. Afşar, G. Li, and I. E. Gordon (2016), Line strengths of rovibrational and rotational transitions in the $X^2\prod$ ground state of OH, *Journal of Quantitative Spectroscopy and Radiative Transfer*, *168*, 142 – 157, doi:https://doi.org/10.1016/j.jqsrt.2015.07.021.

Bucholtz, A., W. Skinner, V. Abreu, and P. Hays (1986), The dayglow of the O_2 atmospheric band system, *Planetary and Space Science*, *34*(11), 1031 – 1035, doi:https://doi.org/10.1016/0032-0633(86)90013-9.

Buehler, S., P. Eriksson, T. Kuhn, A. von Engeln, and C. Verdes (2005), ARTS, the atmospheric radiative transfer simulator, *Journal of Quantitative Spectroscopy and Radiative Transfer*, *91*(1), 65 – 93, doi:https://doi.org/10.1016/j.jqsrt.2004.05.051.

Burch, D. E., and D. A. Gryvnak (1969), Strengths, widths, and shapes of the oxygen lines near 13,100 cm- 1 (7620 å), *Applied optics*, *8*(7), 1493–1499.

Burkholder, J., S. Sander, J. Abbatt, J. Barker, R. Huie, C. Kolb, M. Kurylo, V. Orkin, D. Wilmouth, and P. Wine (2015), Chemical kinetics and photochemical data for use in atmospheric studies: evaluation number 18, *Tech. rep.*, Jet Propulsion Laboratory, California Institute of Technology, Pasadena, CA.

Burrage, M. D., N. Arvin, W. R. Skinner, and P. B. Hays (1994), Observations of the O_2 atmospheric band nightglow by the high resolution Doppler imager, *Journal of Geophysical Research: Space Physics*, *99*(A8), 15,017–15,023, doi:10.1029/94JA00791.

Campbell, I., and C. Gray (1973), Rate constants for $O(^3P)$ recombination and association with $N(^4S)$, *Chemical Physics Letters*, *18*(4), 607 – 609, doi:https://doi.org/10.1016/0009-2614(73)80479-8.

Chamberlain, J. (1995), *Physics of the Aurora and Airglow: International Geophysics Series*, vol. 41, American Geophysical Union, Washington, D. C.

Chamberlain, J., and D. Hunten (1987), *Theory of planetary atmospheres: An Introduction to their physics and chemistry*, International Geophysics Series, Academic Press.

Chamberlain, J. W., C. Y. Fan, and A. B. Meinel (1954), A new O_2 band in the infrared auroral spectrum, *Astrophysical Journal*, *120*, 560, doi:10.1086/145944.

Chandra, S., C. H. Jackman, E. L. Fleming, and J. M. Russell III (1997), The seasonal and long term changes in mesospheric water vapor, *Geophysical Research Letters*, *24*(6), 639–642, doi:10.1029/97GL00546.

Chanin, M.-L., and A. Hauchecorne (1981), Lidar observation of gravity and tidal waves in the stratosphere and mesosphere, *Journal of Geophysical Research: Oceans*, *86*(C10), 9715–9721, doi:10.1029/JC086iC10p09715.

Chapman, S., and R. Lindzen (1970), *Atmospheric tides: thermal and gravitational*, D. Reidel Publishing Company, Dordrecht, Holland.

Charters, P. E., R. G. Macdonald, and J. C. Polanyi (1971), Formation of vibrationally excited OH by the reaction H + O_3, *Applied Optics*, *10*(8), 1747–1754, doi:10.1364/AO.10.001747.

Chen, Q. (2019a), The AtmoSHINE external straylight analysis-2019-09-v1.0, *Tech. rep.*, Research Centre Jülich and University of Wuppertal.

Chen, Q. (2019b), The AtmoSHINE in-orbit visibility calibration-2019-12-v1.0, *Tech. rep.*, Research Centre Jülich and University of Wuppertal.

Chen, Q., M. Kaufmann, Y. Zhu, J. Liu, R. Koppmann, and M. Riese (2019), Global nighttime atomic oxygen abundances from GOMOS hydroxyl airglow measurements in the mesopause region, *Atmospheric Chemistry and Physics*, *19*(22), 13,891–13,910, doi:10.5194/acp-19-13891-2019.

Copeland, R. A., G. P. Smith, M. M. Mlynczak, and K. S. Kalogerakis (2006), Deactivation of highly vibrationally excited oh by o atoms, *Eos Trans. AGU*, *87*(52), fall Meet. Suppl., Abstract SA21A-0225.

Cosby, P. C., and T. G. Slanger (2007), OH spectroscopy and chemistry investigated with astronomical sky spectra, *Canadian Journal of Physics*, *85*(2), 77–99, doi:10.1139/p06-088.

Dandekar, B., and J. Turtle (1971), Atomic oxygen concentration from the measurement of the [OI] 5577 å emission of the airglow, *Planetary and Space Science*, *19*(8), 949 – 957, doi:https://doi.org/10.1016/0032-0633(71)90145-0.

Dawkins, E. C. M., A. Feofilov, L. Rezac, A. A. Kutepov, D. Janches, J. Höffner, X. Chu, X. Lu, M. G. Mlynczak, and J. Russell III (2018), Validation of SABER v2.0 operational temperature data with ground-based lidars in the Mesosphere-Lower Thermosphere region (75-105 km), *Journal of Geophysical Research: Atmospheres*, *123*(17), 9916–9934, doi:10.1029/2018JD028742.

de Wit, R. J., R. E. Hibbins, P. J. Espy, and N. J. Mitchell (2013), Interannual variability of mesopause zonal winds over Ascension Island: Coupling to the stratospheric QBO, *Journal of Geophysical Research: Atmospheres*, *118*(21), 12,052–12,060, doi:10.1002/2013JD020203.

Dehn, A. (2012), Quality readme file for GOMOS level 1b data version GOMOS/6.01, *Tech. Rep. ENVI-GSOP-EOGD-QD-12-0116*, European Space Agency.

Dickinson, P. H. G., R. C. Bolden, and R. A. Young (1974), Measurement of atomic oxygen in the lower ionosphere using a rocket-borne resonance lamp, *Nature*, *252*, pages 289–291, doi:https://doi.org/10.1038/252289a0.

Dickinson, P. H. G., W. C. Bain, L. Thomas, E. R. Williams, D. B. Jenkins, and N. D. Twiddy (1980), The determination of the atomic oxygen concentration and associated parameters in the lower ionosphere, *Proceedings of the Royal Society of London. Series A, Mathematical and Physical Sciences*, *369*(1738), 379–408.

Dickinson, R. E. (1984), Infrared radiative cooling in the mesosphere and lower thermosphere, *Journal of Atmospheric and Terrestrial Physics*, *46*(11), 995 – 1008, doi:https://doi.org/10.1016/0021-9169(84)90006-0.

Donahue, T. M., B. Guenther, and R. J. Thomas (1973), Distribution of atomic oxygen in the upper atmosphere deduced from Ogo 6 airglow observations, *Journal of Geophysical Research (1896-1977)*, *78*(28), 6662–6689, doi:10.1029/JA078i028p06662.

Dunkerton, T. (1978), On the mean meridional mass motions of the stratosphere and mesosphere, *Journal of the Atmospheric Sciences*, *35*(12), 2325–2333, doi:10.1175/1520-0469(1978)035<2325:OTMMMM>2.0.CO;2.

Dunkerton, T. J. (1982), Theory of the Mesopause Semiannual Oscillation, *Journal of the Atmospheric Sciences*, *39*(12), 2681–2690, doi:10.1175/1520-0469(1982)039<2681:TOTMSO>2.0.CO;2.

Dyer, M. J., K. Knutsen, and R. A. Copeland (1997), Energy transfer in the ground state of OH: Measurements of OH(v=8,10,11) removal, *The Journal of Chemical Physics*, *107*(19), 7809–7815, doi:10.1063/1.475094.

Eberhart, M., S. Löhle, B. Strelnikov, J. Hedin, M. Khaplanov, S. Fasoulas, J. Gumbel, F.-J. Lübken, and M. Rapp (2019), Atomic oxygen number densities in the mesosphere–lower thermosphere region measured by solid electrolyte sensors on WADIS-2, *Atmospheric Measurement Techniques*, *12*(4), 2445–2461, doi:10.5194/amt-12-2445-2019.

Ern, M., P. Preusse, J. C. Gille, C. L. Hepplewhite, M. G. Mlynczak, J. M. Russell III, and M. Riese (2011), Implications for atmospheric dynamics derived from global observations of gravity wave momentum flux in stratosphere and mesosphere, *Journal of Geophysical Research: Atmospheres*, *116*(D19), doi:10.1029/2011JD015821.

ESA (2010), European space agency-Envisat GOMOS product handbook, `http://envisat.esa.int/handbooks/gomos/CNTR.html`, [Online; accessed 8-November-2016].

Evans, W. F. J., and E. J. Llewellyn (1973), Atomic hydrogen concentrations in the mesosphere and the hydroxyl emissions, *Journal of Geophysical Research*, *78*(1), 323–326, doi:10.1029/JA078i001p00323.

Evans, W. F. J., D. M. Hunten, E. J. Llewellyn, and A. V. Jones (1968), Altitude profile of the infrared atmospheric system of oxygen in the dayglow, *Journal of Geophysical Research (1896-1977)*, *73*(9), 2885–2896, doi:10.1029/JA073i009p02885.

Evans, W. F. J., I. C. McDade, J. Yuen, and E. J. Llewellyn (1988), A rocket measurement of the O_2 Infrared Atmospheric (0-0) band emission in the dayglow and a determination of the mesospheric ozone and atomic oxygen densities, *Canadian Journal of Physics*, *66*(11), 941–946, doi:10.1139/p88-151.

Feofilov, A. G., and A. A. Kutepov (2012), Infrared radiation in the mesosphere and lower thermosphere: Energetic effects and remote sensing, *Surveys in Geophysics*, *33*(6), 1231–1280, doi:10.1007/s10712-012-9204-0.

Fetzer, E. J., and J. C. Gille (1994), Gravity wave variance in LIMS temperatures. part i: Variability and comparison with background winds, *Journal of the Atmospheric Sciences*, *51*(17), 2461–2483, doi:10.1175/1520-0469(1994)051<2461:GWVILT>2.0.CO;2.

Fischer, H., M. Birk, C. Blom, B. Carli, M. Carlotti, T. von Clarmann, L. Delbouille, A. Dudhia, D. Ehhalt, M. Endemann, J. M. Flaud, R. Gessner, A. Kleinert, R. Koopman, J. Langen, M. López-Puertas, P. Mosner, H. Nett, H. Oelhaf, G. Perron,

J. Remedios, M. Ridolfi, G. Stiller, and R. Zander (2008), MIPAS: an instrument for atmospheric and climate research, *Atmospheric Chemistry and Physics*, *8*(8), 2151–2188, doi:10.5194/acp-8-2151-2008.

Fomichev, V. I., W. E. Ward, S. R. Beagley, C. McLandress, J. C. McConnell, N. A. McFarlane, and T. G. Shepherd (2002), Extended Canadian Middle Atmosphere Model: Zonal-mean climatology and physical parameterizations, *Journal of Geophysical Research: Atmospheres*, *107*(D10), ACL 9–1–ACL 9–14, doi:10.1029/2001JD000479.

Fomichev, V. I., C. Fu, J. de Grandpré, S. R. Beagley, V. P. Ogibalov, and J. C. McConnell (2004), Model thermal response to minor radiative energy sources and sinks in the middle atmosphere, *Journal of Geophysical Research: Atmospheres*, *109*(D19), doi:10.1029/2004JD004892.

Forbes, J. M. (1982a), Atmospheric tides: 1. model description and results for the solar diurnal component, *Journal of Geophysical Research: Space Physics*, *87*(A7), 5222–5240, doi:10.1029/JA087iA07p05222.

Forbes, J. M. (1982b), Atmospheric tide: 2. the solar and lunar semidiurnal components, *Journal of Geophysical Research: Space Physics*, *87*(A7), 5241–5252, doi:10.1029/JA087iA07p05241.

French, W. J. R., G. B. Burns, K. Finlayson, P. A. Greet, R. P. Lowe, and P. F. B. Williams (2000), Hydroxyl (6-2) airglow emission intensity ratios for rotational temperature determination, *Annales Geophysicae*, *18*(10), 1293–1303, doi:10.1007/s00585-000-1293-2.

Fritts, D. C., and M. J. Alexander (2003), Gravity wave dynamics and effects in the middle atmosphere, *Reviews of Geophysics*, *41*(1), doi:10.1029/2001RG000106.

Fritts, D. C., and R. A. Vincent (1987), Mesospheric momentum flux studies at Adelaide, Australia: Observations and a gravity wave-tidal interaction model, *Journal of the Atmospheric Sciences*, *44*(3), 605–619, doi:10.1175/1520-0469(1987)044<0605:MMFSAA>2.0.CO;2.

Fritts, D. C., R. B. Smith, M. J. Taylor, J. D. Doyle, S. D. Eckermann, A. Dörnbrack, M. Rapp, B. P. Williams, P.-D. Pautet, K. Bossert, N. R. Criddle, C. A. Reynolds, P. A. Reinecke, M. Uddstrom, M. J. Revell, R. Turner, B. Kaifler, J. S. Wagner, T. Mixa, C. G. Kruse, A. D. Nugent, C. D. Watson, S. Gisinger, S. M. Smith, R. S. Lieberman, B. Laughman, J. J. Moore, W. O. Brown, J. A. Haggerty, A. Rockwell, G. J. Stossmeister, S. F. Williams, G. Hernandez, D. J. Murphy, A. R. Klekociuk, I. M. Reid, and J. Ma (2016), The Deep Propagating Gravity Wave Experiment (DEEPWAVE): An airborne and ground-based exploration of gravity wave propagation and effects from

their sources throughout the lower and middle atmosphere, *Bulletin of the American Meteorological Society*, *97*(3), 425–453, doi:10.1175/BAMS-D-14-00269.1.

Fukuyama, K. (1976), Airglow variations and dynamics in the lower thermosphere and upper mesosphere-1. diurnal variation and its seasonal dependency, *Journal of Atmospheric and Terrestrial Physics*, *38*(12), 1279 – 1287, doi:https://doi.org/10.1016/0021-9169(76)90136-7.

Gao, H., J.-B. Nee, and J. Xu (2012), The emission of oxygen green line and density of O atom determined by using ISUAL and SABER measurements, *Annales Geophysicae*, *30*(4), 695–701, doi:10.5194/angeo-30-695-2012.

Gao, H., J. Xu, and G.-M. Chen (2016), The responses of the nightglow emissions observed by the TIMED/SABER satellite to solar radiation, *Journal of Geophysical Research: Space Physics*, *121*(2), 1627–1642, doi:10.1002/2015JA021624.

Garcia, R. R., and S. Solomon (1983), A numerical model of the zonally averaged dynamical and chemical structure of the middle atmosphere, *Journal of Geophysical Research: Oceans*, *88*(C2), 1379–1400, doi:10.1029/JC088iC02p01379.

Garcia, R. R., and S. Solomon (1985), The effect of breaking gravity waves on the dynamics and chemical composition of the mesosphere and lower thermosphere, *Journal of Geophysical Research: Atmospheres*, *90*(D2), 3850–3868, doi:10.1029/JD090iD02p03850.

Garcia, R. R., T. J. Dunkerton, R. S. Lieberman, and R. A. Vincent (1997), Climatology of the semiannual oscillation of the tropical middle atmosphere, *Journal of Geophysical Research: Atmospheres*, *102*(D22), 26,019–26,032, doi:10.1029/97JD00207.

Garcia, R. R., D. R. Marsh, D. E. Kinnison, B. A. Boville, and F. Sassi (2007), Simulation of secular trends in the middle atmosphere, 1950-2003, *Journal of Geophysical Research: Atmospheres*, *112*(D9), doi:10.1029/2006JD007485.

García-Comas, M., B. Funke, M. López-Puertas, D. Bermejo-Pantaleón, N. Glatthor, T. von Clarmann, G. Stiller, U. Grabowski, C. D. Boone, W. J. R. French, T. Leblanc, M. J. López-González, and M. J. Schwartz (2012), On the quality of MIPAS kinetic temperature in the middle atmosphere, *Atmospheric Chemistry and Physics*, *12*(13), 6009–6039, doi:10.5194/acp-12-6009-2012.

García-Comas, M., B. Funke, A. Gardini, M. López-Puertas, A. Jurado-Navarro, T. von Clarmann, G. Stiller, M. Kiefer, C. D. Boone, T. Leblanc, B. T. Marshall, M. J. Schwartz, and P. E. Sheese (2014), MIPAS temperature from the stratosphere to the lower thermosphere: Comparison of vM21 with ACE-FTS, MLS, OSIRIS, SABER,

SOFIE and lidar measurements, *Atmospheric Measurement Techniques*, *7*(11), 3633–3651, doi:10.5194/amt-7-3633-2014.

Goldman, A., W. Schoenfeld, D. Goorvitch, C. Chackerian, H. Dothe, F. Mélen, M. Abrams, and J. Selby (1998), Updated line parameters for OH X2∏-X2∏ (v",v') transitions, *Journal of Quantitative Spectroscopy and Radiative Transfer*, *59*(3), 453 – 469, doi:https://doi.org/10.1016/S0022-4073(97)00112-X, atmospheric Spectroscopy Applications 96.

Good, R. (1976), Determination of atomic oxygen density from rocket borne measurement of hydroxyl airglow, *Planetary and Space Science*, *24*(4), 389 – 395, doi:https://doi.org/10.1016/0032-0633(76)90052-0.

Gordon, I., L. Rothman, C. Hill, R. Kochanov, Y. Tan, P. Bernath, M. Birk, V. Boudon, A. Campargue, K. Chance, B. Drouin, J.-M. Flaud, R. Gamache, J. Hodges, D. Jacquemart, V. Perevalov, A. Perrin, K. Shine, M.-A. Smith, J. Tennyson, G. Toon, H. Tran, V. Tyuterev, A. Barbe, A. Császár, V. Devi, T. Furtenbacher, J. Harrison, J.-M. Hartmann, A. Jolly, T. Johnson, T. Karman, I. Kleiner, A. Kyuberis, J. Loos, O. Lyulin, S. Massie, S. Mikhailenko, N. Moazzen-Ahmadi, H. Müller, O. Naumenko, A. Nikitin, O. Polyansky, M. Rey, M. Rotger, S. Sharpe, K. Sung, E. Starikova, S. Tashkun, J. V. Auwera, G. Wagner, J. Wilzewski, P. Wcisło, S. Yu, and E. Zak (2017), The HITRAN2016 molecular spectroscopic database, *Journal of Quantitative Spectroscopy and Radiative Transfer*, *203*, 3 – 69, doi:https://doi.org/10.1016/j.jqsrt.2017.06.038, HITRAN2016 Special Issue.

Gottwald, M., F.-J. Diekmann, and T. Fehr (2011), ENVISAT - SCIAMACHY's host, in *SCIAMACHY - Exploring the Changing Earth's Atmosphere*, XVI, 225, Springer Netherlands, doi:10.1007/978-90-481-9896-2.

Greer, R., D. Murtagh, I. McDADE, P. Dickinson, L. Thomas, D. Jenkins, J. Stegman, E. Llewellyn, G. Witt, D. Mackinnon, and E. Williams (1986), ETON 1: A data base pertinent to the study of energy transfer in the oxygen nightglow, *Planetary and Space Science*, *34*(9), 771 – 788, doi:https://doi.org/10.1016/0032-0633(86)90074-7.

Greet, P. A., W. J. R. French, G. B. Burns, R. P. Williams, P. F. B.and Lowe, and K. Finlayson (1997), OH(6-2) spectra and rotational temperature measurements at Davis, Antarctica, *Annales Geophysicae*, *16*(1), 77–89, doi:10.1007/s00585-997-0077-3.

Grygalashvyly, M., E. Becker, and G. R. Sonnemann (2012), Gravity wave mixing and effective diffusivity for minor chemical constituents in the Mesosphere/Lower Thermosphere, *Space Science Reviews*, *168*(1), 333–362, doi:10.1007/s11214-011-9857-x.

Grygalashvyly, M., M. Eberhart, J. Hedin, B. Strelnikov, F.-J. Lübken, M. Rapp, S. Löhle, S. Fasoulas, M. Khaplanov, J. Gumbel, and E. Vorobeva (2019), Atmospheric band fitting coefficients derived from a self-consistent rocket-borne experiment, *Atmospheric Chemistry and Physics*, *19*(2), 1207–1220, doi:10.5194/acp-19-1207-2019.

Gumbel, J., D. P. Murtagh, P. J. Espy, G. Witt, and F. J. Schmidlin (1998), Odd oxygen measurements during the Noctilucent Cloud 93 rocket campaign, *Journal of Geophysical Research: Space Physics*, *103*(A10), 23,399–23,414, doi:10.1029/98JA02155.

Hagan, M. E., and J. M. Forbes (2003), Migrating and nonmigrating semidiurnal tides in the upper atmosphere excited by tropospheric latent heat release, *Journal of Geophysical Research: Space Physics*, *108*(A2), doi:10.1029/2002JA009466.

Hays, P. B., V. J. Abreu, M. E. Dobbs, D. A. Gell, H. J. Grassl, and W. R. Skinner (1993), The high-resolution doppler imager on the Upper Atmosphere Research Satellite, *Journal of Geophysical Research: Atmospheres*, *98*(D6), 10,713–10,723, doi:10.1029/93JD00409.

Hays, P. B., J. F. Kafkalidis, W. R. Skinner, and R. G. Roble (2003), A global view of the molecular oxygen night airglow, *Journal of Geophysical Research: Atmospheres*, *108*(D20), doi:10.1029/2003JD003400.

Heaps, H. S., and G. Herzberg (1952), Intensity distribution in the rotation-vibration spectrum of the OH molecule, *Zeitschrift für Physik A Hadrons and nuclei*, *133*(1), 48–64, doi:10.1007/BF01948682.

Hecht, J. H., A. Z. Liu, R. L. Walterscheid, R. G. Roble, M. F. Larsen, and J. H. Clemmons (2004), Airglow emissions and oxygen mixing ratios from the photometer experiment on the turbulent oxygen mixing experiment (tomex), *Journal of Geophysical Research: Atmospheres*, *109*(D2), doi:10.1029/2002JD003035.

Hedin, J., J. Gumbel, J. Stegman, and G. Witt (2009), Use of o_2 airglow for calibrating direct atomic oxygen measurements from sounding rockets, *Atmospheric Measurement Techniques*, *2*(2), 801–812, doi:10.5194/amt-2-801-2009.

Heller, J. W., A. B. Christensen, J. H. Yee, and W. E. Sharp (1991), Mesospheric temperature inferred from daytime observation of the O_2 atmospheric (0, 0) band system, *Journal of Geophysical Research: Space Physics*, *96*(A11), 19,499–19,505, doi:10.1029/91JA02131.

Henderson, W. R. (1974), Atomic oxygen profile measurements, *Journal of Geophysical Research (1896-1977)*, *79*(25), 3819–3826, doi:10.1029/JA079i025p03819.

Hervig, M., and D. Siskind (2006), Decadal and inter-hemispheric variability in polar mesospheric clouds, water vapor, and temperature, *Journal of Atmospheric and Solar-Terrestrial Physics*, *68*(1), 30 – 41, doi:https://doi.org/10.1016/j.jastp.2005.08.010, phenomena of the Summertime Mesosphere.

Holton, J. (2004), *An Introduction to dynamic meteorology*, International geophysics series, Academic Press.

Houghton, J., F. Taylor, and C. Rodgers (1984), *Remote sounding of atmospheres*, vol. 5, Cambridge University Press.

Huestis, D. L. (2002), *Current laboratory experiments for planetary aeronomy*, pp. 245–258, American Geophysical Union (AGU), doi:10.1029/130GM16.

Jacobi, C., K. Fröhlich, C. Viehweg, G. Stober, and D. Kürschner (2007), Midlatitude mesosphere/lower thermosphere meridional winds and temperatures measured with meteor radar, *Advances in Space Research*, *39*(8), 1278 – 1283, doi:https://doi.org/10.1016/j.asr.2007.01.003.

John, S. R., and K. K. Kumar (2012), TIMED/SABER observations of global gravity wave climatology and their interannual variability from stratosphere to mesosphere lower thermosphere, *Climate Dynamics*, *39*(6), 1489–1505, doi:10.1007/s00382-012-1329-9.

Kalicinsky, C., P. Knieling, R. Koppmann, D. Offermann, W. Steinbrecht, and J. Wintel (2016), Long-term dynamics of OH^* temperatures over central Europe: trends and solar correlations, *Atmospheric Chemistry and Physics*, *16*(23), 15,033–15,047, doi:10.5194/acp-16-15033-2016.

Kalogerakis, K. S. (2019), A previously unrecognized source of the O_2 atmospheric band emission in Earth's nightglow, *Science Advances*, *5*(3), doi:10.1126/sciadv.aau9255.

Kalogerakis, K. S., G. P. Smith, and R. A. Copeland (2011), Collisional removal of $OH(X^2\prod, v = 9)$ by O, O_2, O_3, N_2, and CO_2, *Journal of Geophysical Research: Atmospheres*, *116*(D20), doi:10.1029/2011JD015734.

Kalogerakis, K. S., D. Matsiev, R. D. Sharma, and P. P. Wintersteiner (2016), Resolving the mesospheric nighttime 4.3 μm emission puzzle: Laboratory demonstration of new mechanism for $OH(v)$ relaxation, *Geophysical Research Letters*, *43*(17), 8835–8843, doi:10.1002/2016GL069645.

Kalogerakis, K. S., D. Matsiev, P. C. Cosby, J. A. Dodd, S. Falcinelli, J. Hedin, A. A. Kutepov, S. Noll, P. A. Panka, C. Romanescu, and J. E. Thiebaud (2018),

New insights for mesospheric OH: Multi-quantum vibrational relaxation as a driver for non-local thermodynamic equilibrium, *Annales Geophysicae*, *36*(1), 13–24, doi: 10.5194/angeo-36-13-2018.

Kaufmann, M., and P. Knieling (2013), Calculation of the contamination of GRIPS spectra at 1.5 μm by OH(4-2) emissions, *Tech. rep.*, Research centre Jülich and University of Wuppertal.

Kaufmann, M., C. Lehmann, L. Hoffmann, B. Funke, M. López-Puertas, C. Savigny, and M. Riese (2008), Chemical heating rates derived from SCIAMACHY vibrationally excited OH limb emission spectra, *Advances in Space Research*, *41*(11), 1914 – 1920, doi:https://doi.org/10.1016/j.asr.2007.07.045.

Kaufmann, M., M. Ern, C. Lehmann, and M. Riese (2013), The response of atomic hydrogen to solar radiation changes, in *Climate And Weather of the Sun-Earth System (CAWSES): Highlights from a priority program*, pp. 171–188, Springer Atmospheric Sciences.

Kaufmann, M., Y. Zhu, M. Ern, and M. Riese (2014), Global distribution of atomic oxygen in the mesopause region as derived from SCIAMACHY O(^{1}S) green line measurements, *Geophysical Research Letters*, *41*(17), 6274–6280, doi:10.1002/2014GL060574.

Kaufmann, M., F. Olschewski, K. Mantel, B. Solheim, G. Shepherd, M. Deiml, J. Liu, R. Song, Q. Chen, O. Wroblowski, D. Wei, Y. Zhu, F. Wagner, F. Loosen, D. Fröhlich, T. Neubert, H. Rongen, P. Knieling, P. Toumpas, J. Shan, G. Tang, R. Koppmann, and M. Riese (2018), A highly miniaturized satellite payload based on a spatial heterodyne spectrometer for atmospheric temperature measurements in the mesosphere and lower thermosphere, *Atmospheric Measurement Techniques*, *11*(7), 3861–3870, doi:10.5194/amt-11-3861-2018.

Kaye, J. A. (1988), On the possible role of the reaction O + HO_2 $\rightarrow$ OH + O_2 in OH airglow, *Journal of Geophysical Research: Space Physics*, *93*(A1), 285–288, doi: 10.1029/JA093iA01p00285.

Khomich, V., A. Semenov, and N. Shefov (2008), *Airglow as an indicator of upper atmospheric structure and dynamics*, Springer Berlin Heidelberg.

Kim, Y., S. D. Eckermann, and H. Chun (2003), An overview of the past, present and future of gravity-wave drag parametrization for numerical climate and weather prediction models, *Atmosphere-Ocean*, *41*(1), 65–98, doi:10.3137/ao.410105.

Klenerman, D., and I. W. M. Smith (1987), Infrared chemiluminescence studies using a SISAM spectrometer. reactions producing vibrationally excited OH, *Journal of the*

Chemical Society, Faraday Transactions 2: Molecular and Chemical Physics, *83*, 229–241, doi:10.1039/F29878300229.

Knutsen, K., M. J. Dyer, and R. A. Copeland (1996), Collisional removal of OH ($X^2\prod$,v=7) by O_2 , N_2, CO_2, and N_2O, *The Journal of Chemical Physics*, *104*(15), 5798–5802, doi:10.1063/1.471311.

Koppmann, R. (2015), Lecture notes in Introduction to atmospheric physics, University of Wuppertal.

Kramer, R., S. Wüst, C. Schmidt, and M. Bittner (2015), Gravity wave characteristics in the middle atmosphere during the CESAR campaign at Palma de Mallorca in 2011/2012: Impact of extratropical cyclones and cold fronts, *Journal of Atmospheric and Solar-Terrestrial Physics*, *128*, 8 – 23, doi:https://doi.org/10.1016/j.jastp.2015.03.001.

Krasnopolsky, V. A. (2011), Excitation of the oxygen nightglow on the terrestrial planets, *Planetary and Space Science*, *59*(8), 754 – 766, doi:https://doi.org/10.1016/j.pss.2011.02.015.

Krassovsky, V., B. Potapov, A. Semenov, V. Sobolev, M. Shagaev, and N. Shefov (1977), On the equilibrium nature of the rotational temperature of hydroxyl airglow, *Planetary and Space Science*, *25*(6), 596 – 597, doi:https://doi.org/10.1016/0032-0633(77)90067-8.

Krassovsky, V. I. (1963), Chemistry of the upper atmosphere, in *Proceedings of Space Research Conference*, edited by W. Priester, p. 96.

Kyrölä, E., J. Tamminen, V. Sofieva, J. L. Bertaux, A. Hauchecorne, F. Dalaudier, D. Fussen, F. Vanhellemont, O. Fanton d'Andon, G. Barrot, M. Guirlet, A. Mangin, L. Blanot, T. Fehr, L. Saavedra de Miguel, and R. Fraisse (2010), Retrieval of atmospheric parameters from GOMOS data, *Atmospheric Chemistry and Physics*, *10*(23), 11,881–11,903, doi:10.5194/acp-10-11881-2010.

Kyrölä, E., L. Blanot, J. Tamminen, V. Sofieva, J. L. Bertaux, A. Hauchecorne, F. Dalaudier, D. Fussen, F. Vanhellemont, O. F. d'Andon, and G. Barrot (2012), Algorithm theoretical basis document version 3.0, *Tech. Rep. GOM-FMI-TN-040*, Finnish Meteorological Institute and ACRI-ST and LATMOS-IPSL and Institut d'Aéronomie Spatiale de Belgique.

Lacoursiére, J., M. J. Dyer, and R. A. Copeland (2003), Temperature dependence of the collisional energy transfer of OH(v=10) between 220 and 310 K, *The Journal of Chemical Physics*, *118*(4), 1661–1666, doi:10.1063/1.1530581.

Lange, G. (1982), Messung der infraroremission von OH^* und O_2 ($^1\Delta_G$) in der mesosphäre, Ph.D. thesis, University of Wuppertal.

Lednyts'kyy, O., C. von Savigny, K.-U. Eichmann, and M. G. Mlynczak (2015), Atomic oxygen retrievals in the MLT region from SCIAMACHY nightglow limb measurements, *Atmospheric Measurement Techniques*, *8*(3), 1021–1041, doi:10.5194/amt-8-1021-2015.

Lednyts'kyy, O., C. von Savigny, and M. Weber (2017), Sensitivity of equatorial atomic oxygen in the MLT region to the 11-year and 27-day solar cycles, *Journal of Atmospheric and Solar-Terrestrial Physics*, *162*, 136 – 150, doi:https://doi.org/10.1016/j.jastp.2016.11.003, layered Phenomena in the Mesopause Region.

Li, F., A. Z. Liu, and G. R. Swenson (2005), Characteristics of instabilities in the mesopause region over Maui, Hawaii, *Journal of Geophysical Research: Atmospheres*, *110*(D9), doi:10.1029/2004JD005097.

Lieberman, R., J. Oberheide, M. Hagan, E. Remsberg, and L. Gordley (2004), Variability of diurnal tides and planetary waves during November 1978-May 1979, *Journal of Atmospheric and Solar-Terrestrial Physics*, *66*(6), 517 – 528, doi:https://doi.org/10.1016/j.jastp.2004.01.006, dynamics and Chemistry of the MLT Region - PSMOS 2002 International Symposium.

Lieberman, R. S. (1991), Nonmigrating diurnal tides in the equatorial middle atmosphere, *Journal of the Atmospheric Sciences*, *48*(8), 1112–1123, doi:10.1175/1520-0469(1991)048<1112:NDTITE>2.0.CO;2.

Lindzen, R. S. (1967), Thermally driven diurnal tide in the atmosphere, *Quarterly Journal of the Royal Meteorological Society*, *93*(395), 18–42, doi:10.1002/qj.49709339503.

Lindzen, R. S. (1981), Turbulence and stress owing to gravity wave and tidal breakdown, *Journal of Geophysical Research: Oceans*, *86*(C10), 9707–9714, doi:10.1029/JC086iC10p09707.

Lindzen, R. S., and J. R. Holton (1968), A theory of the Quasi-Biennial Oscillation, *Journal of the Atmospheric Sciences*, *25*(6), 1095–1107, doi:10.1175/1520-0469(1968)025<1095:ATOTQB>2.0.CO;2.

Liou, K. (2002), *An Introduction to atmospheric radiation*, International Geophysics, Elsevier Science.

Liu, A. Z. (2009), Estimate eddy diffusion coefficients from gravity wave vertical momentum and heat fluxes, *Geophysical Research Letters*, *36*(8), doi:10.1029/2009GL037495.

Liu, H.-L., P. B. Hays, and R. G. Roble (1999), A numerical study of gravity wave breaking and impacts on turbulence and mean state, *Journal of the Atmospheric Sciences*, *56*(13), 2152–2177, doi:10.1175/1520-0469(1999)056<2152:ANSOGW>2.0.CO;2.

Liu, J. (2019), Study on a miniaturized satellite payload for atmospheric temperature measurements, Ph.D. thesis, University of Wuppertal.

Liu, J., D. Wei, O. Wroblowski, Q. Chen, K. Mantel, F. Olschewski, M. Kaufmann, and M. Riese (2019), Analysis and correction of distortions in a spatial heterodyne spectrometer system, *Applied Optics*, *58*(9), 2190–2197.

Liu, W., J. Xu, A. K. Smith, and W. Yuan (2015), Comparison of rotational temperature derived from ground-based OH airglow observations with TIMED/SABER to evaluate the Einstein coefficients, *Journal of Geophysical Research: Space Physics*, *120*(11), 10,069–10,082, doi:10.1002/2015JA021886.

Llewellyn, E. J., N. D. Lloyd, D. A. Degenstein, R. L. Gattinger, S. V. Petelina, A. E. Bourassa, J. T. Wiensz, E. V. Ivanov, I. C. McDade, B. H. Solheim, J. C. McConnell, C. S. Haley, C. von Savigny, C. E. Sioris, C. A. McLinden, E. Griffioen, J. Kaminski, W. F. Evans, E. Puckrin, K. Strong, V. Wehrle, R. H. Hum, D. J. Kendall, J. Matsushita, D. P. Murtagh, S. Brohede, J. Stegman, G. Witt, G. Barnes, W. F. Payne, L. Piché, K. Smith, G. Warshaw, D. L. Deslauniers, P. Marchand, E. H. Richardson, R. A. King, I. Wevers, W. McCreath, E. Kyrölä, L. Oikarinen, G. W. Leppelmeier, H. Auvinen, G. Mégie, A. Hauchecorne, F. Lefèvre, J. de La Nöe, P. Ricaud, U. Frisk, F. Sjoberg, F. von Schéele, and L. Nordh (2004), The OSIRIS instrument on the Odin spacecraft, *Canadian Journal of Physics*, *82*(6), 411–422, doi:10.1139/p04-005.

Lomb, N. R. (1976), Least-squares frequency analysis of unequally spaced data, *Astrophysics and Space Science*, *39*, 447–462, doi:10.1007/BF00648343.

London, J. (1980), Radiative energy sources and sinks in the stratosphere and mesosphere, in *Proceedings of the NATO Advanced Study Institute on Atmospheric Ozone and its Variation and Human Influences*, edited by M. Nicolet and A. C. Aikin, p. 703.

Long, D., D. Havey, M. Okumura, C. Miller, and J. Hodges (2010), O_2 A-band line parameters to support atmospheric remote sensing, *Journal of Quantitative Spectroscopy and Radiative Transfer*, *111*(14), 2021 – 2036, doi:https://doi.org/10.1016/j.jqsrt.2010.05.011.

López-González, M., E. Rodríguez, M. García-Comas, M. López-Puertas, I. Olivares, J. Ruiz-Bueno, M. Shepherd, G. Shepherd, and S. Sargoytchev (2017), Semidiurnal tidal activity of the middle atmosphere at mid-latitudes derived from O_2 atmo-

spheric and OH(6-2) airglow SATI observations, *Journal of Atmospheric and Solar-Terrestrial Physics*, *164*, 116 – 126, doi:https://doi.org/10.1016/j.jastp.2017.08.014.

Makhlouf, U. B., R. H. Picard, and J. R. Winick (1995), Photochemical-dynamical modeling of the measured response of airglow to gravity waves: 1. basic model for OH airglow, *Journal of Geophysical Research: Atmospheres*, *100*(D6), 11,289–11,311, doi:10.1029/94JD03327.

Malhotra, G., J. M. Ruohoniemi, J. B. H. Baker, R. E. Hibbins, and K. A. McWilliams (2016), HF radar observations of a quasi-biennial oscillation in midlatitude mesospheric winds, *Journal of Geophysical Research: Atmospheres*, *121*(21), 12,677–12,689, doi:10.1002/2016JD024935.

Marsh, D. R., R. R. Garcia, D. E. Kinnison, B. A. Boville, F. Sassi, S. C. Solomon, and K. Matthes (2007), Modeling the whole atmosphere response to solar cycle changes in radiative and geomagnetic forcing, *Journal of Geophysical Research: Atmospheres*, *112*(D23), n/a–n/a, doi:10.1029/2006JD008306, d23306.

Marshall, B. T., L. E. Deaver, R. E. Thompson, L. L. Gordley, M. J. McHugh, M. E. Hervig, and J. M. Russell III (2011), Retrieval of temperature and pressure using broadband solar occultation: SOFIE approach and results, *Atmospheric Measurement Techniques*, *4*(5), 893–907, doi:10.5194/amt-4-893-2011.

Massimo Cardaci, R., and Q. Lannone (2012), ENVISAT-1 products specifications - volume 10:GOMOS products specifications, *Tech. Rep. PO-RS-MDA-GS-2009/IDEAS-SER-IPF-SPE-1124*, Serco SpA.

Mayr, H. G., and J. G. Mengel (2005), Interannual variations of the diurnal tide in the mesosphere generated by the quasi-biennial oscillation, *Journal of Geophysical Research: Atmospheres*, *110*(D10), doi:10.1029/2004JD005055.

McDade, I., and E. Llewellyn (1988), Mesospheric oxygen atom densities inferred from night-time OH meinel band emission rates, *Planetary and Space Science*, *36*(9), 897 – 905, doi:https://doi.org/10.1016/0032-0633(88)90097-9, special Issue: Atomic Oxygen Abundance in Thermosphere.

McDade, I., D. Murtagh, R. Greer, P. Dickinson, G. Witt, J. Stegman, E. Llewellyn, L. Thomas, and D. Jenkins (1986), ETON 2: Quenching parameters for the proposed precursors of $O_2(b^1\sum_g^+)$ and $O(^1S)$ in the terrestrial nightglow, *Planetary and Space Science*, *34*(9), 789 – 800, doi:https://doi.org/10.1016/0032-0633(86)90075-9.

McDade, I., E. Llewellyn, R. Greer, and D. Murtagh (1987a), ETON 6: A rocket measurement of the O_2 infrared Atmospheric (0-0) band in the nightglow, *Planetary*

and Space Science, *35*(12), 1541 – 1552, doi:https://doi.org/10.1016/0032-0633(87)90079-1.

McDade, I., E. Llewellyn, D. Murtagh, and R. Greer (1987b), Eton 5: Simultaneous rocket measurements of the OH meinel $\Delta v = 2$ sequence and (8,3) band emission profiles in the nightglow, *Planetary and Space Science*, *35*(9), 1137 – 1147, doi:https://doi.org/10.1016/0032-0633(87)90020-1.

McDade, I. C. (1991), The altitude dependence of the $OH(X^2\prod)$ vibrational distribution in the nightglow: Some model expectations, *Planetary and Space Science*, *39*(7), 1049 – 1057, doi:https://doi.org/10.1016/0032-0633(91)90112-N.

McDade, I. C., and E. J. Llewellyn (1986), The photodissociation of vibrationally excited ozone in the upper atmosphere, *Journal of Photochemistry*, *32*(2), 133 – 138, doi:https://doi.org/10.1016/0047-2670(86)87001-0.

McDade, I. C., E. J. Llewellyn, R. G. H. Greer, and G. Witt (1984), Altitude dependence of the vibrational distribution of $O_2(c^1\sum_u^-)$ in the nightglow and the possible effects of vibrational excitation in the formation of $O(^1S)$, *Canadian Journal of Physics*, *62*(8), 780–788, doi:10.1139/p84-108.

Meinel, A. B. (1950a), OH emission bands in the spectrum of the night sky, *Astrophysical Journal*, *111*, 555, doi:10.1086/145296.

Meinel, A. B. (1950b), OH emission bands in the spectrum of the night sky. II., *Astrophysical Journal*, *112*, 120, doi:10.1086/145321.

Meinel, A. B. (1950c), O_2 emission bands in the infrared spectrum of the night sky, *Astrophysical Journal*, *112*, 464, doi:10.1086/145360.

Melo, S. M., H. Takahashi, B. Clemesha, P. P. Batista, and D. Simonich (1996), Atomic oxygen concentrations from rocket airglow observations in the equatorial region, *Journal of Atmospheric and Terrestrial Physics*, *58*(16), 1935 – 1942, doi:https://doi.org/10.1016/0021-9169(95)00192-1, atmospheric Studies by Optical Methods.

Melo, S. M. L., I. C. McDade, and H. Takahashi (2001), Atomic oxygen density profiles from ground-based nightglow measurements at 23∘S, *Journal of Geophysical Research: Atmospheres*, *106*(D14), 15,377–15,384, doi:10.1029/2000JD900820.

Mende, S. B., G. R. Swenson, S. P. Geller, R. A. Viereck, E. Murad, and C. P. Pike (1993), Limb view spectrum of the Earth's airglow, *Journal of Geophysical Research: Space Physics*, *98*(A11), 19,117–19,125, doi:10.1029/93JA02282.

Mertens, C. J., F. J. Schmidlin, R. A. Goldberg, E. E. Remsberg, W. D. Pesnell, J. M. Russell III, M. G. Mlynczak, M. López-Puertas, P. P. Wintersteiner, R. H. Picard, J. R. Winick, and L. L. Gordley (2004), SABER observations of mesospheric temperatures and comparisons with falling sphere measurements taken during the 2002 summer MaCWAVE campaign, *Geophysical Research Letters*, *31*(3), doi:10.1029/2003GL018605.

Mies, F. H. (1974), Calculated vibrational transition probabilities of OH($X^2\prod$), *Journal of Molecular Spectroscopy*, *53*(2), 150 – 188, doi:https://doi.org/10.1016/0022-2852(74)90125-8.

Migliorini, A., J. C. Gérard, L. Soret, G. Piccioni, F. Capaccioni, G. Filacchione, M. Snels, and F. Tosi (2015), Terrestrial OH nightglow measurements during the Rosetta flyby, *Geophysical Research Letters*, *42*(13), 5670–5677, doi:10.1002/2015GL064485.

Miller, C. E., D. Crisp, P. L. DeCola, S. C. Olsen, J. T. Randerson, A. M. Michalak, A. Alkhaled, P. Rayner, D. J. Jacob, P. Suntharalingam, D. B. A. Jones, A. S. Denning, M. E. Nicholls, S. C. Doney, S. Pawson, H. Boesch, B. J. Connor, I. Y. Fung, D. O'Brien, R. J. Salawitch, S. P. Sander, B. Sen, P. Tans, G. C. Toon, P. O. Wennberg, S. C. Wofsy, Y. L. Yung, and R. M. Law (2007), Precision requirements for space-based data, *Journal of Geophysical Research: Atmospheres*, *112*(D10), doi:10.1029/2006JD007659.

Mlynczak, M. G., and S. Solomon (1991), Middle atmosphere heating by exothermic chemical reactions involving odd-hydrogen species, *Geophysical Research Letters*, *18*(1), 37–40, doi:10.1029/90GL02672.

Mlynczak, M. G., and S. Solomon (1993), A detailed evaluation of the heating efficiency in the middle atmosphere, *Journal of Geophysical Research: Atmospheres*, *98*(D6), 10,517–10,541, doi:10.1029/93JD00315.

Mlynczak, M. G., L. H. Hunt, C. J. Mertens, B. T. Marshall, J. M. Russell, M. López Puertas, A. K. Smith, D. E. Siskind, J. C. Mast, R. E. Thompson, and L. L. Gordley (2013a), Radiative and energetic constraints on the global annual mean atomic oxygen concentration in the mesopause region, *Journal of Geophysical Research: Atmospheres*, *118*(11), 5796–5802, doi:10.1002/jgrd.50400.

Mlynczak, M. G., L. A. Hunt, B. T. Marshall, C. J. Mertens, J. M. Russell, D. Siskind, R. E. Thompson, and L. L. Gordley (2013b), Radiative constraints on the minimum atomic oxygen concentration in the mesopause region, *Geophysical Research Letters*, *40*(14), 3777–3780, doi:10.1002/grl.50725.

Mlynczak, M. G., L. A. Hunt, J. C. Mast, B. Thomas Marshall, J. M. Russell, A. K. Smith, D. E. Siskind, J.-H. Yee, C. J. Mertens, F. Javier Martin-Torres, R. Earl Thompson, D. P. Drob, and L. L. Gordley (2013c), Atomic oxygen in the mesosphere and lower thermosphere derived from SABER: Algorithm theoretical basis and measurement uncertainty, *Journal of Geophysical Research: Atmospheres*, *118*(11), 5724–5735, doi:10.1002/jgrd.50401.

Mlynczak, M. G., L. A. Hunt, B. T. Marshall, C. J. Mertens, D. R. Marsh, A. K. Smith, J. M. Russell, D. E. Siskind, and L. L. Gordley (2014), Atomic hydrogen in the mesopause region derived from SABER: Algorithm theoretical basis, measurement uncertainty, and results, *Journal of Geophysical Research: Atmospheres*, *119*(6), 3516–3526, doi:10.1002/2013JD021263, 2013JD021263.

Mlynczak, M. G., L. A. Hunt, J. M. Russell, and B. T. Marshall (2018), Updated SABER night atomic oxygen and implications for SABER ozone and atomic hydrogen, *Geophysical Research Letters*, *45*(11), 5735–5741, doi:10.1029/2018GL077377.

Murtagh, D., I. Mcdade, R. Greer, J. Stegman, G. Witt, and E. Llewellyn (1986), ETON 4: An experimental investigation of the altitude dependence of the $O_2(a^3\sum_u^+)$ vibrational populations in the nightglow, *Planetary and Space Science*, *34*(9), 811 – 817, doi:https://doi.org/10.1016/0032-0633(86)90077-2.

Murtagh, D., J. Stegman, G. Witt, E. Llewellyn, and I. McDade (1987), A twilight measurement of the OH(8-3) meinel band and atmospheric temperature, *Planetary and Space Science*, *35*(9), 1149 – 1155, doi:https://doi.org/10.1016/0032-0633(87)90021-3.

Murtagh, D., G. Witt, J. Stegman, I. McDade, E. Llewellyn, F. Harris, and R. Greer (1990), An assessment of proposed $O(^1S)$ and $O_2(b^1\sum_g^+)$ nightglow excitation parameters, *Planetary and Space Science*, *38*(1), 43 – 53, doi:https://doi.org/10.1016/0032-0633(90)90004-A.

Newnham, D. A., and J. Ballard (1998), Visible absorption cross sections and integrated absorption intensities of molecular oxygen (O_2 and O_4), *Journal of Geophysical Research: Atmospheres*, *103*(D22), 28,801–28,815, doi:10.1029/98JD02799.

Noll, S., W. Kausch, S. Kimeswenger, S. Unterguggenberger, and A. M. Jones (2015), OH populations and temperatures from simultaneous spectroscopic observations of 25 bands, *Atmospheric Chemistry and Physics*, *15*(7), 3647–3669, doi:10.5194/acp-15-3647-2015.

Noll, S., W. Kausch, S. Kimeswenger, S. Unterguggenberger, and A. M. Jones (2016), Comparison of VLT/X-shooter OH and O_2 rotational temperatures with consideration

of TIMED/SABER emission and temperature profiles, *Atmospheric Chemistry and Physics*, *16*(8), 5021–5042, doi:10.5194/acp-16-5021-2016.

Nowlan, C., C. McElroy, and J. Drummond (2007), Measurements of the O_2 A- and B-bands for determining temperature and pressure profiles from ACE-MAESTRO: Forward model and retrieval algorithm, *Journal of Quantitative Spectroscopy and Radiative Transfer*, *108*(3), 371 – 388, doi:https://doi.org/10.1016/j.jqsrt.2007.06.006.

Oberheide, J., and J. M. Forbes (2008), Tidal propagation of deep tropical cloud signatures into the thermosphere from TIMED observations, *Geophysical Research Letters*, *35*(4), doi:10.1029/2007GL032397.

Oberheide, J., M. E. Hagan, R. G. Roble, and D. Offermann (2002), Sources of nonmigrating tides in the tropical middle atmosphere, *Journal of Geophysical Research: Atmospheres*, *107*(D21), ACL 6–1–ACL 6–14, doi:10.1029/2002JD002220.

Oberheide, J., D. Offermann, J. M. Russell III, and M. G. Mlynczak (2006), Intercomparison of kinetic temperature from 15 μm CO_2 limb emissions and $OH^*(3,1)$ rotational temperature in nearly coincident air masses: SABER, GRIPS, *Geophysical Research Letters*, *33*(14), doi:10.1029/2006GL026439.

Offermann, D., and K. U. Grossmann (1973), Thermospheric density and composition as determined by a mass spectrometer with cryo ion source, *Journal of Geophysical Research*, *78*(34), 8296–8304, doi:10.1029/JA078i034p08296.

Offermann, D., V. Friedrich, P. Ross, and U. V. Zahn (1981), Neutral gas composition measurements between 80 and 120 km, *Planetary and Space Science*, *29*(7), 747 – 764, doi:https://doi.org/10.1016/0032-0633(81)90046-5.

Offermann, D., R. Gerndt, G. Lange, and H. Trinks (1983), Variations of mesopause temperatures in Europe, *Advances in Space Research*, *3*(1), 21 – 23, doi:https://doi.org/10.1016/0273-1177(83)90200-4.

Offermann, D., K.-U. Grossmann, P. Barthol, P. Knieling, M. Riese, and R. Trant (1999), Cryogenic Infrared Spectrometers and Telescopes for the Atmosphere (CRISTA) experiment and middle atmosphere variability, *Journal of Geophysical Research: Atmospheres*, *104*(D13), 16,311–16,325, doi:10.1029/1998JD100047.

Offermann, D., M. Jarisch, M. Donner, W. Steinbrecht, and A. Semenov (2006), OH temperature re-analysis forced by recent variance increases, *Journal of Atmospheric and Solar-Terrestrial Physics*, *68*(17), 1924 – 1933, doi:https://doi.org/10.1016/j.jastp.2006.03.007, long-term Trends and Short-term Variability in the Upper, Middle and Lower Atmosphere.

Offermann, D., P. Hoffmann, P. Knieling, R. Koppmann, J. Oberheide, and W. Steinbrecht (2010), Long-term trends and solar cycle variations of mesospheric temperature and dynamics, *Journal of Geophysical Research: Atmospheres*, *115*(D18), doi: 10.1029/2009JD013363.

Offermann, D., O. Goussev, C. Kalicinsky, R. Koppmann, K. Matthes, H. Schmidt, W. Steinbrecht, and J. Wintel (2015), A case study of multi-annual temperature oscillations in the atmosphere: Middle Europe, *Journal of Atmospheric and Solar-Terrestrial Physics*, *135*, 1 – 11, doi:https://doi.org/10.1016/j.jastp.2015.10.003.

Ohoyama, H., T. Kasai, Y. Yoshimura, H. Kimura, and K. Kuwata (1985), Initial distribution of vibration of the OH radicals produced in the $H + O_3 \rightarrow OH(X^2 \prod 1/2,3/2) + O_2$ reaction. chemiluminescence by a crossed beam technique, *Chemical Physics Letters*, *118*(3), 263 – 266, doi:https://doi.org/10.1016/0009-2614(85)85312-4.

Oliva, E., L. Origlia, S. Scuderi, S. Benatti, I. Carleo, E. Lapenna, A. Mucciarelli, C. Baffa, V. Biliotti, L. Carbonaro, G. Falcini, E. Giani, M. Iuzzolino, F. Massi, N. Sanna, M. Sozzi, A. Tozzi, A. Ghedina, F. Ghinassi, and M. Pedani (2015), Lines and continuum sky emission in the near infrared: Observational constraints from deep high spectral resolution spectra with GIANO-TNG, *Astronomy and Astrophysics*, *581*, doi:10.1051/0004-6361/201526291.

Ortland, D. A., P. B. Hays, W. R. Skinner, and J.-H. Yee (1998), Remote sensing of mesospheric temperature and $O_2(1\sum)$ band volume emission rates with the high-resolution Doppler imager, *Journal of Geophysical Research: Atmospheres*, *103*(D2), 1821–1835, doi:10.1029/97JD02794.

Osterbrock, D., J. Fulbright, A. Martel, M. Keane, S. Trager, and G. Basri (1996), Night-sky high-resolution spectral atlas of OH and O_2 emission lines for Echelle spectrograph wavelength valibration, *Publications of the Astronomical Society of the Pacific*, *108*, 277, doi:10.1086/133722.

Osterbrock, D. E., J. P. Fulbright, and T. A. Bida (1997), Night-sky high-resolution spectral atlas of OH emission lines for Echelle spectrograph wavelength calibration. ii., *Publications of the Astronomical Society of the Pacific*, *109*(735), 614.

Panka, P. A., A. A. Kutepov, K. S. Kalogerakis, D. Janches, J. M. Russell, L. Rezac, A. G. Feofilov, M. G. Mlynczak, and E. Yiğit (2017), Resolving the mesospheric nighttime 4.3 μm emission puzzle: Comparison of the $CO_2(\nu_3)$ and $OH(\nu)$ emission models, *Atmospheric Chemistry and Physics*, *17*(16), 9751–9760, doi:10.5194/acp-17-9751-2017.

Panka, P. A., A. A. Kutepov, L. Rezac, K. S. Kalogerakis, A. G. Feofilov, D. Marsh, D. Janches, and E. Yiğit (2018), Atomic oxygen retrieved from the SABER 2.0- and

1.6-μm radiances using new first-principles nighttime OH(v) model, *Geophysical Research Letters*, *45*(11), 5798–5803, doi:10.1029/2018GL077677.

Parameswaran, K., M. Sasi, G. Ramkumar, P. R. Nair, V. Deepa, B. Murthy, S. Nayar, K. Revathy, G. Mrudula, K. Satheesan, Y. Bhavanikumar, V. Sivakumar, K. Raghunath, T. Rajendraprasad, and M. Krishnaiah (2000), Altitude profiles of temperature from 4 to 80 km over the tropics from MST radar and lidar, *Journal of Atmospheric and Solar-Terrestrial Physics*, *62*(15), 1327 – 1337, doi:https://doi.org/10.1016/S1364-6826(00)00124-3.

Paul, B. (2008), Technical concepts orientation, rotation, velocity and acceleration, and the SRM, *Tech. rep.*, SEDRIS.

Pautet, P.-D., M. J. Taylor, W. R. Pendleton, Y. Zhao, T. Yuan, R. Esplin, and D. McLain (2014), Advanced mesospheric temperature mapper for high-latitude airglow studies, *Applied Optics*, *53*(26), 5934–5943, doi:10.1364/AO.53.005934.

Pedatella, N. M., and J. M. Forbes (2012), The quasi 2 day wave and spatial-temporal variability of the OH emission and ionosphere, *Journal of Geophysical Research: Space Physics*, *117*(A1), doi:10.1029/2011JA017186.

Perminov, V. I., A. I. Semenov, and N. N. Shefov (2007), On rotational temperature of the hydroxyl emission, *Geomagnetism and Aeronomy*, *47*(6), 756–763, doi:10.1134/S0016793207060084.

Picone, J. M., A. E. Hedin, D. P. Drob, and A. C. Aikin (2002), NRLMSISE-00 empirical model of the atmosphere: Statistical comparisons and scientific issues, *Journal of Geophysical Research: Space Physics*, *107*(A12), SIA 15–1–SIA 15–16, doi:10.1029/2002JA009430, 1468.

Pitts, M. C. (1999), Retrieval of temperature and pressure profiles for the Stratospheric Aerosol and Gas Experiment III, Ph.D. thesis, College of William and Mary.

Preusse, P., S. Schroeder, L. Hoffmann, M. Ern, F. Friedl-Vallon, J. Ungermann, H. Oelhaf, H. Fischer, and M. Riese (2009), New perspectives on gravity wave remote sensing by spaceborne infrared limb imaging, *Atmospheric Measurement Techniques*, *2*(1), 299–311, doi:10.5194/amt-2-299-2009.

Ratnam, M. V., G. K. Kumar, B. V. K. Murthy, A. K. Patra, V. V. M. J. Rao, S. V. B. Rao, K. K. Kumar, and G. Ramkumar (2008), Long-term variability of the low latitude mesospheric SAO and QBO and their relation with stratospheric QBO, *Geophysical Research Letters*, *35*(21), doi:10.1029/2008GL035390.

Remsberg, E. (2010), Observed seasonal to decadal scale responses in mesospheric water vapor, *Journal of Geophysical Research: Atmospheres*, *115*(D6), doi:10.1029/2009JD012904.

Riese, M., and R. Müller (2016), Lecture notes in Climate change: understanding the forecast, Research centre Jülich and University of Wuppertal.

Riese, M., D. Offermann, and G. Brasseur (1994), Energy released by recombination of atomic oxygen and related species at mesopause heights, *Journal of Geophysical Research: Atmospheres*, *99*(D7), 14,585–14,593, doi:10.1029/94JD00356.

Riese, M., R. Spang, P. Preusse, M. Ern, M. Jarisch, D. Offermann, and K. U. Grossmann (1999), Cryogenic Infrared Spectrometers and Telescopes for the Atmosphere (CRISTA) data processing and atmospheric temperature and trace gas retrieval, *Journal of Geophysical Research: Atmospheres*, *104*(D13), 16,349–16,367, doi:10.1029/1998JD100057.

Rigamonti, A., and P. Carretta (2009), *Structure of matter: An introductory course with problems and solutions*, Springer Milan, Milano, doi:10.1007/978-88-470-1129-8.

Roble, R. G. (1995), *Energetics of the Mesosphere and Thermosphere*, pp. 1–21, American Geophysical Union (AGU), doi:10.1029/GM087p0001.

Rodgers, C. D. (2000), *Inverse methods for atmospheric sounding: Theory and practice*, World Scientific, Singapore.

Rothman, L., I. Gordon, A. Barbe, D. Benner, P. Bernath, M. Birk, V. Boudon, L. Brown, A. Campargue, J.-P. Champion, K. Chance, L. Coudert, V. Dana, V. Devi, S. Fally, J.-M. Flaud, R. Gamache, A. Goldman, D. Jacquemart, I. Kleiner, N. Lacome, W. Lafferty, J.-Y. Mandin, S. Massie, S. Mikhailenko, C. Miller, N. Moazzen-Ahmadi, O. Naumenko, A. Nikitin, J. Orphal, V. Perevalov, A. Perrin, A. Predoi-Cross, C. Rinsland, M. Rotger, M. Šimečková, M. Smith, K. Sung, S. Tashkun, J. Tennyson, R. Toth, A. Vandaele, and J. V. Auwera (2009), The HITRAN 2008 molecular spectroscopic database, *Journal of Quantitative Spectroscopy and Radiative Transfer*, *110*(9), 533 – 572, doi:https://doi.org/10.1016/j.jqsrt.2009.02.013, HITRAN2008 special issue.

Rothman, L., I. Gordon, Y. Babikov, A. Barbe, D. C. Benner, P. Bernath, M. Birk, L. Bizzocchi, V. Boudon, L. Brown, A. Campargue, K. Chance, E. Cohen, L. Coudert, V. Devi, B. Drouin, A. Fayt, J.-M. Flaud, R. Gamache, J. Harrison, J.-M. Hartmann, C. Hill, J. Hodges, D. Jacquemart, A. Jolly, J. Lamouroux, R. L. Roy, G. Li, D. Long, O. Lyulin, C. Mackie, S. Massie, S. Mikhailenko, H. Müller, O. Naumenko, A. Nikitin, J. Orphal, V. Perevalov, A. Perrin, E. Polovtseva, C. Richard, M. Smith,

E. Starikova, K. Sung, S. Tashkun, J. Tennyson, G. Toon, V. Tyuterev, and G. Wagner (2013), The HITRAN2012 molecular spectroscopic database, *Journal of Quantitative Spectroscopy and Radiative Transfer*, *130*, 4 – 50, doi:https://doi.org/10.1016/j.jqsrt.2013.07.002, HITRAN2012 special issue.

Rottman, G. J., T. N. Woods, and W. McClintock (2006), SORCE solar UV irradiance results, *Advances in Space Research*, *37*(2), 201 – 208, doi:https://doi.org/10.1016/j.asr.2005.02.072, thermospheric-Ionospheric-Geospheric(TIGER)Symposium.

Rousselot, P., C. Lidman, J.-G. Cuby, G. Moreels, and G. Monnet (2000), Night-sky spectral atlas of OH emission lines in the near-infrared, *Astronomy and Astrophysics*, *354*, 1134–1150.

Russell, J. P., and R. P. Lowe (2003), Atomic oxygen profiles (80-94 km) derived from Wind Imaging Interferometer/Upper Atmospheric Research Satellite measurements of the hydroxyl airglow: 1. validation of technique, *Journal of Geophysical Research: Atmospheres*, *108*(D21), 4662, doi:10.1029/2003JD003454.

Russell, J. P., W. E. Ward, R. P. Lowe, R. G. Roble, G. G. Shepherd, and B. Solheim (2005), Atomic oxygen profiles (80 to 115 km) derived from Wind Imaging Interferometer/Upper Atmospheric Research Satellite measurements of the hydroxyl and greenline airglow: local time-latitude dependence, *Journal of Geophysical Research: Atmospheres*, *110*(D15), doi:10.1029/2004JD005570.

Russell III, J. M., M. G. Mlynczak, L. L. Gordley, J. J. T. Jr., and R. W. Esplin (1999), Overview of the SABER experiment and preliminary calibration results, in *Optical Spectroscopic Techniques and Instrumentation for Atmospheric and Space Research III*, vol. 3756, edited by A. M. Larar, pp. 277 – 288, International Society for Optics and Photonics, SPIE, doi:10.1117/12.366382.

Sander, S., R. Friedl, J. Barker, D. Golden, M. Kurylo, P. Wine, J. Abbatt, J. Burkholder, C. Kolb, G. Moortgat, et al. (2006), Chemical kinetics and photochemical data for use in atmospheric studies, evaluation number 15, *Tech. rep.*, Jet Propulsion Laboratory, California Institute of Technology, Pasadena, CA.

Sander, S., J. Abbatt, J. Barker, J. Burkholder, R. Friedl, D. Golden, R. Huie, M. Kurylo, G. Moortgat, V. Orkin, and P. Wine (2011), Chemical kinetics and photochemical data for use in atmospheric studies: evaluation number 17, *Tech. rep.*, Jet Propulsion Laboratory, California Institute of Technology, Pasadena, CA.

Sargoytchev, S. I., S. Brown, B. H. Solheim, Y.-M. Cho, G. G. Shepherd, and M. J. López-González (2004), Spectral airglow temperature imager (SATI): a ground-based instrument for the monitoring of mesosphere temperature, *Applied optics*, *43*(30), 5712–5721, doi:10.1364/AO.43.005712.

Scargle, J. D. (1982), Studies in astronomical time series analysis. II - statistical aspects of spectral analysis of unevenly spaced data, *Astrophysical Journal*, *263*, 835–853, doi:10.1086/160554.

Scargle, J. D. (1989), Studies in astronomical time series analysis. III. Fourier Transforms, autocorrelation functions, and cross-correlation functions of unevenly spaced data, *Astrophysical Journal*, *343*, 874, doi:10.1086/167757.

Schmidt, C., K. Höppner, and M. Bittner (2013), A ground-based spectrometer equipped with an ingaas array for routine observations of OH(3-1) rotational temperatures in the mesopause region, *Journal of Atmospheric and Solar-Terrestrial Physics*, *102*, 125 – 139, doi:https://doi.org/10.1016/j.jastp.2013.05.001.

Schmidt, H., G. P. Brasseur, M. Charron, E. Manzini, M. A. Giorgetta, T. Diehl, V. I. Fomichev, D. Kinnison, D. Marsh, and S. Walters (2006), The HAMMONIA chemistry climate model: Sensitivity of the mesopause region to the 11-year solar cycle and CO_2 doubling, *Journal of Climate*, *19*(16), 3903–3931, doi:10.1175/JCLI3829.1.

Schöch, A., G. Baumgarten, D. C. Fritts, P. Hoffmann, A. Serafimovich, L. Wang, P. Dalin, A. Müllemann, and F. J. Schmidlin (2004), Gravity waves in the troposphere and stratosphere during the MaCWAVE/MIDAS summer rocket program, *Geophysical Research Letters*, *31*(24), doi:10.1029/2004GL019837.

Sharma, R. D., P. P. Wintersteiner, and K. S. Kalogerakis (2015), A new mechanism for OH vibrational relaxation leading to enhanced CO_2 emissions in the nocturnal mesosphere, *Geophysical Research Letters*, *42*(11), 4639–4647, doi:10.1002/2015GL063724.

Sharp, W. E. (1980), Absolute concentrations of $O(^3P)$ in the lower thermosphere at night, *Geophysical Research Letters*, *7*(7), 485–488, doi:10.1029/GL007i007p00485.

Sharp, W. E. (1991), The measurement of atomic oxygen in the mesosphere and lower thermosphere, *Planetary and Space Science*, *39*(4), 617–626.

Sharp, W. E., and D. Kita (1987), In situ measurement of atomic hydrogen in the upper mesosphere, *Journal of Geophysical Research: Atmospheres*, *92*(D4), 4319–4324, doi:10.1029/JD092iD04p04319.

Sheese, P. E., E. J. Llewellyn, R. L. Gattinger, A. E. Bourassa, D. A. Degenstein, N. D. Lloyd, and I. C. McDade (2010), Temperatures in the upper mesosphere and lower thermosphere from OSIRIS observations of O_2 A-band emission spectra, *Canadian Journal of Physics*, *88*(12), 919–925, doi:10.1139/p10-093.

Sheese, P. E., I. C. McDade, R. L. Gattinger, and E. J. Llewellyn (2011), Atomic oxygen densities retrieved from Optical Spectrograph and Infrared Imaging System observations of O_2A-band airglow emission in the mesosphere and lower thermosphere, *Journal of Geophysical Research: Atmospheres*, *116*(D1), doi:10.1029/2010JD014640.

Sheese, P. E., K. Strong, E. J. Llewellyn, R. L. Gattinger, J. M. Russell III, C. D. Boone, M. E. Hervig, R. J. Sica, and J. Bandoro (2012), Assessment of the quality of OSIRIS mesospheric temperatures using satellite and ground-based measurements, *Atmospheric Measurement Techniques*, *5*(12), 2993–3006, doi:10.5194/amt-5-2993-2012.

Sheese, P. E., E. J. Llewellyn, R. L. Gattinger, and K. Strong (2014), OH meinel band nightglow profiles from OSIRIS observations, *Journal of Geophysical Research: Atmospheres*, *119*(19), 11,417–11,428, doi:10.1002/2014JD021617.

Silber, I., C. Price, C. Schmidt, S. Wüst, M. Bittner, and E. Pecora (2017), First ground-based observations of mesopause temperatures above the Eastern-Mediterranean Part I: Multi-day oscillations and tides, *Journal of Atmospheric and Solar-Terrestrial Physics*, *155*, 95 – 103, doi:https://doi.org/10.1016/j.jastp.2016.08.014.

Šimečková, M., D. Jacquemart, L. S. Rothman, R. R. Gamache, and A. Goldman (2006), Einstein A-coefficients and statistical weights for molecular absorption transitions in the HITRAN database, *Journal of Quantitative Spectroscopy and Radiative Transfer*, *98*(1), 130 – 155, doi:https://doi.org/10.1016/j.jqsrt.2005.07.003.

Siskind, D. E., D. R. Marsh, M. G. Mlynczak, F. J. Martin-Torres, and J. M. Russell (2008), Decreases in atomic hydrogen over the summer pole: Evidence for dehydration from polar mesospheric clouds?, *Geophysical Research Letters*, *35*(13), n/a–n/a, doi:10.1029/2008GL033742, l13809.

Sivjee, G. G., and R. M. Hamwey (1987), Temperature and chemistry of the polar mesopause OH, *Journal of Geophysical Research: Space Physics*, *92*(A5), 4663–4672, doi:10.1029/JA092iA05p04663.

Slanger, T., and G. Black (1979), Interactions of O_2 ($b^1\sigma_g^+$) with O(^{3}P) and O_3, *The Journal of Chemical Physics*, *70*(7), 3434–3438.

Slanger, T. G., and R. A. Copeland (2003), Energetic oxygen in the upper atmosphere and the laboratory, *Chemical Reviews*, *103*(12), 4731–4766, doi:10.1021/cr0205311, pMID: 14664631.

Slanger, T. G., D. A. Pejaković, O. Kostko, D. Matsiev, and K. S. Kalogerakis (2017), Atmospheric dayglow diagnostics involving the O_2(b-X) atmospheric band emission: Global Oxygen and Temperature (GOAT) mapping, *Journal of Geophysical Research: Space Physics*, *122*(3), 3640–3649, doi:10.1002/2016JA023502.

Smith, A., and J. Perlwitz (2015), Middle atmosphere: Planetary waves, in *Encyclopedia of Atmospheric Sciences (Second Edition)*, edited by G. R. North, J. Pyle, and F. Zhang, second edition ed., pp. 1 – 11, Academic Press, Oxford, doi:https://doi.org/10.1016/B978-0-12-382225-3.00229-2.

Smith, A. K. (2004), Physics and chemistry of the mesopause region, *Journal of Atmospheric and Solar-Terrestrial Physics*, *66*(10), 839 – 857, doi:https://doi.org/10.1016/j.jastp.2004.01.032, upper Atmosphere Tutorials from the 2001 Joint CEDAR SCOSTEP Meeting.

Smith, A. K. (2012a), Global dynamics of the MLT, *Surveys in Geophysics*, *33*(6), 1177–1230, doi:10.1007/s10712-012-9196-9.

Smith, A. K. (2012b), Interactions between the lower, middle and upper atmosphere, *Space Science Reviews*, *168*(1), 1–21, doi:10.1007/s11214-011-9791-y.

Smith, A. K., and G. P. Brasseur (1991), Numerical simulation of the seasonal variation of mesospheric water vapor, *Journal of Geophysical Research: Atmospheres*, *96*(D4), 7553–7563, doi:10.1029/91JD00226.

Smith, A. K., and D. R. Marsh (2005), Processes that account for the ozone maximum at the mesopause, *Journal of Geophysical Research: Atmospheres*, *110*(D23), doi:10.1029/2005JD006298.

Smith, A. K., D. R. Marsh, and A. C. Szymczak (2003), Interaction of chemical heating and the diurnal tide in the mesosphere, *Journal of Geophysical Research: Atmospheres*, *108*(D5), doi:10.1029/2002JD002664.

Smith, A. K., D. R. Marsh, J. M. Russell, M. G. Mlynczak, F. J. Martin-Torres, and E. Kyrölä (2008), Satellite observations of high nighttime ozone at the equatorial mesopause, *Journal of Geophysical Research: Atmospheres*, *113*(D17), n/a–n/a, doi:10.1029/2008JD010066, d17312.

Smith, A. K., D. R. Marsh, M. G. Mlynczak, and J. C. Mast (2010), Temporal variations of atomic oxygen in the upper mesosphere from SABER, *Journal of Geophysical Research: Atmospheres*, *115*(D18), doi:10.1029/2009JD013434.

Smith, A. K., R. R. Garcia, D. R. Marsh, and J. H. Richter (2011), WACCM simulations of the mean circulation and trace species transport in the winter mesosphere, *Journal of Geophysical Research: Atmospheres*, *116*(D20), doi:10.1029/2011JD016083.

Smith, A. K., M. López-Puertas, J. Xu, and M. G. Mlynczak (2015), The heating efficiency of the exothermic reaction H+O_3 in the mesosphere, *Journal of Geophysical Research: Atmospheres*, *120*(24), 12,739–12,747, doi:10.1002/2015JD024061.

Smith, G. P., and R. Robertson (2008), Temperature dependence of oxygen atom recombination in nitrogen after ozone photolysis, *Chemical Physics Letters*, *458*(1), 6 – 10, doi:https://doi.org/10.1016/j.cplett.2008.04.074.

Smith, I. W. M. (1984), The role of electronically excited states in recombination reactions, *International Journal of Chemical Kinetics*, *16*(4), 423–443, doi:10.1002/kin.550160411.

Smith, S. A., D. C. Fritts, and T. E. Vanzandt (1987), Evidence for a saturated spectrum of atmospheric gravity waves, *Journal of the Atmospheric Sciences*, *44*(10), 1404–1410, doi:10.1175/1520-0469(1987)044<1404:EFASSO>2.0.CO;2.

Sonnemann, G., and M. Grygalashvyly (2005), Solar influence on mesospheric water vapor with impact on NLCs, *Journal of Atmospheric and Solar-Terrestrial Physics*, *67*(1), 177 – 190, doi:https://doi.org/10.1016/j.jastp.2004.07.026, solar Activity Forcing of the Middle Atmosphere.

Stephens, G. (1994), *Remote sensing of the lower atmosphere: An introduction*, Oxford University Press.

Strobel, D. F. (1978), Parameterization of the atmospheric heating rate from 15 to 120 km due to O_2 and O_3 absorption of solar radiation, *Journal of Geophysical Research: Oceans*, *83*(C12), 6225–6230, doi:10.1029/JC083iC12p06225.

Sugita, T., T. Yokota, T. Nakajima, H. Nakajima, K. Waragai, M. Suzuki, A. Matsuzaki, Y. Itou, H. Saeki, and Y. Sasano (2001), Temperature and pressure retrievals from O_2 A-band absorption measurements made by ILAS: retrieval algorithm and error analyses, in *Optical Remote Sensing of the Atmosphere and Clouds II*, *Proceedings of Society of Photo-Optical Instrumentation Engineers*, vol. 4150, edited by Y. Sasano, J. Wang, and T. Hayasaka, pp. 94–105, doi:10.1117/12.416949.

Suzuki, H., K. Shiokawa, M. Tsutsumi, T. Nakamura, and M. Taguchi (2008), Atmospheric gravity waves identified by ground-based observations of the intensity and rotational temperature of OH airglow, *Polar Science*, *2*(1), 1 – 8, doi:https://doi.org/10.1016/j.polar.2007.12.002.

Suzuki, H., M. Taguchi, Y. Kanai, and N. Takeyama (2009), Fast spectrometer for ground-based observations of OH rotational temperature, *Applied Optics*, *48*(6), 1119–1127, doi:10.1364/AO.48.001119.

Suzuki, S., K. Shiokawa, Y. Otsuka, S. Kawamura, and Y. Murayama (2013), Evidence of gravity wave ducting in the mesopause region from airglow network observations, *Geophysical Research Letters*, *40*(3), 601–605, doi:10.1029/2012GL054605.

Swenson, G., Y. Yee, F. Vargas, and A. Liu (2018), Vertical diffusion transport of atomic oxygen in the mesopause region consistent with chemical losses and continuity: Global mean and inter-annual variability, *Journal of Atmospheric and Solar-Terrestrial Physics*, *178*, 47–57, doi:https://doi.org/10.1016/j.jastp.2018.05.014.

Takahashi, H., and P. P. Batista (1981), Simultaneous measurements of OH(9,4), (8,3), (7,2), (6,2) and (5,1) bands in the airglow, *Journal of Geophysical Research: Space Physics*, *86*(A7), 5632–5642, doi:10.1029/JA086iA07p05632.

Takahashi, H., Y. Sahai, and P. Batista (1984), Tidal and solar cycle effects on the OI 5577 å, NaD and OH(8,3) airglow emissions observed at 23°s, *Planetary and Space Science*, *32*(7), 897 – 902, doi:https://doi.org/10.1016/0032-0633(84)90013-8.

Takahashi, H., B. Clemesha, and P. Batista (1995), Predominant semi-annual oscillation of the upper mesospheric airglow intensities and temperatures in the equatorial region, *Journal of Atmospheric and Terrestrial Physics*, *57*(4), 407 – 414, doi:https://doi.org/10.1016/0021-9169(94)E0006-9.

Takahashi, H., D. Gobbi, P. Batista, S. Melo, N. Teixeira, and R. Buriti (1998), Dynamical influence on the equatorial airglow observed from the South American sector, *Advances in Space Research*, *21*(6), 817 – 825, doi:https://doi.org/10.1016/S0273-1177(97)00680-7, proceedings of the C0.1 Symposium of COSPAR Scientific Commission C.

Talaat, E. R., and R. S. Lieberman (1999), Nonmigrating diurnal tides in mesospheric and lower-thermospheric winds and temperatures, *Journal of the Atmospheric Sciences*, *56*(24), 4073–4087, doi:10.1175/1520-0469(1999)056<4073:NDTIMA>2.0.CO;2.

Tapping, K. F. (2013), The 10.7cm solar radio flux (F10.7), *Space Weather*, *11*(7), 394–406, doi:10.1002/swe.20064.

Taylor, M., M. Hapgood, and P. Rothwell (1987), Observations of gravity wave propagation in the OI (557.7 nm), Na (589.2 nm) and the near infrared OH nightglow emissions, *Planetary and Space Science*, *35*(4), 413 – 427, doi:https://doi.org/10.1016/0032-0633(87)90098-5.

Thomas, R. J. (1981), Analyses of atomic oxygen, the green line, and Herzberg bands in the lower thermosphere, *Journal of Geophysical Research: Space Physics*, *86*(A1), 206–210, doi:10.1029/JA086iA01p00206.

Thomas, R. J. (1990), Atomic hydrogen and atomic oxygen density in the mesopause region: Global and seasonal variations deduced from Solar Mesosphere Explorer

near-infrared emissions, *Journal of Geophysical Research: Atmospheres*, *95*(D10), 16,457–16,476, doi:10.1029/JD095iD10p16457.

Thomas, R. J., and R. A. Young (1981), Measurement of atomic oxygen and related airglows in the lower thermosphere, *Journal of Geophysical Research: Oceans*, *86*(C8), 7389–7393, doi:10.1029/JC086iC08p07389.

Tikhonov, A., and V. Arsenin (1977), *Solutions of ill-posed problems*, Scripta series in mathematics, Winston, Washington D.C., USA.

Trinks, H., D. Offermann, U. von Zahn, and C. Steinhauer (1978), Neutral composition measurements between 90- and 220-km altitude by rocket-borne mass spectrometer, *Journal of Geophysical Research*, *83*, 2169–2176, doi:10.1029/JA083iA05p02169.

Tsuda, T. (2014), Characteristics of atmospheric gravity waves observed using the MU (Middle and Upper atmosphere) radar and GPS (Global Positioning System) radio occultation, *Proceedings of the Japan Academy, Series B*, *90*(1), 12–27, doi:10.2183/pjab.90.12.

Turnbull, D., and R. Lowe (1989), New hydroxyl transition probabilities and their importance in airglow studies, *Planetary and Space Science*, *37*(6), 723 – 738, doi:https://doi.org/10.1016/0032-0633(89)90042-1.

Turnbull, D. N., and R. P. Lowe (1983), Vibrational population distribution in the hydroxyl night airglow, *Canadian Journal of Physics*, *61*(2), 244–250, doi:10.1139/p83-033.

Ulwick, J., K. Baker, D. Baker, A. Steed, W. Pendleton, K. Grossmann, and H. Brückelmann (1987), Mesospheric minor species determinations from rocket and ground-based i.r. measurements, *Journal of Atmospheric and Terrestrial Physics*, *49*(7), 855 – 862, doi:http://dx.doi.org/10.1016/0021-9169(87)90024-9.

van der Loo, M. P. J., and G. C. Groenenboom (2007), Theoretical transition probabilities for the OH Meinel system, *The Journal of Chemical Physics*, *126*(11), 114,314, doi:10.1063/1.2646859.

van der Loo, M. P. J., and G. C. Groenenboom (2008), Erratum: "Theoretical transition probabilities for the OH Meinel system" [J. Chem. Phys. 126, 114314 (2007)], *The Journal of Chemical Physics*, *128*(15), 159,902, doi:10.1063/1.2899016.

van Gijsel, J. A. E., D. P. J. Swart, J.-L. Baray, H. Bencherif, H. Claude, T. Fehr, S. Godin-Beekmann, G. H. Hansen, P. Keckhut, T. Leblanc, I. S. McDermid, Y. J. Meijer, H. Nakane, E. J. Quel, K. Stebel, W. Steinbrecht, K. B. Strawbridge, B. I.

Tatarov, and E. A. Wolfram (2010), GOMOS ozone profile validation using ground-based and balloon sonde measurements, *Atmospheric Chemistry and Physics*, *10*(21), 10,473–10,488, doi:10.5194/acp-10-10473-2010.

Varandas, A. (2004), Reactive and non-reactive vibrational quenching in O+OH collisions, *Chemical Physics Letters*, *396*(1), 182 – 190, doi:https://doi.org/10.1016/j.cplett.2004.08.023.

Vincent, R. A. (2015), The dynamics of the mesosphere and lower thermosphere: a brief review, *Progress in Earth and Planetary Science*, *2*(1), 4, doi:10.1186/s40645-015-0035-8.

Vincent, R. A., A. Hertzog, G. Boccara, and F. Vial (2007), Quasi-lagrangian superpressure balloon measurements of gravity-wave momentum fluxes in the polar stratosphere of both hemispheres, *Geophysical Research Letters*, *34*(19), doi:10.1029/2007GL031072.

Volland, H. (1988), *Atmospheric tidal and planetary waves*, Atmospheric and Oceanographic Sciences Library, Springer Netherlands, doi:10.1007/978-94-009-2861-9.

von Clarmann, T., N. Glatthor, U. Grabowski, M. Höpfner, S. Kellmann, M. Kiefer, A. Linden, G. M. Tsidu, M. Milz, T. Steck, G. P. Stiller, D. Y. Wang, H. Fischer, B. Funke, S. Gil-López, and M. López-Puertas (2003), Retrieval of temperature and tangent altitude pointing from limb emission spectra recorded from space by the Michelson Interferometer for Passive Atmospheric Sounding (MIPAS), *Journal of Geophysical Research: Atmospheres*, *108*(D23), doi:10.1029/2003JD003602.

von Savigny, C., K.-U. Eichmann, E. J. Llewellyn, H. Bovensmann, J. P. Burrows, M. Bittner, K. Hp̈pner, D. Offermann, M. J. Taylor, Y. Zhao, W. Steinbrecht, and P. Winkler (2004), First near-global retrievals of OH rotational temperatures from satellite-based Meinel band emission measurements, *Geophysical Research Letters*, *31*(15), doi:10.1029/2004GL020410.

von Savigny, C., I. C. McDade, K.-U. Eichmann, and J. P. Burrows (2012), On the dependence of the OH^* meinel emission altitude on vibrational level: SCIAMACHY observations and model simulations, *Atmospheric Chemistry and Physics*, *12*(18), 8813–8828, doi:10.5194/acp-12-8813-2012.

Wachter, P., C. Schmidt, S. Wüst, and M. Bittner (2015), Spatial gravity wave characteristics obtained from multiple OH(3-1) airglow temperature time series, *Journal of Atmospheric and Solar-Terrestrial Physics*, *135*, 192 – 201, doi:https://doi.org/10.1016/j.jastp.2015.11.008.

Wallace, J. M., and P. V. Hobbs (2006), *Atmospheric science: an introductory survey, second edition*, *International Geophysics*, vol. 92, Academic Press, San Diego.

Ward, W. E., J. Oberheide, M. Riese, P. Preusse, and D. Offermann (1999), Tidal signatures in temperature data from CRISTA 1 mission, *Journal of Geophysical Research: Atmospheres*, *104*(D13), 16,391–16,403, doi:10.1029/1998JD100109.

Williams, A., and C. Rodgers (1972), Radiative transfer by the 15 μm CO_2 band in the mesosphere, in *Proceedings of the International Radiation Symposium*, Sendai, Japan.

Williams, P. (1996), OH rotational temperatures at Davis, Antarctica, via scanning spectrometer, *Planetary and Space Science*, *44*(2), 163 – 170, doi:https://doi.org/10.1016/0032-0633(95)00126-3.

Witt, G., J. Stegman, D. Murtagh, I. McDade, R. Greer, P. Dickinson, and D. Jenkins (1984), Collisional energy transfer and the excitation of $O_2(b^1\sum_g^+)$ in the atmosphere, *Journal of Photochemistry*, *25*(2), 365 – 378, doi:https://doi.org/10.1016/0047-2670(84)87038-0.

Wu, D. L., P. Preusse, S. D. Eckermann, J. H. Jiang, M. de la Torre Juarez, L. Coy, and D. Y. Wang (2006), Remote sounding of atmospheric gravity waves with satellite limb and nadir techniques, *Advances in Space Research*, *37*(12), 2269 – 2277, doi:https://doi.org/10.1016/j.asr.2005.07.031.

Wüst, S., C. Schmidt, M. Bittner, I. Silber, C. Price, J.-H. Yee, M. G. Mlynczak, and J. M. Russell (2017), First ground-based observations of mesopause temperatures above the Eastern-Mediterranean Part II: OH^*-climatology and gravity wave activity, *Journal of Atmospheric and Solar-Terrestrial Physics*, *155*, 104 – 111, doi:https://doi.org/10.1016/j.jastp.2017.01.003.

Wüst, S., T. Offenwanger, C. Schmidt, M. Bittner, C. Jacobi, G. Stober, J.-H. Yee, M. G. Mlynczak, and J. M. Russell III (2018), Derivation of gravity wave intrinsic parameters and vertical wavelength using a single scanning OH(3-1) airglow spectrometer, *Atmospheric Measurement Techniques*, *11*(5), 2937–2947, doi:10.5194/amt-11-2937-2018.

Xu, J., A. K. Smith, W. Yuan, H.-L. Liu, Q. Wu, M. G. Mlynczak, and J. M. Russell III (2007), Global structure and long-term variations of zonal mean temperature observed by TIMED/SABER, *Journal of Geophysical Research: Atmospheres*, *112*(D24), doi:10.1029/2007JD008546.

Xu, J., A. K. Smith, H.-L. Liu, W. Yuan, Q. Wu, G. Jiang, M. G. Mlynczak, J. M. Russell III, and S. J. Franke (2009), Seasonal and quasi-biennial variations in the migrating diurnal tide observed by Thermosphere, Ionosphere, Mesosphere, Energetics and Dynamics (TIMED), *Journal of Geophysical Research: Atmospheres*, *114*(D13), doi:10.1029/2008JD011298.

Xu, J., A. K. Smith, G. Jiang, H. Gao, Y. Wei, M. G. Mlynczak, and J. M. Russell III (2010), Strong longitudinal variations in the OH nightglow, *Geophysical Research Letters*, *37*(21), doi:10.1029/2010GL043972.

Xu, J., H. Gao, A. K. Smith, and Y. Zhu (2012), Using TIMED/SABER nightglow observations to investigate hydroxyl emission mechanisms in the mesopause region, *Journal of Geophysical Research: Atmospheres*, *117*(D2), doi:10.1029/2011JD016342.

Yee, J.-H., G. Crowley, R. G. Roble, W. R. Skinner, M. D. Burrage, and P. B. Hays (1997), Global simulations and observations of $O(^1S)$, $O_2(^1\sum)$ and OH mesospheric nightglow emissions, *Journal of Geophysical Research: Space Physics*, *102*(A9), 19,949–19,968, doi:10.1029/96JA01833.

Yntema, L. (1909), On the brightness of the sky and total amount of starlight, *Publications of the Kapteyn Astronomical Laboratory Groningen*, *22*, 1–55.

Zhang, S., R. Peterson, R. Wiens, and G. Shepherd (1993), Gravity waves from O_2 nightglow during the AIDA '89 campaign I: emission rate/temperature observations, *Journal of Atmospheric and Terrestrial Physics*, *55*(3), 355 – 375, doi:https://doi.org/10.1016/0021-9169(93)90074-9, arecibo initiative dynamics of the atmosphere, AIDA act '89.

Zhu, Y. (2016), Atomic oxygen derived from SCIAMACHY $O(^1S)$ and OH airglow measurements in the Mesopause region, Ph.D. thesis, University of Wuppertal.

Zhu, Y., and M. Kaufmann (2018), Atomic oxygen abundance retrieved from SCIAMACHY hydroxyl nightglow measurements, *Geophysical Research Letters*, *45*(17), 9314–9322, doi:10.1029/2018GL079259.

Zhu, Y., and M. Kaufmann (2019), Consistent nighttime atomic oxygen concentrations from O_2 A-band, $O(^1S)$ green-line, and OH airglow measurements as performed by SCIAMACHY, *Geophysical Research Letters*, *46*(14), 8536–8545, doi:10.1029/2019GL083550.

Zhu, Y., M. Kaufmann, M. Ern, and M. Riese (2015), Nighttime atomic oxygen in the mesopause region retrieved from SCIAMACHY $O(^1S)$ green line measurements and

its response to solar cycle variation, *Journal of Geophysical Research: Space Physics*, *120*(10), 9057–9073, doi:10.1002/2015JA021405.